EXPERIMENTAL INVESTIGATION OF HEAT TRANSFER AND FLOW CHARACTERISTICS IN VARIOUS GEOMETRIES OF 2-PASS INTERNAL COOLING PASSAGES OF GAS TURBINE AIRFOILS

THÈSE N° 2670 (2002)

PRÉSENTÉE À LA FACULTÉ SCIENCES ET TECHNIQUES DE L'INGÉNIEUR

SECTION DE GÉNIE MÉCANIQUE

ÉCOLE POLYTECHNIQUE FÉDÉRALE DE LAUSANNE

POUR L'OBTENTION DU GRADE DE DOCTEUR ÈS SCIENCES TECHNIQUES

PAR

Denis CHANTELOUP

ingénieur diplômé de l'Ecole Centrale de Lille, France
et de nationalité française

acceptée sur proposition du jury:

Prof. A. Bölcs, directeur de thèse
Dr S. Parneix, rapporteur
Prof. J. Thome, rapporteur
Prof. B. Weigand, rapporteur

Lausanne, EPFL
2002

ACKNOWLEDGEMENTS

The present study has been conducted during my employment at the Laboratory of Applied Thermodynamics and Turbomachinery at the Swiss Federal Institute of Technology (EPFL-LTT). This study was funded by the Swiss Office of Science in cooperation with the Brite-Euram Internal Cooling of Turbine Blades project (contract number: BRPR-CT97-0600, project number: BE97-4022).

I would like to thank the director of the thesis, Prof. Bölcs, for his support and backing during the project. His experience and knowledge were indispensable for the successful work during the project. His leadership was very agreeable and his confidence in my work was very motivating. Many thanks go further to my friends and colleagues for the interesting discussions and advises, and also to our secretaries, Ms. Despont and Ms. Saidi, for their help.

Special thanks go to Mr. Vogel for his help with the data reduction system and to Diploma students Mr. Dunkel, Mr. D'Urbano, Mr. D'Orgeville, Mr. Juaneda and Mr. Pinguet for their valuable work on this thesis work. I would also like to thank Mr. Arzel and Ms. Hermanson for their advice during the CFD mesh generation.

This experimental study would not have been possible without the work of our technicians Mr. Mottier, Mr. Rudaz, Mr. Rougnon and Mr. Zurmühle.

Furthermore, I am grateful to Dr. B.V. Johnson and prof. B. Weigand for their assistance and advice to the project.

I would also like to thank prof. B. Weigand and Dr. S. Parneix for their participations as members of the thesis jury. A thanks is also due to Prof. P. Monkewitz for his function as president of the jury.

The development of the transient TLC technique would not have been possible without the support of Prof. Thome who agreed to lend his high speed camera and temperature measurement devices to our institute and also accepted to be a member of the jury.

Finally I would like to thank my parents for their guidance and help in all situations and Anne for her understanding, patience, and support.

ABSTRACT

An experimental investigation of the flow and heat transfer characteristics in internal coolant passages of gas turbine airfoils have been conducted.

The PIV method was employed for the flow measurements. A stereoscopic PIV system was used and automated. The stereoscopic method allowed measuring the three velocity components in measurement planes. The system was capable of measuring 100 planes in each configuration. Each measurement plane was composed of 30*30 measurement points.

The transient liquid crystal technique was adopted for the heat transfer measurements. Full surface Nusselt number distributions were obtained on all the five outer walls of the test models. The transient TLC technique was adapted in large-scale models of internal cooling channels. The gas temperature evolution in location and time was taken into account in the data processing.

CFD simulations have been performed in the measured passage configurations. For the calculations, the unstructured flow solver FLUENT/UNS was employed.

A test rig was designed and constructed for the experiments to meet the requirements of the intended investigation. For the present investigation, the test section was a large-scale model of a two-pass coolant passage with a sharp 180° bend. Four different coolant passage configurations were tested:

- A passage with 45° ribs (baseline configuration).
- A passage similar to the baseline configuration with extraction holes simulating film-cooling extraction.
- A passage with film-cooling extraction and a turning vane in the bend region.
- A passage with ribs 50% bigger than in the baseline configuration. This passage also had a turn region back wall angled at 30° to the incoming flow.

The four configurations were tested at three Reynolds numbers (25,000, 50,000, 70,000 based on the hydraulic diameter). The configurations with extraction were tested at three extractions (30%, 40%, 50% of the inlet massflow).

For the first time, the PIV and TLC techniques were employed simultaneously for a detailed investigation of the turbulent flow and heat transfer characteristics within internal coolant passages connected with 180° turns. The following conclusions can be drawn:

- 3D-streamlines were extracted from the flow measurements in the various cooling channels. The streamlines underlined the strong influence of both the ribs and the bend geometry on the creation of the secondary flow motion in the channels. The secondary flow motion dominates the heat transfer in the entire cooling channel. In the fully developed region, the rib-induced vortex governs the heat transfer distribution on the ribbed walls behind the ribs, and also on the sidewalls. In the bend region, the bend corner flow cells (with low streamwise velocity motion) deviate the bend incoming flow. They act as if the sharp bend geometry was modified. This geometry modification is very dependant on the studied configuration. The resulting heat transfer distribution is thus strongly configuration dependant.

- The regions of high heat transfer in the channels have been linked with high impinging flow regions. High gradients of mean impinging velocity components near the walls induce high heat transfer on the wall. In these regions, the Nusselt number showed a good correlation with the Reynolds normal stress corresponding to the impinging velocity.
- The configurations with extractions have the best thermal performances at all the tested Reynolds numbers. The variation of the extraction ratio does not modify substantially the thermal performances.
- CFD tools has benefited from the tremendous progress of computing power. 3D simulations of internal cooling configurations are now possible. CFD predictions have gained accuracy in such highly 3D flow problems. The predictions compared well with the measurements, with worst discrepancies of 25%.

RESUME

Des mesures d'écoulement et de transfert de chaleur ont été conduites dans des modèles de canaux de refroidissement interne d'aubes de turbines à gaz.

Les mesures d'écoulements ont été effectuées à l'aide d'un système PIV stéréoscopique. Ce système permet de mesurer les trois composantes des vecteurs vitesses. Le système de mesures a été automatisé afin de pouvoir mesurer 100 plans dans chaque configuration. Chaque plan de mesure contient 30*30 points de mesures.

La méthode cristaux liquides transitoire a été adoptée pour l'obtention des mesures de transfert de chaleur. La répartition surfacique du nombre de Nusselt a pu être obtenue sur les cinq murs extérieurs des modèles de test. La méthode cristaux liquides transitoire a été adaptée à ces modèles à grande échelle. Ainsi l'évolution en temps et en position de la température du gaz a été prise en compte dans la réduction de données.

Des simulations numériques ont été effectuées dans les géométries de test à l'aide du code de calcul non structuré FLUENT/UNS.

Un banc d'essai a été conçu et construit afin de remplir le cahier des charges des mesures à effectuer. La section de test consiste en un modèle à large échelle d'un canal de refroidissement à deux canaux droits connectés par un tournant à 180°. Quatre géométries différentes ont été testées :

- Un canal équipé de ribs à 45° (configuration de base).
- Un canal similaire à la configuration de base, muni de trous simulant l'extraction de fluide de refroidissement pour le refroidissement externe par film de l'aube.
- Un canal muni à la fois de trous d'extraction et d'un guide d'écoulement dans le tournant.
- Un canal dont les ribs sont 50% plus gros que dans les autres canaux. Ce dernier canal est aussi équipé d'un mur final du tournant orienté à 30° par rapport à l'écoulement arrivant dans le tournant.

Les quatre configurations ont été testées à trois régimes d'écoulement (Reynolds basé sur le diamètre hydraulique=25,000, 50,000 ou 70,000). L'extraction dans les configurations concernées a été ajustée à 30%, 40% ou 50% du débit massique d'entrée du canal.

Pour la première fois, les méthodes PIV stéréoscopiques et cristaux liquides ont été utilisées simultanément afin d'obtenir une description détaillée de l'écoulement turbulent et du transfert de chaleur dans des canaux à deux jambes connectées par un tournant à 180°. Les conclusions suivantes peuvent être dégagées de cette étude :

- L'extraction des lignes de courant 3D a souligné la forte influence des ribs et de la géométrie du tournant sur la création de l'écoulement secondaire dans les canaux. L'écoulement secondaire domine le transfert de chaleur dans la globalité du canal. Dans la partie pleinement développée du canal amont, le tourbillon engendré par les ribs détermine la répartition de transfert de chaleur sur les murs rugueux ainsi que sur les murs lisses. Dans le tournant,

les tourbillons d'angles dévient l'écoulement arrivant dans le tournant. Ils « modifient » la géométrie du tournant. La répartition du transfert de chaleur qui en résulte est donc très dépendante de la géométrie du tournant.

- Les régions de fort transfert de chaleur ont été reliées avec l'écoulement impactant sur les parois. Les forts gradients à la paroi de la vitesse impactante moyenne induisent un fort coefficient de transfert de chaleur sur la paroi. Dans ces régions, une corrélation peut être trouvée entre le transfert de chaleur et la vitesse impactante fluctuante.
- Les configurations avec extraction ont les meilleures performances thermiques. La variation du taux d'extraction ne modifie pas les performances thermiques.
- Les récents progrès du matériel informatique ont permis d'accroître les possibilités des simulations numériques en mécanique des fluides. Les simulations 3D dans les canaux de refroidissement interne sont maintenant possibles. La précision des simulations a augmenté. Les prédictions effectuées dans le présent travail sont justes à 25%.

TABLE OF CONTENTS

NOMENCLATURE

FLOW VARIABLES

X	Cartesian coordinate in axial direction	[m]
Y	Cartesian coordinate in cross direction	[m]
Z	Cartesian coordinate in horizontal direction	[m]
r	Cylindrical coordinate in radial direction	[m]
θ	Cylindrical coordinate in streamwise direction	[°]
U	Mean velocity component in axial (X) direction	[m/s]
V	Mean velocity component in cross (Y) direction	[m/s]
W	Mean velocity component in vertical (Z) direction	[m/s]
U_ϕ	Mean velocity component in streamwise direction in bend	[m/s]
U_r	Mean velocity component in radial direction in bend	[m/s]
u'	Fluctuating velocity component in axial direction	[m/s]
v'	Fluctuating velocity component in cross duct direction	[m/s]
w'	Fluctuating velocity component in vertical direction	[m/s]
$\overline{u'v'}$	Cartesian components of turbulent shear stress	[m^2/s^2]
$\overline{u'w'}$	Cartesian components of turbulent shear stress	[m^2/s^2]
$\overline{v'w'}$	Cartesian components of turbulent shear stress	[m^2/s^2]
U_b	Bulk mean velocity	[m/s]
$\dot{q}_m$	Massflow	[kg/s]
Re	Reynolds number : $Re = \rho U_b D_H / \mu$	
Tu	Turbulence intensity : $Tu = \sqrt{\frac{1}{3}(u'^2 + v'^2 + w'^2)} \Big/ U_b$	
Mag	Velocity magnitude : $Mag = \sqrt{U^2 + V^2 + W^2} \Big/ U_b$	
k	Turbulent kinetic energy : $k = \left\{\frac{1}{2}(u'^2 + v'^2 + w'^2)\right\} \Big/ U_b^2$	

EXTRACTION VARIABLES

SR	Local suction ratio (single hole mean velocity / local channel mean velocity)
C_{extrac}	Global suction ratio (channel inlet massflow / total extracted massflow)

GEOMETRICAL VARIABLES

D	Height and width of passage legs: 0.1 m	[m]
D_H	Hydraulic diameter D_H =D	[m]
L	Test section length	[m]
l	Accumulated length	[m]
B	Thickness of web: 0.01 m	[m]
S	Section length in bend at 90° section: 0.105 m	[m]
p	Rib pitch	[m]

e	Rib height	[m]

PIV VARIABLES

Δt	Time between exposures	[s]
N_I	Particle image density	[-]
D_I	Size of interrogation window	[-]
M	Camera Magnification	[-]
N_x	Number of vectors in horizontal direction	[-]
N_y	Number of vectors in vertical direction	[-]
d_{int}	Diameter of interrogation spot	[m]
u	In-plane velocity component	[m]
v	In-plane velocity component	[m]
w	Out-of-plane velocity component	[m]
Δz	Thickness of light sheet	[m]
Δx	Particle Displacement	[m]
L	Distance from the camera to the object plane	[m]
H	Distance of the cameras perpendicular to the object plane	[m]
β	Viewing angle	[°]

HEAT TRANSFER VARIABLES

T	Temperature	[K]
$\dot{Q}$	Heat flux	[W]
α	Heat transfer coefficient	[W/m^{2}K]
Λ	Plexiglas thermal diffusivity : $\Lambda = k/(\rho C_p)$	[m^2/s
T	Dimensionless temperature : $T = (T_{LC} - T_i)/(T_G - T_i)$	
Nu	Nusselt number : $Nu = \alpha D_H / k$	
Nu_0	Nusselt number from the Dittus-Boelter correlation	
Pr	Prandtl number	
St	Stanton number : $St = Nu/(\mathrm{Re\,Pr})$	
η	Thermal performance	

PRESSURE LOSS VARIABLES

f	Friction factor
f_0	Friction factor from the Blasius equation
C_f	Coefficient of friction : $C_f = f/4$
K_I	Pressure coefficient

STATISTICAL VARIABLES

μ_x	Mean value
Av-dev	Average deviation
$\overline{U}$	Time averaged value
T	Time interval

s^2	Sample variance
s	Sample standard deviation
σ^2	Variance
N	Sample size
$\overline{x}$	Sample mean value of x
t	Student t variable
ε	Normalized error
χ^2	Statistical variable
γ	Confidence coefficient

Other Variables

ρ	Density	[kg/m^3]
k	Thermal conductivity	[W/mK]
c_p	Specific heat	[J/kgK]
μ	Dynamic viscosity	[kg/ms]

Subscripts

b	related to bulk
θ	related to streamwise direction in bend
H	related to hydraulic diameter
r	related to radial direction in bend
G	related to gas
wall	related to the model surface
i	related to initial time
LC	related to liquid crystals
in	related to inlet

1 INTRODUCTION

Electricity and heat are important requirements for our daily life. Three basic energy sources are commonly used: conversion of primary energy in form of fossil fuels, nuclear power, and renewable energy. Nuclear energy seems to be the best suited, since it generates heat and electricity without the exhaust of greenhouse gases and therefore does not pollute the environment. However, the disposal of the nuclear waste that is produced during the energy conversion is still an unsolved problem that limits the practicability of this technique. Renewable energies in form of wind, water, and solar can produce clean energy, but unfortunately they are not always available and often require large amounts of land for the installation of power stations. Therefore, nowadays most of the energy relies on the burning of fossil fuels in form of gas or petrol.

The gas turbines work principle relies on conversion of fossil fuels (gas, petrol, oil) into energy. They are more and more often used for power generation. They provide a large range of unit sizes and fast starting times. They are often used to cover short peaks in the electricity generation. The progress in the gas turbine domain has made them competitive with steam turbines. Recent achievements in increasing cycle efficiencies and engine power have made them very interesting as stand-alone machines as well, even in domains which were formerly reserved to steam turbines.

Another application of gas turbines is transportation. They are used as engines in ground, see and air transportation (trains, ships and airplanes). As far as aero-engines are concerned, the trends currently known in civil aviation - increasing volume of air-traffic and large long-range aircrafts - were closely related to the advances in the development of aero-engines, which became more and more powerful and economic.

The basic principle of gas turbines (conversion process of primary energy in form of fossil fuels into energy) is not free from difficulties and losses. The losses must be minimized in order to ensure the optimal use of the available resources, the minimal operating costs and the protection of our environment. A further development and improvement of the underlying techniques for the conversion of the fossil energy is necessary.

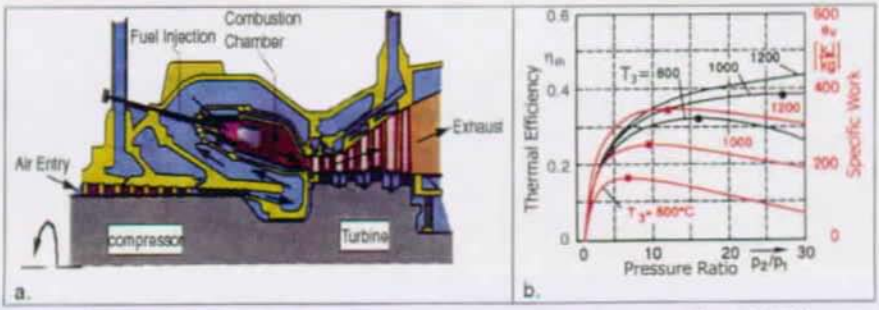

Figure 1: Brayton cycle and influence of the turbine inlet temperature on thermal efficiency and specific work (Beitz and Küttner [5]).

Gas turbines are rotational mechanical power generation devices working according to the Brayton cycle. Air at ambient conditions is drawn into the compressor where its temperature and pressure are raised. The high-pressure air proceeds into the combustion chamber where the fuel is burned at constant pressure. The resulting high temperature gas enters the turbine where it expands to atmospheric pressure. The major part of the energy gained in the turbine drives the compressor. The excess in energy can be used for production of electrical power, or to create thrust in the case of aero-engines (see Figure 1a).

The thermal efficiency of the Brayton cycle depends on the pressure ratio across the compressor part as well as the temperature level at the turbine inlet. Besides the thermal efficiency, the turbine inlet temperature also influences the specific work, which translates directly in power output that can be obtained with a given machine size (and weight). Figure 1b shows the behavior of both parameters for a real machine. It can be seen that raising the inlet temperature has the primary effect of increasing the optimum pressure ratio, which has a positive effect for both thermal efficiency and specific work output.

The maximum thermodynamic temperature of the gas turbine cycle is limited by the availability of material that can withstand high temperatures and stresses at the turbine inlet. State-of-the-art gas turbines are designed to operate at turbine inlet temperatures of approximately 1600K to 1800K (up to 2000K in aero-engine demonstrators). Modern materials can withstand temperatures of about 1200K. Effective cooling is therefore applied to the turbine components that are exposed to the hot stream. The required cooling air is usually drawn from the exit of the compressor. Gas turbines use about 15% (up to 25% in aero-engines) of the compressor mass flow for this cooling task. Since the cooling air does only partly participate in the expansion in the turbine, it causes a loss in efficiency, which counteracts the gain in efficiency that is achieved due to the higher turbine inlet temperature. Modern gas turbine design requirement focuses therefore on the optimisation of the cooling technique and the minimization of the cooling air consumption.

Nowadays, R&D activities aim at improving the capability of gas turbines through:

1.) In aero-engines: Improved cooling effectiveness, high-temperature materials with thermal barrier coating and increased flow path efficiency with reducing leakage.

2.) In land-based gas turbines: Combustion issues, high-temperature materials with thermal barrier coating and advanced turbine blade cooling.

A great effort is thus to be made in improving the blade cooling techniques.

Two kinds of cooling methods are used in turbine blade cooling: internal and external cooling. Internal cooling includes convection cooling and impingement cooling whereas external cooling techniques include local film cooling, full-coverage cooling, and transpiration cooling, e.g. in Lakshminarayana [80] (see Figure 4a).

Figure 2a shows the gain in turbine inlet temperature, which was allowed by the various cooling technique introduction over the past 50 years. Figure 2b gives the cooling effectiveness of each cooling technique (The cooling effectiveness measures how well the coolant temperature potential is used to reduce the wall temperature in respect to the hot gas temperature).

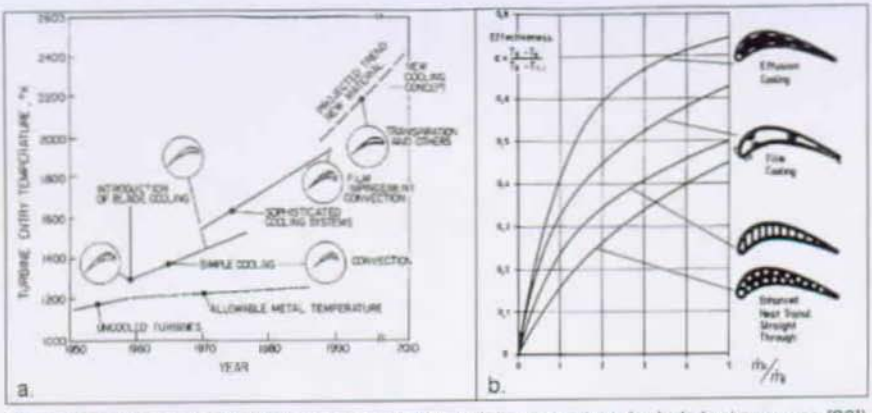

Figure 2: impact of cooling techniques on turbine inlet temperature (a: Lakshminarayana [80]) and cooling effectiveness (b: Hennecke [62]).

A one-dimensional heat transfer analysis of a gas turbine blade gives the cooling effectiveness versus a non-dimensional coolant massflow m^* and an internal coolant channel efficiency η:

$$\varepsilon = \frac{m^* \eta}{(1 + m^* \eta)} \tag{1.1}$$

The effectiveness of (1.1) can be modified when film cooling is added:

$$\varepsilon = \frac{m^* \eta + \eta_{film}(1-\eta)}{(1 + m^* \eta - \eta_{film}\eta)} \tag{1.2}$$

where η_{film} is the film cooling effectiveness.

Figure 3: Cooling effectiveness of internally cooled blades and of internally and externally (film) cooled blades

Figure 3 gives the cooling effectiveness of a gas turbine blade versus the non-dimensional coolant massflow. The results are obtained from (1.1) in the cases without film cooling and from (1.2) in the cases with film cooling ($\eta_{film} = 0.3$). Several internal channel cooling effectiveness are plotted. One conclusion of this graph is that internal cooling contributes to the major part of the blade cooling. Therefore improving the internal cooling capabilities is of high priority.

Internal cooling is achieved by coolant gas flowing in channels inside the blade. The coolant air passes through complex passages as illustrated in Figure 4. The straight sections of these coolant passages are connected by 180° turns (bends). To enhance heat transfer in the passage, ribs or pin-fins roughen the walls, and bend turning devices are installed. The prediction of the heat transfer in these coolant passages is extremely difficult. This is due to the complex fluid mechanics of the coolant flow that is influenced by the effects of curvature and roughness in the passage as well as rotation.

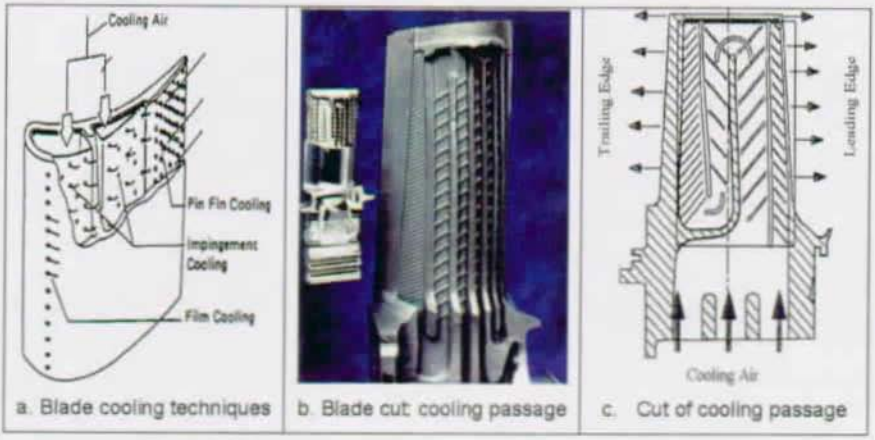

Figure 4: Blade cooling techniques – Internal cooling passages.

The major problem encountered in internal cooling is that the engine cooling system must be designed to minimise the use of compressor bleed air for cooling purposes to achieve maximum benefits of the high inlet gas temperature. There is particularly a great need to increase the understanding of heat transfer and flow characteristics within unsteady high turbulence and highly 3-D flows, which flow inside cooling channels. It is also important to determine the local heat transfer distribution in rotor coolant passages, under rotation, taking into account the effects of both Coriolis and buoyancy forces. Recent developments in numerical techniques for fluid flow and heat transfer have lead to a better understanding of these phenomena. However, the numerical heat transfer predictions are not yet sufficiently accurate for design purposes. Consequently, the analysis and design of internal coolant passages is still performed empirically based on the data collected from a large number of experiments. This is especially true for the complicated heat transfer pattern in the turning region of stationary or rotating coolant passages with rib-roughened walls.

In order to improve understanding of complex 3D flow phenomena for design purposes on the one hand, and performance of CFD tools on the other hand, detailed measurements are necessary. Detailed flow and heat transfer measurements in 45° ribbed channels connected with 180° turns are needed. The combination of the heat transfer and flow results can explain the relation between the two physical variables. The present thesis work aims at providing an understanding of these phenomena in various widely used internal coolant geometry, at several flow conditions.

2 STATE OF THE ART

The previous chapter has highlighted the need of cooling the gas turbine blades, since the gas turbine operating temperatures are far above the permissible metal temperatures. Nowadays, there is a strong development for new methods in film cooling. The reader is referred for example to the literature cited in Han et al. [53]. The present study focuses on the internal cooling, which contributes substantially to the overall efficiency of the blade. The present chapter will be limited to reviewing a few selected publications that deal with common internal cooling techniques. Other reviews are available in Weigand et al. [132], Weigand et al. [133] and Han et al. [53].

2.1 Current status

2.1.1 Heat transfer measurements in internal coolant passages

Impingement

Among all heat transfer techniques, jet impingement has the most significant potential to increase the local heat transfer coefficient. Martin [97] describes the flow and heat transfer phenomena in single impinging jets. It also gives correlations. Han and Dutta [52] gives a review of impingement cooling.

There are several arrangements possible with cooling jets and different aspects need to be considered before optimising an efficient heat transfer design. Indeed, the geometry, the number of impingement holes and the target surface geometry are very important for the effectiveness of the cooling method. Some studies focused on the effects of jet size and distribution, cooling channel cross-section, target surface shape on the heat transfer distribution (Bunker and Metzger [10]). Huang et al. [70], Florschuetz et al. [40] and Metzger et al. [98] included in their study the inline or staggered arrangement, the cross flow effect and the distances between the holes.

Turbulence promoters

Most of actual cooling channels are equipped with turbulence promoters to increase heat transfer. Literature references studied the benefit of using dimples, fin pins in the trailing edge (Terekhov et al. [122] and Moon et al. [101]) or various turbulent promoters (Delta-shape Armstrong and Winstanley [3], 3D ribs Liou and Hwang [90]). A comparison of the heat transfer performance for 12 different vortex generator geometries was also given by Liou et al. [89].

- Ribs

Very commonly used features to increase heat transfer in gas turbine blades are ribs, as they are easy to manufacture and result in a good heat transfer augmentation. The ribs trip the boundary layer periodically and cause repeating flow pattern within the passage, which lead to a high turbulence level in the core flow. Because of the technical importance of these features, a large number of papers exist about the thermal performance of turbulators.

Many studies, as for example, Webb et al. [131], Hsieh and Hong [69], Han [50], Liou and Kao [91] have focused on the effect of ribs with an angle of attack of $\beta=90°$ to the main flow direction. They found that the periodically placed ribs enhance heat

transfer and friction in the straight section of the passage. The increase in heat transfer coefficient and friction is due to the flow separation and reattachment in the vicinity of the ribs. Flow separation enhances the turbulence of core flow and reattachment results in thinner boundary layers and fluid transport from the cold bulk towards the walls. This increases the driving temperature difference and therefore the heat transfer.

Rib angle

Han et al. [58] investigated the effect of ribs with an angle of attack of β=90°, 60°, 45°, and 30° on the heat transfer and pressure drop in a square duct. The rib pitch-to-height ratio (p/e) varied from 10 to 20. They found that for both p/e ratios, best thermal performance was achieved at angles of attack of 30° and 45°. The average Nusselt number at β=30° was about 5 percent higher than at β=90° while the average friction factor was about 20-45 percent lower. At β=45°, the average heat transfer was about 25 percent larger than for β=90°, and the average friction remained the same. The results for p/e=20 showed trends similar to those of p/e=10; however, the friction and heat transfer enhancement were relatively reduced.

Several references describe area-averaged heat transfer results, performed mainly with thermocouples (Mochizuki et al. [100] and Han et al. [61]). Correlations presented in Han and Park [56] and Han and Chandra [51], have been built in single pass channel for several Re numbers and geometrical characteristics. Detailed full surface heat transfer measurements have also been published (Wang et al. [129], Rau et al. [111]).

Channel width-to-height ratio (W/H)

The impact of the channel cross-section width-to-height ratio (*W/H*) is noticeable on both flow and heat transfer characteristics. Han [50] noted that Nu/Nu_0 values increase as *W/H* increases (*W/H* range: 0.5-2). Park et al. [102] showed that the optimum channel configuration versus the thermal performances is *W/H=1* with 45° inclined ribs.

Rib pitch-to-height ratio (p/e)

Han et al. [54] and Han et al. [58] studied the influence of the rib pitch-to-height ratio (*p/e*). They showed that the channel friction factor and the heat transfer coefficient reach a maximum at *p/e=10*. The value *p/e=10* is the optimum value, since the thermal performance is also maximum.

Rib height-to hydraulic diameter ratio (e/D)

Taslim and Wadworth [121], Han et al. [54] and Han et al. [58] determined that the friction factor increases as the rib height-to hydraulic diameter ratio (*e/D*) increases. They also showed that the area-averaged Nusselt number increases as *e/D* increases. However, the thermal performances decrease as *e/D* increases. Taslim and Wadworth [121] found its optimum rib configuration to be *p/e*=8.5-10 and *e/D*=0.133.

- Film cooling flow extraction

As film cooling is an widely used cooling method for modern turbine blades, the influence of flow extraction from the internal coolant passages must be studied. Byerley et al. [12] measured local heat transfer coefficients around the entrance to a normal hole. They reported considerable heat transfer coefficient variations (six times the plain duct local value) around the entrance. Shen et al. [117] noted that in

presence of normal ribs, the heat transfer in the vicinity of the holes was increased of about 25%.

Lau et al. [85] studied the effect of the hole diameter in a coolant channel. It appeared that small-diameter holes more increase the heat transfer than large-diameter holes.

Thurman and Poinsatte [123] focused on varying bleed rates and rib placement relative to hole locations. It showed that the location of the holes near the ribs leads to a higher heat transfer than the holes located in the middle of the rib-module.

Although detailed heat transfer measurements in coolant channels with film cooling holes are available in the literature, the flow in such ducts has not been described to the author's knowledge.

- Bend region

The effect of the bend on the heat transfer in smooth and ribbed stationary passages has been experimentally studied by Johnson and Launder [74], Metzger and Sahm [99], Han and Chandra [51], Han and Zhang [59], and Ekkad and Han [35]. The secondary flows and flow separation at the tip of the web influence the heat transfer in the bend. As the flow progresses through the bend of a smooth passage, the presence of the secondary flow causes higher heat transfer on the top and bottom wall as well as on the outer wall. This was attributed to the higher turbulence of the flow and impingement in conjunction with the transport of cold fluid from the bulk towards the walls. Downstream of the bend, high turbulence mixing by flow separation and reattachment on the web leads to an additional increase of the heat transfer. In passages, where oblique ribs are mounted in the straight sections, the ribs create a secondary flow, which interacts with the curvature induced secondary flow in the bend. This leads to very complicated flow fields in the turning region.

Web thickness

Liou et al. [93] studied the flow characteristics in 180° turns with various web thickness (0.1-0.5D_H). The results showed that the upstream flow is not influenced by the web thickness. A large web thickness shortens the reattachment length of the recirculating cell at the web tip downstream of the bend.

Turning vane

The introduction, the location and the orientation of a turning vane in smooth 2-pass coolant channels, has been investigated in Plevich [104]. It was shown that turning vanes reduce the pressure losses and enhance the flow characteristics. Bonhoff et al. [7] and Schnieder et al. [116], respectively predicted and measured, flow fields, pressure drop and heat transfer in 2-pass coolant passages with and without turning vanes. They showed that the turning vane decreased the pressure drop and homogenised the heat transfer distribution in the bend. Although detailed heat transfer measurements in coolant channels with turning vanes are available in literature, to the author's knowledge the flow in such ducts has not been described from measurements.

2.1.2 Flow measurements in internal coolant passages

In the present study, the particle-image-velocimetry (PIV) method was employed for the investigation of the flow field in a model of stationary two-pass coolant passages. PIV was chosen for this study because it provides a high data acquisition

rate and a good spatial resolution of the measured flow fields. The measurement with a single-camera PIV system of the highly three-dimensional flows in coolant channels and bends can contain substantial errors. The out-of-plane motion of the tracers (perpendicular to the light sheet plane) produces a systematic measurement error depending on the distance from the optical axis, e.g. Lourenco [96]. In principle, an error correction for the in-plane components is feasible if the out-of-plane component of the flow is known. However, Schabacker and Bölcs [113] applied the correction to single-camera 3D PIV velocity measurements and showed that the effect of the out-of-plane motion cannot be corrected completely, although the correction does improve the measurement accuracy. This measurement error can be avoided by using a stereoscopic PIV setup. Prasad and Adrian [106] presented a comprehensive analysis of the translation method and an application to rotating disc flow. Westerweel and Nieuwstadt [134] reported on three-dimensional velocity measurements with an angular digital two-camera stereoscopic PIV system. A stereoscopic digital PIV system, based on the angular displacement method, was used for the present investigation. This PIV system is capable of simultaneously measuring all three velocity-components. Subsequently, an ensemble average of the velocity data in identical spatial windows is calculated to determine the mean and fluctuating velocity field. Further information on the PIV methods and hardware requirements is given in Raffel et al. [107].

Smooth channels

Laser-Doppler velocity measurements in rotating and stationary two-pass smooth passages with rounded-corner bend have been reported by Cheah et al. [27]. They provide detailed information on the flow in the bend region and the downstream flow development for the stationary and rotating passage that can be used for code validation purposes. However, the rounded outer corners in the bend did not simulate typical coolant passage geometries and the orthogonal axis of rotation used did not coincide with the typical rotation axis of a turbine blade.

Ribbed channels

- 90° ribs

Several studies described flow characteristics in idealized geometries of internal cooling channels. Rau et al. [111] showed the 3D flow, and the impinging secondary flow effects on the heat transfer distribution in a straight channel with 90° inclined ribs. They showed that the secondary flow pattern strongly determines the hot spots and cold spots in the channel.

Schabacker [112] showed that with 90° ribs in the upstream leg of the passage, three rib modules are required for the flow to reach a developed flow condition for the mean velocities. Near the ribbed walls, the turbulent kinetic energy of the flow and the Reynolds stresses reach the developed state downstream of the 5th rib module. In the duct centre, the turbulence structure is developing upstream of the 10^{th} rib module.

- 45° ribs

Schabacker [112] and Schabacker et al. [115] determined the rib presence and rib angle effects on the streamwise flow in 2-pass internal cooling channels. He also described the strong impact of the ribs on the secondary flow field. Chanteloup and Bölcs [21] studied the flow characteristics in a similar channel, with different rib locations. This geometry is the baseline case of the present thesis work. Bons and Kerrebrock [9] gave flow results in a straight smooth rotating channel, measured with

PIV. They showed the effect of both Coriolis acceleration and buoyancy, on the smooth channel flow characteristics.

Bend region

The heat transfer in the bend region of the passages is influenced by the curvature-induced secondary flow that develops there. Humphrey et al. [71] conducted a comprehensive study of turbulent flow in a 90° bend with strong curvature. From the study, they concluded that in the bend a secondary flow motion was established. The secondary flow was formed by the imbalance between the radial pressure gradient and the centrifugal force that acted on the fluid. Due to the streamline curvature, a radial pressure gradient developed across the bend section with a higher pressure near the outer radius surface. The pressure imbalance acted on the slowly moving fluid near the sidewalls of the bend and displaced it along the sidewalls from the outer to the inner radius wall. Near the symmetry plane, the turning of the high momentum fluid produced centrifugal forces that drove the flow radially towards the outer radius wall. Consequently, a secondary flow field with two counter-rotating vortices develops in the bends of stationary passages.

Schabacker et al. [114] showed that the flow in the bend region of a sharp 180° bend is characterized by the development of a strong Dean-type secondary flow. The secondary flow consists of two counter-rotating vortices that transport fluid in the bend centre from the inner walls towards the outer. Close to the outer walls, the secondary flow is convected to the inner wall. In both outer corners, zones of recirculating flow were measured. The secondary flow causes a strong impingement of the flow on the outer walls at the bend exit.

Schabacker [112] showed that the staggered 45° ribs in the upstream and downstream legs of a two-pass cooling channel connected with a sharp 180° bend, strongly influence the secondary flow field in the bend. In the centreplate of the bend, the streamwise and radial velocity components of the flow close to the outer wall are smaller than the corresponding values in the a smooth channel. However, a stronger radial velocity motion occurs near the inner wall in a passage with 90° rib arrangement. The turbulence in the bend region of the ribbed passage is higher than in a smooth channel.

Liou and Chen [88] performed LDV measurements of the developing flow through a smooth duct with a 180° straight-corner turn. Tse and Steuber [124] reported 3D LDV measurements in a rotating square serpentine coolant passage with skewed ribs. Liou et al. [92] studied the effect of different web thickness on the flow in a stationary two-pass passage. Elfert and Jarius [38] measured the flow field with 2D-PIV in a triangular passage, connected with a 180° bend.

Table 1 gives some references dealing with the various channel geometrical and flow characteristics, which were mentioned in the previous paragraphs. The list of Table 1 is not exhaustive. It gives to the reader an overview of the current published state of the art in ribbed channel internal cooling.

Channel part	Geometrical / flow characteristics	References
Straight channels (1st pass of the channel)	**Re**	Hsieh and Hong [68], Liou and Kao [95], Liou et al. [94], Faramarzi and Logan [39], Kumaran et al. [79], Taslim et al. [119], Thurman and Poinsatte [123], Rau et al. [111]
	X/D_H	Han and Park [56], Han et al. [55], Chyu and Natarajan [29], Han et al. [61], Han and Zhang [60], Lau et al. [85], Astarita and Cardone [4], Gao and Sundén [42]
	W/H	Han [50], Han and Park [56], Park et al. [102], Cardone et al. [14], Liou et al. [89], Haasenritter and Weigand [48], Takeishi and Aoki [118]
	Grooves	Zhang et al. [135]
Correlation		Hong and Hsieh [67], Han and Chandra [51], Han and Chandra [51], Han and Park [56], Han [49], Gee and Webb [44]
Ribs	**Bakward facing step**	Vogel and Eaton [126], Acharya et al. [1], Durret et al. [33]
	Rib angle	Han et al. [54], Han et al. [57], Han and Park [56], Han et al. [55], Chyu and Wu [30], Lau et al. [82], Han et al. [61], Lau et al. [84], Lau et al. [83], Han and Zhang [59], Han and Zhang [60], Lau et al. [81], Park et al. [102], Kukreja et al. [78], Mochizuki et al. [100], Ekkad et al. [37], Cho et al. [28], Gao and Sundén [42], Haasenritter and Weigand [48], Takeishi and Aoki [118]
	p/e	Webb [130], Han et al. [54], Han et al. [57], Lau et al. [84], Rau et al. [111], Cardone et al. [15]
	e/D	Han et al. [54], Han et al. [57], Taslim and Wadsworth [120]
	Rib shape	Han et al. [61], Lau et al. [84], Han and Zhang [60], Kukreja et al. [78], Rau et al. [111], Kukreja and Lau [77], Ekkad et al. [37], Liou et al. [89], Gao and Sundén [42], Chyu and Natarajan [29], Lau et al. [83], Lau et al. [81], Kukreja and Lau [77], Cho et al. [28]
	Rib placement	Han et al. [55], Lau et al. [82], Lau et al. [83]
Second pass	**General**	Chandra and Han [17], Han and Zhang [59], Ekkad and Han [36], Hirota et al. [65], Iacovides et al. [72], Cardone et al. [15], Astarita and Cardone [4], Ekkad and Han [36]
	X/D_H	Cardone et al. [14]
	Rib angle	Ekkad and Han [36]
Bend	**General**	Han and Zhang [59], Ekkad and Han [34], Cardone et al. [14], Liou et al. [93], Hirota et al. [65], Iacovides et al. [72], Cardone et al. [15], Astarita and Cardone [4]
	Re	Schnieder et al. [116]
	Turning vane	Schnieder et al. [116], Bonhoff et al. [7]
	Web	Liou et al. [93]
Film off-take holes	**General**	Byerley et al. [13], Kumaran et al. [79], Lau et al. [85], Byerley et al. [12], Taslim et al. [119], Shen et al. [117], Ekkad et al. [37], Thurman and Poinsatte [123]
	Hole length, Hole diameter	Lau et al. [85], Shen et al. [117]
	Suction ratio	Byerley et al. [13], Byerley et al. [12], Gillepsie et al. [45]
	Hole location	Thurman and Poinsatte [123]
	Hole angle	Gillepsie et al. [45]

Table 1: Literature related to measurements in internal coolant channels with ribs.

2.1.3 CFD advances in internal coolant passages

Numerical analysis becomes more and more important in the process of optimisation. 3D heat transfer calculations are run in complex geometries. Introduction of unstructured meshes has enabled meshing of internal channel geometries and calculating the complex flow patterns. Numerical investigations were able to predict the pressure loss quite well. However, accurate predictions of the heat transfer are very difficult to achieve, because of the required very good numerical resolution of the near wall layer, leading to very large grids and high computational effort. Iacovides and Launder [73] and Prakash and Zerkle [105] give reviews of calculation progress in internal cooling CFD.

Schabacker [112] compared CFD calculations and flow measurements (2D-3C PIV) in channels connected with sharp 180° turns. In a smooth channel, the flow is relatively well predicted. However, discrepancies occur in the recirculating zone prediction, at the web tip downstream of the bend. In a channel with 90° ribs, the flow development in the upstream leg is almost predicted, with small discrepancies in turbulent kinetic energy. In the bend region, the corner flow features are not captured by CFD. The recovery region in the downstream leg encounters the same problems as in the smooth channel. In a channel with 45° ribs, the flow is more complex than in a channel with 90° ribs. CFD predicts approximately the overall flow behaviour. Like in the 90° rib case, the bend corner flows are not predicted, and the recirculating cell at the web tip downstream of the bend is over predicted. The discrepancies were mainly due, according to the author, to the coarse mesh used.

More recently, Haasenritter and Weigand [48] predicted the heat transfer in a triangular channel. The heat transfer was well predicted on the ribbed walls, but showed larger differences on the smooth walls. Haasenritter et al. [47] calculated the heat transfer in a rib-module with staggered 45° ribs. A 2-layer k-epsilon turbulence model was used and gave good agreement with experiments. Rathjen et al. [109] compared mass transfer measurements and calculations in a rotating two-pass square channel with staggered 45° ribs. The numerical method seemed to be capable to predict the heat transfer in non-rotating channels, but showed significant discrepancies in rotating channels.

It can be shown, that in complex flow configurations, e.g. a flow in a ribbed channel, turbulence is far away from local isotropy, an assumption which is used in every linear eddy viscosity model Launder [86]. An improvement can be gained with a fine grid low-Reynolds-number treatment and a modeling, which can take anisotropy into account as for example the V2F-model Parneix et al. [103] or a full Reynolds stress closure without wall functions.

Bonhoff et al. [8] tested several turbulence models in a channel with staggered 45° ribs. It showed that all the turbulence models had problems in calculating accurately the heat transfer. The Reynolds Stress Model was noted to be slightly the best turbulence model. Hermanson et al. [63] tested three turbulence models (k-epsilon, 2-layer, V2F) in inclined staggered ribbed channels. It noted that that the V2F model agreed very well with measurement results. Thus the V2F model was better than the two other turbulence models.

2.2 Motivation and objective of the work

It was shown in the previous paragraphs that internal cooling of turbine blades is essential for efficient turbine engine performance. The knowledge of flow and heat transfer phenomena in internal coolant channels is a great need. Many industrial and academic institutes are working in improving this knowledge. However, despite the great efforts made in this field, several lacks of knowledge still occur:

1. *Lack of heat transfer measurements:* A few precise and detailed heat transfer measurement data are available in two-pass coolant channels. The heat transfer correlations used nowadays in the design process of internal coolant channels come mainly from straight coolant channels. There is a need of knowledge of detailed measurements in two-pass cooling channels in order to explain and understand weaknesses of current internal cooling channel configurations.
2. *Lack of combined heat transfer and flow measurements*: A few published references mention the combined effect of heat transfer and flow characteristics behind 90° ribs, but none give results behind 45° ribs and in turn regions. However, a lot of present cooling channels are multi-pass channels, equipped with 45° ribs. The knowledge of detailed flow measurements in the entire channel volume, combined with full surface heat transfer on the channel walls, is needed to understand the effect of both 45° ribs and bend geometries on the flow, and in turn on the detailed heat transfer characteristics in the channel. Furthermore, in order to develop new concepts in internal cooling channels, it is important to understand the relationship between the geometry (ribs or bend), the flow field and the heat transfer in the cooling channels. Thus spatially detailed data are needed.
3. *Lack of measurement benchmark*: Confidence in CFD can be gained if the CFD tools are validated and improved. There is a great need of benchmark for CFD prediction validation. CFD needs both flow (mean velocities and turbulence fluctuations) and heat transfer to validate and elaborate new turbulence models and meshing strategies.

The present thesis work proposes to give a contribution to the internal cooling community. The aim of the present study is to fill some of the lack mentioned previously. The objectives of the work are:

1. *Measurements*: Measurement techniques were developed in order to obtain accurate results with high spatial resolutions. Velocity and heat transfer measurements were performed in four internal cooling-channel models.
    - To present the three mean velocity components and Reynolds stresses in two-pass cooling channels connected with sharp 180° turns. A stereoscopic PIV system was automated in order to measure the flow characteristics in the full bend region volume.
    - To give the full surface heat transfer measurements on all the channel walls. A transient Thermochromic Liquid Crystal (TLC) technique has been validated and implemented in the large-scale cooling-channel models.
2. *Knowledge of heat transfer and flow phenomena*: The full surface heat transfer measurements and the full volume flow measurements are combined in the four channel models, in order to give the relationship between the flow and heat transfer.

- To show a comparison between present measurements and literature results. It gives the confidence level of the present work conclusions.
- To extend to the bend region the actual knowledge of heat transfer and flow in the fully developed region.
- To present complete flow and heat transfer sets of data in the fully developed region of a 2-pass internal coolant channel. This configuration is representative of most of current cooling channel configurations.
- The full surface heat transfer distribution of the present work allows giving an explanation of literature area-averaged heat transfer results, in the upstream leg of the channel, in the bend region and downstream of the bend.
- To relate the flow and heat transfer distributions in four coolant-channel geometries with 45° ribs, in the fully developed region, and also in the bend region.
- To show how the vortex structure influences the heat transfer distribution in the fully developed region and in the bend region of four various 2-pass coolant channels with 45° rib arrangements.
- To quantify the influence of parameter designs on the thermal performances (the Reynolds number, the rib size, the bend geometry are taken into account).

3. *Contribution to validation and improvement of current CFD tools*: CFD calculations were performed in two of the four internal cooling-channel geometries.
   - To determine and quantify discrepancies of actual numerical calculations in the measured configurations.
   - To give heat transfer and flow measurement results as a benchmark for CFD code and meshing strategy validation.

of the components. The total model test section including the test section entrance is turned 90° around the *X*-axis to obtain additional measurement planes without changing the flow conditions in the passage (Figure 6c). This allows an easy optical access for PIV measurements to the locations of interest.

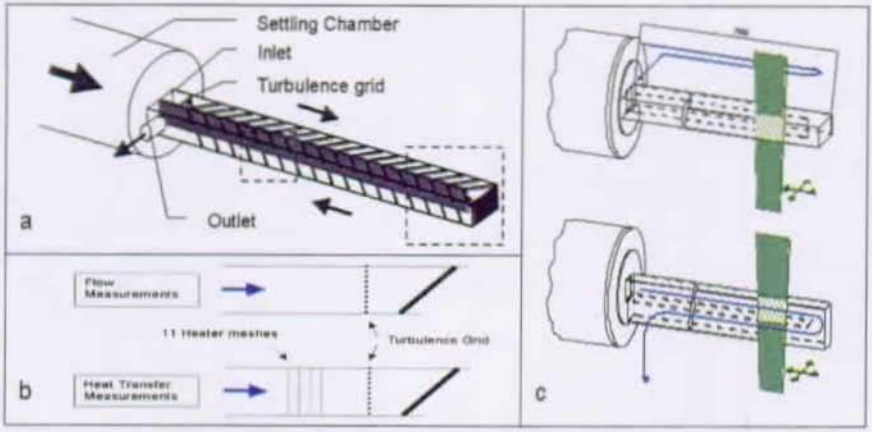

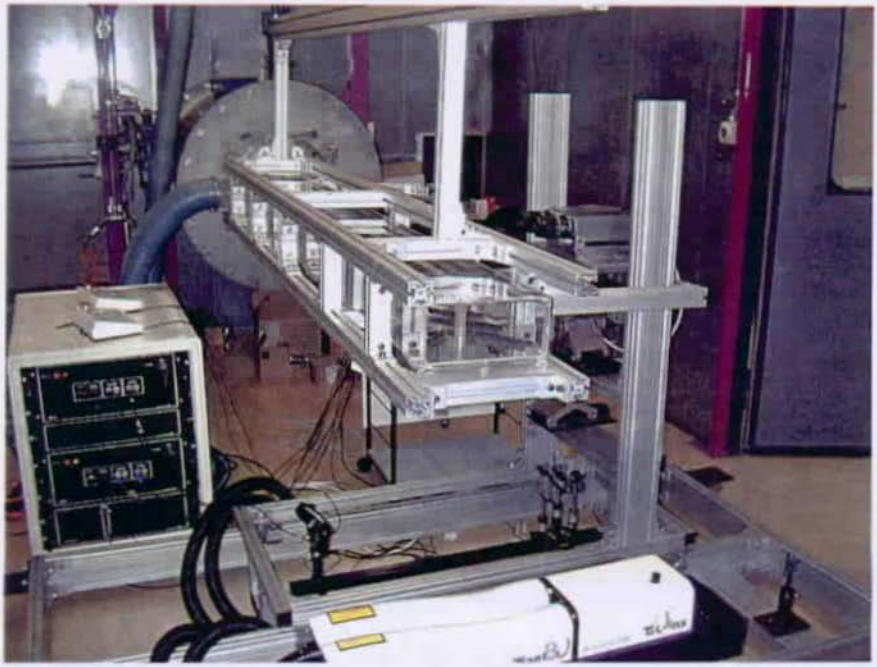

Figure 6: The internal coolant passage test facility and the stereoscopic PIV system.

3 TEST FACILITY

A test facility was designed and constructed for the present experiments. In this chapter an overview over the facility and the investigated passage models is given.

3.1 Compressor and air installation

An isothermal turbo-compressor driven by a 700 kW electric motor supplied the test rig with air. Figure 5 shows a diagram of the installation.

The massflow through the test rig is adjusted by an appropriate combination of valves. The valve 1 adjusts the total massflow through the test model. The total massflow is controlled by the flow meter A (5864S Brooks heat element flow meter). Extraction through the holes in models simulating film-cooling extraction is adjusted by increasing the inner configuration pressure level. The butterfly valve 2, far downstream of the test section exit, adjusts the backpressure. A 5864S Brooks flow meter (flow meter B), measures the exit massflow downstream of the butterfly valve. It allows adjusting the extracted massflow.

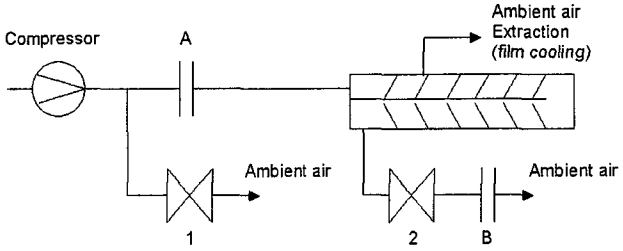

Figure 5: Air supply installation for the low wind tunnel test facility.

3.2 Test stand

A sketch of the test section is shown in Figure 6. The air enters the settling chamber with an inner diameter of 600mm via a 150mm tube and a conical entrance section with an angle of 30°. The settling chamber is equipped with a combination of perforated plates, honeycombs and meshes to reduce unsteadiness and swirl in the flow. A bell mouth entry leads the air from the settling chamber to the test channel. The regions of interest are located in the bend region and in the downstream leg, $10D_H$ downstream of the bend (see dashed boxes in Figure 6a).

The settling chamber outlet is equipped with heaters for heat transfer measurements (Figure 6b). During the flow measurements, the heaters are removed form the channel. A turbulence grid is placed downstream of the heaters in both flow and heat transfer measurements, to reach the same turbulence level at the channel inlet.

A modular concept was chosen for the test section that allows an easy exchange

3.3 Test models

Four test models were used in the scope of the present work. Geometrical characteristics are shown and summarised in Figure 7.

		Configuration			
		Base.	1	2	3
Test section length	L [D_H]	20	20	20	20
Aspect ratio	W/H	1	1	1	1
Bend cross section	S [D_H]	1	1	1	1
Length of divider plate	[D_H]	19	19.6	19	19
Thickness of divider plate	B [D_H]	0.2	0.2	0.2	0.2
Rib cross-section	[D_H^2]	0.1	0.1	0.1	0.1
Rib pitch	P [D_H]	1	1.5	1	1
Rib height	e [D_H]	0.1	0.15	0.1	0.1
Rib angle upstream leg	[deg]	45	45	45	45
Rib angle downstream leg	[deg]	45	45	45	60

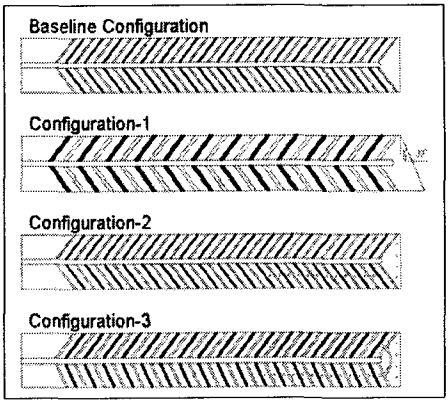

Figure 7: Definition of the test model geometries.

The baseline configuration, configuration-2 and configuration-3 have the same inner geometry characteristics. The baseline configuration test section is a two-pass, cooling passage model of a gas turbine blade. The outer walls of the test section are made of 5-mm-thick extruded Plexiglas to obtain good optical properties for the PIV experiment. The thickness of the web or web between the two passages is $0.2D_H$. The tip of the web is cylindrically shaped with a $0.1D_H$ radius. Eighteen square ribs are mounted on each of the top and bottom walls in each of the upstream and downstream passages of the model (18 * 4).

The configuration-2 has two series of holes for film cooling simulation. It has been chosen to place these holes solely in the bottom wall. The first series of holes is placed in the bend region, $0.2D_H$ apart from the end wall. Four $0.073D_H$-diameter holes are equally located between the leading and the trailing outer walls. Twelve $0.082D_H$-diameter holes are located downstream of the bend, the rib pitch to hole pitch ratio is set to 2, in order to have two holes per rib-pitch, leading to a hole pitch to hole diameter ratio of 6. This series is situated on the bottom wall downstream leg centreline ($Z = -0.6$).

The configuration-3 is also fitted with extraction holes and with a semi-circular turning vane placed inside the bend region. The $0.1D_H$ thick turning vane has a mean radius of $0.6D_H$, and is fitted with $0.1D_H$-diameter rounded tips. The tips extend up to $X = 0.05$ into the straight upstream and downstream legs.

The configuration-1 geometry differs from the others. The hydraulic diameter and P/e remains the same, but in this case, $e/D_H = 0.15$, yielding a $1.5D_H$ distance between two consecutive ribs. The bend end wall is also inclined 30° from the upstream centreline.

3.4 Coordinate system

A Cartesian coordinate system is used for the straight passages and a cylindrical coordinate system is used for the bend region. The definition of the coordinate systems in the test facility is shown in Figure 8a. The origin for both coordinate systems is set on the bottom wall at the centre of the rounded end of the web. In the Cartesian (X, Y, Z) system, X is defined as positive in the streamwise direction of the flow downstream of the bend exit, Y is defined positive vertically upwards in the horizontal test section orientation, and Z is defined as positive towards the upstream sidewall. In the cylindrical (θ, r, Y) coordinate system, the radial component r is defined as positive in the direction towards the outer wall, the streamwise component θ is defined as positive following the flow along the circular path centred on the centre of the circular bend tip, and Y is defined as in the Cartesian system.

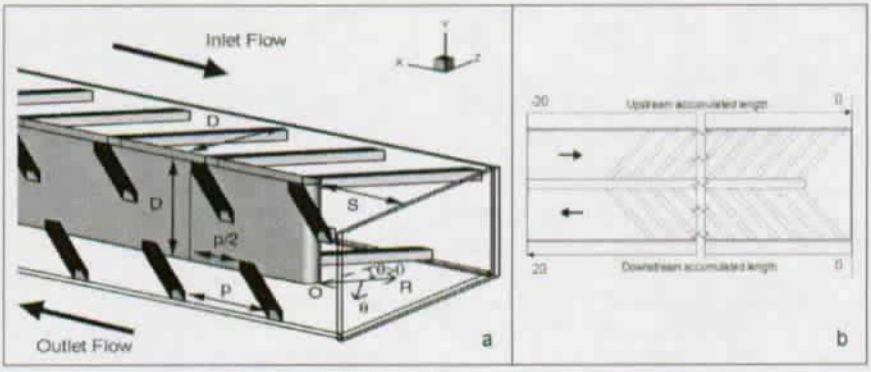

Figure 8: Definition of the coordinate systems.

The accumulated length from the channel inlet is utilised as abscissa in area-averaged heat transfer plots. The accumulated duct length is defined as the accumulated distance relative to the channel back wall in the turning region. The accumulated distance is made non-dimensional with the duct hydraulic diameter. The accumulated distance starts at $-20D_H$ at the channel entry section, continues through to $0D_H$ at the opposite back wall and ends at $+20D_H$ at the channel exit section (see Figure 8b).

3.5 Flow conditions, measurement program

The PIV measurements were obtained with air as working medium, with a flow Reynolds number of 50,000 (corresponding to a bulk velocity: $U_b = 7.58 m/s$), at the entrance of the test section. The Reynolds number is based on the 0.1 m hydraulic diameter with an air temperature of 20 C. Upstream of the test-rig, the mass flow is measured by means of a 5864S Brooks flow meter with a 1-percent accuracy. The turbulence level is approximately 3 percent at the model inlet. An experimental study was conducted to assess the effect a varying test section orientation on the flow. The small flow condition variations are within the measurement uncertainty and can

therefore be neglected for the experiments.

The static pressure and the hole massflow, were recorded for $Re = 30{,}000$, $Re = 50{,}000$ and $Re = 70{,}000$, based on the hydraulic diameter.

Heat transfer measurements were conducted with three Reynolds numbers of 25,000, 50,000, and 70,000. In the configurations simulating extraction for film cooling, the global extraction through the holes, was set to 30%, 40% and 50% of the inlet massflow. All the five outer walls of the tested channels were measured and post processed in each configuration. Measurements were made up to $6D_H$ upstream of the bend region, in the bend region and up to $6D_H$ downstream of the bend. Additional measurements were performed in a rib module $10D_H$ downstream of the bend, on all the outer walls.

		Re number								
		25 000			50 000			70 000		
Baseline Conf.	PIV meas.				X					
	HT meas.	X			X			X		
	Presure drop	X			X			X		
Configuration-1	PIV meas.				X					
	HT meas.	X			X			X		
	Presure drop	X			X			X		
		Extraction of Inlet massflow								
		30%	40%	50%	30%	40%	50%	30%	40%	50%
Configuration-3	PIV meas.						X			
	HT meas.		X	X	X	X	X	X	X	X
	Presure drop		X	X	X	X	X	X	X	X
	Hole Cd		X	X	X	X	X	X	X	X
Configuration-2	PIV meas.						X			
	HT meas.		X	X	X	X	X	X	X	X
	Presure drop		X	X	X	X	X	X	X	X
	Hole Cd		X	X	X	X	X	X	X	X

Figure 9: Test matrix of the flow and heat transfer measurements.

4 MEASUREMENT TECHNIQUES

4.1 The 2 Dimensions – 3 Components (2D-3C) PIV technique

4.1.1 Basics of PIV

The fundamental principle of the **P**article-**I**mage-**V**elocimetry (PIV) method is relatively simple. The output of a powerful light source, which is usually a laser, is transformed into a thin sheet of light that is projected into the flow. The sheet illuminates small tracer particles of suitable properties within the flow as illustrated in Figure 10. The particles scatter light into a lens that is located at a right angle to the light sheet. Since the time interval Δt between the light pulses is known, the magnitude and direction of the displacement of the particles yields the velocity. The displacements must be small enough so that $\Delta x/\Delta t$ is a good approximation of the velocity. This implies that the trajectory of the particles must be nearly straight and the speed along the trajectory should be approximately constant. This condition can be achieved by choosing Δt to be small compared to the Taylor micro scale of the Lagrangian velocity field. Either a photographic camera or a CCD video camera can be used as recording medium. PIV systems that employ CCD cameras are often referred to DPIV systems.

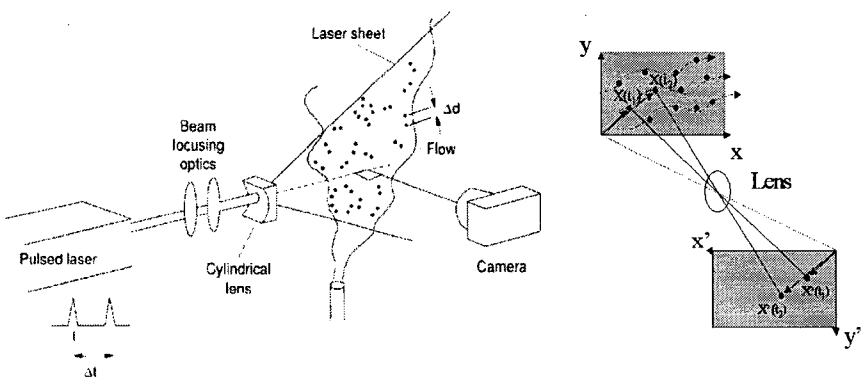

Figure 10: Principle of the PIV technique.

The progress of the PIV technique over the last years followed closely the development of computing and imaging technique. This is because of the high demands that PIV makes on these techniques. The basic set-up of a PIV system consists of:

- A light source, which is usually monochromatic in order to shape the light into a thin light sheet.
- Lenses and mirrors for the creation and the projection of the light sheet into the

test area.

- An imaging system that records the images either on photographic film or on a solid-state image array such as CCD.
- A powerful computer and software for the processing of the vector fields.

With such a system, 2D flows can be investigated. For the study of 3D flows, it is additionally helpful to have:

- A traversing system for an easy positioning of the light sheet and the imaging system into the position of interest.
- A software for the visualization of 3D flows.

The PIV method can be classified according to the number of pulses and frames that are employed (Adrian [2]).

In the simplest version, two pulses are superimposed on a single frame. It is the so-called auto-correlation method. For this method, small demands are made to the imaging device since both light pulses are recorded on the same frame. Nevertheless, a good accuracy of the measurements requires high spatial resolution of the imager, which can only be provided by photographic recordings or high-resolution CCD cameras. Furthermore, for flows without a predefined flow direction, additional devices have to be added to the system to prevent the problem of the ambiguity of the flow direction.

More advanced PIV systems record two particle images due to the first and second light pulse on two consecutive frames. Since the sequence of the frames is known, the cross-correlation between the interrogation windows in the images can be calculated to obtain the velocity magnitude and direction of the flow. The major advantage of this method is that no image-shifting device is required. Furthermore, the dynamic range of the cross-correlation estimator of single-exposed frames is larger than the one of the auto-correlation estimator if the later is formed without image shifting. The higher signal-to-noise ratio of the cross-correlation estimator also allows for smaller interrogation window sizes and therefore an increase of the spatial resolution of the vector field. More details on both methods are given in Raffel et al. [107].

The cross-correlation approach on the other hand requires very fast CCD cameras that are capable of recording the particles due to the first and second light pulse on two consecutive frames. Electronic CCD cameras that meet the requirements of cross-correlation PIV for the high-resolution measurement of three-dimensional, highly turbulent air flow became commercially available in 1996. From 1996 to 1998 (beginning of the present thesis in 1998), a digital stereoscopic PIV system has been developed. It is described in details in Schabacker [112].

4.1.2 The stereoscopic DPIV system

The PIV technique has found successful applications in flows, where the light sheet can be orientated parallel to the main flow direction. This guarantees a sufficiently small out-of-plane velocity component and ensures that most particles stay within the light sheet between exposures. However, most flows of practical interest are three-dimensional. In such flows, particles have a significant velocity component perpendicular to the light sheet.

Lourenco [96] stated that a systematic error is introduced in the measurements of three-dimensional flow due to the limitation of the paraxial assumption that is made for classical PIV. The situation is illustrated in Figure 11a, where an identical in-plane displacement Δx_0 and out-of-plane displacement Δz of a particle at 3 different positions in the object plane is assumed.

The figure reveals that due to the paraxial assumption, 3 different apparent displacements Δx_1, Δx_2, and Δx_3 will be recorded in the image plane. The error is small near the optical axis of the viewing system and increases with increasing viewing angle β. A more detailed illustration of the situation is shown in Figure 11b, which will be used for the following assessment of the perspective error. The perspective error increases with increasing out-of-plane velocity and increasing distance from the optical axis.

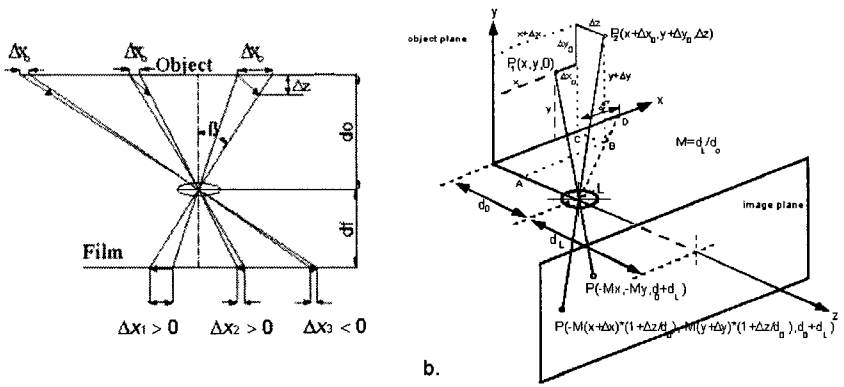

Figure 11: Perspective error induced by out-of-plane velocity.

For typical PIV measurements, this error can be significant and strongly affects the measurement accuracy. With the present DPIV, the maximum viewing angle is approximately β=4.5° (100 x 100 mm field of view, 700mm distance between lens and object-plane for a typical recording situation in the passage model). If one assumes an out-of-plane velocity W equal to the in-plane velocity U, which is reasonable in the bend region, the fractional error in the U velocity can be calculated to

$$\frac{U_{Correct} - U_{PIV}}{U_{Correct}} \approx 8\%.$$

This problem can be overcome using the stereoscopic PIV method, which measures all three velocity components simultaneously. The flow is viewed from two different directions to extract the three-dimensional motion of the particles in the light sheet plane. The stereoscopic method can roughly be divided into two different approaches: the *angular displacement method* and the *translation method* (Gauthier and Riethmuller [43]).

The PIV set-up for the translation method suffers from the small common field of view. With standard camera devices, a common field of view of approximately 30 x 100 mm^2 could be obtained, which is too small for the planned application. From

the study, it was therefore concluded that the angular displacement method is superior to the translation method for the measurements in the coolant passage.

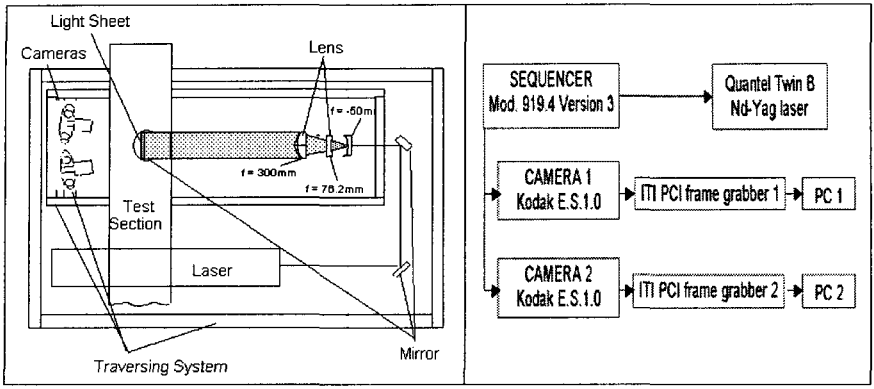

Figure 12: Arrangement of laser and lenses on the traversing system; synchronisation diagram.

The 2D-3C stereoscopic PIV is described in Figure 12.

Di-Ethyl-Exyl-Sebacat (DEHS) from TOPAS is used as light scattering droplets for the PIV experiments. This light scattering liquid appeared non-toxic, compared to olive oil or paraffin oil used in the past. A DLR- made Aerosol Generator using Laskin Nozzles generates 1-3 µm-diameter DEHS droplets. The droplets are injected upstream of the settling chamber to guarantee a homogeneous seeding density in the test section. The particles produce good light scattering in the 90° direction according to the Mie law.

A 1.5-mm thick light sheet that illuminates the particles is created by a Quantel Twins B Nd-Yag double oscillator pulsed laser. The laser provides light pulses having a maximum energy of 320mJ at a wavelength of 532 nm. The time delay between a pair of pulses can be adjusted from 1µs to 1s with pulse duration of 5 ns. A plano-concave lens (-30 mm focal length) combined with two plano-cylindrical lenses (76.2 and 300 mm focal length) transform the beam into the vertical light sheet.

The imaging system consists of two independent Kodak ES1.0 cameras, each having its own PC. A Nikon Nikkor 55mm lens is mounted on each camera. The ES1.0 has a CCD interline transfer sensor with a pixel array of 1008(H) by 1018(V) pixels. Each pixel measures nine microns square with a 60 percent fill factor using a micro lens. The camera outputs 8 bit digital images with 256 grey levels. For a typical recording situation, the cameras are placed with an oblique angle of 4.5° at a distance of 0.7m from the light sheet plane. The pulse separation time is about 40 µs. The complete system, including laser, light sheet optics and camera, is mounted on a traversing system that allows an easy traverse to the position of interest.

The laser components (flash lamp and Q-switch) and the cameras are triggered by 10Hz TTL signals that are dispatched to all the elements with specific delays. As the different delays between both Flash lamps on the one hand, and between each Flash lamp and its Pockel cell on the other hand, are all different, they are generated

by a programmable sequencer: SEQUENCER Mod.919.4, made by the DLR Goettingen. The sequencer allows the generation of complex pulse patterns on multiple channels. The pulse width, the pulse interval, the number of pulses and the output channel number are freely programmable and their resolution is of 50ns.

The frame grabber is an Imaging Technology PCI frame grabber with 2 MB memory onboard. The PCs are equipped with 384 MB RAM and 14 GB hard disk space. During the PIV measurement series, 10 images are written in real time into the PC's RAM memory. Subsequently, the acquisition is stopped and the images are saved on the hard disk. The automation of the process allows storing 5000 frames per measurement plane.

4.1.3 Data reduction

The 3D PIV measurements are obtained from the combination of two 2-dimensional vector fields; each of them measured from two different observation locations (the right and left cameras). The recordings from the right and left cameras are interrogated independently with the PIV software package VISIFLOW from AEA Technology. The cross-correlation analysis method is used with an interrogation window size of 64 by 64 pixels and 50 percent overlap between the interrogation windows. The frames provided by the cameras have a 992*992-pixel^2 resolution, which yield a 30 by 30 velocity-vector field per measurement plane. The raw data contains a small number of spurious vectors (<0.1 percent). The vector field is filtered with a predefined velocity magnitude threshold. Vectors that do not fall within the thresholds are removed and the remaining gaps are filled in with a weighted average of the surrounding vectors.

From the processed vector fields, the instantaneous three-dimensional velocity field can be reconstructed. Matlab reconstruction software was developed at the EPFL-LTT. With angular PIV systems, where both cameras observe the light sheet from the same side, the corresponding interrogation positions in the right and left images do not match in general. Therefore, a calibration of the camera system is performed which also corrects for the distortion of the images in the lenses and the Plexiglas walls of the passage. A description of the calibration procedure is given in Schabacker [112].

In addition to the mean-velocity field, the normal and shear stress quantities of the flow are required to evaluate numerical codes. In order to obtain PIV measurements in these forms, the statistical distribution of the velocity components is determined in identical spatial windows from a series of instantaneous PIV measurements. From these statistical distributions, the ensemble average and the statistical central moments are calculated to determine the desired mean-velocity field and Reynolds stresses.

4.1.4 Investigation of turbulent flows with PIV systems

4.1.4.1 Description of turbulent flow

Turbulent flows are highly complex. The principle problem for the description of a turbulent flow is that the velocity pattern of a turbulent flow is always changing and never repeats, so that even if it were possible to measure the complete sequence of

changes, the measurements would relate only to that particular experiment. General significance can therefore be attached only to the statistical specification of the velocity field, i.e. the joint probability distribution function (pdf) which determines the probability of occurrence of any combination of velocities at points in space-time. For the description of turbulent flow motion, it is convenient to decompose the velocity into a mean and a fluctuating part.

The mean part of the velocity, $\bar{U}$, is the time-averaged value

$$\bar{U} = \frac{1}{T}\int_{t_0}^{t_0+T} U(x,y,z,t)dt \tag{4.1}$$

where the time interval T is considerably longer than the period of the longest fluctuation, but shorter than the unsteadiness of the average velocity.

The fluctuating part of the velocity, u', is that time varying portion that differs from the average value

$$U = \bar{U} + u' \tag{4.2}$$

It can be shown that the time average of the fluctuations is zero (Hinze [64]), since the fluctuations are equally distributed on either side of the average. However, the average of the square of the fluctuating quantity is positive. Thus, Equation is

$$\overline{u'^2} = \frac{1}{T}\int_{t_0}^{t_0+T} (u'^2)dt > 0 \tag{4.3}$$

The contribution of the turbulent flow motion to the kinetic energy of the mean motion is defined as the turbulent kinetic energy

$$k = \frac{1}{2}(\overline{u'^2} + \overline{v'^2} + \overline{w'^2}) \tag{4.4}$$

If the concept of decomposing the turbulent velocity into mean and fluctuating velocity components is introduced into the Navier-Stokes equations of motion of a fluid, a new set of equations is obtained, Frost and Moulden [41].

One important feature of the resulting Reynolds equations is the additional apparent turbulent shear stress tensor

$$-\rho\overline{u_i u_j} = -\rho\begin{pmatrix} \overline{u'^2} & \overline{u'v'} & \overline{u'w'} \\ \overline{v'u'} & \overline{v'^2} & \overline{u'w'} \\ \overline{w'u'} & \overline{w'v'} & \overline{w'^2} \end{pmatrix} \tag{4.5}$$

This tensor describes the contribution of the turbulent random fluctuations to the shear stresses that occur in the flow.

4.1.4.2 Statistics of turbulent flow

Since turbulent flow motion cannot be covered by an explicit mathematical relationship, statistical methods have to be employed for the description of the flow. A turbulent flow therefore is considered to be known if the probability density distribution of the turbulent velocity components can be determined. However, this is very often

not possible in practice. For this reason, the random field of the turbulent flow is characterized by statistical properties.

In a turbulent flow, velocity is the primary variable of interest. For the description of a three-dimensional turbulent velocity field, the three velocity components must be known. The turbulent velocity field can therefore be understood as a random vector field. Each one of the velocity components making up the field is a random variable, and the prediction of the probability of a given velocity at some point in space and time in a three-dimensional probability density function is required.

The measurement of turbulent flows always yields a finite number of observed values. Hence, the exact knowledge of the probability density function is not available. Therefore, the mean value of the measured velocities is calculated by taking the instantaneous velocity measurements of the sample, summing the values, and dividing by the number of samples.

$$\overline{x} = \hat{\mu}_x = \frac{1}{N}\sum_{i=1}^{N} x_i \tag{4.6}$$

In a similar manner, a measure of the fluctuating velocities can be obtained from the sample variance

$$s_x^2 = \hat{\sigma}_x^2 = \frac{1}{N-1}\sum_{i=1}^{N}(x_i - \overline{x})^2 \tag{4.7}$$

In the equations **x** and $\mathbf{s^2}$ are the *sample mean* and *sample variance*, respectively. The number of observations N used to compute the estimates is called the *sample size*. The hats (^) over μ and σ indicate that these sample values are used as estimators for the mean value and variance of x.

In order to obtain the mean velocity field and the turbulence quantities from the PIV measurements, the ensemble average of the velocity data in identical spatial windows within a series of PIV images must be calculated. The instantaneous velocity fields that are obtained from each PIV measurement consist of N_x times N_y vectors, depending on the interrogation window size of the PIV analysis. For DPIV, a matrix of 30 x 30 vector for a 64 x 64 pixels interrogation window size and 60 x 60 vectors for a 32 x 32 pixels window are obtained. The physical size of the interrogation window in the flow field depends on the scale of the recording. For a typical recording situation where the total channel height of 100mm is seen in the image, a 32 x 32 pixels interrogation windows results in a square region of approximately 3.2 x 3.2 mm in the flow field. The velocity vector that is calculated within such an interrogation window represents the average instantaneous velocity in a region of the flow with the size of the interrogation window and the thickness of the light sheet. This volume is equivalent to the probe volume of point-wise measurement techniques and the cell size of CFD simulations.

4.1.5 Uncertainty in PIV measurements

Schabacker and Bölcs [113], Schabacker et al. [114], Schabacker [112] demonstrated the applicability of the presented stereoscopic PIV technique in details. Following are comments on small variations from those measurements (see also Raffel et al. [107]).

The spatial resolution, detection rate, accuracy, and reliability of the PIV

measurements depend critically upon the careful selection of a number of parameters of the PIV system and the fluid motion. A set of six non-dimensional parameters that are the most significant in optimizing PIV performance can be identified. They are: the data validation criterion, the particle image density, the relative in-plane image displacement, the relative out-of-plane displacement, a velocity gradient parameter, and the ratio of the mean image diameter to the interrogation window size. For a detailed discussion of these parameters, the reader is referred to Raffel et al. [107].

Here only an indication of the PIV parameters shall be given.

$N_I > 15$	Choose high density seeding.
$\frac{\sqrt{u^2+v^2} * \Delta t * M}{d_{int}} < \frac{1}{3}$	Choose the particle displacement smaller than 33% of the interrogation window size.
$\frac{w * \Delta t}{\Delta z} < \frac{1}{3}$	Choose the out-of-plane particle displacement smaller than 33% of the light sheet thickness.
$\frac{\lvert\delta u\rvert * M * \Delta t}{d_{int}} < \frac{1}{20}$	Choose the interrogation window size small in order to minimize the velocity variation δu due to spatial gradients in the interrogation window.

Thus, both relative in-plane and out-of-plane displacements should be less than one third which is slightly better than for the double-exposure single frame systems.

For the present case, the mean number of particles per interrogation window (64 by 64 pixel^2) was set to 30-40. The average in-plane displacement of the particles is approximately 6 pixels, which is less than $0.25D_I$ in each direction, D_I being the characteristic dimension of the interrogation window. The optimal light sheet position for PIV measurement has the beam waist in the middle of the measurement section. It provides a constant light sheet thickness in the measurement section. In the present investigation, the light sheet energy is so intense in the beam waist that the model Plexiglas walls are burned by the light sheet. The beam waist is placed outside of the section, which leads to a 10 percent variation of the light sheet thickness (mean thickness ≈ 1.2 mm) inside the section. An experimental study showed that the results are not significantly affected by the variation.

It must be noted that the absence of *peak locking* is another condition to be verified in order to have PIV results of quality (see Raffel et al. [107]). This effect mainly occurs when the image size of the particles is smaller than a pixel. The displacement vectors are thus biased towards integer values of pixel numbers. A two-dimensional histogram of typical measurement plane revealed that no *peak locking* were present in the present measurements.

The estimation of the flow quantities involves the estimation of the confidence interval, as opposed to a single point value, which will include the measured flow quantity with a known degree of uncertainty. A confidence interval can be established for the mean value μ_x based on the sample value x and s as follows.

$$\overline{x} - \frac{St_{n\alpha/2}}{\sqrt{N}} \le \mu_x < \overline{x} + \frac{St_{n\alpha/2}}{\sqrt{N}} \qquad n = N-1 \tag{4.8}$$

In Equation (4.8), the random variable t_n is Student's variable with n degree of freedom at 1-γ confidence coefficient. Equation (4.8) states that the true value μ_x falls

within the noted interval with a confidence coefficient of 1-γ, or, in a more common terminology, with a confidence of 100(1-γ) %.

The fractional confidence interval in estimating the mean value μ_x is obtained from

$$\varepsilon_\mu = \frac{\mu_x \pm \overline{x}}{\mu_x} = \pm \frac{st_{n,\gamma/2}}{\mu_x \sqrt{N}} \tag{4.9}$$

where s/μ_x is analogue to the local turbulence level of the flow. The number of samples required to report the mean velocity with a given fractional accuracy is thus dependent on the local turbulence level of the flow. Furthermore it can be stated that the average value $\overline{x}$ has more precision than any of its parts x_i by the factor $1/\sqrt{N}$.

A similar confidence interval can be established for the variance σ^2 based on the sample variance s^2 from a sample of size N

$$\frac{ns^2}{\chi^2_{n;\gamma/2}} \leq \sigma_x^2 < \frac{ns^2}{\chi^2_{n;1-\gamma/2}} \qquad n = N-1 \tag{4.10}$$

In Equation (4.10), the random variable χ^2 is the chi-square variable with n degrees of freedom. In contrast to the mean velocity, the confidence interval for the flow turbulence s^2 is thus independent of the turbulence level of the flow.

Using the method of Bendat and Piersol [6], the statistical uncertainty for the mean velocity values of the present measurements is in the order of 1 percent with a confidence level of 95 percent. The uncertainty of the mean velocity depends on the normal stresses and, as a consequence, is higher in regions where the turbulence level is high. The uncertainty level of the normal stresses in the Reynolds tensor, with a confidence level of 95 percent, is 8 percent of the normal stress values. The uncertainty of the normal stresses depends only on the number of samples and on the confidence level. Further details of the uncertainty method are given in Schabacker [112].

4.2 The liquid crystal transient heat transfer technique

For the present study, transient heat transfer experiments were performed using liquid crystals to determine the surface temperature. The transient technique is well described in Wang [127]. The transient liquid crystal technique consists in monitoring the surface temperature evolution in time with a step change in the gas temperature. The particularity of the present study is that it has been applied in a large-scale model of a coolant channel with a 2m distance from the inlet to the outlet. Moreover, all five walls were recorded simultaneously.

4.2.1 Measurement method

Eleven, fast response, fine mesh heaters were fitted to the duct inlet to produce the step change in gas temperature. This heater comprises a mesh of stainless steel wires, 40μm in diameter woven at a pitch of approximately 100μm, with an open area of 38% (see Wang et al. [128] for more details). A turbulence grid similar to the one used for the PIV experiments was placed downstream of the fine heater meshes. The heaters associated to the turbulence grid create at the channel inlet, the same flow

characteristics as those of the flow experiments.

The meshes were connected in series to two 5kW power generators. Two 6684A models from Agilent-Technologies were used. The power supply was limited in current (256A) and in voltage (40V), therefore eleven meshes were connected in series to reach the required power to increase the gas temperature.

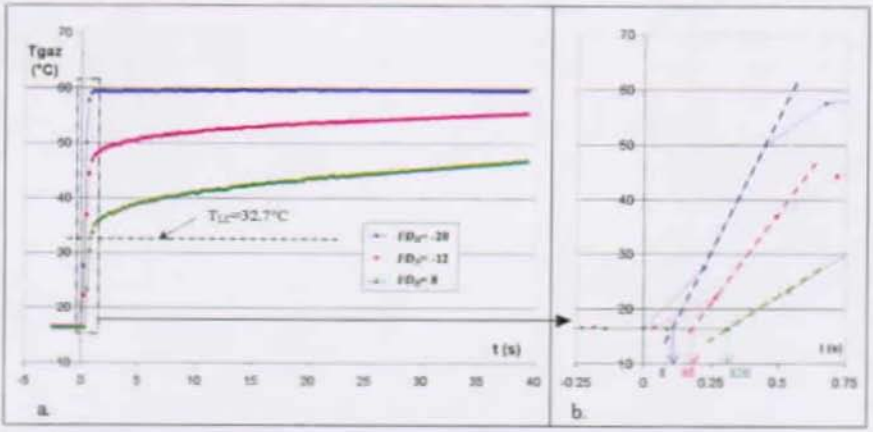

Figure 13: a: Gas temperature increase at various I/D locations for heat transfer post processing. b: detailed temperature evolution at initial time.

Figure 13a shows a typical variation of temperature with time in the test channel. At the inlet, the heaters create a step change in temperature of 75% and 99% of the total temperature increase, in 0.4s and 0.6s respectively. The temperature distribution across the inlet section is constant with a spatial variation of less than 3% of the total temperature step.

The initial time of gas temperature steps at various I/D_H locations in the channel, is delayed from the channel inlet to the channel outlet. The convection by the main stream is responsible for the delay, which can be of 1s at Re=25,000. A procedure was adopted to dispose on this delay. Figure 13b shows the determination of the initial time. A linear interpolation of 2 points in the step allows determining the initial time. The heat transfer coefficient reduction is performed from this initial time.

In the present experiments, the heat transfer coefficient α is obtained by using the 1D unsteady heat conduction equation, treating the wall material as "semi-infinite". This assumption limits the allowable measurement time. Vogel and Weigand [125] showed, that the maximum allowable measurement time can be calculated from $t_{max} = \left(0.25L^2\right)/\Lambda$, where L is the model thickness and Λ the thermal diffusivity of the model material. In the present study, a 5mm thick Plexiglas model was used to obtain good optical properties for PIV experiments; the maximum allowable time is $t = 64s$, which is longer than the typical measurement duration of $38s$. Tests were performed and revealed that this assumption is verified in the present models.

4.2.2 Data acquisition

During the transient experiment, the colour variation of the liquid crystal signal coating is captured with six miniature colour CCD cameras (TELI CS 5130, 6000 Tokyo Electronic Industry Co; resolution 752x582 pixels) located around the test section. Each camera view is independently recorded on a digital support during the transient experiment. The use of the Digital Video format (DV) storage has been chosen to ensure precise colour image signal restitution at a constant image frequency and without any noise generation, which was not the case for previous analogue VHS system. Moreover DV tapes contain by default the time and recording date information, which simplifies search for a specific sequence and storage of the various data measurements.

All the five test model outer walls are measured using twelve camera views. Six cameras are adjusted around the test section. They allow a parallel acquisition of the video sequences. Two independent tests are necessary for each Reynolds number to capture the twelve video sequences.

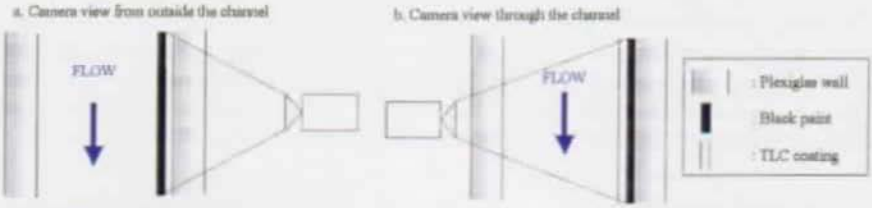

Figure 14: Liquid crystal and black coating layers in heat transfer experiments.

It must be noted that the liquid crystals (TLC) are directly applied on the surface of the model Plexiglas wall as shown in Figure 14a. This setup allows measuring all the outer walls at the same time without optical access restriction due to the opposite ribs. Preliminary tests were conducted to determine the influence of the camera view direction upon the measurements (see Figure 14b). The results were not significantly different between the two cases. The time delay introduced by the black coating to the TLC time response was considered negligible and does not influence the heat transfer coefficient measurements.

The quality of heat transfer measurements depends on the temperature measurement accuracy. The latter is in turn greatly dependant on the acquisition frequency. In order to obtain a good determination of the start of step change in temperature, a 4Hz frequency was chosen (see Figure 13). This distribution describes well the gas temperature evolution in time. It provides a good quality of data reduction using the method presented in 4.2.3. Nine data acquisition systems (HP 34970A with 34902A modules) were used in parallel to measure temperatures. In-house built Labview software running on a PC controlled and triggered the systems via GPIB connections. One data acquisition system (HP 34970A with 34907A module) provided TTL signals to LEDs located in the camera filed of views. The TTL signals were synchronized with both the power input in the heater meshes, and the temperature acquisition devices. The image and temperature acquisitions were related one with another in order to perform the data reduction.

4.2.3 Data reduction

4.2.3.1 1-D transient heat transfer: gas temperature step change

The 1-D transient conduction equation, with typical initial conditions and boundary conditions on the test surface, is used to obtain the non-dimensional temperature at the convective boundary surface:

$$\frac{T_{wall}(x,y,t)-T_i}{T_G-T_i}=1-\exp^{\alpha(x,y)^2\frac{\Lambda\cdot t}{\lambda^2}}\ erfc\left(\frac{\alpha(x,y)\sqrt{\Lambda\cdot t}}{\lambda}\right) \qquad (4.11)$$

Three variables need to be extracted from the experiments to obtain the heat transfer coefficient. These variables are the initial temperature (T_i), the wall temperature ($T_{wall}(x,y,t)$, which is time dependent), and the gas temperature (T_G).

The initial temperature T_i was measured in the Plexiglas model, after a thermal balance was reached between the gas temperature and the model outer surface temperature. An air conditioning device adjusted the test room temperature to be equal to the initial channel gas temperature. A zero temperature gradient was therefore established throughout the test section walls in the initial conditions.

The TLC temperature (equivalent to $T_{wall}(x,y,t)$) selected by the data reduction system was calibrated at 32.7°C. This temperature corresponds to the mean temperature of the Hue band filtered by the data reduction software. The same Hue-intensity band filter was used for all the data reduction in the present work.

Figure 15: Time processing of the T_{LC} temperature appearance.

Figure 15 shows the typical $T_{wall}(x,y,t)$ data reduction sequence, which determines the wall temperature appearance time of every pixel in the interrogated area. Note that no measurement was performed on the ribs, due to lack of optical access. The transient heat transfer measurement method consists in monitoring the surface temperature evolution by acquiring the colour signal of a liquid crystal coating applied on the test section. By using a single layer of narrow-band thermo-chromic liquid crystals (Hallcrest BM/R30.5C0.7W/C17-10), the evolution of the local surface temperature $T_{wall}(x,y,t)=T_{LC}$ is obtained from a hue capturing technique. The CCD colour cameras record the colour change in the liquid crystal coating. The video signal of each view is digitally stored on DV tapes.

Video sequences of each camera are subsequently transferred to a computer as AVI format sequences. The AVI movie files are coded in a PAL DV format, i.e. 25 images per second with a resolution of 720x576 pixels. In order to be compatible with the image-processing program, the movie file is eventually converted into a set of image files in a 24-bits RGB TIFF format with a reduced spatial resolution of 400x300.

An in-house program written using the commercial LabView language and the IMAQ™ image processing functions (National Instrument), reduces the time appearance of the selected TLC temperature over the full surface. The optimum spatial resolution (versus CPU time consumption) was set to 1 measurement point for 2mmx2mm. Powerful coordinate transformations are applied on the digital video sequences for undesired zones noise signal filtering or light non-homogeneities. The coordinate transformation also allows disposing on the lens optical aberrations. A hue colour value threshold of the calibrated liquid crystal signal gives very precise temperature levels of the recorded surface. The processing of the TIFF sequence gives the appearance time of the selected TLC temperature. An ASCII file is obtained with time values for each pixel location. Note that blue colour means low appearance time, thus high heat transfer and red colour means high appearance time, thus low heat transfer.

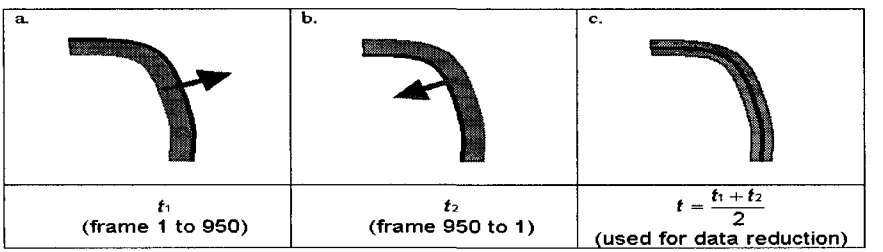

Figure 16: Procedure to determine the exact T_{LC} time appearance.

The hue filtering technique keeps only hue values corresponding to the calibrated temperature. The filtered zone has a certain width larger than one pixel, which permits to identify the time appearance (see D'Urbano [32] for details). It leads to an uncertainty in time appearance of the calibrated temperature. Note that this uncertainty gets greater in regions where the heat transfer coefficients are low (i.e. for long measurement times). For time measurements of 35s, the band needs approximately 4s to pass by a pixel. It yields a 2.5% relative uncertainty in the heat transfer coefficient.

A procedure described in Figure 16, was utilised to eliminate this uncertainty on the appearance time determination. The basic idea is to choose the time when the middle of the filtered band passes by a selected pixel. Indeed, the band middle corresponds the best to the calibrated temperature. Figure 16a shows the time t_1 detected by the data reduction software for a measured sequence going from frame 1

to 950. By reversing the same sequence and applying the time detection algorithm again, the time t_2 is determined (Figure 16b). The mean value $t = (t_1 + t_2)/2$ (Figure 16c) is calculated. This time value is utilised in the data reduction process.

4.2.3.2 1-D transient heat transfer: gas temperature evolution in time

The use of heater grids introduces a double dependence of the gas temperature on time and *X*-location (see Figure 13a). In typical tests, the gas temperature reached approximately 70°C after 40s. Downstream of the inlet, due to heat exchange with the channel walls, the temperature increase is no longer a step. For a given *X*, the gas temperature is an increasing function of time (Ekkad and Han [35]). When the gas temperature change can be expressed as a series of *n* summed step functions, the Plexiglas surface temperature $T_{wall}(t) = T_{LC}$ can be expressed

$$T_{wall}(t) = T_{LC} = T_i + \sum_{j=1}^{n} (T_{G,j} - T_{G,j\_1}) \cdot F(t - t_j) \tag{4.12}$$

with

$$\beta_j = \frac{\alpha\sqrt{\Lambda \cdot (t - t_j)}}{\lambda} \tag{4.13}$$

and

$$F(t - t_j) = \left\{1 - \exp(\beta_j^2)\ \ erfc(\beta_j)\right\} \tag{4.14}$$

An iterative calculation is used to determine the value of the heat transfer coefficient from the above equations.

Thermocouples were placed along the channel to measure the gas temperature evolution in function of time and X-location. They were located in the centre of one of the secondary flow vortices ($Z = +0.43$ and $Y = 0.33$ in the upstream leg, ($Z = -0.77$ and $Y = 0.33$ in the downstream leg). The thermocouples were $1D_H$ distant from one another in the region of interest, and 2Dh apart in regions where no measurements were taken. A consistent behaviour in terms of continuity was observed all along the channel.

The gas temperature was considered constant for every measurement point in a cross section (X=constant). A linear interpolation of the gas temperature was performed for every location between the thermocouples. Lines of interpolation in the baseline case are shown in Figure 17. In the bend region, a linear interpolation based on the θ angle was chosen. In both the bend and the straight legs, a linear interpolation based on the curved distance between the thermocouples was taken.

Figure 17b shows the evolution of three gas temperatures along the baseline case test channel. These temperatures were obtained from CFD predictions performed at Rolls-Royce Germany during the ICTB project. The centreline temperature, the bulk temperature and the temperature at EPFL thermocouple measurement locations are plotted.

EPFL gas temperature thermocouples were placed at locations near the centre of the lower secondary vortex (Chanteloup [18]). The temperature at the centre of a vortex is usually more stable than at other locations in the cross section.

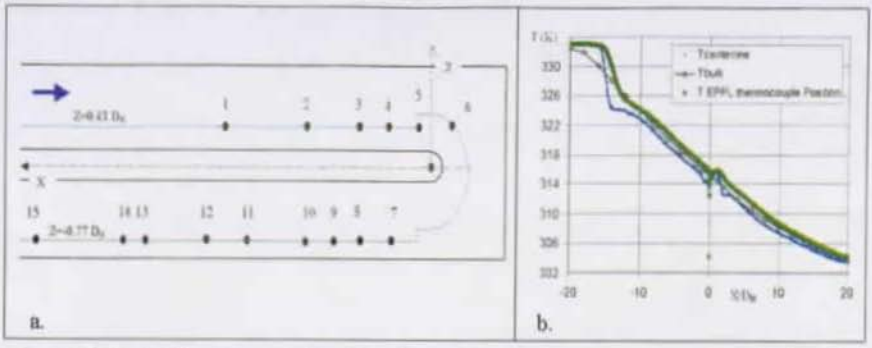

Figure 17: Typical thermocouple locations for gas temperature measurements in the baseline configuration.

Another advantage of this location is shown in Figure 17b. The gas temperature is closer to the bulk temperature than the centreline temperature. Along the channel the absolute value of the difference between the bulk and thermocouple temperatures remains low: $|T_{bulk} - T_{thermocouple}|_{max} < 1°C$. Note that the temperature jump observed at $X = 0$ has no influence on the data processing, since no thermocouple was placed in the bend region; a linear interpolation of two thermocouples, upstream and downstream of the bend, was calculated to obtain the bend gas temperature.

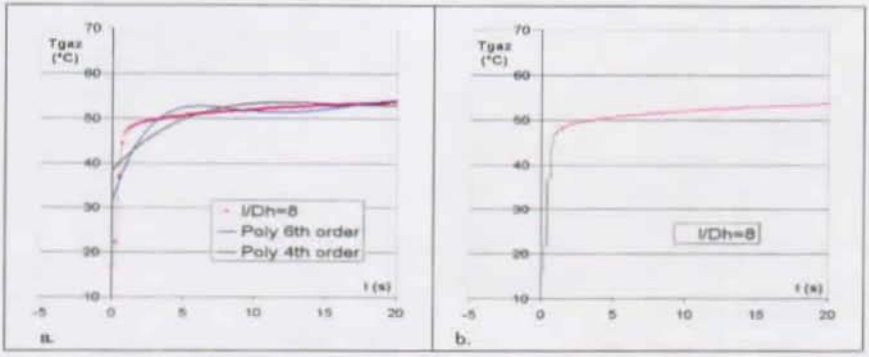

Figure 18: Gas temperature interpolation, polynomial and step-by-step methods.

Note that a polynomial interpolation of the gas temperature is also feasible to take into account the temperature dependence on time showed in Figure 13. It was tested in a preliminary study and reported in D'Orgeville [31]. Figure 18 shows the interpolation of the gas temperature at $l/D_H = 8$ already plotted in Figure 13. Polynomials of the 4th and the 6th orders are plotted. It is showed that the temperature ratio $|T_{interpol} - T_{measur}|/T_{measur}$ is greater than 10% for times lower than 5s. It introduces uncertainty in the heat transfer results of about 20%. Polynomial orders of 12 are

necessary to keep $|T_{interpol} - T_{measur}| < 1°C$. However, this high order leads to numerical accuracy problems as well as excessive time consumption in the data reduction process. Therefore a step-by-step function (so-called Duhamel method) was used in the present study to approximate the gas temperature. Figure 18b shows the step-by-step function used to approximate the temperature measurements at $l/D_H = 8$ already plotted in Figure 13.

4.2.4 Validation and accuracy of the liquid crystal transient technique

4.2.4.1 Comparison with steady state measurements

Heat transfer measurements were performed in a preliminary test rig. The main goal was to setup and validate the transient measurement technique in long cooling channels. Figure 19a shows a picture of the preliminary rig. The test rig is equipped with a straight channel, which has the same geometrical characteristics as the two-pass channels (i.e. square channel with $D_H = 0.1m$). The Reynolds number was fixed to 34,000 due to limitation of the blowers' power.

A 40mm thick Plexiglas plate was used in the preliminary channel to compare transient and steady state measurements. Figure 19b shows the Plexiglas plate. It was located in the fully developed flow region and was provided with a single 90° square rib (side $0.12D_H$). The rib allows the flow to be highly turbulent. It is representative of flows in channels with turbulators. Furthermore Butler and Baughn [11] showed that thermal boundary conditions can strongly affect laminar flow heat transfer results, whereas in high turbulent flows, the effect is less.

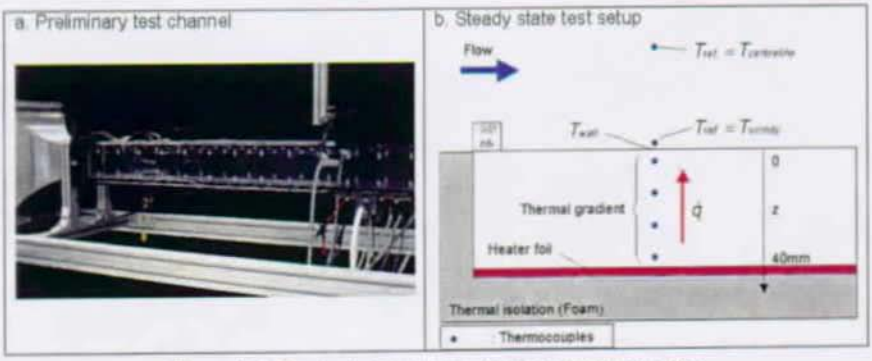

Figure 19: Steady state heat transfer measurement setup.

Two heat transfer measurement techniques have been used to measure the heat transfer downstream of the 90° rib. The first one was the transient heat transfer technique described in §4.2. The second one was a steady state technique. Figure 19b shows the steady state apparatus. A heater foil creates a heat flux inside the 40mm thick Plexiglas plate. 6 thermocouples located inside the plate verified that the heat flux was constant and homogenous (1.5% difference between two measured locations along the centreline, 50mm far one from another). The heat flux and heat

transfer coefficients are reduced with the following equations:

$$\dot{q} = -\lambda \frac{\partial T}{\partial z} \qquad \text{(1-dimensional heat conduction)} \tag{4.15}$$

$$\dot{q} = \alpha(T_{ref} - T_{wall}) \tag{4.16}$$

The heat transfer coefficient is calculated from Equation (4.16). The wall temperature is calculated from Equation (4.15) when z is equal to zero. The gas reference temperature can be chosen along the centreline or in the vicinity of the wall. The transient gas reference temperature for this specific test was chosen to be $T_{centreline}$.

Measurements were performed at 6 various heat flux (the standard deviation of the measurements was less than 5%). The average heat transfer coefficient of a $1cm^2$ zone located $1.25D_H$ downstream of the rib along the centreline was chosen for comparison of the measurement techniques.

Table 2 summarises the results of both measurement techniques. For the analysis of the results, it should be mentioned that the wall thermal boundary conditions influence the heat transfer coefficient. Indeed, in a fully developed channel turbulent flow, the heat transfer coefficient is 5% higher for a constant heat flux wall than for a constant temperature wall (Kays and Crawford [76]). In the present experiments, both transient and steady state (with $T_{ref} = T_{centreline}$) techniques give results with $\Delta\alpha/\alpha < 2\%$. These results are within the measurement technique uncertainty. This gives an indication on the confidence of the transient technique used in the present work. Note that the variation of the reference gas temperature yields a 10% error on $\Delta\alpha/\alpha$. This gives an indication of the maximum error that can be done due to the gas reference temperature.

Measurement Technique	$\alpha[W/m^2K]$
Steady state ($T_{ref} = T_{vicinity}$)	24.2
Steady state ($T_{ref} = T_{centreline}$)	26.6
Transient ($T_{ref} = T_{centreline}$)	26.3

Table 2: Heat transfer coefficient results from various measurement techniques.

4.2.4.2 Comparison with previous referenced results

So far several measurement techniques have been compared in the EPFL test rigs. Referenced works describe heat transfer measurements results in straight channel with 45° rib arrangements. For more details, the reader is referred to **Appendix A** (p147). The comparison of present measurements with several typically used correlations, and with full surface heat transfer measurement techniques are shown in details.

Measurements were performed in the preliminary test rig described in Figure 19, in a similar channel as in Rau [110] (p84). The results are compared in the present paragraph. Details of this comparison are given in D'Orgeville [31]. The main conclusion can be drawn as follows.

Rau [110] made steady state heat transfer measurements in a straight channel. The channel was equipped on one wall with 45° rib arrangement, $e/D_H = 0.1$ and $p/e = 0.1$. The Reynolds number was 30,000. The area-averaged result between two consecutive ribs was $Nu/Nu_0 = 1.85$. The conclusion from the results is that the present measurements technique gives results, which are coherent with previous referenced works. The transient technique applied in the present preliminary channel gave a value of $Nu/Nu_0 = 1.80$. Note that some differences occurred in the full surface heat transfer distribution. These differences were attributed to geometrical differences (wall roughness, flow differences, location of the ribs on the heater foil...) between Rau [110] and the present study. A comparison with ribbed channels is also shown in A.2.3. Full surface heat transfer results are compared with present results of the baseline configuration fully developed flow region.

Several references describe correlations in internal coolant passages. These correlations were developed for smooth and rib roughened channels. They were directly derived from measurements or based on a momentum/heat transport analogy. A complete description of these correlations is given in A.2.1. The present measurements in the upstream leg baseline configuration are within 10% difference from the correlations, for all the three Reynolds numbers studied. This good comparison between the measurements and correlations completes the validation of the transient heat transfer measurement technique that will be used for the present study.

A comparison with mass transfer measurements in a similar channel to the baseline configuration was performed. Results and conclusions are given in A.1.2.

4.2.4.3 Accuracy of the liquid crystal transient technique

Due to time consumption of the data reduction process, only single heat transfer experiments were conducted in each test case. The error in the heat transfer measurements was calculated using the method described in Höcker [66]. It estimates the maximum absolute error, e.g. the worst-case scenario. It showed that for $f(x_1,...,x_k)$ a function of the number of variables $x_1,...,x_k$, the absolute error can be approximate by the total differential of f:

$$\Delta f = \sum_{i=1}^{k} \left| \frac{\partial f}{\partial x_i} \right| \Delta x_i \qquad (4.17)$$

The error analysis of heat transfer experiments is based on Equation (4.11). The heat transfer coefficient can be considered as a function of T_{LC}, T_G, T_i and t. Thus the errors ΔT_{LC}, ΔT_G, ΔT_i and Δt must be determined.

Table 3 gives the errors on the single variables. T_G and T_i are measured with thermocouples. A thermocouple calibration procedure showed that the error on temperature measurement is 0.1°C. The liquid crystal calibration gave an error on T_{LC} of 0.1°C. The error on time detection is due to the camera image acquisition frequency. The camera recorded 25 frames per second. Thus the error on t is one frame.

ΔT_{LC}	ΔT_G	ΔT_I	Δt
0.1°C	0.1°C	0.1°C	0.04s

Table 3: Measurement uncertainties on variables governing the heat transfer coefficient data reduction.

Höcker [66] showed that the error can be minimised by adjusting measurement parameters such as the model material and the dimensionless temperature $T = (T_{LC} - T_I)/(T_G - T_I)$.

In the present study, the heat transfer coefficients are in the order of $20 W/m^2K$ to $200 W/m^2K$. Using Höcker [66]'s method, this leads to optimum dimensionless temperatures between $0.2 < T < 0.4$. Thus it was chosen to set the various temperatures at $T_I \approx 18°C$, $T_G \approx 70°C$, $T_{LC} \approx 32.7°C$, in order to obtain an average dimensionless temperature $T = 0.28$. The maximum error, taking into account the variable errors given in Table 3, can be estimated to ±8% on the heat transfer coefficient, with the assumption that the latter is constant during the experiment.

Note that a statistical analysis was carried out in the preliminary test section to assess the quality of single heat transfer measurements. A set of 20 experiments was analysed. Differences between each single experiment and the averaged value were determined for every pixel in the test section. The deviation reached an overall maximum of 3.5% for very few locations, whereas the average deviation was in the order of 1%.

4.2.5 Terminology of the presented results

4.2.5.1 Channel wall terminology

Figure 20 gives a definition of regions and walls in the baseline configuration. The names listed in the figure will be used in the following parts in the baseline configuration as well as in the three other test channels.

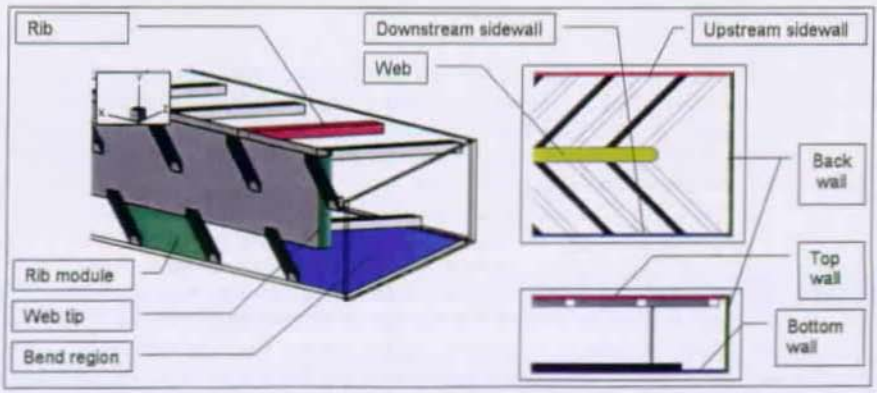

Figure 20: Terminology of the test channel walls.

4.2.5.2 Extraction of heat transfer results

In the present thesis, Nu numbers were normalised using the Dittus-Boelter equation (Equation (4.18)) for a circular smooth channel. The normalisation allows better comparison to previous referenced investigations. The Prandtl number exponent n=0.3 corresponds to the case when the gas temperature is higher than the wall temperature. Heat transfer measurements were conducted for three Reynolds numbers: 25,000, 50,000 and 70,000. The three Dittus-Boelter normalisation values, calculated from the Equation (4.18), are summarised in Table 4.

$$Nu_{DB} = Nu_0 = 0.023 Re^{0.8} Pr^{0.3} \qquad (4.18)$$

Re	25000	50000	70000
Nu_0	88.17	118.69	155.36

Table 4: Dittus-Boelter Nusselt numbers for the various Reynolds numbers measured.

The heat transfer results are given in three different formats. Full surface contours provide a global view of both the heat transfer levels and heat transfer gradients on the area of interest.

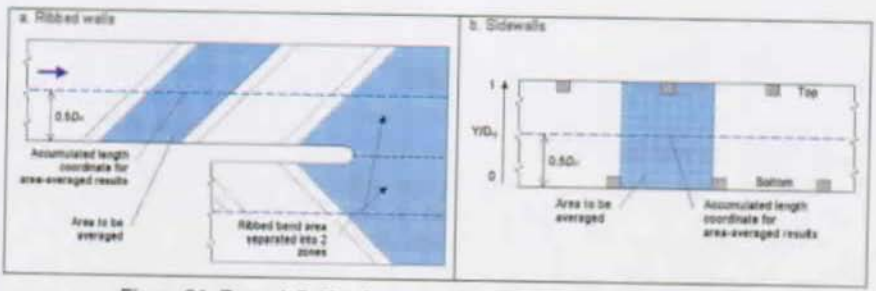

Figure 21: Zone definition for area averaging of heat transfer results.

In addition to the heat transfer full surface contours, the area-averaged values between two adjacent ribs are determined. Figure 21 gives a definition of the surfaces that are averaged, for both ribbed walls (Figure 21a) and sidewalls (Figure 21b) of the channel. Heat transfer area-averaged values are assigned to the location half way in between the ribs along the surface centreline.

A better knowledge of the two-dimensional heat transfer distribution on the coolant channel surfaces can improve the cooling efficiency of the internal cooling system. Therefore heat transfer gradients in spanwise and streamwise directions are given in this thesis. They can provide useful information on the manner of using the coolant channels, in order to achieve homogeneous temperature in the blade.

A normalisation procedure is used in order to identify the heat transfer gradients. Sub-zones heat transfer results are normalised by the full surface area-averaged Nusselt number ($N = Nu_{zone}/Nu_{full\_surface}$). This normalisation compares sub-zone

Nusselt number with the full surface area-averaged value described in Figure 21. Values of 1, >1 or <1 in this normalization mean that the Nusselt number of the interrogated area is respectively equal, greater or lesser than the full surface area-averaged Nusselt number.

This normalisation allows comparing spanwise and streamwise Nu/Nu_0 gradients for various Reynolds numbers or extractions, although full surface Nu/Nu_0 values are different. Figure 22a-c gives a definition of the sub-zones on both ribbed walls and sidewalls.

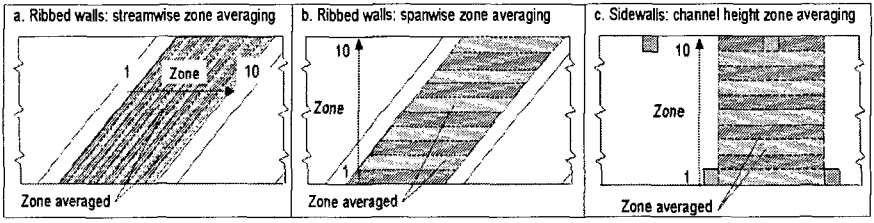

Figure 22: Zone definition for zone averaging of heat transfer results.

4.3 Additional measurement techniques

4.3.1 Ejection hole velocity measurements

In the configurations simulating the film extraction, the global extraction was adjusted as described in 3.1. Extraction through each hole was quantified by single hole velocity measurements. The velocity was measured at the outlet of the holes, with a 9mm diameter turbine flow meter probe placed 2mm apart from the hole (Y direction). The measured velocity is consequently an average of the free jet velocity profile. A precise positioning device allowed placing of the probe at each hole outlet.

The sum of single hole based on hole velocity measurements was compared to the total massflow extracted measured by the massflow meters (§3.1). The hole velocity measurement technique yields a 3% error in the hole massflow measurements.

4.3.2 Static pressure measurements

Static pressure measurements in the configurations were performed with a DRUCK LPM 5480 differential pressure transmitter, with a 6N/m2-accuracy.

Pressure taps were placed in the rib modules of the four configurations. Pressure taps were located in the top wall at mid distance between the ribs, and aligned with the centreline. They were separated $2D_H$ one from another. Static pressure measurements were taken for Re=25,000, 50,000 and 70,000, and for every extraction in the configuration-2 and configuration-3 cases.

$$f = 4 \cdot C_f = \frac{\Delta P}{L} \cdot \frac{D_H}{\frac{1}{2}\rho U_{b,in}^2} \tag{4.19}$$

Friction factors f and coefficient of friction C_f were determined from the pressure measurements, following Equation (4.19). ΔP is the static pressure difference between two measurement points and L is the distance between these points, along the centreline.

4.4 Time and memory requirement

The present part gives an overview of the computer resources and time requirements that are needed to perform measurements similar to the ones presented in this thesis. The results can be extrapolated if the acquisition of an exhaustive database for CFD validation is required.

For the performance of the present work, computer resources were composed of two dual-450MHz-processor workstations. Each workstation was equipped with 768Mb RAM and 60Gb hard disk space. The operating system was Windows NT workstation 4.0. These resources were up-to-date in 1998 (beginning of the present thesis work) and still present sufficient calculation capacities in 2002.

Figure 23 gives an overview of the four main tasks necessary to the measurements (all the sub-tasks are given and commented in Juaneda [75]). The *Measurements* task gathers all the times when the test rig is running (data acquisition). These times are representative of the test rig occupation time. The *Data processing* and *Data reduction* tasks are tasks when the data are analysed by software. These tasks are representative of the computer utilisation. The hard disk memory required is maximal during these tasks. The *Manual tasks* are all the human interventions necessary in order to link all the tasks and sub-tasks. Note that the total number of tasks, total required time and memory required are given for the measurement of one single measurement plane.

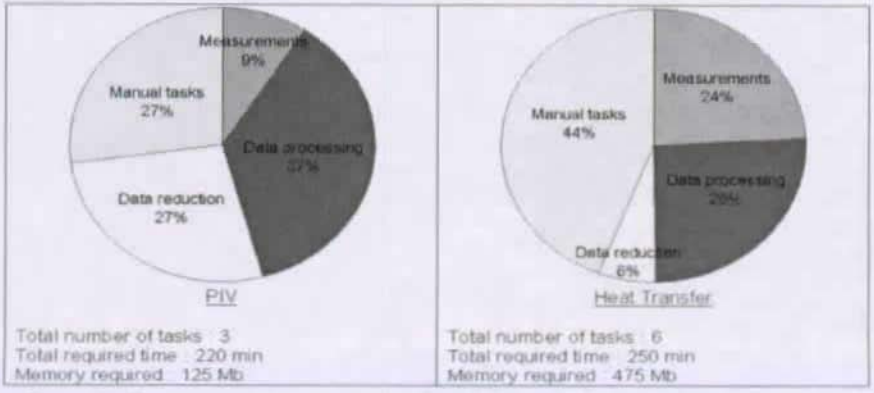

Figure 23: Time and memory requirements for a single measurement plane; flow and heat transfer measurements.

It can be noticed from these charts that the manual tasks are important, despite the automation of most of the data processing and data reduction. There are two different reasons depending on the measurement technique.

In Schabacker [112], it was shown that for PIV measurements the manual tasks were 5.9% of the global time. The present value of 27% is due to the hardware and software improvement in the present work. The manual tasks have been reduced since data processing and data reduction have been fully automated. They only consist of the data transfer between every task. On the other hand the computer speed has been multiplied by a factor 5. Thus the fraction of manual tasks becomes more important. A solution could be to upgrade the LTT PIV system to a commercial system, which could gather the data processing and reduction tasks, in turn reducing the manual tasks.

Concerning the heat transfer measurements, the manual tasks are due to data transfer between numerous software used during the data processing. This software is a combination of in-house built and commercial software. A solution could be to create in-house built programs replacing the commercial software. It would lead to single data processing software, in turn reducing the manual tasks. Note that the spatial resolution mentioned in 4.2.3.1 can be increased by a factor 4 only by updating the computer resources for data reduction.

Conclusions of chapter 4

Chapter 4 gives a description of the measurement techniques used to perform the present study.

The flow measurements were performed with a 2D-3C (2 dimensions-3 components) PIV measurement system. The PIV system used is an in-house built system. This system allowed measurement of mean velocity components and Reynolds stresses. The measurement capability had been validated in previous works performed in the institute low wind tunnel test facility.

The measurement system has been updated and automated in order to increase the efficiency and the accuracy of the flow measurements. The updated system allowed capturing 5000 frames for statistical analysis, per measurement plane. Around 100 planes could be measured per channel configuration, with a measurement cell resolution of 6 mm and an overlap of 50%. The uncertainty on the mean velocity components is of the order of 1%. One plane was measured in 20 minutes, and 200 minutes were needed for the global post processing, on 1998 state of the art computers.

The heat transfer measurements were performed with a system based on the transient liquid crystal technique. The technique was adapted to large scale models of internal coolant channels (2m long). Therefore the reference gas temperature evolution in time and location was taken into account: The Duhamel theorem was applied. The reference gas temperature was measured in the centre of the 45° rib-induced vortex. This temperature has proven to be closer to the bulk temperature than the centreline temperature.

The in-house system was calibrated versus other measurement techniques and versus published results. The uncertainty of the measurements is 8%.

The measurement technique was applied so that all the five outer walls of the channels could be measured. The measurement system allows measuring 6 camera views (30cm*30cm per camera view in the present case) in parallel. The liquid crystals were painted directly on the Plexiglas models allowing the image capture from the outside of the models. The data reduction system was optimised to reduce the time consumption. The complete measurement system (including limitations of the data reduction computer resources) yielded a 2mm*2mm resolution was per measurement point. Thus 3 Reynolds numbers and 3 extraction ratios were measured in 4 various internal cooling channel geometries.

5 2-PASS COOLANT CHANNEL WITH 45° RIB ARRANGEMENT

5.1 Fully developed flow region

The knowledge of fully developed flow region heat transfer characteristics is of prime interest in coolant channels for several reasons. First, the major part of internal cooling systems is composed of straight channels. Thus the heat transfer accuracy in the fully developed region has a direct impact on the global cooling system heat transfer accuracy. Second, CFD codes are more and more used as design tools and they need to be validated. The basis of the validation is the testing of mesh dependency, turbulence models, etc, in periodic rib modules of fully developed regions. As a consequence, the heat transfer fully developed flow region is well described in literature. However, most of the published work concentrate on area-averaged results.

A detailed description of the heat transfer fully developed region in the baseline configuration will be given in the present chapter. Heat transfer and flow results will also be given. The combination of both heat transfer and flow results will be highlighted. In addition to this paragraph, a comparison with several previous published works given in A. This comparison allows determining the confidence range of the present heat transfer measurement technique.

5.1.1 Area-averaged heat transfer

Figure 24a shows Nu/Nu_0 area-averaged values in the fully developed region of the baseline configuration. Reynolds number was set to 50,000. One value is plotted for every rib module on the ribbed walls. Zones are plotted every $0.5D_H$ on the sidewalls. The location in the model is between $14D_H$ and $17D_H$ from the channel inlet.

The values of the three walls have reached a plateau value, indicating that the flow is in the fully developed region. Both ribbed wall values are oscillating around 2.05, whereas the sidewall values are oscillating around 2.25. Note that the bend vicinity (beginning at $l=-1$) affects the Nusselt distribution on the sidewalls in the region $-3<l<-1$. It is not the case on the ribbed walls. It seems that the ribs are still dominating the heat transfer phenomena in this region.

Figure 24b gives the mean values of Nu/Nu_0 area-averaged values from the plateau area. The table also gives the value average deviation to the mean value. The average deviation is calculated from the following Equation (5.1).

$$Av-dev=\frac{\frac{1}{n}\sum|x-\bar{x}|}{\bar{x}} \qquad (5.1)$$

The average deviation is less than 1% for all the three walls. This gives an indication of the good repetitivity of the measurements in the fully developed region. Differences between one rib to the other are thought to be due to measurement errors and also to small flow distribution differences.

It should be mentioned that the outer wall area-averaged values seem to be

higher than the ribbed wall values, which is not the desired effect of a rib-equipped cooling channel. In fact, the ribs themselves are not taken into account in the area averaging. According to literature, taking into account the 45° ribs increases the *between ribs* area-averaged value by about 33%. It produces full rib module area-averaged values higher than the upstream sidewall values (e.g. $Nu/Nu_0 \approx 2.1 * 1.33 = 2.8$ on the ribbed walls against $Nu/Nu_0 = 2.25$ on the sidewalls). Note that other published works reported similar results on both ribbed walls (rib excluded) and outer sidewalls (see A.2.2 and A.2.3).

Present measurement results in the fully developed flow were compared to a correlation for 45° rib-arrangements presented in Han and Park [56] (Han). The correlation was extrapolated beyond Han's test range ($0.047 < e/D_H < 0.078$). The result from the present study is an average of measurements in the fully developed section of the first leg.

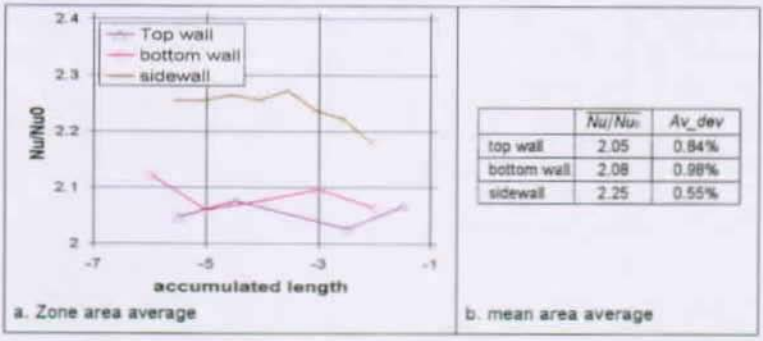

	$\overline{Nu/Nu_0}$	Av_dev
top wall	2.05	0.84%
bottom wall	2.08	0.98%
sidewall	2.25	0.55%

Figure 24: Fully developed area-averaged Nusselt number (Baseline configuration, Re=50,000).

5.1.2 Flow characteristics

A comparison of velocity components in the developed flow region of a similar coolant passage was presented by Bonhoff et al. [8]. The measurements showed that the flow with a 45°-rib arrangement differs from the flow in a similar passage with a 90°-rib arrangement Schabacker et al. [115]. With 90° ribs, a developed flow condition in terms of mean velocity and turbulent kinetic energy was achieved after 3 rib modules. The flow in the passage with 45° rib arrangement requires a longer development length; at least 8 rib modules are needed to achieve a developed flow condition for the mean velocity components and 12 rib modules are required for the turbulent kinetic energy of the flow. In the present configuration, 18 rib-modules are placed in the upstream leg, to produce a developed flow field before the 180° bend.

The velocity components downstream of the 16th rib module are judged to be in a developed flow region. Figure 25 gives the three velocity component profiles as well as the turbulent kinetic energy in the fully developed region. Velocity results were extracted from lines normal to the ribbed walls, at Z=0.6. The profiles are repetitive from one rib module to the other. The velocity profiles are also equal from a $2.7D_H$

distance upstream of the bend to a $0.7D_H$ distance from the bend. This demonstrates the weak disturbance of the flow field as the flow approaches the bend region.

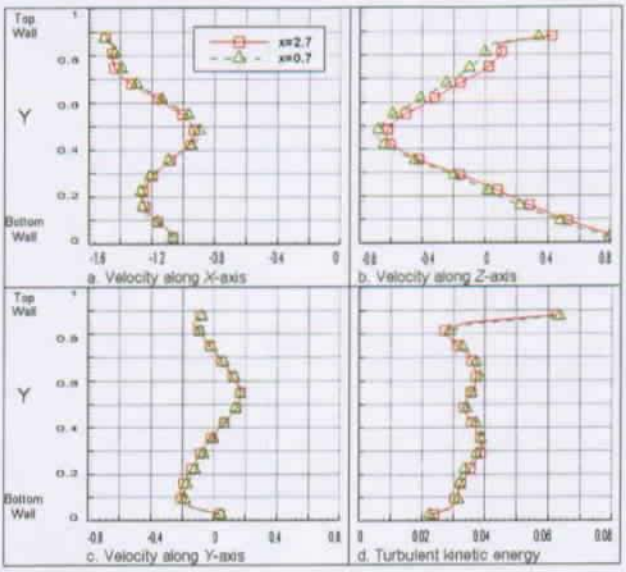

Figure 25: Velocity component periodicity in the bend vicinity (upstream leg, Z=0.6).

5.1.2.1 Velocity profiles $3D_H$ upstream of the bend

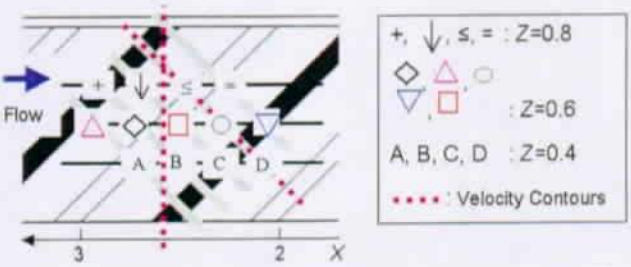

Figure 26: Location definition of velocity profiles (Figure 27) and contours (Figure 28 and Figure 29).

a. Overview of the graph: mean velocity profiles

Z	Streamwise Velocity	Cross-stream Velocity	Vertical Velocity
0.4	a.1.	b.1.	c.1.
0.6 (passage center)	a.2.	b.2.	c.2.
0.8	a.3.	b.3.	c.3.

b. Mean velocity profiles

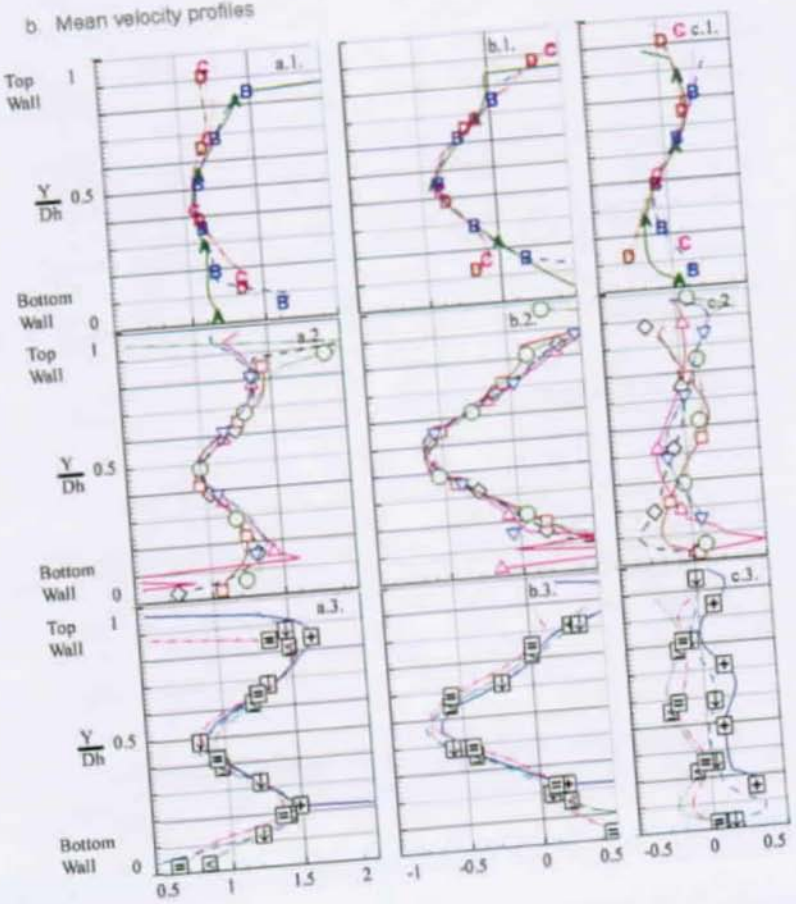

c. Turbulent kinetic energy profiles

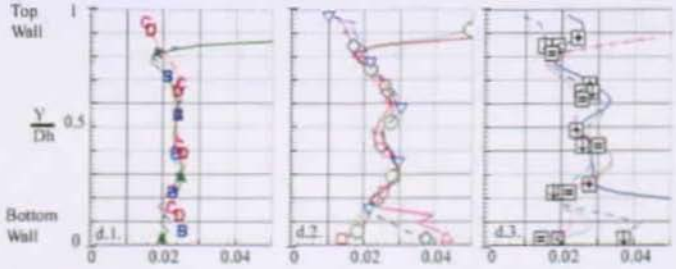

Figure 27: Velocity profiles in the 16th rib module, normalized by Ub. (a: Streamwise velocity, U; b: Velocity along Z-axis, W; c: Vertical velocity along Y-axis, V; d: turbulent kinetic energy; 1: $Z=0.4D_H$; 2:$Z=0.6D_H$; 3:$Z=0.8D_H$). See Figure 26 for exact locations in the rib module.

The streamwise (U), spanwise (W) and normal (V) velocity profiles at selected streamwise and spanwise locations are shown in Figure 27 and Figure 28. The streamwise locations are between $X = 2.1$ and 3.1 (All the distances are normalised by D_H).

Figure 26 defines the location of the velocity profiles given in Figure 27. The profiles were extracted from measurement planes along the Y-direction. Data from values of $Y = 0.06$ to 0.94 are plotted except at the rib surfaces where the closest value of has a $\Delta Y = 0.06$. The measurement procedures with this PIV set of optics has a probe dimension of $\Delta Y = 0.06$. At values of Y closer than 0.06 to the wall, spurious results were obtained due to wall light reflections. The cross-stream locations are at $Z = 0.4$, 0.6 and 0.8. Note that the web wall location is at $Z = 0.1$.

Figure 27b shows the mean velocity profiles extracted from measurement planes shown in Figure 26. As noted by Bonhoff et al. [8], the streamwise velocity profiles have two peaks for values of Y approximately equal to 0.2 and 0.8. These are attributed to the acceleration of the flow as it crosses the ribs at $Y = 0.1$ and 0.9 for the top and bottom walls, respectively. In the region near the downstream wall, $Z = 0.8$, the velocity profiles are close to a single shape. The velocity at the centreline is near 0.9. The two peaks in the rib region are between 1.3 and 1.6. The flow at the centreline of the passage ($Y = 0.5$ and $Z = 0.6$), also has a streamwise velocity of approximately 0.9. The streamwise velocities in the peak regions vary from 1.25 to 1.6 or more. This large variation is attributed to measurement locations close to the ribs, e.g., $X = 2.63$. The streamwise velocities at $Z = 0.4$, have a common minimum of $U = 1.07$. The velocity profiles near to the walls vary depending upon streamwise location.

The cross-stream velocity profiles show a well-behaved increase in velocity as the fluid moves from the web or upstream wall to the outer or downstream wall. The peak velocities of 0.4 at $Z = 0.4$ increase to 0.65 at $Z = 0.8$.

The streamwise and spanwise velocity profiles are symmetrical against the horizontal plane $Y = 0.5$, whereas the velocities normal to the ribbed walls have a more complex shape, which reflects the secondary flow pattern caused by the ribs. The velocity directions near the walls, e.g., $Y = 0.1$ and 0.9 are compatible with the

single large secondary flow cell.

The turbulent kinetic energy profiles (Figure 27c) are complex in terms of the velocity profiles and proximity to the wall. For all three spanwise locations, the minimum value of k/U_b^2 is about 0.025. A local minimum occurs near $Y = 0.5$ where the velocity gradients are low. Local maximum values occur in the high shear regions in the central part of the passage and near the walls.

5.1.2.2 Velocity contours in a cross section $3D_H$ upstream of the bend

Figure 28 shows the developed velocity contours, located at $X = 2.58$ in the upstream leg. Note that the secondary flow field and the contour maps of the velocity components in the cross-section included in the graph were obtained from the combination of the measurement planes as shown in Figure 26, and thus should only be regarded as a qualitative representation of the flow. Spurious vectors were included during the interpolation procedure.

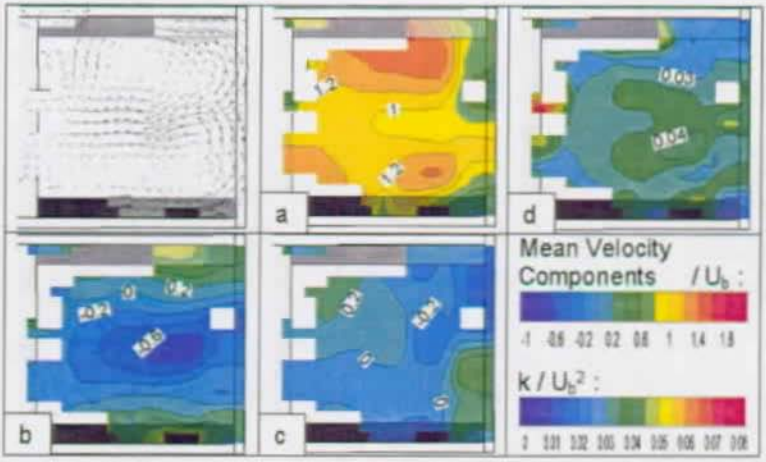

Figure 28: Velocity contours in the 16th rib module at X=2.58, normalized by Ub. (a: Streamwise velocity, U; b: Velocity along Z-axis, W; c: Vertical velocity along Y-axis, V; d: Turbulent kinetic energy).

Unlike the flow behind 90° ribs, the vortices behind inclined ribs are not stagnant, but move along the ribs and then join the main flow. This interaction between main flow and rib-induced vortices causes the setup of a strong secondary flow motion in the passage leg. The secondary flow consists of two counter-rotating vortices that drive fluid from the duct centre towards the web and back to the sidewall along the ribbed walls as shown in Figure 28.

The axial velocity contour map of the flow in the y-z cross-section plane in Figure 28a shows that the skewed ribs transform the almost uniform inlet profile into two regions of high axial velocity reaching $U/U_b = 1.4 - 1.6$. The streamwise velocity profile can be explained as follows. Regions of high streamwise velocities are located in the centre of the two secondary vortices. They are due to the flow contraction due to

the ribs. Low streamwise velocity regions take place near the outer sidewall. These low streamwise velocity regions are transported towards the channel centre by the strong secondary flow motion along the $Y = 0.5$ plane. As the flow reaches the inner web, it is accelerated by the main flow to values up to $U/U_b = 1.2$.

The vertical velocity component reveals the approximately symmetrical character of the secondary flow motion, about the $Y = 0.5$ plane. Strong vertical velocity motion towards the web with a peak value of $W/U_b = -0.65$ occurs halfway between duct centre and sidewall. The flow impinges on the web with a speed of $0.2U_b$. Near the ribbed walls, the fluid is driven back to the sidewall with a velocity of W/U_b=0.4.

5.1.2.3 Velocity contours in a plane normal to the ribs

Figure 29 shows velocity contours in a plane normal to the ribs, $3D_H$ upstream of the bend. The view angle normal to the ribs enables characterisation of the recirculating zone, which occurs downstream of the rib. The diameter of the recirculating vortex is approximately $0.1D_H$. Flow reattachment downstream of the ribs occurs at a distance of approximately 2 rib-heights, perpendicular to the rib axis. Schabacker [112] made a study of other sections and showed that the reattachment length behind the rib remains constant in a large portion of the rib module. Towards the outer sidewall, the reattachment length increases, due to the wall effect as shown in 5.1.3.2. Note the strong flow impingement on the bottom wall in the corner between the rib and the web (left hand side rib in the figure). High turbulent kinetic energy values are encountered in this recirculating area, the heat transfer pattern will certainly be affected. Note also that Casarsa et al. [16] mentioned that the vortex in the recirculation zone behind a 90° rib is a "statistical vortex", which is not present in instantaneous measurements. The vortex downstream of the rib at 45° in the present study is a "real" vortex, since it is present in both instantaneous and mean measurements.

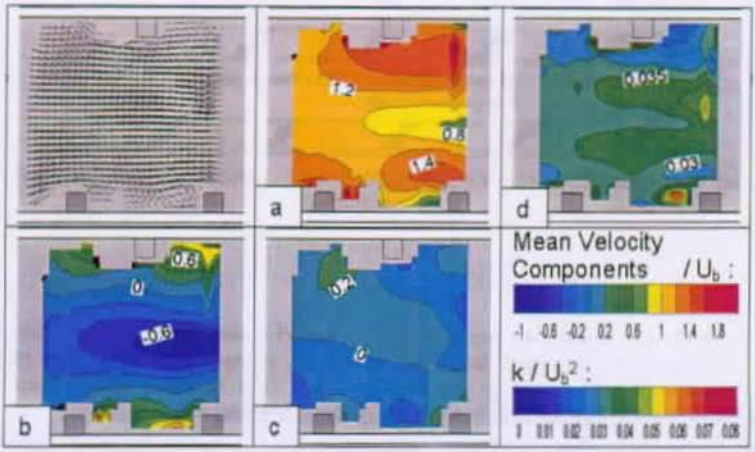

Figure 29: Baseline configuration velocity contours in a plane normal to the ribs, normalized by Ub. (a: Streamwise velocity, U; b: Velocity along Z-axis, W; c: Vertical velocity along Y-axis, V; d: Turbulent kinetic energy).

5.1.3 Full surface heat transfer

An interpolation of PIV measurements, based on an inverse distance algorithm, allowed obtaining 3D-streamlines in the fully developed flow region. A total of twenty-four measurement planes, each of them provided with nine hundred measurement points (30 by 30), were used in the fully developed flow region of the baseline configuration. Fifteen planes parallel to the Y-axis and nine planes parallel to the XZ-plane allowed to create a representation of the 3D flow field in the fully developed region. The interpolated volume and the measurement planes are shown in Figure 30.

The extraction of streamlines in the fully developed region of the baseline case, combined with the full description of the heat transfer contours on the walls, gives two main results. It relates the flow and heat transfer distributions in the fully developed region of coolant channel with 45° ribs. It shows how the vortex structure influences the heat transfer distribution in the near bend fully developed region of a 2-pass coolant channel with 45° rib arrangements.

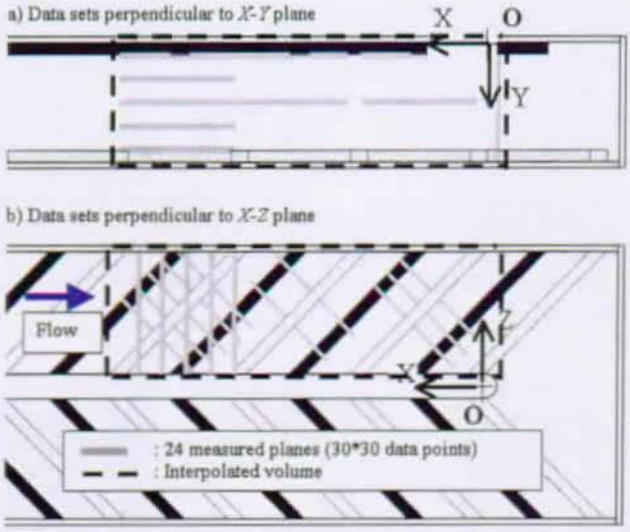

Figure 30: Interpolation volume in the baseline configuration for 2D- and 3D-streamline extraction.

5.1.3.1 Flow streamlines

Figure 31 shows streamline patterns over and downstream a rib in the 16th rib module. Data are extracted from measurement planes normal to the ribs. The streamlines are plotted along the local *X'*-axis. Due to laser light reflection, no measurements are available in the vicinity of the walls and ribs.

As *Z'* increases from location 1 towards location 3, the recirculation cell evolves including the main stream flow above it, and the stagnation point on the bottom wall. The vortex centre moves from both the downstream edge of the rib and the ribbed

wall. The recirculation cell size increases.

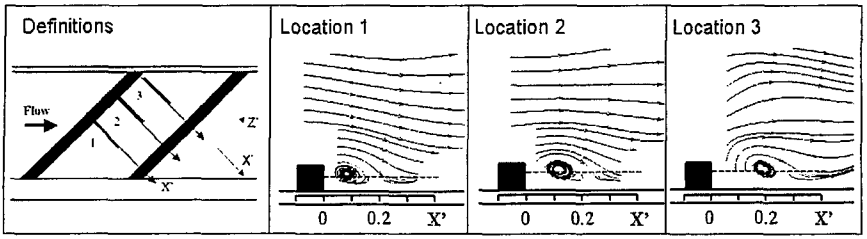

Figure 31: 2D-streamline details in the vicinity of a rib.

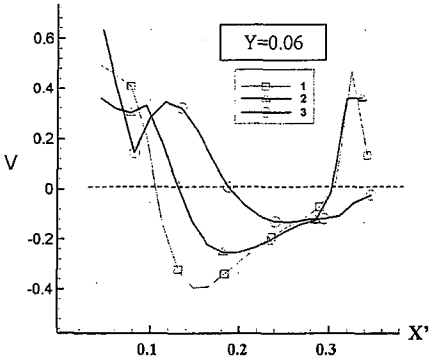

Figure 32: Impinging velocity profiles on the bottom wall downstream of a rib.

Vertical velocities (normal to the bottom wall) are shown in Figure 32. The profiles are extracted from the Figure 31 planes, along $Y = 0.06$ lines (represented by dashed lines in Figure 31). Note that negative and positive velocities indicate impinging flow and motion away from the wall, respectively.

As the flow moves along the rib from the web towards the outer wall, the recirculation cell increases in size as it moves from the downstream wall of the rib. The centre location of the vortex, characterised by V zero-values, are located at $X' = 0.11$ in plane-1 and at $X' = 0.19$ in plane-3. The angle of the vortex centreline to the ribs increases from 4° between plane-1 and plane-2, to 11° between plane-2 and plane-3. V minima, indicating impinging velocity maxima, are shifted away from the rib. The V minima shift angle increases from 7° between plane-1 and plane-2, to 12° between plane-2 and plane-3. The length of the negative velocity region, indicating the impinging area of the flow, also increases as the flow moves towards the outer wall. The absolute values of the impinging velocity decrease as the impinging area increases.

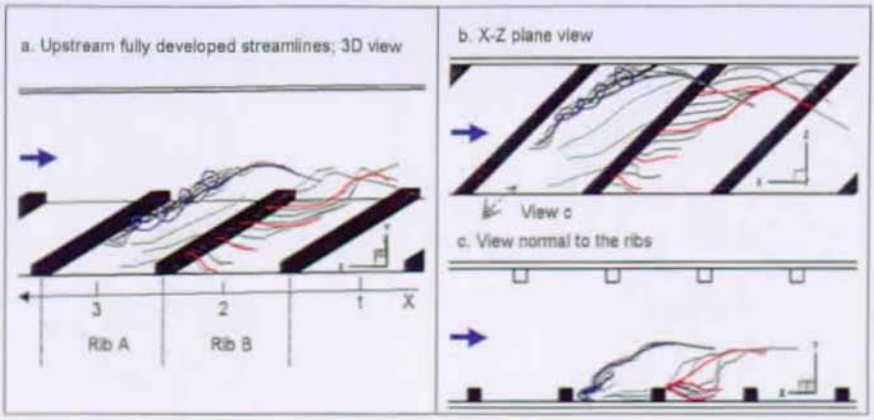

Figure 33: 3D-streamlines in the near bottom wall region.

Streamlines extracted from the full set of PIV measurements are plotted in Figure 33; the streamlines were chosen to start at several locations in order to identify characteristics of the flow field in the fully developed region. The streamline colour helps to distinguish the start location. The upstream fully developed region extents from $X = 3.5$ to $X = 0.5$. The ribbed bottom wall ($Y = 0$) and the outer sidewall ($Z = 1.1$) are shown. Note that the view direction goes through the web, which is not plotted here to clarify the figure.

Streamlines plotted downstream of the ribs show the location and size of the recirculation cell. In the rib-module A, streamlines (blue) start in the core of the recirculating cell, pointing at the recirculating cell itself. In the rib-module B, the streamlines (red) start just above the upper rib surface; they go over the recirculating cell and underline the flow reattachment downstream of the recirculating cell.

In the rib-module A upstream corner between the rib and the web, a recirculating cell starts. As Z increases, the flow inside the recirculating cell is directed along the rib with a convective velocity of $1.2U_b$. The flow develops into a vortex shape along the rib; this is the rib-induced vortex typically mentioned in literature on skewed rib arrangements. As also shown in Schabacker [112] and in Figure 31, the vortex size is increasing as the distance to the web increases. The vortex centre is directed in the streamwise direction as Z increases, yielding in greater reattachment distances from the rib downstream wall.

As the vortex is approaching the outer wall, the vortex strength decreases and the streamlines impinge on the outer wall. The streamlines from the bottom rib region are guided along the outer wall up to $Y = 0.5$, and meet the flow coming from the top wall. This produces two counter-rotating cells already described in 5.1.2.2. The streamlines go as a sheet in the centre of the channel, towards the web. They reach the web $2D_H$ downstream of the impact area on the outer wall.

The part of the flow located above the ribbed wall (green streamlines), between the reattachment line and the next rib, is divided in two regions, separated by a line linking the web-upstream rib corner and the outer wall-downstream rib corner. The part of the flow located upstream of this line undergoes the vortex influence and is directed towards the outer wall. This portion of the flow impinges on the outer wall in

the region $1.9 > X > 2.4$, $Y < 0.3$. The part of the flow located downstream of the separation line, undergoes the effect of the mainstream flow. This region is characterised by low impingement. The flow is directed towards the downstream rib, with velocities parallel to the ribbed wall.

The conclusion from these data is that the complex flow induced by the 45° rib arrangement causes the development of a secondary vortex behind each rib. The main source of the flow characteristics in the straight legs is the vortex induced by the ribs. This vortex structure must be accurately predicted to obtain accurate local heat transfer simulations from the CFD predictions

5.1.3.2 Heat transfer characteristics

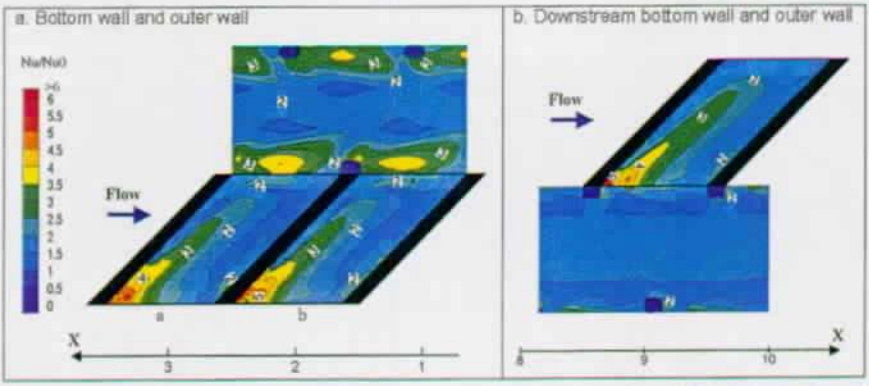

Figure 34: 2D-view heat transfer distributions on the bottom and outer walls in fully developed flow regions.

Heat transfer measurements were conducted in the same model to accompany the flow results. Following are data and discussion on the heat transfer results in the fully developed region (16th and 17th rib module).

Figure 34a shows the heat transfer distribution in the 16th and 17th rib modules, located at $3.5 > X > 1$ in the upstream leg. Two walls are shown, the bottom and the outer walls. Nu / Nu_0 contours are plotted, where Nu_0 is the Dittus-Boelter correlation value for a smooth channel: in the present case, $Nu_0 = 118.7$. The periodic heat transfer distribution from rib to rib shows that the region is near fully developed. Small differences may be attributed to the presence of the turn ($1D_H$ downstream).

On the ribbed wall, four regions can be identified in the rib-module heat transfer distribution. Along the upstream rib, an area of high heat transfer occurs. The Nu / Nu_0 ratio decreases from the web towards the outer wall. The maxima values (up to six times Nu_0), are located between 0.1 to $0.2D_H$ from the rib downstream wall. The angle of the maxima line to the rib is approximately 14°. Next to the outer wall, another region of relatively high heat transfer occurs; Nu / Nu_0 values reach 2.5. A similar region is located next to the downstream rib. Between these three regions, in the rib-module centre, low heat transfer occurs: The Nu / Nu_0 values are between 1 and 1.5,

which are almost the same as in a smooth channel.

Two regions are clearly detectable on the sidewall where the vortex impacts. A region of high Nu/Nu_0 values is located at mid distance between the ribs. It is $0.5D_H$ long and occupies the space $0.3 > Y > 0$ on the outer wall. Nu/Nu_0 values are over 3 in this region. Small differences occur near the top wall due to the channel geometry. Around the channel centre plane ($Y = 0.5$), heat transfer is lower with Nu/Nu_0 values between 1 and 2. Note that the symmetrical channel geometry, which creates two separate flow regions placed apart the $Y = 0.5$ plane, yields a symmetrical heat transfer distribution in the two channel regions: $Y < 0.5$ and $Y > 0.5$.

Results on the same walls were presented in Rau [110] with a directly opposing 45° rib arrangement (see also Figure 93). The distribution was similar to the present study on the bottom wall with the same order of magnitude of Nu/Nu_0. On the outer wall, some differences between the present results and Rau [110] occurred due to the symmetric, instead of the staggered rib arrangement in the present experiments.

Due to optical access restrictions, measurements on the web or second side wall were not obtained in the first leg of the model. However, measurements were taken $10D_H$ downstream of the bend in the second leg of the model. The rib arrangement in the configuration is such that the web of the upstream leg and the downstream outer wall of the second leg, have a similar position, compared to the channel flow field. The ribbed wall heat transfer distributions in Figure 34a and Figure 34b are very similar and Chanteloup and Bölcs [21] showed that at $X = 4$, the flow has almost reached fully developed conditions. Thus measurements on the outer wall in the second leg (Figure 34b) are representative of the upstream web heat transfer.

The differences between the sidewalls in Figure 34a and b are noticeable. The heat transfer levels are much higher on the wall where the vortex, behind the ribs, impinges. Two regions are present: A low heat transfer region is located near the ribbed walls, with values $1 < Nu/Nu_0 < 1.5$. Around the centre line, a region of higher heat transfer values occurs ($1.5 < Nu/Nu_0 < 2$).

Rau [110] also noted big differences in the full surface heat transfer distribution between both smooth walls in its configuration. The 45° rib arrangement leads to high inhomogeneous heat transfer between all channel walls; ribbed walls area-averaged values are 25% and 40% higher than the outer and web walls respectively. The conclusion is that the rib-induced flow has a great impact on the heat transfer distribution, between the ribs on the ribbed walls, and on the sidewalls. Note that Rau [110] found an Area-averaged Nusselt number ratio (Sidewall to ribbed wall without considering the rib) approximately equal to the one of the present study (see Table 12).

5.1.3.3 Combination of flow and heat transfer measurements

3D-views of the flow streamlines superimposed on the heat transfer distribution are shown in Figure 35 and Figure 36. In Figure 35, the streamlines of Figure 33a are superimposed on the heat transfer distribution of Figure 34a. Note that for readability reasons, only seven Nu/Nu_0 contour values are plotted.

The combination of flow streamlines and heat transfer shows the strong influence of the rib-induced secondary flow on the heat transfer. Regions of high Nu/Nu_0 values can be explained by the shape and location of the rib-induced vortex. Near the web behind the rib, the vortex begins in the region of highest heat transfer, up to 6

times the smooth channel Dittus-Boelter correlation value. The vortex develops along the rib, it coincides on the bottom wall with the U-shape high heat transfer area behind the rib. The reattachment zone corresponds to the high heat transfer region on the bottom wall. The varying reattachment length leads to a high Nusselt number region at 30° angle to the streamwise direction. This corresponds to the angle of the maximum impinging velocity shown in Figure 32. The decrease of the impinging velocity leads to a negative Nusselt number gradient in the Z direction. As the vortex impinges on the outer wall, another region of high heat transfer occur, yielding a high heat transfer area on the sidewall ($Nu/Nu_0 > 3$ for $Y < 0.3$). Around the $Y = 0.5$ plane on the outer wall, velocity vectors are away from the outer wall, which leads to a low heat transfer region.

Part of the flow, which is not directed in the rib-induced vortex, remains parallel to the walls. It induces lower heat transfer regions on the walls. The flow passes over the recirculating cell in the upstream rib vicinity, and goes towards the bottom wall in the middle of the rib-module. It induces a region of low Nusselt number. Nu/Nu_0 values reach 1, which indicates that the heat transfer coefficient is approximately the same as in a smooth channel.

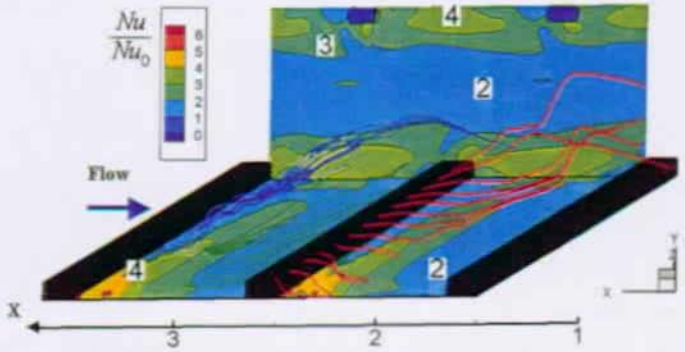

Figure 35: Combined heat transfer distribution and 3D-streamlines in the vicinity of the bottom and outer walls: 3D view.

Figure 36 shows the same region with the heat transfer results of Figure 34 and with streamlines plotted from the centre of the channel. These streamlines are not previously shown. They are representative of the part of the flow that moves towards the web in the middle of the channel around the $Y = 0.5$ plane. Two 2D views are added to Figure 36 to identify the streamline 3D locations (along X-Y and X-Z planes). The streamlines do not show any vortex in the middle of the channel. The flow crosses the channel as sheets parallel to the ribbed walls. The flow is smoothly directed towards the downstream direction by the mainstream motion. The impact on the web is weaker than on the outer wall. This explains the relatively low heat transfer coefficient on the web; Nu/Nu_0 values between 1 and 2 in the web centre part.

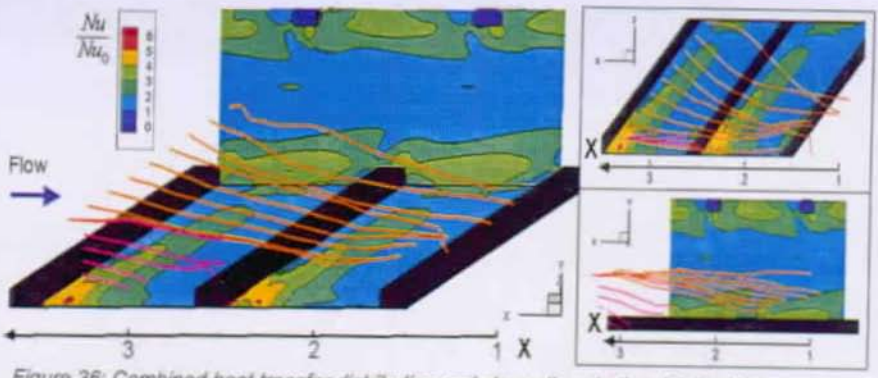

Figure 36: Combined heat transfer distribution and streamlines in the vicinity of the web and $Y = 0.5$ plane; 3D- and 2D-views.

Several conclusions can be drawn from these results, which can help to define the results to check when a comparison with CFD predictions is involved.

The two secondary vortices in channel cross-sections are due to the interaction of the rib induced and the mainstream flows. A secondary motion divides the flow along the channel into two separate regions. The flow in the two halves ($Y < 0.5$ and $Y > 0.5$) is constrained to remain in the same region along both straight legs.

A rib-induced vortex develops downstream of the ribs, impinges on the outer wall along the bottom wall, flows towards the top wall along the outer wall for $Y < 0.5$, and goes back towards the web along the $Y = 0.5$ plane. As the vortex develops along the rib, the vortex size increases, and the centre moves from the rib and from the ribbed wall.

5.1.4 Spanwise heat transfer gradients

Figure 37 shows the spanwise (cross-stream along Z-axis) distribution of Nu in the baseline configuration 4th upstream rib module and 4th downstream rib module. The surfaces plotted were divided into 10 zones equally distributed along the spanwise (Z) or channel height (Y) directions. For each zone, the N value was calculated. N is defined as the sub-zone area-averaged Nusselt number normalised by the full surface area-averaged Nusselt number (see Figure 22). Reynolds numbers was set to 50,000.

Figure 37a shows the heat transfer distribution versus the channel height on the sidewall. The heat transfer distribution is nearly symmetric along the centreline $Y = 0.5$. This confirms the similar influence of both ribbed walls. High heat transfer coefficient gradients occur on the sidewall. Nu values fluctuate by 80% of the Nu full surface area-averaged value in one third of the channel height (between zone 10-20% and 30-40%). Note that the distribution is not completely symmetrical around $Y = 0.5$. This is due to the zone definition, which includes a top rib without including a bottom rib. Indeed, an area of low heat transfer, located just above the bottom rib (see $0 > Y > 0.3$ in Figure 33), is not taken into account. This increases the values slightly for $Y < 0.3$ compared to $Y > 0.7$.

Figure 37b shows the heat transfer gradients on the upstream leg bottom wall. The zone was chosen adjacent to the sidewall zone shown in Figure 37a.

A region of high heat transfer is present at the rib root, near the web ($0.1 > Z > 0.3$). The area between 10-20% D_H ($0.2 > Z > 0.3$) reaches a value of 1.4 times the area-averaged *Nu* value. It is due to the U-shape high heat transfer zone induced by vortex structures in 45° rib arrangements. The vortex influence shown in 5.1.3 is also noticeable near the outer wall. Indeed, the impact on the outer wall reveals a positive gradient between the regions 80-90% and 90-100%.

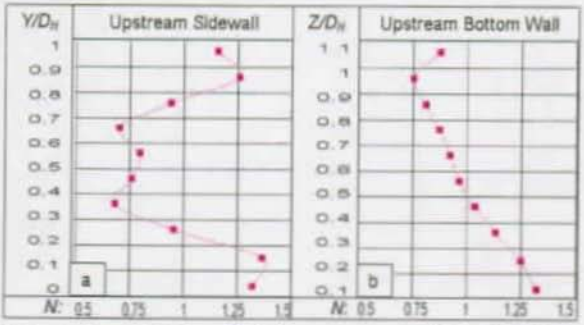

Figure 37: Spanwise and channel height zone averaged heat transfer gradients.

5.2 Bend region

5.2.1 Geometrical characteristics

Multi pass coolant channels are linked with 180° turns. The turns are abrupt change of geometry in the cooling system. They induce pressure losses due to bend-induced secondary flow (Dean vortices) and flow detachment at the web tip. On the other hand, the heat transfer benefits from the flow modifications created by the bend and is enhanced in the bend region.

The bend geometry is usually optimised to reduce the losses. The web size, the space between the web tip and back wall are optimised (see Schnieder et al. [116]). The web thickness also influences the flow field and thus the heat transfer distribution (Liou et al. [93]) Geometrical features such as turning vanes are added in order to help the flow rotation (Plevich [104]). The ribs are orientated in both the upstream and downstream legs in order to minimise the losses induced by the secondary flow field (Mochizuki et al. [100]).

In the baseline configuration, the bend geometry was selected in order to respect the main rules, but also in order to allow CFD calculation with reasonable mesh sizes. The web is $0.2D_H$ thick. The web tip is rounded. The ribs are orientated to avoid change of rotation in the secondary flow field, which could induce additional pressure loss.

5.2.2 Pressure loss

The turn region plays an important role in the global coolant passage pressure losses. The bend is difficult to define in terms of pressure distribution. It can be defined as the region between two parts of the channels where fully developed flow conditions occur. For the present study, it has been chosen geometrically: the channel part between two points located in the centre of the top rib modules, at $X = 1D_H$ upstream and $X = 1D_H$ downstream of the bend. The pressure coefficient following this definition, is $K_l = \Delta P \Big/ \frac{1}{2}\rho U_b^2 = 3.62$. It corresponds to an equivalent length of $L_{eq} = K_l \frac{D_H}{f} = 13.7D_H$, if f is the fully developed friction factor.

5.2.3 Area-averaged heat transfer

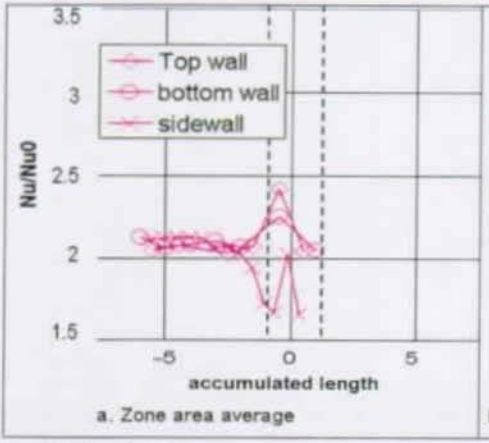

$\overline{Nu/Nu_0}$	Bend up	Bend down	Bend mean
top wall	2.42	2.04	2.23
bottom wall	2.25	2.04	2.15
sidewall	2.16	1.75	1.95

b. area average values

Figure 38: Bend region area-averaged Nusselt number (baseline configuration, Re=50,000).

The ribbed wall Nu/Nu_0 values are strongly influenced by the bend itself. The bend walls are split into two zones; the upstream zone ($Z > 0$) and the downstream zone ($Z < 0$). The bend influence is noticeable by heat transfer enhancement in the first half of the bend region, of 8% and 18% compared to the fully developed values for the bottom and top walls, respectively. The area-averaged results of the second half of the bend are approximately equal to the fully developed values. The fluctuations in the bend regions are larger on the top wall than on the bottom wall. This is due to the top

wall ribs extending into the bend.

The outer smooth walls, which are the upstream outer sidewall, the bend back wall and the downstream outer sidewall, have a heat transfer distribution slightly different from the ribbed walls. The plateau value in the upstream leg is disturbed by the bend, up to $2.5D_H$ from the back wall. It indicates that the flow undergoes the bend effect. The flow accelerates towards the web at the bend inlet, and the rib-induced impinging flow strength on the outer wall diminishes at the bend inlet. The upstream outer wall minimum value occurs in the corner between the sidewall and the back wall ($Nu/Nu_0 = 1.75$). This is due to the recirculating cell in the upstream bend corner. On the back wall, the major part of the incoming flow impinges in the $Z > 0$ region. The $Z < 0$ part has a heat transfer level as high as the last zone of the upstream sidewall.

5.2.4 Flow characteristics

5.2.4.1 Flow unsteadiness

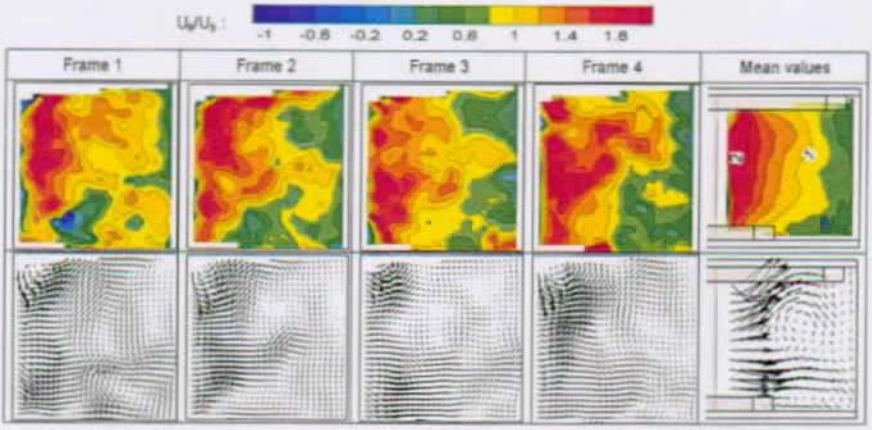

Figure 39: Flow unsteadiness in the bend of the baseline configuration ($\theta = 90$deg).

The flow in the bend region is more complex than in the ribbed region. The flow in the bend starts with the secondary structure from the ribs at $\theta = 0$deg. Analysis of 100 PIV data sets at $\theta = 0°$, 45°, 90° 135° and 180° in the bend showed that the secondary flow or vortex structure has the vortex core at different locations in the instantaneous flow fields. This variation appears to be due to unsteadiness in the flow.

Figure 39 gives an example of 4 instantaneous frames and the mean value calculated from 1250 frames. The plane is located is at $\theta = 90$deg in the bend region. All the measured secondary velocity vectors (30x30) are plotted in the instantaneous frames, whereas 15x15 vectors are plotted in the mean result view. For clarity reasons, the vector scaling is smaller in the instantaneous frames. This scaling allows stressing the differences between one frame and another.

The unsteadiness of the flow appears obvious in the measurement sequence of

instantaneous frames. The sizes, locations and even directions of rotation of the secondary flow vortices vary from one frame to the other. The sizes can double and the location of the vortices' centres can move of more than $0.5D_H$. The streamwise component patterns are also strongly modified by the unsteadiness.

The variations of streamwise and secondary flow patterns occur in the entire channel; in the upstream leg, in the bend and in the downstream leg. Furthermore, the variation in core location appears to increase as the flow progresses through the bend. It becomes less unsteady in the downstream leg as the flow recovers from the bend effect.

In the data reduction process, the unsteadiness is calculated as an increased turbulence fluctuation. Thus numerical simulation of the flow may require unsteady flow calculations rather than Reynolds-stress turbulence modelling in order to capture the unsteadiness effects on the heat transfer distribution.

5.2.4.2 Mean velocity contours

Kinetic turbulent energy, mean streamwise velocity contours and secondary flow vectors obtained at $\theta = 0°$, 45°, 90°, 135° and 180° in the bend are presented in Figure 40. As noted before, these average velocity results were obtained from 1250 full-field data sets. For this set of results, the orientation of the view is always into the oncoming flow with the web at the left-hand side of the figure.

At $\theta = 0°$, the streamwise velocity distribution and the secondary flow pattern in the centre region show the effects of the bend. However the secondary flow near the top and bottom wall that is connected with the rib orientation has decreased from that shown in Figure 28 for the developed flow between ribs. The streamwise flow near the inner web has begun to accelerate, indicating that this flow has entered the bend region. Note that near the web, all the secondary flow vectors are toward the web. The first leg rib arrangement induces a secondary flow, which directs the flow towards the web, helping the flow to follow the 180° turn.

At $\theta = 45°$, the streamwise velocity increases to more than 2 near the inner web and has a small region of negative velocities in the lower outside corner region. The high streamwise velocity near the inner web is compatible with the conservation of angular momentum in the bend region. Note that near the web, the secondary flow vectors are away from the web.

At $\theta = 90°$, the streamwise velocities of the flow have decreased near the web. The size of the region near the web where the secondary flow is away from the web has increased. The upper secondary cell seen at 45 ° continues but the lower cell has disappeared.

At $\theta = 135°$, the flow has separated from the web and streamwise velocities are negative. The average position of the vortex cell has moved toward the web and the secondary flow is generally away from the web. The streamwise velocity has a negative value near the outer wall, indicating a small recirculation cell.

At $\theta = 180°$, a small region of recirculation occurs near the web and the lower wall. The upper rib, which extends into the bend region, has influenced the flow near the upper wall and probably decreased recirculation in that region. The secondary flow that remains from the bend is orientated towards the outer sidewall in the channel centre plane. It justifies the rib orientation downstream of the bend, which keeps the same secondary cell rotation directions. Note that the highest streamwise velocities have moved from near the web to the outer half of the passage and are 1.5 to 2.0

times the bulk velocity.

These profiles provide good details for CFD validation in regions of high velocity gradients and recirculating areas. Note that high turbulent kinetic energy values (~10%) are located in region of high shear, i.e. in region of high streamwise velocity gradients.

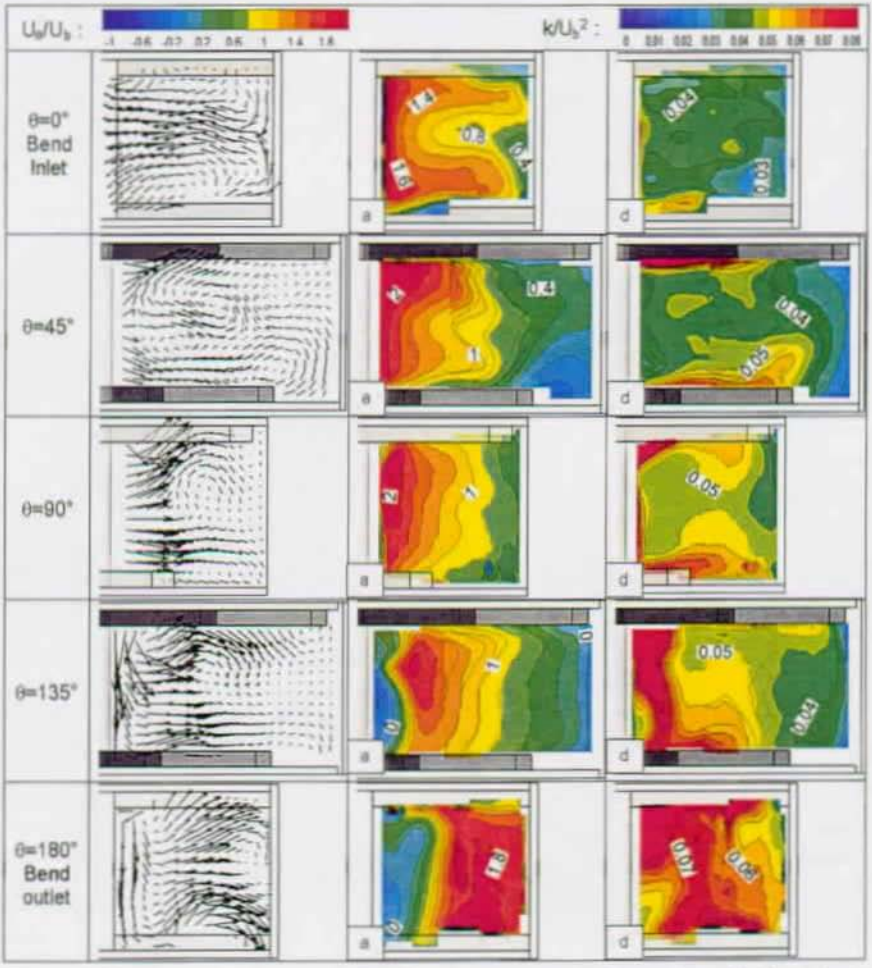

Figure 40: Baseline configuration turbulent kinetic energy, mean streamwise velocity contours and secondary flow vectors obtained at θ=0°, 45°, 90°, 135° and 180° in the bend, normalized by U_b. (a: Streamwise velocity, U; d: Turbulent kinetic energy).

5.2.4.3 *Full surface heat transfer*

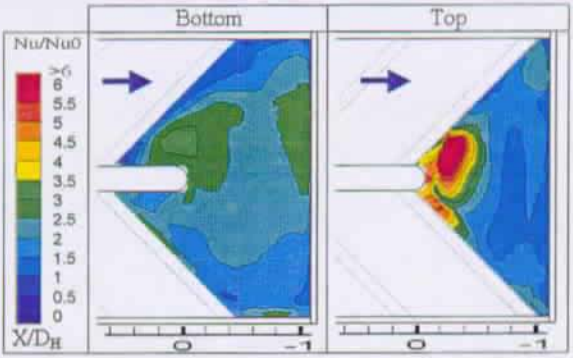

Figure 41: Baseline configuration bend region: Heat transfer distribution (Re=50,000).

Figure 41 shows the full surface heat transfer distribution in the bend region of the baseline configuration. It gives information on the effect of the placement of the last rib just upstream of the bend.

It was mentioned in 5.2.3 that the area-averaged surface values on the bottom wall are lower than on the top walls, by about 5%. Indeed, in a more detailed description of the distribution, the bottom and top wall are different. No high heat transfer gradients occur on the bottom wall. Nu/Nu_0 values remain lower than 3.5. Two higher Nu/Nu_0 regions nevertheless appear at the web tip and along the back wall upstream part ($0 < Z < 0.8$). On the top wall, the bend region heat transfer distribution is separated into two zones, $0 > X > -0.6$ near the web tip, and $-0.6 > X > -1.1$ near the back wall. The region $0 > X > -0.6$ is a region with high heat transfer, Nu/Nu_0 is higher than 6 in the core of this region: heat transfer gradients are high. Although not shown here, the region is well correlated with the high impinging velocity region that was measured in the $Y = 0.85$ plane. This will certainly lead to a cold spot near the web tip. The region $-0.6 > X > -1.1$ has lower heat transfer values ($Nu/Nu_0 \approx 1-1.5$). Gradients are relatively low in this second region.

It must be stated that the total surface in the bend region is 90% bigger on the bottom wall than on the top wall. Furthermore, the area-averaged value on the upstream bottom ribbed walls ($Z>0$) is 8% higher than the fully developed area-averaged value. As a consequence, the bottom wall will cool the bend region more efficiently than the straight channel, but with lower gradients than on the top wall. The bottom and top wall locations (versus suction and pressure side) should then be chosen with care.

Note that a full description of the recirculation cells and of the 3D-streamlines in the baseline configuration is given in 6.2.4.4. Paragraph 6.2.4.4 adds information on the manner the 180° turn flow field influences the heat transfer distribution.

5.3 Downstream leg region

5.3.1 Pressure loss

Table 5 shows a comparison between the upstream and downstream leg mean friction factors. They were calculated from pressure differences measured in six different rib modules. In the downstream leg, the three rib modules immediately downstream of the bend were not taken into account in the calculation of the mean value.

The friction factors are the same in the upstream and downstream legs. The variations are in the order of the measurement technique accuracy. This shows that the pressure distribution recovers rapidly from the bend effect. Note that in the three rib modules just downstream of the bend, the pressure distribution is disturbed by the bend. Pressure taps are located in the vicinity of the web tip recirculation cell. It yields negative friction factors in this channel region. Schnieder et al. [116] noticed the same phenomena.

Re= 50, 000	Upstream leg	Downstream leg
C_f	0.0657	0.0659

Table 5: Upstream and downstream leg friction factors (baseline configuration, Re=50,000).

5.3.2 Area-averaged heat transfer

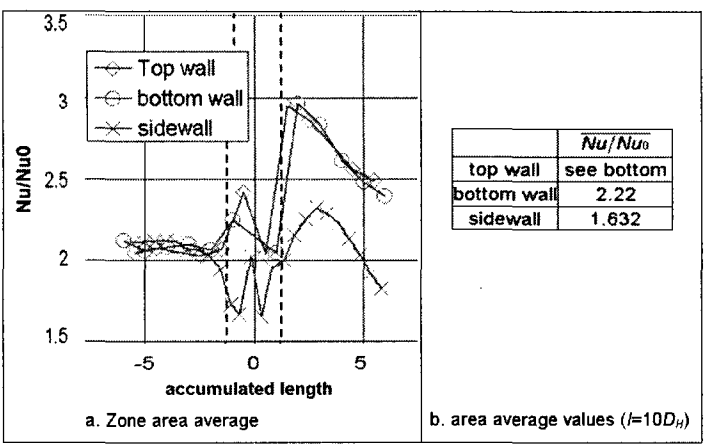

Figure 42: Downstream leg region area-averaged Nusselt number (baseline configuration, Re=50,000).

Downstream of the bend is another region with relatively large variations in heat

transfer. Figure 42a gives the heat transfer results in the vicinity of the bend (upstream, in the bend and downstream). Figure 42b gives the area-averaged values $10D_H$ downstream of the bend. Note that top wall values are not available, since the data acquisition was not good enough in that plane to allow area averaging. However, it can be noticed from full surface heat transfer results, that both ribbed walls have approximately the same distribution; in turn it should give the same area-averaged value.

The ribbed wall heat transfer values recover from the bend effect. The heat transfer levels evolve in a same manner for both the top and bottom walls and the Nu/Nu_0 values are approximately equal. They reach a peak value in the first two ribs downstream of the bend, up to 50% higher than in the fully developed region. The heat transfer decreases farther downstream, as the flow recovers from the 180° turn. Note that $10D_H$ downstream of the turn, the heat transfer level is still 5% to 10% higher than in the fully developed region.

The sidewall has a heat transfer distribution slightly different from the ribbed walls. The heat transfer level increases from the downstream bend corner, where a recirculating cell takes place, to a maximum value at $l/D_H = 2.5$ downstream of the back wall, where the turning flow impinges on the outer wall. The heat transfer values rapidly decrease to levels lower than the fully developed levels; $Nu/Nu_0 = 1.63$ $10D_H$ downstream of the bend against 2.25 upstream of the bend. This behaviour is due to the symmetrical rib arrangement between both the upstream and downstream channel legs (see 5.1.3.2).

5.3.3 Flow characteristics

The streamwise velocity contours immediately downstream of the bend, $0.0 < X < 4.0$, at five heights are shown in Figure 44. The secondary flow vectors from the same region are presented in Figure 43. Note that spurious vectors in the velocity vector fields are due to the interpolation of regions with lack of measurements.

The secondary flow vectors show the flow characteristics in the flow reattachment and adjustment region. The velocity vectors are mainly directed towards the outer wall instead of the web, due to the rib orientation in the downstream leg. Downstream of the first two ribs (top and bottom walls), the secondary flow shape is already composed of two rib induced counter-rotating vortices. Their size and magnitude reach the level of the fully developed flow at $X = 2.66$.

The streamwise velocity contours at $Y = 0.89$ for $0.0 < X < 1.0$ are markedly different from those at the same heights for $1.0 < X < 4.0$. The streamwise velocity in the regions around the ribs appears to readjust to rib dominated flow within a shorter distance than the flow in the central portion of the coolant passage, $Y = 0.3$, 0.5, and 0.7. The flow at $X = 4.0$ does not reach the same streamwise velocity distribution as measured for the developed flow region of the upstream leg.

The streamwise velocity contour shape needs more distance than the secondary flow to readapt to the fully developed flow shape; at $X = 3.66$, one can not observe the same distribution as in the fully developed region. This is especially true near the outer wall where values of 1.4 are still reached.

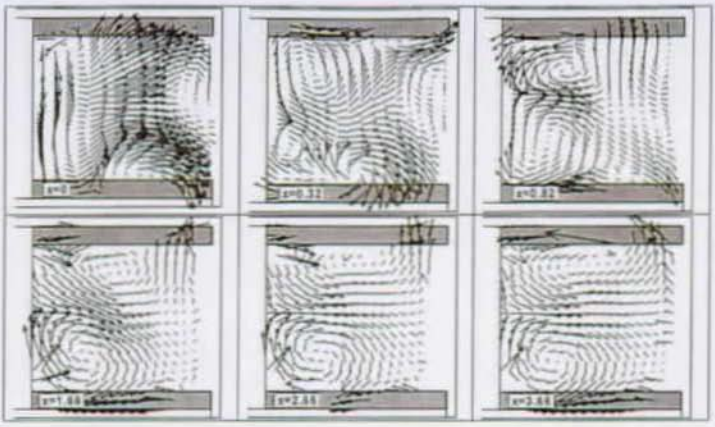

Figure 43: Baseline configuration secondary flow vectors for 0.0 < X < 3.66.

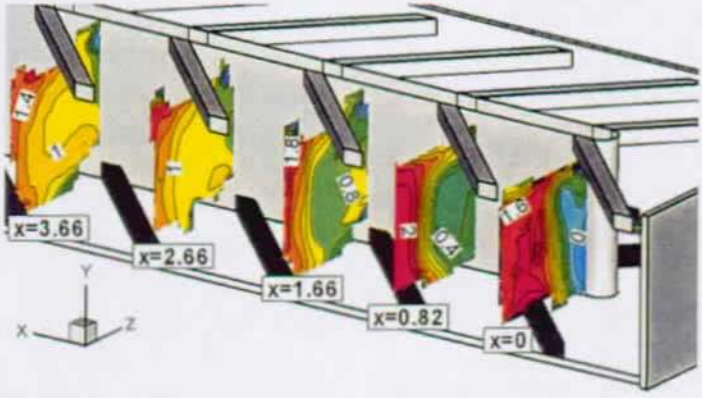

Figure 44: Baseline configuration streamwise velocity components in downstream leg cross sections for 0.0 < X < 3.66.

5.3.4 Full surface heat transfer

5.3.4.1 Ribbed walls

Figure 45 shows full surface heat transfer distributions in the downstream leg of the baseline configuration. Both ribbed wall results are discussed in the following paragraphs. Heat transfer results are connected to flow measurements presented in Figure 43 and Figure 44.

As already mentioned in 5.3.2, downstream of the bend, the heat transfer levels on the ribbed walls are clearly higher than in the upstream leg. In terms of full surface

distribution, the rib induced heat transfer shape is the same as in the fully developed region, with higher levels. It can be explained by the locally high streamwise velocity shown in the vicinity of the outer sidewall (Figure 44). The high velocity takes place at the root of the rib induced secondary vortex, thus higher velocities increase the strength of the vortex effect on the heat transfer.

The heat transfer levels decrease as the flow recovers from the bend effect. It comes from the same effect as mentioned in the previous paragraph. The local streamwise velocity decreases as X increases, in turn the heat transfer becomes lower. As the flow homogenises downstream of the bend, the upstream leg fully developed heat transfer pattern is recovered.

In the top wall first rib module, the heat transfer distribution is different from the typical 45° rib induced distribution. The heat transfer is low at the rib root ($Z = -1.1$). The rib root is in the bend and the velocity along the X-axis is low. The rib cannot create the typical rib induced vortex. Near the web tip ($-0.1 > Z > -0.6$), a high heat transfer spot takes place. It is well correlated with the high impinging velocity resulting from the bend induced secondary flow (see $X = 0$ in Figure 43 and $\theta = 90° - 135°$ in Figure 40).

On the bottom wall, the upstream fully developed distribution shape is recovered from the first rib module downstream of the bend. This first rib is placed far enough from the bend, and governs the heat transfer in the adjacent downstream rib module.

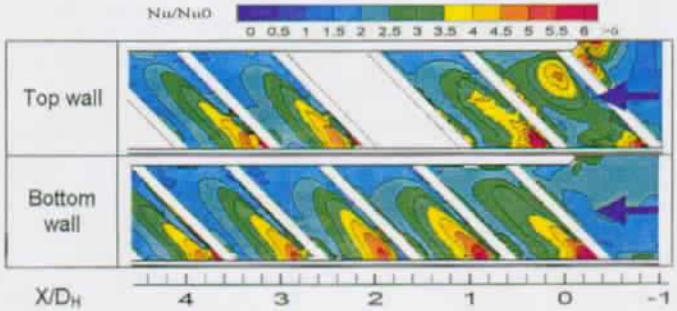

Figure 45: Full surface heat transfer distribution: baseline configuration downstream leg.

5.3.4.2 Sidewalls

Figure 46 shows Nu/Nu_0 distribution on the downstream sidewall for a flow condition of Re=50,000.

The downstream sidewall is characterised by the turning flow impingement zone at approximately $X = 0$. This area is characterised by three regions. Near the bottom wall ($Y < 0.25$), the heat transfer is the highest. In this region, both streamwise and rib-induced secondary flows are high. This is due to the first leg incoming flow, which impinges on the sidewall in this region. Near the top wall ($Y > 0.75$), the heat transfer levels are 66% lower than near the bottom wall. It is due to an approximately 66% lower velocity along the X-axis.

Farther downstream, the flow recovers from the bend effect and the heat transfer

reaches the upstream inner sidewall fully developed values. The heat transfer near the outer side wall seems to be linked to the local streamwise velocity component. Indeed, the flow near the sidewall is approximately parallel to the wall (see Figure 35). Furthermore, if one compare the decrease of velocity to the decrease of heat transfer, the smooth channel Dittus-Boelter law is verified. (e.g. $\left(\frac{Ux=0}{Ux=10}\right)^{0.8}=\left(\frac{2}{1.2}\right)^{0.8}=1.33$ and $\frac{Nux=0}{Nux=10}=\frac{2.3}{1.75}=1.31$. Note the heat transfer profile symmetry (versus $Y=0.5$ plane), which occurs on the downstream sidewall. It is due to the symmetrical secondary flow induced by the ribs.

Farther downstream of the bend ($X=10$), the heat transfer pattern is representative of the web in the upstream leg fully developed flow region (see 5.1.3.2).

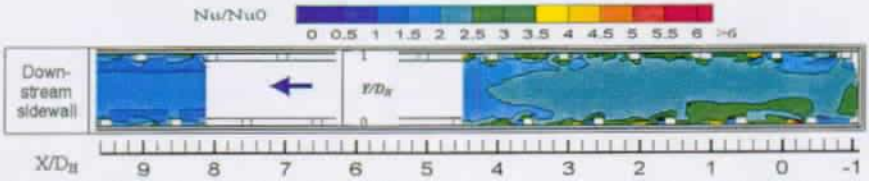

Figure 46: Full surface heat transfer distribution: baseline configuration downstream sidewall.

Conclusions of chapter 5

Chapter 5 presented flow and heat transfer results in a 2-pass coolant channel with 45° rib arrangement. The channel geometry and flow conditions are representative for internal coolant channels of gas turbine airfoils.

Comparison with previous published results (see Appendix A)

- Present measurement values only present a 5-8% difference compared to Han's correlations, which is in the range of both correlation and measurement uncertainties.
- Rathjen [108] performed mass transfer measurements in a similar channel to the present study. The area-averaged mass transfer results are 10% different from the present heat transfer results.
- Rathjen [108] full surface mass transfer and present heat transfer results present similar values in the major part of the channel.
- Rau [110] steady state TLC measurements in a straight channel with parallel 45° ribs presented a difference of less than 5% with the present results.

Combined flow and heat transfer have been described in details in the fully developed flow region, in the 180° turn region, and downstream of the turn. Note that in every region of the channel the Nu/Nu_0 values are always higher than 1, indicating that at every location the 45° rib arrangement better cools the channel than smooth walls.

Fully developed flow region

- The present full field fully developed flow detailed measurements confirmed and gave details on observations made in previous works.
- The two secondary vortices in channel cross-sections were shown to be due to the interaction of the rib induced and the mainstream flows. 3D-streamlines extracted from the full velocity data set highlighted this interaction.
- 45° rib arrangements lead to Nu/Nu_0 area-averaged values of 2.1 on the ribbed walls (2.8 if the rib is taken into account), and 2.25 on the outer sidewall.
- Nu/Nu_0 can vary of a factor 6 in less than $0.3D_H$ in a single rib module.
- The impinging velocities induced by the vortex are strongly linked with the regions of high heat transfer on both ribbed and sidewalls.

Bend region

- The flow characteristics in the bend region are complex; two curvature-induced vortices are added to the two secondary flow rib-induced vortices.
- The flow modifications strongly influence the heat transfer distribution.
- Area-averaged Nu/Nu_0 in the upstream part of the bend is 8% and 18% higher than in the fully developed region, on the bottom and top walls, respectively.
- The location of the last rib in the bend has an impact on the high heat transfer region that occurs at the web tip.
- Nu/Nu_0 values in the downstream part of the bend are approximately equal to the

fully developed region values.

Downstream leg region

- $4.5D_H$ downstream of the bend region, the streamwise velocity has not reached the upstream fully developed profile.
- $3D_H$ downstream of the bend region, the secondary flow has almost reached the upstream leg fully developed secondary flow pattern.
- It takes longer to reach the fully developed Nu/Nu_0 values than to redevelop the secondary flow.
- The sidewall heat transfer distribution differs from the upstream sidewall. This is due to the symmetrical rib placement in the two channel legs.
- $10D_H$ downstream of the bend region, the heat transfer distribution on the outer sidewall is representative of the upstream web heat transfer distribution in the fully developed flow region.

6 INFLUENCE OF DESIGN PARAMETER MODIFICATION

6.1 Influence of Reynolds number

6.1.1 Area-averaged heat transfer

The heat transfer distribution at Re=25,000 and Re=70,000 in Figure 47 are superimposed on the results of Figure 42. The general trend of the heat transfer distribution can be summarised as follow.

On the ribbed walls, the Nu/Nu_0 values are stable in the upstream leg, indicating that the flow is fully developed. This stable value remains the same up to $1D_H$ upstream of the bend. The heat transfer in the upstream leg does not seem to be influenced by the bend. The ribbed wall Nu/Nu_0 values are strongly influenced in the bend itself. Downstream of the bend, the ribbed wall values recover from the bend effect, as mentioned in 5.3.2.

The outer wall heat transfer distribution is different from the ribbed wall distribution. It undergoes the bend effect farther upstream of the bend. Downstream of the bend, the Nu/Nu_0 values decrease to levels lower than in the upstream leg. Note that the recovery length downstream of the bend does not depend on the Reynolds number.

The area-averaged heat transfer results evolve in a similar way for all three Re tested. However at every location in the channel, the Nu/Nu_0 values decrease as Re increases. This is true for the bottom, top and outer walls (upstream sidewall, downstream sidewall and bend back wall). Liou and Kao [91] and Liou et al. [87] showed a similar trend. Note that due to the evolution of the Dittus-Boelter Nusselt number, increasing with Re number, Nu values increase with the Reynolds number.

Only three Reynolds numbers were measured. Thus no trend of Nu/Nu_0 versus Reynolds number can be clearly determined from the data. However if a trend $Nu/Nu_0 = c \cdot Re^{-a}$ is assumed, a values are between 0.1 and 0.2 for all walls in the fully developed region. These are typical values with regard to literature.

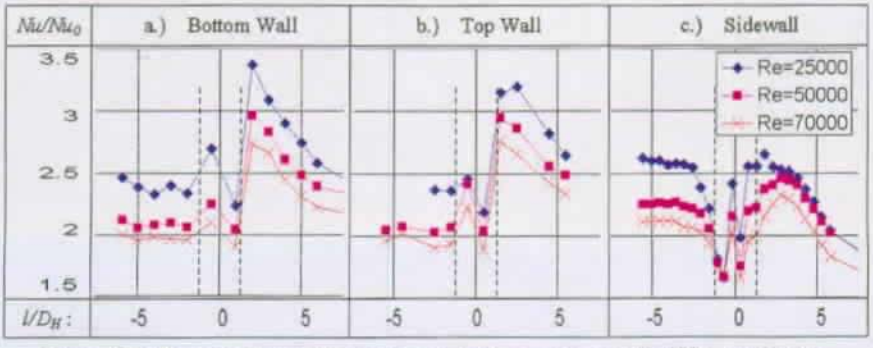

Figure 47: Influence of Reynolds number on the Area-averaged Nu/Nu_0 distribution.

6.1.2 Full surface heat transfer

Figure 48 gives a description of the influence of Reynolds number on the full surface heat transfer distribution. The trends described in the present part are valid for all the channel walls.

The influence of Reynolds number is the same as given in Figure 47; the Nu/Nu_0 ratios decrease as Re increases. Furthermore, the contour shapes once normalised by the Dittus-Boelter values are only slightly modified by Re variation. This trend is valid at every measured location in the channel, except in the bend region. At Re=25,000 in the bend region, a high heat transfer area occurs downstream of the last bottom rib, from $Z = 0.1$ to $Z = 0.9$. It might create high heat transfer gradients with thermal stresses. This can become critical, as the bend region is an important part to homogeneously cool, particularly in industrial gas turbines. Note that although not shown here, the difference at Re=25,000 does not occur on the top wall.

As shown in Figure 103, the heat transfer distribution is very similar on the top wall for all the Reynolds numbers. The global evolution downstream of the bend for Re=50,000 has been described in chapter 5. The U-shape high heat transfer region in the recovery region bears the same characteristics for all three Reynolds numbers. Re does not seem to influence the U-shape region angle behind the ribs. Only the first top wall rib module downstream of the bend is different from the other rib modules, with the same pattern characteristics for each Re. Downstream of the 3rd rib module, the heat transfer distribution looks very similar on both the top and bottom walls. This is the case for all the tested Reynolds numbers. Thus downstream of this location, the bend influence on the flow acts on both walls symmetrically.

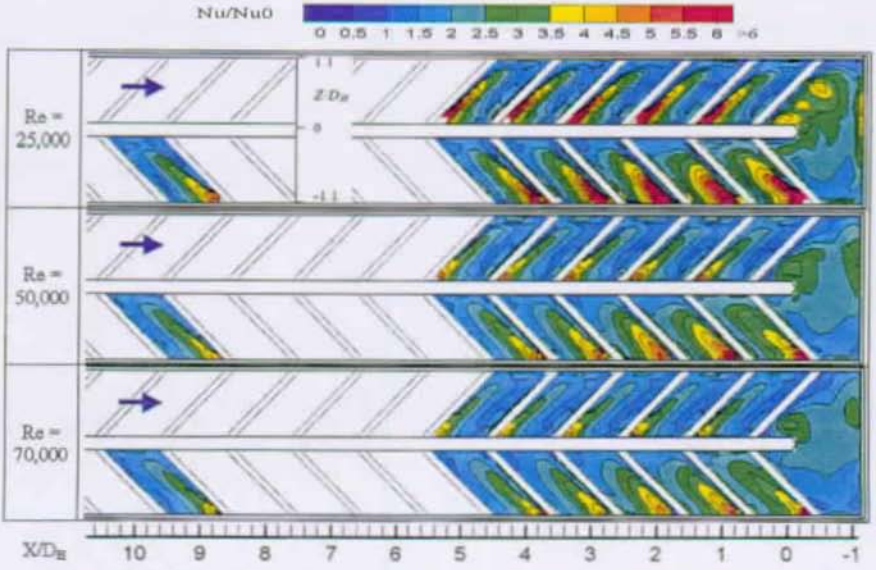

Figure 48: Bottom wall full surface heat transfer distribution: Influence of Re number.

6.1.3 Spanwise and streamwise heat transfer gradients

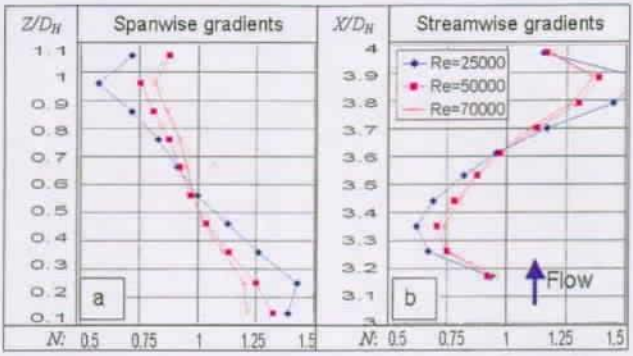

Figure 49: Bottom wall heat transfer gradients: Influence of Reynolds number.

The evolution of N values along the spanwise direction has been described in 5.1.4. Figure 49 gives information on the N value evolution with the Reynolds number. Conclusions of this graph are that the heat transfer gradients on the ribbed walls are higher as Reynolds number decreases. Between 10% and 90% ($0.2 > Z > 1$), the heat transfer distribution is nearly linear for all three Reynolds numbers, with a slope depending largely on the Re. The steepest slope occurs for Re=25,000, with plot extreme values reaching –40% to +40% of $Nu_{full\_surface}$.

Figure 49b shows bottom wall heat transfer gradients in the streamwise direction. They are plotted in the same rib module as in Figure 37. The surfaces plotted were decomposed into 10 zones parallel to the ribs equally distributed along the streamwise (X) direction. Note that no values are available for $3.15 < X < 4$, since no measurements were performed on the rib ($3 < X < 3.15$).

In the upstream leg, streamwise gradients of N are as high as spanwise gradients. Values for Re=25,000 range from –40% to +60% of the full surface area-average value. Values are symmetrically distributed around the rib module centre, with 40% of the values higher, and 40% lower than 1. It can be noticed that immediately downstream of the rib ($X < 4$), gradients are slightly higher than downstream of the rib module centre ($X < 3.5$).

It can be seen in Figure 49 that as Re increases the gradients of N diminish, and the N values are closer to 1. One could imagine that the N values could tend to 1 as the Reynolds number would further increase. One explanation could be that the ribs, which are geometrical singularities at low Re, tend to become global geometrical characteristics at high Re. The rib arrangement might be compared to a roughness at high Reynolds numbers, yielding a homogeneous heat transfer distribution. Note that additional measurements are needed to confirm this trend.

6.2 Influence of extraction

Extracting a part of the flow from the channel through holes modifies the heat

transfer distribution along the channel. The extraction simulates film-cooling holes from the internal side. The present part quantifies the effect of extracting 30% up to 50% of the inlet massflow in the baseline configuration geometry (baseline geometry + extraction = configuration-2). The next paragraphs also relate the flow characteristics inside the channel to the heat transfer distribution on the walls.

6.2.1 Massflow extraction characteristics

Massflow measurements have been performed for each hole, quantifying the ejection distribution along the configuration-2 channel. Figure 50 gives details of the massflow distribution, as well as the bulk massflow present in the channel with regard to the hole number. The measurements shown in Figure 50 were taken at Re=50,000 and C_{extrac}=50% (C_{extrac} = channel inlet massflow / total extracted massflow). Both quantities are normalized by the inlet massflow, 0.089kg/s. Note that upstream of the 1st hole, the bulk massflow ratio is 1, and 0.5 downstream of the 17th hole.

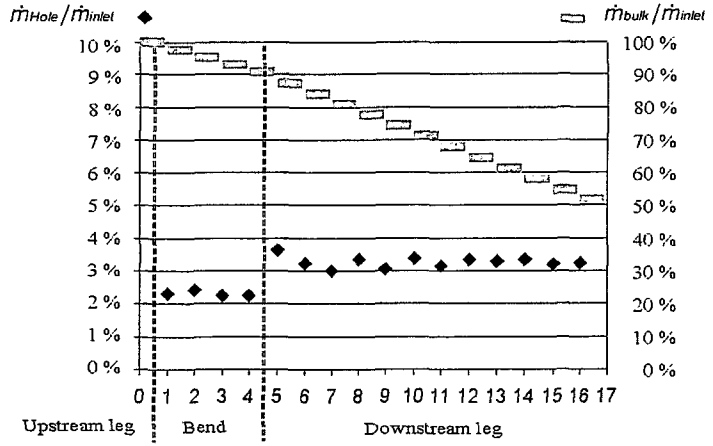

Figure 50: Hole velocity distribution and remaining bulk massflow along the configuration-2 (Re=50,000, C_{extrac}=50%).

The ejection through each hole of the bend is approximately constant, 2.3% of $\dot{m}_{inlet}$. This leads to a 9.2% loss of the inlet massflow in the bend. Downstream of the bend, as the flow recovers to the rib induced developed flow, the ejection through the holes becomes constant. From the 2nd to the 6th rib module, 6.5% of $\dot{m}_{inlet}$ is ejected per rib module. However, the ejection through every second hole of each rib module is greater than through the first hole. The massflow difference between two consecutive holes reaches 10% to 2% in the 2nd and 6th downstream rib modules, respectively. This can be attributed to the recirculating zone downstream of each rib, where the static pressure is less than after the flow reattachment in front of the bottom ribs (in location of every 2nd hole). Note that the influence of the bend can be noticed in the 1st rib module downstream of the bend, increasing the massflow through the 1st hole.

6.2.2 Area-averaged heat transfer

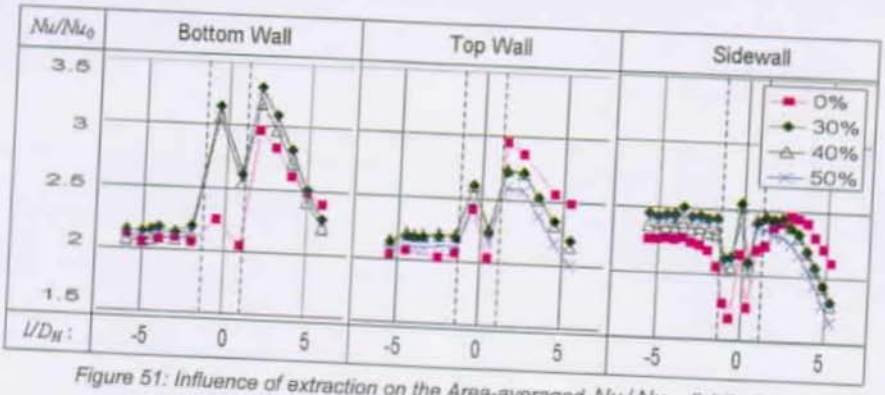

Figure 51: Influence of extraction on the Area-averaged Nu/Nu_0 distribution.

Figure 51 gives area-averaged heat transfer results on the channel walls at Re=50,000. Cases with extraction were added to the 0% extraction (baseline configuration) results plotted in Figure 42.

The upstream leg distribution on all walls is not clearly modified by the extraction. Although the flow field was shown to be influenced by the extraction in this region, it does not influence the area-averaged heat transfer in the upstream leg.

In the bend region and downstream of the bend, the extraction modifies the heat transfer on all walls.

On the bottom wall, which is provided with the extraction holes, the bend region Nu/Nu_0 distribution is strongly increased by the extraction. In the upstream part of the bend wall, Nu/Nu_0 values are 38% higher than in the 0% extraction case. Nu/Nu_0 decreases downstream of the bend. The levels are higher than at 0% extraction immediately downstream of the bend, and they are lower downstream of $l/D_H = 4$. Upstream of $l/D_H = 4$, the presence of the holes provides a heat transfer enhancement, which is high enough to obtain a Nu/Nu_0 level higher than in the 0% case. Downstream of $l/D_H = 4$, 60% of the total extracted massflow has already left the channel, and the enhancement due to the hole is not big enough to obtain the heat transfer levels of the 0% case.

On the top wall, which is not equipped with extraction holes, the heat transfer levels are also influenced by the extraction. In the bend region, the Nu/Nu_0 levels are similar for $C_{extrac} = 0\%$ to 50%. Note that in the bend region, for all the extractions, only 20% of the total extracted massflow has left the channel. In the downstream leg, the heat transfer levels of cases with extraction are lower than in the 0% extraction case. The heat transfer decrease due to the massflow loss along the channel, is not compensated by the heat transfer enhancement around the extraction holes. One consequence is that the Nu/Nu_0 differences are greater than 20%, between the top and the bottom walls in the cases with extraction.

On the outer walls, the presence of extraction improves the heat transfer, in the near upstream bend region, and in the bend region. Nu/Nu_0 values do not collapse

as the flow enters the bend, and the back wall values are also higher than for $C_{extrac} = 0\%$. This can be attributed to the extraction impact on the recirculating cell structure located in the upstream bend corner. The flow is accelerated in the bottom wall region. Thus the impingements on the walls are stronger than in the case with no extraction. Downstream of the bend for $l/D_H < 2.5$, the heat transfer is higher in the cases of extraction. This is due to the flow impingement modification in strength and location, just downstream of the bend. Farther downstream, the heat transfer with extraction is lower than for the 0% extraction case. The explanation is the same as for the top wall; the heat transfer decrease due to the massflow loss along the channel is not compensated by the heat transfer enhancement around the extraction holes.

The main conclusion from this data is that the influence of the extraction is noticeable compared to the case with no extraction. However the various extraction rates studied give line plots that are superimposed. This indicates that the Nusselt number distribution does not seem to depend on the extraction rate in the ranges of Reynolds number and extraction studied. It can be explained as follow: Byerley et al. [12] showed that the local suction ratio (SR = single hole mean velocity / local channel mean velocity) has a great impact on the heat transfer distribution around the holes. Tests showed that SR increases for a particular hole as C_{extrac} increases. The heat transfer enhancement associated with the SR increase, seem to compensate the heat transfer fall associated with higher channel massflow loss.

Several references led to similar conclusions with 90° rib arrangements. Thurman and Poinsatte [123] studied a triple-pass channel, with eight holes in the first pass and with a suction ratio SR=4.9. They found extraction to have appreciable effects on the full surface heat transfer distribution. Shen et al. [117] used a single-pass channel with five holes and with SR=1.85 to 5.07. They showed that the extraction raised the averaged heat transfer value from the 0% extraction ribbed wall by about 25%, independently of the suction ratio. Ekkad et al. [37] used a two-pass channel with 20 holes in both the upstream and downstream leg, and a SR=0.8. They found that the extraction did not modify the area-averaged Nu/Nu_0 ratios. This conclusion is thought to be due to the suction ratio differences with the other references and with the present study ($SR \simeq 6$ in the bend region and $3.5 < SR < 11$ in the downstream leg).

It must be mentioned that for the previously presented results, Nu_0 was based on the channel inlet conditions. The Nusselt number can be normalised by the Dittus-Boelter Nusselt number based on the local channel flow conditions, in order to isolate the impact of the extraction. Table 6 shows Nusselt numbers normalised by local Dittus-Boelter Nusselt numbers. The local Dittus-Boelter Nusselt numbers were calculated using the channel local massflow plotted in Figure 50. Values given in Table 6 were extracted from the bottom wall 5th rib module downstream of the bend. The results show that with a normalisation based on local flow properties, the Nusselt number increases as the extraction increases, i.e. as the suction ratio increases.

Total Extraction	5th rib Nu/Nu_{0_local}
0%	2.3
30%	2.8
40%	3
50%	3.3

Table 6: Bottom wall 5th downstream rib module Nusselt number normalized by local Dittus-Boelter Nusselt number.

6.2.3 Full surface heat transfer

6.2.3.1 Bottom wall

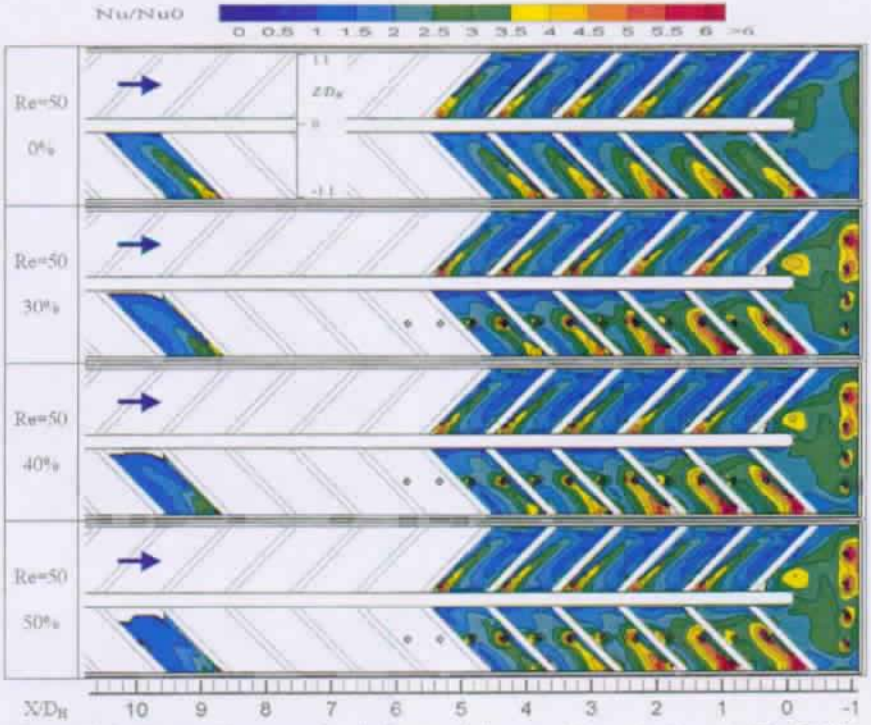

Figure 52: Bottom wall heat transfer distribution: influence of the extraction rate (Re=50,000 and Nu_0 is based on the channel inlet flow conditions).

Figure 52 shows the full surface Nu/Nu_0 distribution on the bottom wall of the baseline configuration, for a flow condition of Re=50,000 and for four extractions.

Upstream of the bend, the heat transfer distribution is typical of fully developed flow region in channels with 45° rib arrangements. Adding extraction does not seem to influence the heat transfer distribution upstream of the bend.

The extraction influences the heat transfer distribution in the bend. The global shape of the contours is the same as in the case with 0% extraction, but the mean level of heat transfer is higher. Figure 51 showed an increase of about 38%. The two high heat transfer regions at the web tip and along the upstream part of the back wall are still present. A heat transfer increase takes place at every hole location. It is due to the decrease of the thermal boundary layer in the vicinity of the holes.

In the downstream leg, the extraction presence influences the heat transfer distribution. The U-shape high heat transfer region (due to the 45° rib arrangement) is

present in all the rib modules. The heat transfer increases around the holes in a same manner as in the bend. The Nu/Nu_0 levels decrease farther downstream in the leg due to the massflow extraction, but no evolution can be clearly noticed when modifying the extraction.

Note that at $X/D_H = 10$, Nu/Nu_0 values are higher as the extraction is low, i.e. as the local massflow increases. Indeed, in this region, no extraction occurs anymore, and the local channel massflow dominates the heat transfer levels.

6.2.3.2 Top and side walls

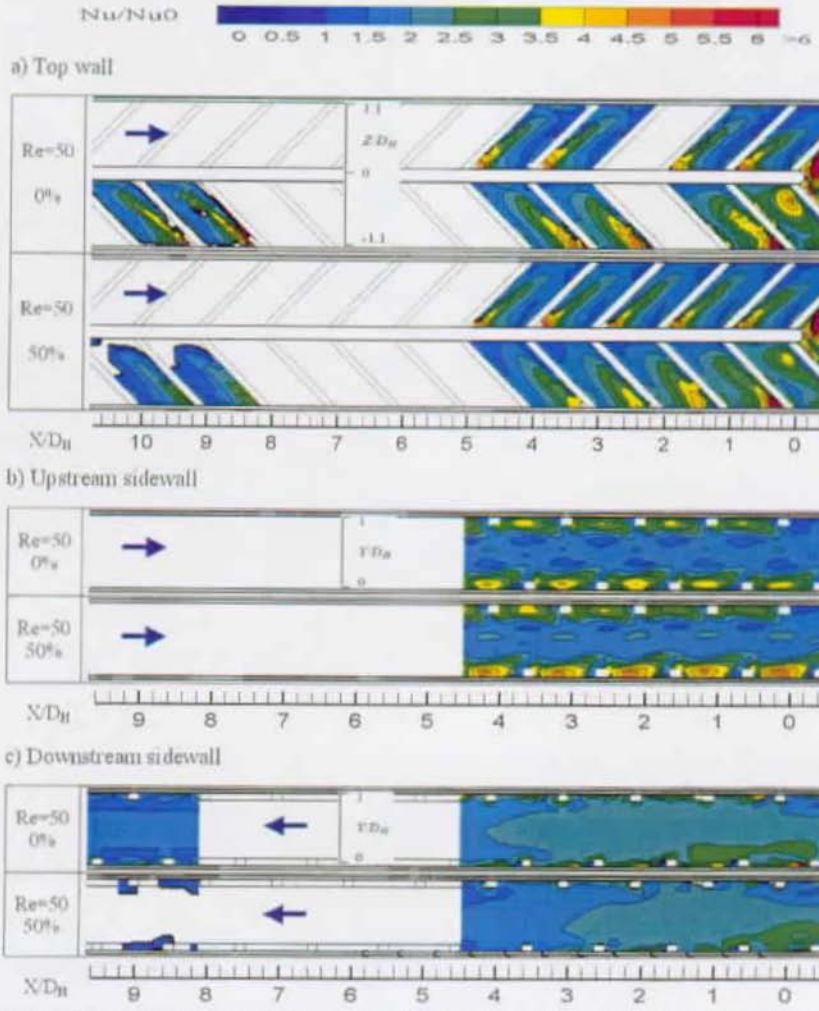

Figure 53:Top wall and sidewalls heat transfer distribution: influence of extraction (Re=50,000 and Nu_0 is based on the channel inlet flow conditions).

Figure 53 shows heat transfer distributions on the top, upstream and downstream sidewalls. Measurements at Re=50,000 are shown for $C_{extrac} = 0\%$ and 50%. Other extractions are not plotted since the results are similar to the 50% extraction.

Figure 53a shows Nu/Nu_0 distribution on the top wall of the $C_{extrac} = 0\%$, for a flow condition of Re=50,000. The upstream heat transfer distribution is similar to the one of the bottom wall. This can be attributed to the symmetrical shape of the secondary flow field about the centre plane $Y = 0.5$.

The bend region heat transfer distribution is divided into two zones, $0 > X > -0.6$ near the web tip, and $-0.6 > X > -1.1$ near the back wall. The region $0 > X > -0.6$ is a region with high heat transfer; Nu/Nu_0 is higher than 6 in the core of this region. It is due to the strong flow impact on the wall, which is shown in figure 4 of Chanteloup and Bölcs [24]. The region $-0.6 > X > -1.1$ has lower heat transfer values ($Nu/Nu_0 \approx 1-1.5$) and gradients are relatively low in this second region.

In the downstream leg, the heat transfer recovers from the bend effect less rapidly than on the bottom wall. The first downstream rib module shows a distribution shape different from the typical 45° inclined rib shape. Two regions of high heat transfer ($Nu/Nu_0 > 5$) are located at the rib root, near the outer wall and near the web tip. The heat transfer distributions in the rib modules further downstream are similar to that of the downstream rib modules of the bottom wall.

Adding extraction in the channel influences the heat transfer distribution on the top wall less than on the bottom wall, because the extraction occurs on the bottom wall. The Nu/Nu_0 contours are located approximately at the same place with or without extraction. The levels are also very similar.

Figure 53b shows Nu/Nu_0 distribution on the upstream sidewall for a flow condition of Re=50,000. The fully developed heat transfer distribution on this wall has been described in 5.1.3.2. In the case with 0% extraction, the heat transfer distribution is almost symmetrical about the $Y = 0.5$ plane. In the case with extraction, the heat transfer is higher near the bottom wall than near the top wall. It indicates the effect of the extraction on the secondary flow field. The effect of extraction is also noticeable as the flow approaches the bend. From $X = 4$ to $X = -1$, Nu/Nu_0 levels decrease near the top wall, whereas they increase near the bottom wall. Both effects compensate each other, giving a stable area-averaged value.

Figure 53c shows a Nu/Nu_0 distribution on the downstream sidewall for a flow condition of Re=50,000. The influence of extraction is noticeable. At $X > 0$ (part in the bend region), the flow impinges in a different manner on the sidewall. The heat transfer is thus higher near the bottom wall and lower near the top wall in the configuration-2 than in the baseline configuration. Farther downstream, the heat transfer distribution in configuration-2 is not symmetrical about the $Y = 0.5$ plane. The maxima Nu/Nu_0 values are at $Y = 0.3$. This is due to the modification of the secondary flow towards the bottom wall shown in Figure 54. Note that at $X = 10D_H$, no measurements are available in configuration-2. This is due to the low heat transfer coefficient in this region, combined with the small local massflow (half of the inlet massflow at extraction 50%). Thus the wall temperature had not reached the T_{LC} level after 38 seconds of test.

6.2.4 Bend region

The influence of extraction is particularly noticeable in the bend region. The following part describes the flow characteristics and the heat transfer in the configuration-2, at Re=50,000 and C_{extrac} = 50%. Two dimensional vector field and 3D-streamlines are given to explain how the flow is directed through the 180° turn.

The main objective of the present part is to relate the flow field and the heat transfer. As more planes were measured in configuration-2 than in the baseline configuration, this configuration has been selected to describe the flow field inside the bend. Note that the shape of the streamlines is not strongly affected by the number of measurement planes available in the bend region. Tests were made and showed that the main influence is noticeable on shape details of the streamlines (vortex size, vortex exact location).

Another objective of this part is to show the influence of the extraction in the bend region. Comparisons will be given between the configuration-2 and the baseline configuration. The influence of the extraction rate will also be shown.

6.2.4.1 Flow characteristics at 50% extraction

Cross sections

The main influence of the extraction on the flow field is shown in Figure 54.The major difference with the baseline configuration occurs when comparing the secondary flow motion.

In the upstream leg, the upper vortex (Y>0.5) occupies 70% of the cross section in the case of extraction. The counter-rotating vortex induced by the bottom ribs only occupies the Y<0.3 area. The streamwise component is also influenced by this asymmetry, showing a high velocity zone in the upper part.

The flow in the bend region is more complex than in the ribbed region. The flow in the bend starts with the secondary structure from the ribs at θ=0°. At θ=0°, the streamwise velocity distribution and the secondary flow patterns in the center region show the effects of the bend. The streamwise flow near the inner web has begun to accelerate, indicating that this flow has entered the bend region. The secondary flow pattern is symmetrically distributed with respect to the mid plane (Y=0.5) for the baseline configuration, whereas in the configuration-2, the secondary flow near the outer wall is mainly directed towards the bottom wall. The main impact is the inclusion of a high streamwise velocity core in the channel center region. Note that near the web of both configurations, all the secondary flow vectors are toward the web.

At θ=45°, the streamwise velocity increases to more than 2 near the inner web, and has a small region of negative velocities in the lower outside corner region. The high streamwise velocity near the inner web is compatible with the conservation of angular momentum in the bend region. The secondary flows are very different from the baseline case, to the configuration-2 case. In the latter, instead of the four vortices present in the baseline case, only two counter-rotating vortices occur. They have the same rotating direction as the two baseline case upper vortices, but are approximately twice their size. Note that near the web, the secondary flow vectors are directed away from the web in both configurations.

At θ=90°, the streamwise velocities of the flow have decreased near the web. The size of the region near the web where the secondary flow is directed away from the web has increased. The upper baseline case secondary cell seen at 45° continues,

but the lower cell has disappeared. The configuration-2 case secondary cells are still present, but their locations have been strongly modified by the bend induced flow (details of this plane are given in Figure 55).

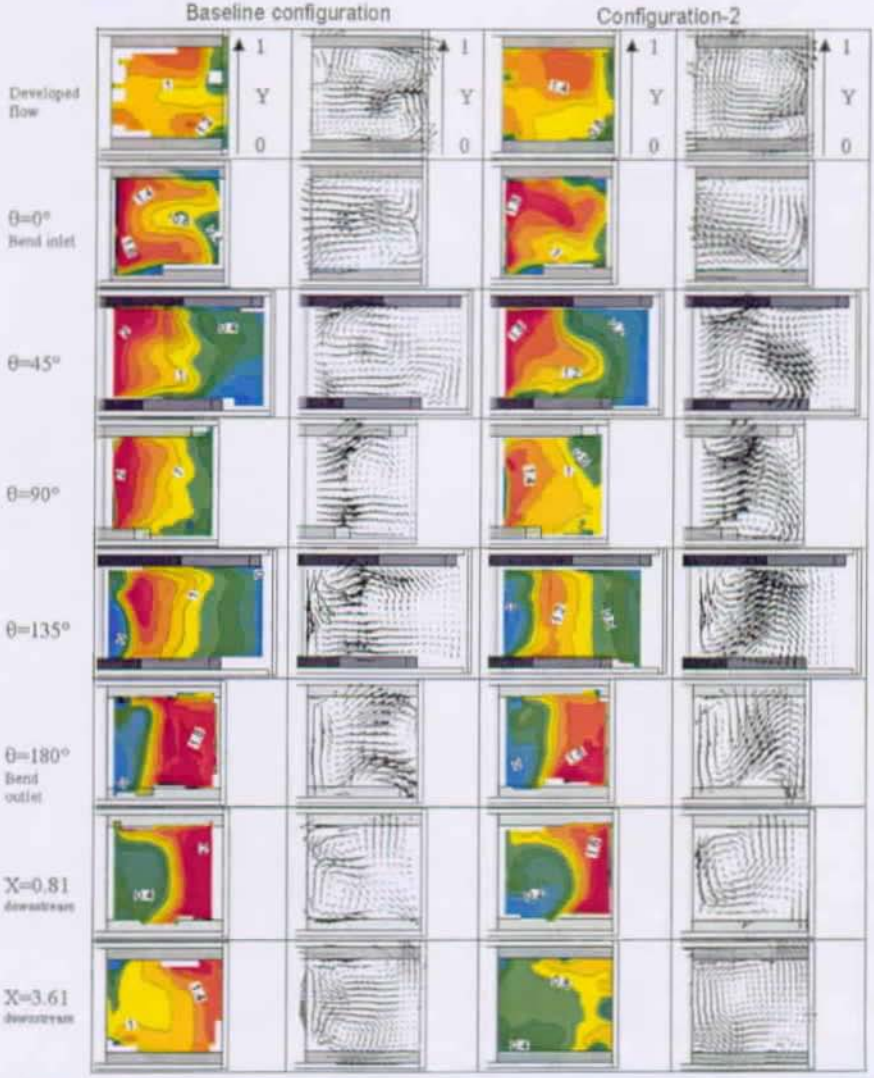

Figure 54: Mean streamwise velocity contours and secondary flow vectors obtained at θ=0°, 45°, 90°, 135° and 180° in the bend: baseline configuration and configuration-2 results. The contour lines values, U_s/U_b , are plotted on the figures.

At θ=135°, the flow has separated from the web and the streamwise velocities are negative. The streamwise velocity contours are similar for both configurations. The streamwise velocity contours have a negative value near the outer wall, indicating a small recirculation cell. The configuration-2 case values are a bit smaller due to the mass flow extracted through the first two holes in the bend. The average position of the baseline vortex cell has moved toward the web, and the secondary flow is generally away from the web. The two configuration-2 vortices continue to develop.

At θ=180°, a small region of recirculation occurs near the web and the lower wall. The rib induced secondary flow motion is redeveloping. The streamwise profiles are similar in both cases. The effect of the flow extraction is, however, increasing in the configuration-2, yielding smaller streamwise velocity magnitudes. Note that the highest streamwise velocities have moved from near the web to the outer half of the passage, and are 1.5 to 2.0 times the bulk velocity. The secondary flow is very different in the configuration-2. The flow goes from the top to the bottom wall along the web, crosses the channel up to the top outer wall, and goes down to the bottom wall along the outer wall. This phenomenon is similar to the upper half of the baseline secondary flow motion.

Downstream of the bend, the secondary flows are redeveloping, having a similar shape to the secondary flow in the upstream leg. The streamwise flow hasn't recovered from the bend effect $0.81D_H$ downstream of the bend. The recirculating cell has disappeared in the baseline configuration, but is still present in the configuration-2 case. Further downstream ($3.6D_H$), the flow has almost recovered from the bend domination. The streamwise and secondary profiles are similar to the inlet profiles, except for the symmetry around the web, due to the rib symmetrical placement each side about the web. The configuration-2 streamwise velocity magnitude has also decreased because of the massflow extracted upstream.

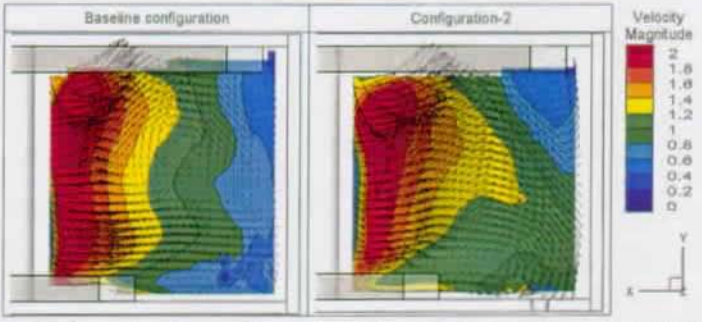

Figure 55: Secondary flow vectors and velocity magnitude contours at $\theta = 90$deg.

Figure 55 gives details of Figure 54 at $\theta = 90$deg. The difference between the baseline configuration and the configuration-2 are noticeable for the two configuration-2 vortices. The vortex located around $Y = 0.7$ in the baseline configuration is displaced towards the bottom wall in the configuration-2. The secondary vectors are stronger, yielding a stronger impact on the bottom wall.

The corner vortex in the top-back wall corner is modified by the extraction. Its size

is less than $0.01D_H^2$ in the baseline configuration, and is around $0.0625D_H^2$ in the configuration-2.

Bend vortices

Figure 56 shows the evolution of the top-back wall corner vortex in the bend region. Details are shown in planes parallel to the sidewalls (Z=constant) in three locations, from the upstream sidewall towards to downstream sidewall. The size of the vortex decreases as the flow approaches the downstream leg. In fact, the vortex follows the main stream and does not remain attached to the back wall. It is still present at $\theta = 135\text{deg}$ as shown in Figure 54. The impact of this vortex on the main flow is a blockage of the incoming flow in the region $Y > 0.6$. Note that the results shown in Figure 56 were interpolated from measurement planes, and can have spurious results due to the interpolation.

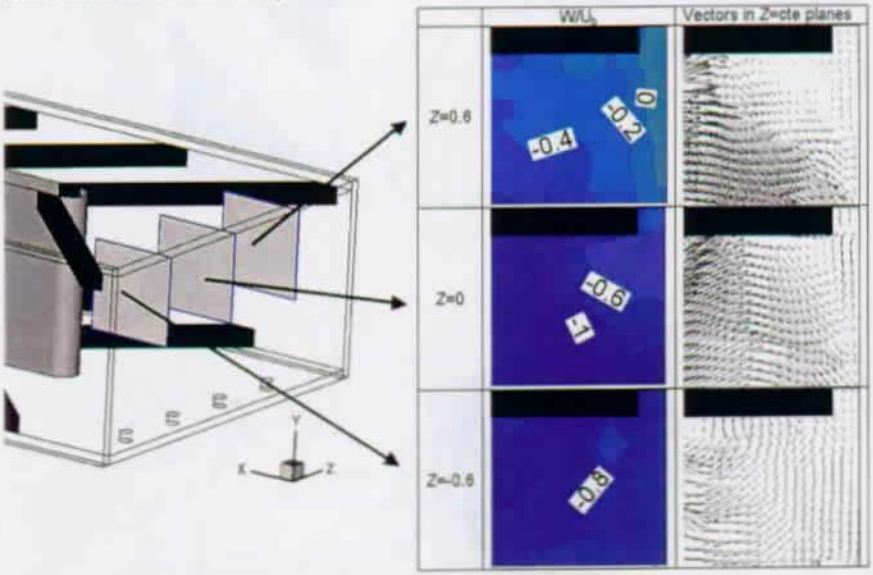

Figure 56: Evolution of the top-back wall corner vortex in the configuration-2 bend region.

A second vortex cell is present in the upstream bend corner, along the side-back wall corner. Figure 57 depicts the evolution of the side-back wall corner vortex along the Y-axis. This recirculation cell is created by the flow deceleration when it enters the bend. The vortex has a conical shape. Its size increases from the bottom wall ($0.25D_H^2$ at $Y = 0.3$) towards the top wall ($0.5D_H^2$ at $Y = 0.7$). The vertical motion of the flow in the cell is low ($< 0.2U_b$). The flow goes towards the bottom wall near the channel centre ($V > 0$) and towards the top wall in the vicinity of the side and back walls ($V < 0$). The incoming flow comes from the upstream leg and rotates around the Y-axis between the web tip and this recirculation cell.

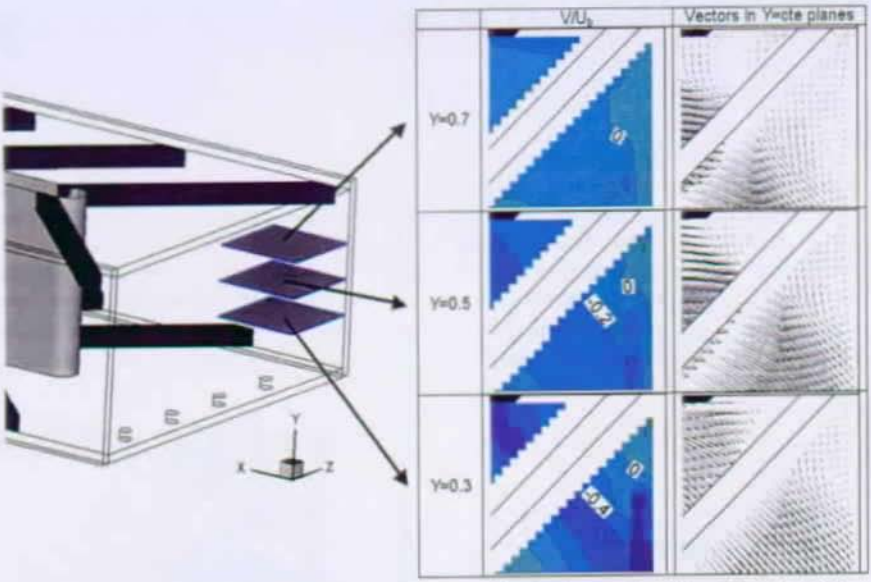

Figure 57: Evolution of the side-back wall corner vortex in the configuration-2 bend region.

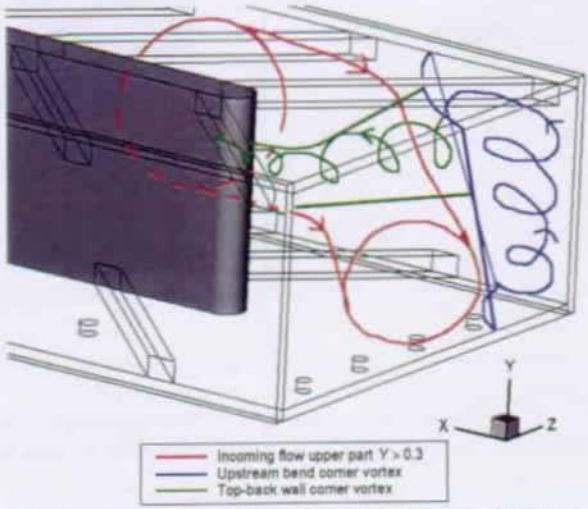

Figure 58: Schematic view of the configuration-2 vortex cells in the bend.

The conclusion can be drawn that these two vortex cells act on the incoming flow as if the channel bend geometry was modified. They smoothen the sharp geometry

corners in the upstream leg near the back wall, and along the top wall. The geometrical shapes of the vortices are summarised in Figure 58. Note that these recirculation cells could be partly avoided by modifying the geometry bend walls. This could also decrease the pressure drop in the bend, which has the bigger contribution to the channel global pressure drop.

Upstream leg counter rotating vortices

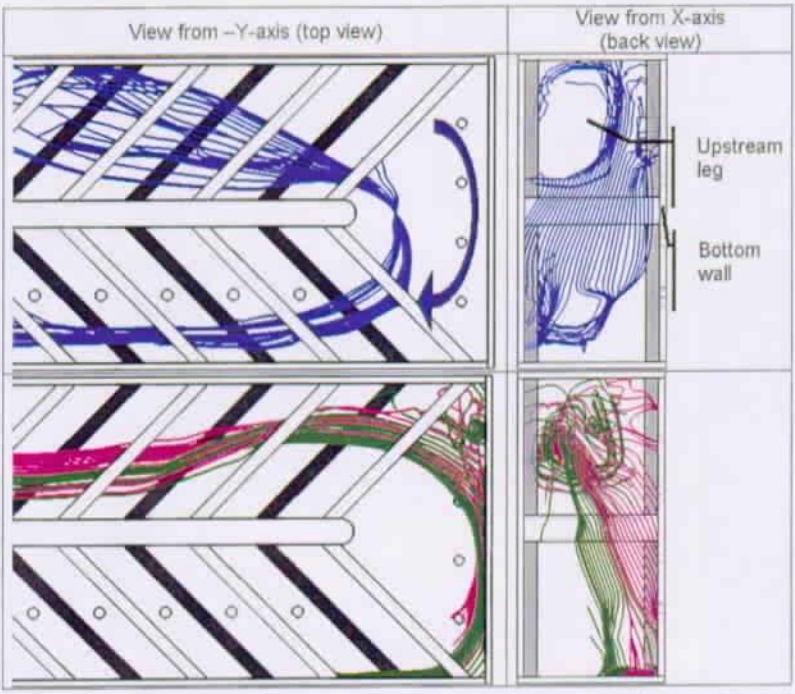

Figure 59: Examples of 3D-streamline evolution from the upstream to the downstream leg (configuration-2).

The two former vortex cells influence the incoming flow. The incoming flow is composed of two counter-rotating vortices. They are located apart from a Y=constant plane; in the configuration-2 $Y = 0.3$. The part of the flow in each vortex mainly remains in its part along the straight legs. Figure 59 gives an overview of the flow paths through the bend region.

The upper flow part ($Y > 0.3$) of the upstream leg is deflected by the bend corner cells. Note that these phenomena are also present in the baseline configuration, with several differences (see 6.2.4.4)

The upstream bend corner cell directs the flow towards the downstream leg. The flow impinges on the back wall, with the centre of impact at $Z = 0.3 - 0.4$, $Y = 0.2 - 0.3$. Note that the flow, which impinges on the back wall at $Y > 0.6$ locations

is coming mainly from the bend corner vortex.

The top-back wall corner cell directs the flow towards the bottom wall. This deviation towards the bottom is emphasized by the aspiration through the bend bottom wall holes. Farther downstream, the main flow is directed towards the downstream sidewall, where it impinges, before going through the downstream leg.

The $Y < 0.3$ flow part of the upstream leg has a lower streamwise velocity than the upper part and it has also a smaller size. Thus it undergoes the effect of the upper part deviation. It is blocked by the upper part and do not impinges on the back wall. At $\theta = 0\,\text{deg}$, it impinges on the bottom wall behind the last bottom rib. At $\theta = 90\,\text{deg}$, it goes through the bend in the vicinity of the web tip ($-0.7 < X$). The part of the flow that crosses the $\theta = 90\,\text{deg}$ plane in $-0.7 < X < -0.35$, goes mainly along the downstream sidewall in the region of high streamwise velocity. The part of the flow that crosses the $\theta = 90\,\text{deg}$ plane in $-0.35 < X < 0$, goes more in the two counter-rotating vortices of the downstream leg.

6.2.4.2 Heat transfer characteristics at 50% extraction

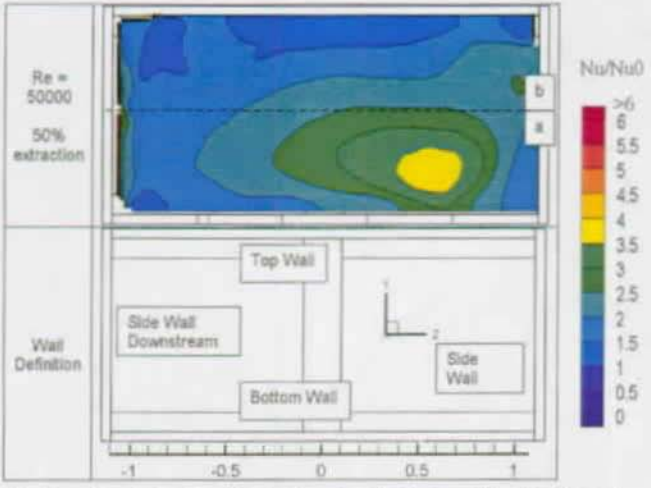

Figure 60: Configuration-2 back wall heat transfer distribution (Re=50,000, C_{extrac} = 50%).

Figure 60 shows the heat transfer distribution on the configuration-2 back wall. The flow characteristics were set to Re=50,000, and $C_{extrac} = 50\%$. Two regions can be identified on the back wall. The line $Y = 0.5$ separates these regions. Two main heat transfer phenomena can be described in these regions.

In region a, a Nu/Nu_0 maximum is located at $Y = 0.25$, $Z = 0.5$. The heat transfer decreases in radial direction from this point. This high heat transfer region is due to the impact of the $Y > 0.3$ upstream leg vortex on the back wall. The heat transfer decreases as Z increases towards the downstream outer sidewall. This decrease is characteristic of a wall jet resulting from an impinging jet on a wall. Note

that near the outer sidewall, a slight increase in heat transfer occurs. It is due to the small recirculating cell present in the downstream bend corner (see Schabacker [112]).

In region b, the heat transfer level is lower than in region a. The heat transfer decreases in two directions: on the one hand as Y increases for $Z<0$ and on the other hand as Z decreases. The heat transfer distribution is created by both the wall jet resulting from the impact on the back wall of the $Y > 0.3$ upstream leg vortex, and of the main stream that is directed towards the downstream leg. It creates the corner vortex already described in 6.2.4.1.

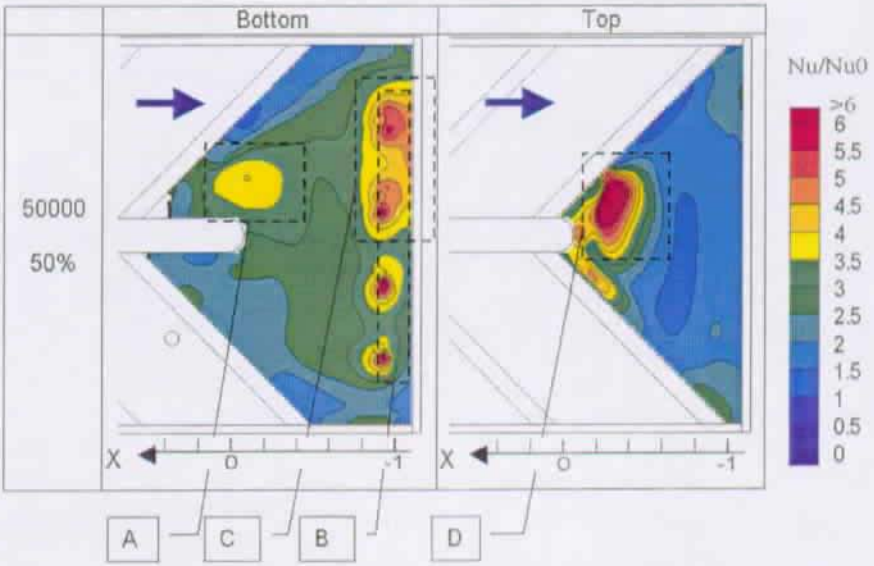

Figure 61: Configuration-2 ribbed wall bend region heat transfer distribution (Re=50,000, C_{extrac} = 50%).

Figure 61 shows the heat transfer distribution on the bend ribbed-walls of configuration-2. The flow characteristics were set to Re=50,000, and C_{extrac} = 50%. Regions can be isolated on both walls in term of heat transfer characteristics: Three regions on the bottom wall (A-C) and one region on the top wall (D).

Region A has Nu/Nu_0 values up to 4. This region is detached from the last bottom rib. Thus the heat transfer increase cannot be attributed directly to the rib induced secondary flow field. It seems to be due to the impact of the $Y < 0.3$ upstream leg vortex on the bottom wall.

Region B takes into consideration the bottom wall surface in the vicinity of the extraction holes. The heat transfer is higher there, with Nu/Nu_0 values higher than 5.5. These local Nu/Nu_0 maxima are due to the aerodynamic and thermal boundary layers, which are decreased in thickness by the holes, thus thin in the vicinity of the walls. The maximum location shifted downstream of the holes is due to the direction of

the flow parallel to the surface in the hole region. The variation of flow characteristics explains the various locations of maxima from one hole to the other.

Region C is the part of region B where $X < -0.8$ and $0 < Z < 0.8$. The heat transfer in this region is high (mean value upper than 4). It is due to the deflection of the $Y > 0.3$ upstream leg vortex towards the bottom wall, after it has impinged on the back wall. In this region, impinging mean and fluctuation velocity components (*Y*-axis) as well as mean component along *Z*-axis (*W*) are maximal in the measurement planes $X = -0.9$. The heat transfer decreases as *Z* decreases towards the downstream outer sidewall.

Region D is a region with high heat transfer on the top wall. Nu/Nu_0 values are higher than 6 on a surface larger than $0.03D_H^2$. Two main phenomena can explain this. First, the last top rib induces a secondary flow at web rib root similar to the fully developed rib-induced secondary vector field. It creates an impinging flow on the top wall immediately downstream of the rib. Second, the streamwise velocity component is high near the web tip, due to the flow acceleration induced by the bend. Thus the impinging velocity is higher than in the fully developed region and yields a higher heat transfer. Note that the streamwise velocity shown in Figure 54 is higher near the top wall than near the bottom. It can explain the higher heat transfer level on the top wall.

The remaining part of the top wall bend region has homogeneous heat transfer. The main flow feature, which is in the vicinity of the top and back wall corner is the vortex described in 6.2.4.1. The velocity components are relatively low there.

It must be mentioned that the high turbulent kinetic energy that is shown in Figure 101 does not seem to influence the heat transfer level neither on the top nor on the bottom wall. This is particularly the case for $\theta = 135°$.

6.2.4.3 Correlation between velocity components and Nusselt number

The global effect of the flow on the bend heat transfer distribution has been described in 6.2.4.2. In the present part, direct comparison between Nu/Nu_0 values and velocity components will be presented. Mean and fluctuating velocity components are shown. The comparisons will be made along lines in the bend, on the back, the top and the bottom walls.

Figure 62 shows the comparison of Nu/Nu_0 and velocity components on the configuration-2 back wall. Nusselt numbers were extracted from the bottom wall at two heights in the channel ($Y = 0.3$ and $Y = 0.7$). Velocity component results were extracted from measurement planes taken parallel to the ribbed walls. The values are plotted 6mm distant from the back wall, at the same heights as the Nusselt numbers. Note that no velocity measurements were taken in the region $-0.1 < Z < 0.1$.

The lines $Y = 0.3$ and $Y = 0.7$ are representative of Figure 60 parts a and b, respectively.

Along the $Y = 0.3$ line, *X*-axis velocity components are correlated more with the heat transfer values. They correspond to impinging velocity components. U is correlated and shifted $0.2D_H$ towards the downstream leg. $\overline{u'^2}$ is better correlated at each *Z*, the maximum coincides with the maximum of the Nusselt number. The other normal stresses are not correlated with the Nusselt number. It seems that the flow acts as an impinging jet on this part of the back wall. Indeed, the W component is correlated for $Z < 0$. It decreases as the Nusselt number decreases, in a similar

manner as in a wall jet resulting from an impinging jet.

Along the $Y = 0.7$ line, correlations between velocity components and Nusselt number are less obvious than at $Y = 0.3$. This is thought to be due to the fact that the flow (top corner vortex) in this region is created by two phenomena: the wall jet resulting from the impact on the back wall and the flow coming from the upstream leg. This complex flow does not seem to be dominated by an effect, which would influence the heat transfer on the back wall.

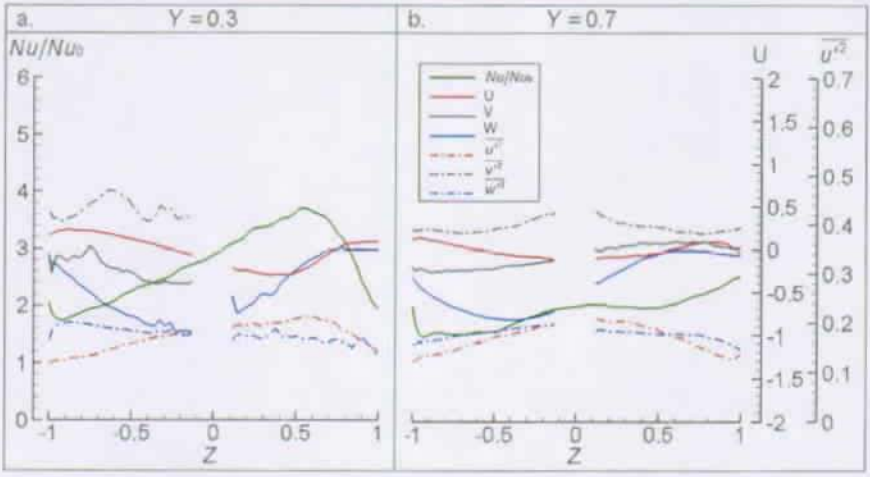

Figure 62: Comparison of Nusselt number and velocity components on the configuration-2 back wall (Nu values: X=-1.1; Velocity values: X=-1.04).

Figure 63 shows the comparison of Nu/Nu_0 and velocity components on the configuration-2 bend ribbed walls. Lines were extracted at $X = -0.9$ on both walls. They cross the extraction hole centres on the bottom wall. Velocity components are taken from measurement planes parallel to the back wall, 6mm distant from the ribbed walls.

On the bottom wall, the trend of the heat transfer distribution is the same as described in the full surface heat transfer part. Nu/Nu_0 maxima occur downstream of the holes. The impinging mean velocity component (V) is the most obviously correlated with the heat transfer. The velocity component parallel to the bottom wall (W) is well correlated with the heat transfer peak downstream of the holes, which confirms the reduction of the hydrodynamic boundary layer at this location.

On the top wall, Nusselt values are more uniform than on the bottom wall ($1.5 < Nu/Nu_0 < 2$). Correlations are not obvious between the heat transfer and the velocity components. As in the back wall case, the flow here belongs to the top-back wall vortex. Thus no velocity component is predominant in the heat transfer determination.

Note that the fluctuating velocities are not equal along the three axis. The turbulence can therefore not be considered as isotropic.

The conclusions from these two figures are that globally there is no obvious correlation between the Nusselt values on the surface and a specific velocity component above the surface. In certain locations or flow configurations, where Nu/Nu_0 gradients are high, correlations can be found between Nusselt and velocity components (i.e. impinging velocity gradients near the wall). This is the case at locations where the flow impinges on the surface. In these regions, Nusselt shows a good correlation with the impinging velocity components, especially with the normal stress normal to the surface. In regions where Nu/Nu_0 values and gradients are low, no velocity component is clearly correlated with Nusselt number.

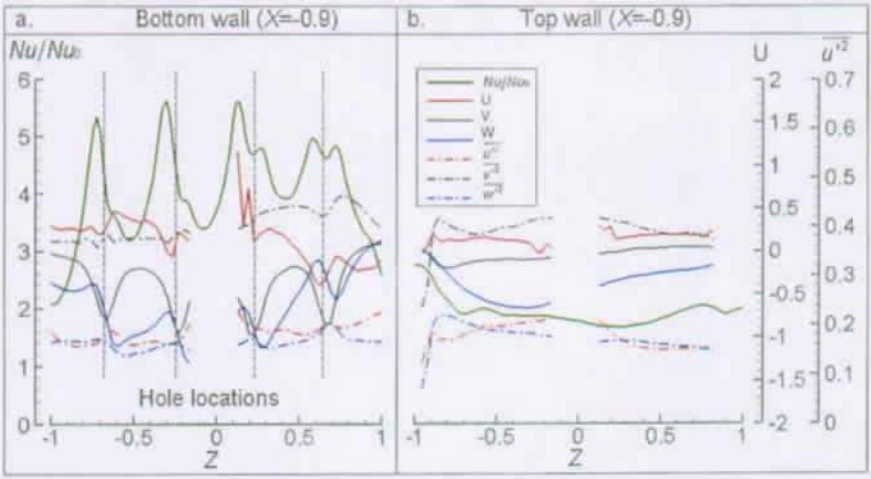

Figure 63: Comparison of Nusselt number and velocity components on the configuration-2 bend ribbed walls (Nu values: a. Y=0, b. Y=1; Velocity values: a. Y=0.06, b. Y=0.94).

6.2.4.4 Influence of flow extraction

0% extraction

An analysis of the streamlines in the baseline configuration bend region was conducted similarly to the one presented in 6.2.4.1. The results of this analysis are summarized in Figure 64. Figure 64a-d present various main flow phenomena in the bend region. The phenomena are decomposed for clarity and are superimposed altogether in Figure 64e. The two bend corner vortices are shown in green (top-back wall corner vortex) and blue (upstream bend corner vortex). The two upstream leg rib-induced vortices are shown in red ($Y > 0.5$) and yellow ($Y < 0.5$). Figure 102 gives an overview of the streamlines where the flow turns into the bend region.

The bend corner vortices present in the configuration-2 (Figure 58) are also present in the baseline configuration. However, their sizes and shapes are strongly modified by the absence of extraction. The upstream bend corner vortex (Figure 64d) is smaller than in configuration-2. The shape is conical with the biggest part near the bottom wall. The vortex does not extent above $Y = 0.5$. The top-back wall corner

vortex is smaller than in configuration-2. It is directed towards the downstream leg by the main streamwise flow.

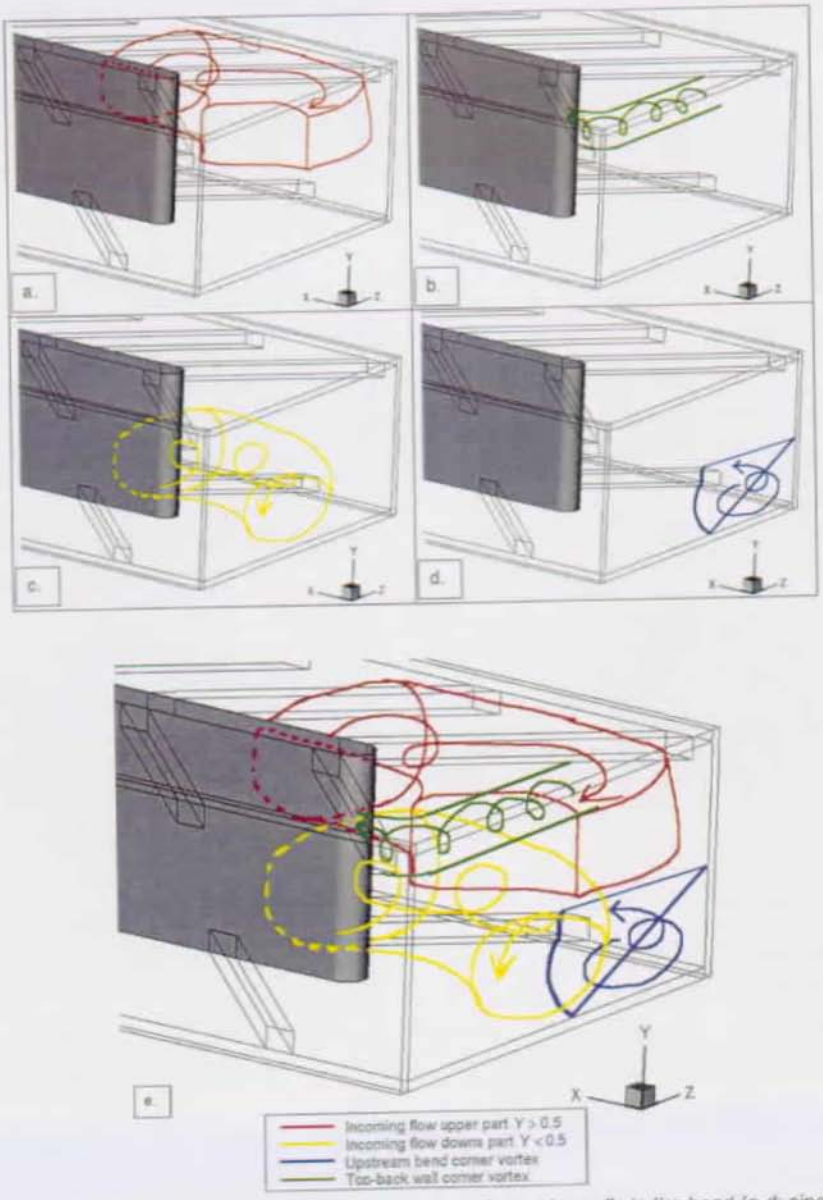

Figure 64: Schematic view of the baseline configuration vortex cells in the bend (a-d: single vortex presented; e: all vortices presented).

The upstream leg part of the flow, which is located in the upper vortex (Figure 64a), turns in the bend region without detachment from the outer walls. The flow at $Y > 0.5$ remains attached to the sidewall and to the back wall without leading to a recirculating cell in the upstream bend corner. The flow turns smoothly towards the bend region outlet. Velocity along the X-axis decreases gently as the distance to the wall corner decreases and no high impinging velocity gradients occur in this region. Thus the impinging flow effect on the back wall is weak for $Y > 0.5$. Note that the flow coming from this upstream leg upper vortex remains mainly in the upper part of the bend and follows in the upper part of the downstream leg.

The upstream leg part of the flow, which is located in the down vortex (Figure 64c), is influenced by the upstream bend corner vortex as it turns inside the bend region. The flow is blocked by the bend corner vortex as it is directed towards the downstream part of the bend. Thus the flow turns less smoothly than the flow upper part in Figure 64a. In turn the flow impinges on the back wall with the center of the vortex at approximately $Z = 0.3 - 0.4$, $Y = 0.2 - 0.3$. Note that the flow coming from this upstream leg down vortex remains mainly in the down part of the bend and follows in the down part of the downstream leg.

The influence of the extraction on the flow field is clearly noticeable in the bend region. A direct comparison between Figure 58 and Figure 64 can be made.

On the one hand the size of the upstream leg upper vortex is modified. It is 70% of the cross section in configuration-2 and 50% in the baseline configuration. On the other hand the top-back wall corner vortex has also decreased in size. These two decreases avoid that the upper part of the flow is directed towards the bottom wall in the back wall region.

The flow impact on the back wall takes place at the same location in both the baseline configuration and configuration-2. However, the impinging velocity is lower in the baseline configuration. This is due to the fact that the upstream bend corner recirculating-cell has decreased in size. As a consequence, the streamwise velocity distribution (in cross sections $\theta = 45\text{deg}$ and $\theta = 90\text{deg}$) is smoother and lower in the baseline configuration than in the configuration-2 (see Figure 54). For instance at the channel centerline ($r = 0.7$, $Y = 0.5$), the streamwise velocity is higher than 1.2 and lower than 1 in the configuration-2 and baseline configuration, respectively.

Examples of streamlines similar to Figure 59 is given in Figure 102 for the baseline configuration.

Variation of extraction

Figure 65 shows the back wall heat transfer distribution in the EPFL baseline configuration geometry for four extractions at Re≈50,000 (0%: baseline configuration, 30-50%: configuration-2).

The extraction does not highly modify the heat transfer distribution. The heat transfer contour shape, which was described in 6.2.4.2, remains similar for all the extractions.

The influence of the extraction is noticeable from the baseline case to the cases with extraction. The heat transfer levels are higher in the cases with extraction, especially at locations of high heat transfer (impact of the incoming flow). Figure 51 stated that the heat transfer level is 38% higher in the upstream part of the bend ($Z > 0$) than in the fully developed region. The modification of heat transfer levels is

due to the bend incoming flow characteristics. As described in 6.2.4.4, the bend corner vortex cells modify the flow impact on the back wall. The impinging velocity is increased in the regions of main impact ($Z = 0.5$, $Y = 0.3$).

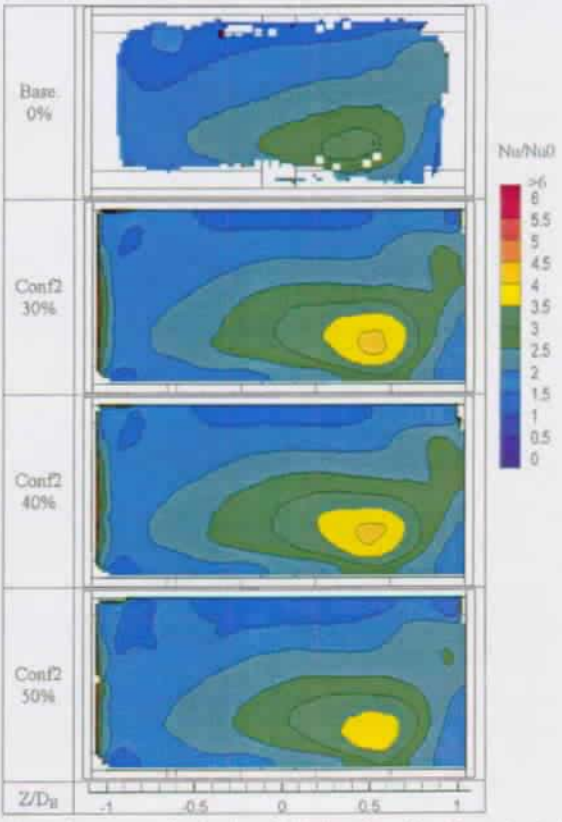

Figure 65: Extraction influence on the back wall: Full surface heat transfer in the baseline and configuration-2.

The extraction does not strongly modify the heat transfer distribution in other areas of the back wall. Heat transfer levels in cases with extraction are 8-10% higher in $Z = -0.3$, $0.5 < Y < 0.7$ than in the case without extraction. The bend corner vortex cells do not have a significant influence on the heat transfer.

The variation of the extraction (30% to 50%) does not influence significantly the heat transfer distribution. The differences are within the range of measurement uncertainties (±8%). It can be attributed to the fact that at the bend outlet, only a maximum of 10% of the inlet massflow has left the channel (Re=50,000, 9% for a 50% total extraction, and 7% for a 30% total extraction). Thus the massflows inside the channel is approximately the same at all three extractions. The local Dittus-Boelter

Nusselt numbers are approximately equal to the Dittus-Boelter Nusselt numbers based on the inlet flow conditions for all the extractions.

Note that these conclusions are also valid for the ribbed walls (see 6.2.3.1 and 6.2.3.2), and also mainly valid for the configuration-3 back wall (Figure 108).

6.2.5 Spanwise and streamwise heat transfer gradients

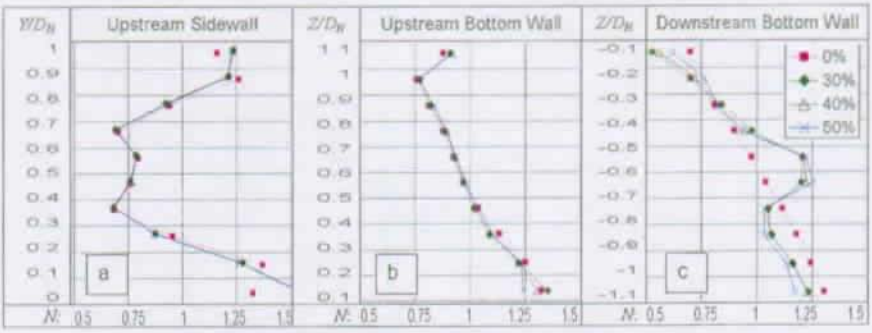

Figure 66: Spanwise heat transfer gradients: Influence of extraction.

Figure 66 shows the influence of extraction N values in the same zones as in Figure 37. Note that N was defined in 4.2.5.2. Results for Re=50,000 flow condition are plotted. Note that the $C_{extrac} = 0\%$ case was plotted in Figure 37. Note also that full surface area-averaged Nu/Nu_0 values for $C_{extrac} = 0\%$ to 50% are approximately equal at the location of the zones plotted (see Figure 51). Thus gradient values relative to extraction also give information on the heat transfer values.

Upstream of the bend, the line plots are globally superimposed, for every extraction in Figure 66a and Figure 66b. Slight differences occur in the vicinity of the ribbed walls in Figure 66a. The spanwise heat transfer gradients in the upstream leg do not seem to be influenced by the extraction occurring in the bend and in the downstream leg.

Downstream of the bend (Figure 66c), the extraction influences the spanwise heat transfer gradients. A high increase of N values takes place around the hole locations ($Z = -0.6$). Values are up to 25% higher than in the case without extraction. This increase is compensated in the high heat transfer region near the downstream sidewall. Values are 10% to 15% lower in the cases with extraction in the region $-0.7 > Z > -1.1$. In the low heat transfer region near the web ($-0.1 > Z > -0.4$), the N values are equal whatever the extraction.

Figure 67 shows the evolution of the N values downstream of the bend, as the flow recovers from the bend effect. Bottom wall rib modules are plotted from the second to the fifth rib modules downstream of the bend.

For $C_{extrac} = 50\%$, the N distribution is dependent on the distance to the bend. The heat transfer enhancement around the hole entrance has less impact in the rib modules just downstream of the bend than in the farther downstream rib modules. This is due to the high streamwise velocity region near the downstream sidewall. This

high velocity flow increases the heat transfer at the rib root, diminishing the hole impact on the full surface heat transfer value. As the flow redevelops farther downstream, the impact of the high velocity region decreases, giving higher relative influence of the hole entrance region.

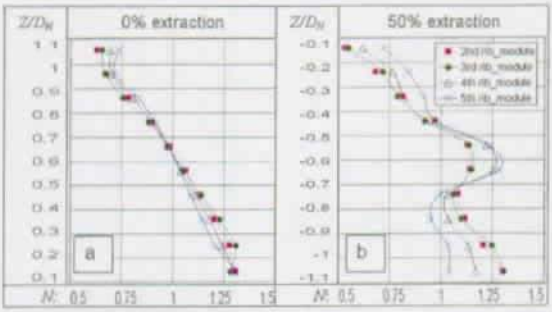

Figure 67: Spanwise heat transfer gradient development downstream of the bend; baseline configuration and configuration-2 (Re=50,000, C_{extrac}=50%).

6.3 Influence of geometrical parameters

The temperature profile at the turbine inlet has evolved with increasing combustion chamber gas temperature of modern gas turbines. The temperature profile is sharp, inducing at the rotor and stator blade end, higher temperature than in former gas turbines. Thus efforts are made in improving the thermal capabilities of coolant channels in the vicinity of the internal coolant channel bends and in the bends themselves. The following part deals with the impact of channel and bend geometrical modifications on the flow field and heat transfer.

6.3.1 e/D_H modification

Configuration-1 was equipped with bigger 45° ribs than the baseline configuration. Plots similar to Figure 25 showed that the flow field upstream of the bend is periodic and not affected by the bend, even at a $1.5D_H$ distance from the bend. In the region $6 > X > 1.5$, the heat transfer distribution can be considered fully developed. Thus the heat transfer is representative of a channel with $e/D_H = 0.15$, $p/e = 10$.

6.3.1.1 Area-averaged heat transfer

The configuration-1 blockage ratio is $e/D_H = 0.15$. As shown in literature (e.g. Taslim and Wadworth [121], Han et al. [58]), the area-averaged Nusselt number increases with e/D_H. In the present study, the fully developed area-averaged Nusselt number is 10% higher in the configuration-1 than in the baseline configuration. Table 7

gives a comparison of area-averaged values on all the three walls in the fully developed flow region at Re=50,000.

Nu/Nu_0	Top wall	Bottom wall	Sidewall
Baseline-Configuration	2.05	2.08	2.25
Configuration-1	2.36	2.28	2.36

Table 7: Fully developed area-averaged Nusselt numbers: influence of e/D_H.

6.3.1.2 Full surface heat transfer

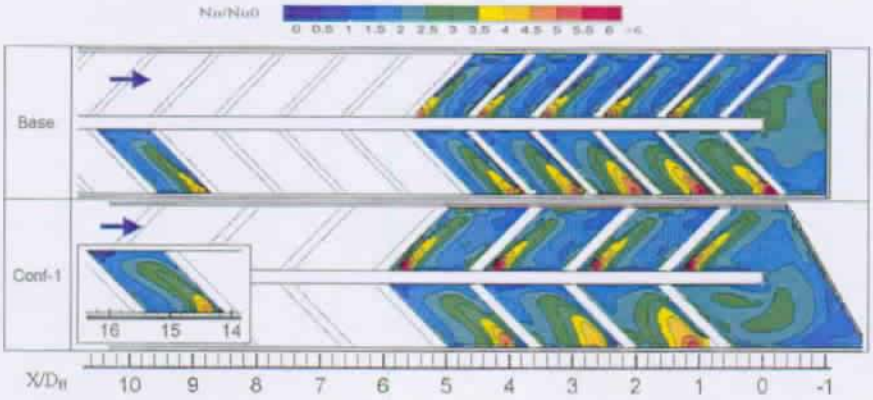

Figure 68: Geometrical parameter e/D_H influence: Full surface heat transfer distribution on the bottom wall.

Figure 68 gives a comparison of full surface Nu/Nu_0 distribution of the bottom wall baseline configuration with configuration-1 at Re=50,000. The blockage ratio in configuration-1 (15%) combined with the pitch of $1.5D_H$ leads to a similar heat transfer distribution shape as in the baseline configuration. Figure 68 suggests that the heat transfer pattern has been scaled by a factor of 1.5. Note that the heat transfer distribution downstream of the last rib is very similar to the distribution downstream of a rib in a fully developed rib module. This confirms that the heat transfer (similar to the flow) is not disturbed by the bend, even at distances close to the bend.

Despite the heat transfer distribution similarity between the baseline configuration and configuration-1, the results of Table 7 show that the area-averaged value is higher than in the baseline configuration. This is due to the fact that the region of high heat transfer ($Nu/Nu_0 > 4$) is larger compared to the full rib module surface in configuration-1 than in the baseline configuration. Indeed in configuration-1, the rib height and the rib pitch have been scale by a factor 1.5, but the distance between the web and the outer sidewall is still $1D_H$. Hence the rib-induced vortex described in 5.1.3 cannot develop in the same manner as in the baseline configuration. Note that as in the baseline configuration, the spanwise heat transfer gradients (as defined in Figure

37) are almost linear on the configuration-1 bottom wall. Gradients on the top wall follow the same linear trend, with some discrepancies.

Downstream of the bend, the heat transfer recovers from the bend effect; in this region the geometrical influence is very important. The blockage ratio of the configuration-1, combined with $p/D_H = 1.5$, leads to a slower decrease of the heat transfer levels downstream of the bend. The configuration-1 area-averaged heat transfer is lower than the baseline heat transfer in the first rib module downstream of the bend. It becomes higher for $X > 5D_H$.

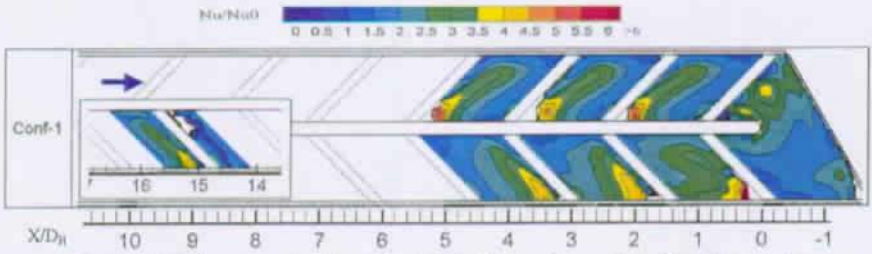

Figure 69: Full surface heat transfer distribution on the configuration-1 top wall.

Figure 69 shows the full surface heat transfer distribution on the configuration-1 top wall. Together with Figure 70, they allow comparing the distribution on configuration-1 ribbed walls.

The fully developed rib module heat transfer distributions are different from the bottom wall to the top wall. First the U-shape high heat transfer region downstream of the rib is more shifted towards the downstream direction on the top wall than on the bottom wall. This is due to the size of the recirculating vortex induced by the ribs, which is bigger behind top ribs than behind bottom ribs. Second no high heat transfer region occurs on the top wall at the location of the vortex impact on the sidewall. This is due to the weak impact of the rib-induced vortex on the top wall. Note that these full surface differences give an explanation of the 4% difference between both ribbed wall values in Table 7. It should be mentioned that these differences lead to a unsymmetrical heat transfer distribution on the side wall (see Figure 106).

Figure 70 gives streamwise velocity components and secondary vectors in X=constant cross sections located in the configuration-1 fully developed flow region. The cross section in Figure 70a is located immediately upstream of a bottom rib, i.e. gives indication of the flow downstream of a top rib. The cross section in Figure 70b is located exactly at the same location compared to a bottom rib.

This figure allows explaining the heat transfer distribution difference between the configuration-1 top and bottom walls. The flow is not symmetrical around the $Y = 0.5$ plane. Hence the flow does not act on both ribbed walls in a similar manner. On the one hand, the flow that impinges behind the ribs, does not come from the same location in the channel. The flow that impinges on the top wall (Figure 70a) seems to come from upstream of the top rib. The flow that impinges on the bottom wall (Figure 70b) comes from the channel centre. On the other hand, the flow that impinges behind the ribs, impinges with higher values normal to the ribbed wall on the top wall than on the bottom wall.

The conclusion from these figures is that there is a difference in heat transfer characteristics between the bottom and the top wall. This difference does not come from the variation of rib pitch or height, since the rib distribution is symmetrical from one ribbed wall to the other. It seems that the bend shape is responsible for this difference. Even though the bend does not perturb the flow in its near vicinity, it could modify the flow distribution in the entire channel, including the far upstream bend region. In turn the heat transfer is affected by the bend effect. This trend is similar to the one mentioned in the configuration-2 with extraction.

Another explanation could also be that the first rib in a channel leg influences the flow distribution in the entire leg. Indeed, the heat transfer distribution in the downstream leg is shifted on the bottom wall, compared to the upstream leg where it is shifted on the top wall. This corresponds, on the one hand to a first bottom rib at the channel inlet, and on the other hand to a first top rib immediately downstream of the bend.

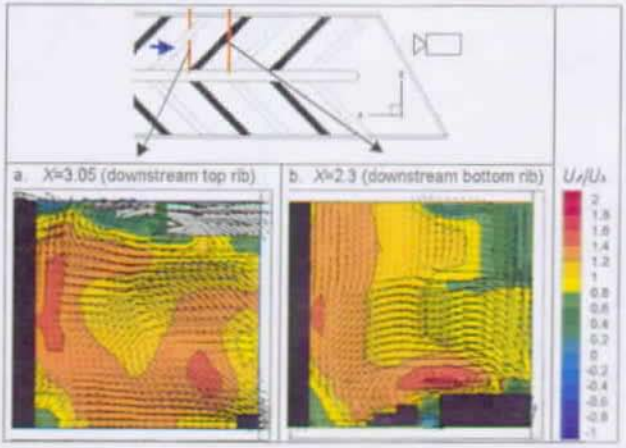

Figure 70: Velocity profiles at X=constant in the configuration-1 fully developed region.

6.3.2 Geometry of bend features

In the previous part, the heat transfer distribution in the fully developed region has been described in the configuration-1. The present part will focus on the bend region. It will investigate how the bend flow structures influence the heat transfer distribution. In a second paragraph, the influence of the introduction of a guide vane inside the bend will be discussed.

6.3.2.1 Variation of back wall angle

Changing the bend back wall angle to the main flow modifies the heat transfer distribution in the upstream part of the bend. Figure 71 gives the full surface heat transfer distribution on the bend walls in the baseline configuration and in the configuration-1. Reynolds number was set to 50,000.

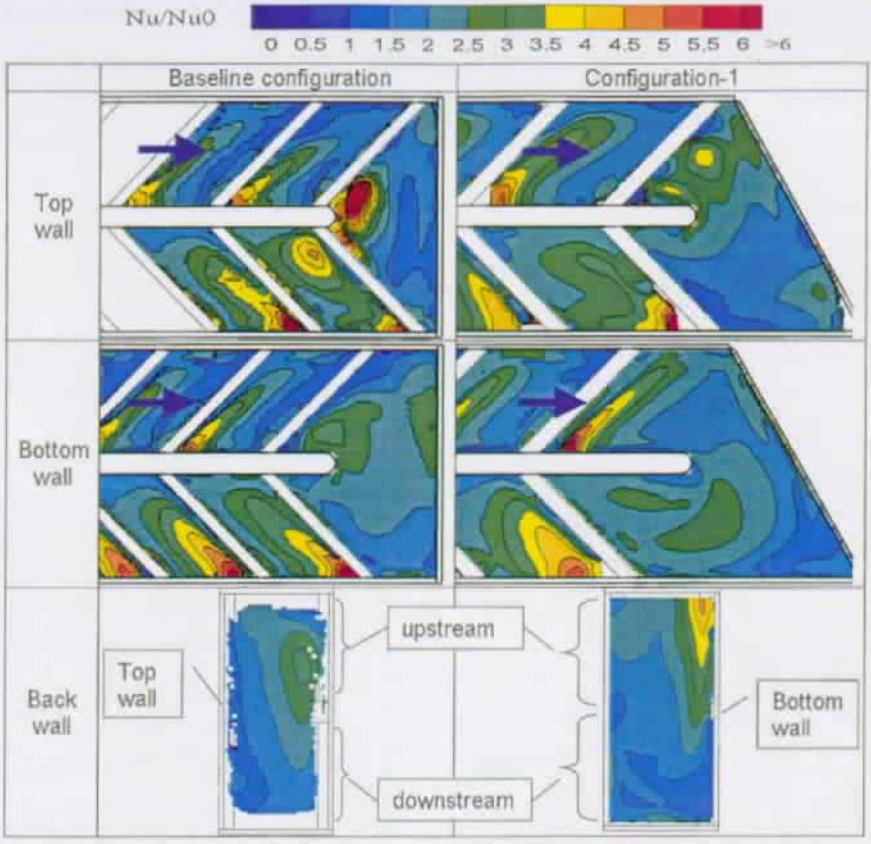

Figure 71: Influence of back wall angle on the heat transfer distribution in the bend region.

On the configuration-1 bottom wall, the last rib upstream of the bend is located $1.25D_H$ upstream of the bend. The distribution behind the last rib is very similar to the fully developed heat transfer distribution. This can explain why the upstream half of the bend has an area-averaged heat transfer value equal to the fully developed region. Note that the Nu/Nu_0 area-averaged values for the upstream part of the bend are 2.36 and 2.5 in the configuration-1 and baseline configuration, respectively.

On the configuration-1 top wall, the last rib is located at $0.5D_H$ upstream of the bend. It is approximately the same location to the web tip, as the last bottom rib in the baseline configuration. Hence the heat transfer distributions downstream of these ribs are similar in both configurations. Note that the Nu/Nu_0 area-averaged values for the upstream part of the bend are 2.5 and 2.42 in the configuration-1 and baseline configuration, respectively.

The bend angle also modifies the heat transfer in the downstream part of the bend. It is especially noticeable in the downstream corner of the bottom wall, where the heat transfer is low. It is due to the large recirculating cell in the downstream

corner of the bend. At this location, dust holes could be placed in the channel, in order to diminish the impact of this recirculating cell.

To summarise, the 30° angle of the bend in configuration-1 and the location of the last ribs upstream of the bend homogenises the heat transfer distributions. The differences between the top and bottom walls are less than in the baseline configuration.

The heat transfer distribution in the configuration-1 and the differences with the baseline configuration can be related to the flow characteristics in the bend region. The configuration-1 flow characteristics are summarised in Figure 72.

At the bend inlet, the flow is accelerated. The secondary flow structures disappear as the flow enters the bend. The small recirculating cell downstream of the last top rib accelerates and directs the flow towards the back-bottom corner (high heat transfer region in Figure 71). No recirculation cell occurs in the upstream bend corner. This is due to the back wall angle, which imposes to the incoming flow a smaller adverse pressure gradient than in the baseline configuration.

As the flow goes through the bend, it is accelerated near the web tip. No top-back wall corner vortex occurs. The flow in the configuration-1 bend region is mixed between the upper part ($Y > 0.5$) and the down part ($Y < 0.5$). The two counter rotating cells of the upstream leg do not remain in their respective channel halves as it was the case in the baseline configuration.

In the downstream part of the bend, a large recirculating cell takes place. Here the streamwise velocity is lower than $0.2U_b$. The size of this cell is bigger near the top wall ($0.5D_H^2$) than near the bottom wall. This cell was shown to be very unsteady when instantaneous velocity vector fields were observed.

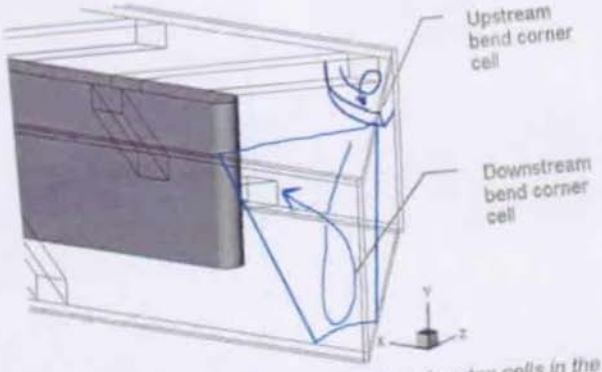

Figure 72: Schematic view of the configuration-1 vortex cells in the bend.

6.3.2.2 *Turning vane*

The turning vane does not strongly influence the heat transfer on the ribbed walls in the bend compared to the configuration-2. One characteristic can however be noted. The turning vane guides the flow at the bend inlet. It distributes the massflow

between the inner and the outer bend regions. This creates a smoother heat transfer distribution in the upstream bend part (see Figure 73).

In the downstream leg, major differences appear between configuration-2 and configuration-3. The region of high heat transfer is not located along the outer wall, but along the channel centreline. This phenomenon is due to the presence of the turning vane. As shown in Chanteloup [19], the high streamwise velocity occurs along the centreline in configuration-3, rather than along the downstream outer wall in configurations without turning vane.

On the back wall, the heat transfer is strongly modified by the turning vane presence. The heat transfer distribution is almost symmetrical around the Y=0.5 axis. Two high heat transfer regions occur at Y=0.25 and Y=0.75 (maximum at Z=0.9). These regions are similar to the one in configuration-2 for Y<0.5, corresponding to the incoming flow impact on the back wall.

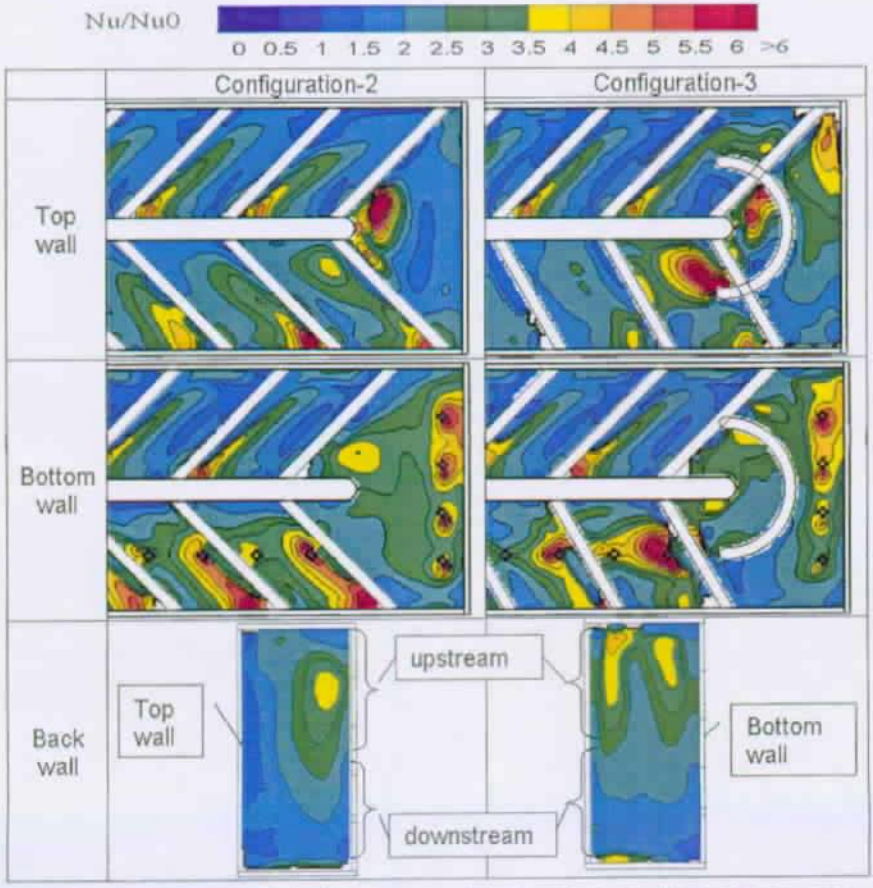

Figure 73: Influence of bend turning vane on the heat transfer distribution in the turn region.

The heat transfer distribution in the configuration-3 bend can be related to the flow characteristics. Streamlines as well as plane cut analysis allowed building the flow representation given in Figure 74.

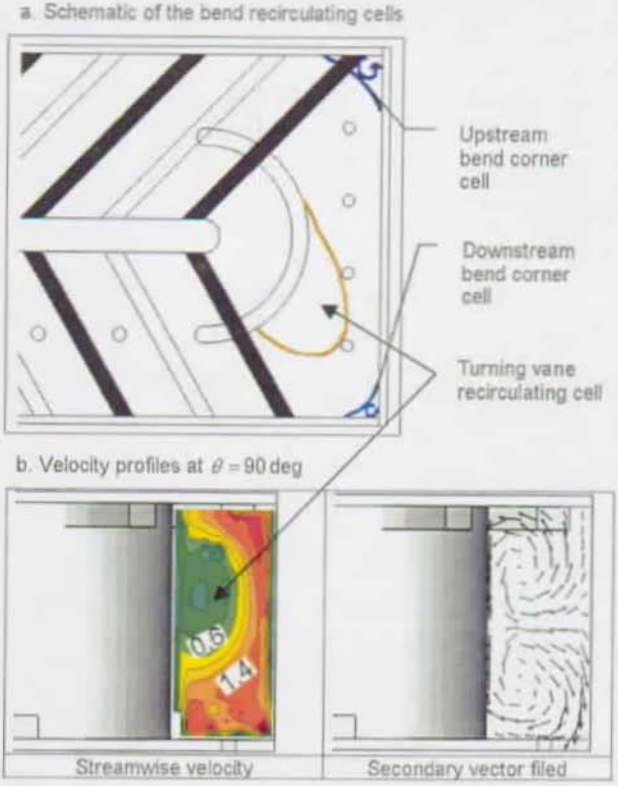

Figure 74: Recirculating cells in the configuration-3 bend region.

A recirculating cell is attached to the turning vane (Figure 74a). This recirculating cell governs the flow in the outer bend passage (part of the bend between the turning vane and the back wall). The recirculating cell blocks the flow at the channel centre. The opening area, which is created for the streamwise motion, is almost symmetrically distributed around the recirculating cell. The flow in the entire outer bend passage is therefore almost symmetrical around Y=0.5.

The upstream-corner recirculating cell is also influenced by the turning vane recirculating cell. This cell modifies the bend incoming flow in order to create a symmetrical distribution in the passage. As a consequence, the upstream corner cell is smaller than in the baseline configuration and in configuration-2.

The symmetrical distribution of the flow governs the heat transfer distribution on the back wall (see Figure 73).

Note that similar to the configuration-2, the incoming flow in the upper part of the channel (Y>0.3) has higher streamwise velocity components than the down part (Y<0.3). It is also directed towards the down part of the back wall, but in configuration-3, the impact on the back wall is symmetrically distributing around the Y=0.5 axis.

6.4 Influence of design parameters on thermal performances

Thermal performances are based on an energetic analysis of the coolant channels. They compare the heat transfer (Nu/Nu_0) to the energy input ($(f/f_0)^{1/3}$) necessary to obtain this heat transfer. It yields the dimensionless parameter:

$$\eta = \frac{Nu/Nu_0}{(f/f_0)^{1/3}} \tag{6.1}$$

with f_0 the friction factor of a smooth channel calculated from the Blasius equation:

$$f_0 = 0.046\mathrm{Re}^{-0.2} \tag{6.2}$$

This part compares the thermal efficiencies of all the tests measured in the present thesis work. Results are given in a matrix similar to the test matrix presented in 3.5. The present part does not aim at providing an optimum geometry for cooling design, since the studied geometry are simple cases far from real-engine designs. But general trends versus geometrical characteristics and flow conditions can be drawn. Note that all the three measured walls are taken into account. The web is not thought to be responsible of major changes in the following results.

6.4.1 Pressure drops

a. Fully developed region

f/f0	Re number								
	25 000			50 000			70 000		
Baseline Conf.	12.6			14.1			15.7		
Configuration-1	17.7			18			19.8		
	Extraction of Inlet massflow								
	30%	40%	50%	30%	40%	50%	30%	40%	50%
Configuration-2		10.9	11.9	12.2	11.5	11.5	13.5	13.7	13.3
Configuration-3		11.8	11.8	12.1	12	12	12.9	12.6	12.2

b. Full bend region ($-6D_H < l < 6D_H$)

f/f0	Re number								
	25 000			50 000			70 000		
Baseline Conf.	19.4			21.3			24.2		
Configuration-1	29.6			29.4			32.2		
	Extraction of Inlet massflow								
	30%	40%	50%	30%	40%	50%	30%	40%	50%
Configuration-2		15.2	14.7	17.8	16.5	15.4	20.4	18.3	17.4
Configuration-3		14.3	13.1	16.2	15.2	14.4	18.2	16.9	15.4

Figure 75: Friction factor matrix for all the present work test cases.

Figure 75a gives the friction factor ratio f/f_0 in the fully developed regions of the various test cases. In all the configurations, f/f_0 increases as Reynolds number increases, which is coherent with previous published works. In configuration-1, f/f_0 is 20% higher than in the baseline configuration. This is due to the e/D_H increase in configuration-1. The extraction does not seem to have a significant effect on the friction factor in the upstream leg. This is due to the fact that in the fully developed region, the inlet massflow is present for all the extractions. Moreover the flow is thought to be similar at all the three extractions.

Figure 75b gives the friction factor ratio f/f_0 in the various channels. The full bend region is taken into account, from $l=-6D_H$ upstream of the bend up to $l=+6D_H$ downstream of the bend. In all the configurations, f/f_0 increases as Reynolds number increases. Configuration-1 results are the highest. The difference with the baseline configuration is higher than in the fully developed region (25-30% difference). This proves that the angle back wall in the bend leads to higher pressure-losses than the square bends. The extraction influences the pressure losses. f/f_0 decreases as the extraction increases from 0% to 50%. This is due to the fact that downstream of the extraction holes, the channel massflow is less as the extraction increases, thus the friction decreases. The turning vane improves the friction factor of 10%, at every flow condition.

6.4.2 Thermal performances

a. Fully developed region

η	Re number		
	25 000	50 000	70 000
Baseline Conf.	1.22	1.04	0.95
Configuration-1	1.19	1.06	0.92

	Extraction of Inlet massflow								
	30%	40%	50%	30%	40%	50%	30%	40%	50%
Configuration-2		1.34	1.28	1.17	1.16	1.16	1.03	1.02	1
Configuration-3		1.25	1.27	1.11	1.09	1.12	0.99	1	1.01

b. Full bend region ($-6D_H < l < 6D_H$)

η	Re number		
	25 000	50 000	70 000
Baseline Conf.	1.06	0.96	0.87
Configuration-1	0.97	0.89	0.78

	Extraction of Inlet massflow								
	30%	40%	50%	30%	40%	50%	30%	40%	50%
Configuration-2		1.28	1.27	1.06	1.09	1.1	0.95	0.97	0.96
Configuration-3		1.21	1.25	1.05	1.08	1.1	0.95	0.96	0.98

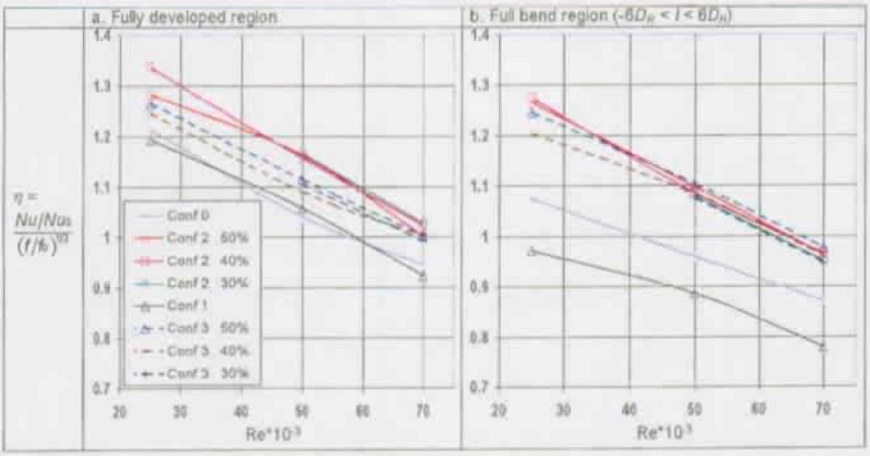

Figure 76: Thermal performances of all the present work test cases.

Figure 76a gives the thermal performances of the various tested channels in the upstream leg fully developed region, at every flow conditions. In the upper part of the figure, a matrix gives numerical values whereas in the down part of the figure, these values are plotted versus Reynolds number. Note that the thermal performances values do not take into account the heat transfer increase of the ribs themselves.

The geometry does not influence so much the thermal performances in the fully developed region. The baseline configuration and configuration-1 results are approximately equal at every Reynolds number. The extraction seems to have an impact on the fully developed thermal performances. The configuration-3 values are 5% higher than the no-extraction-geometry values. The configuration-2 values are another 5% higher than the configuration-3 values. Note that at Re=70,000, the configuration-1 is less efficient than a smooth channel.

Reynolds number has an impact on the thermal performances. As Re increases, the thermal performances decrease in every configuration. It is in agreement with eq. (6.1) since Nu/Nu_0 decreases and f/f_0 increases as Re increases. The trend of the thermal performances can be approximated with a linear function. The slopes of the functions are approximately equal for all the test cases performed in the present work. Note that since only three measurement points are available for each configuration, the slope of the plotted results is not determined with enough accuracy to build a correlation.

Figure 76b gives the thermal performances of the various tested channels in the entire bend region, at every flow condition. In the upper part of the figure, a matrix gives numerical values whereas in the down part of the figure, these values are plotted versus Reynolds number. In general the performances are lower than in the fully developed region. The bend decreases the thermal performances of the channels.

The geometry of the bend and the extraction presence have a bigger influence on the entire bend thermal performances than on the fully developed thermal performances. The configuration-1 suffers the more of its bend geometry. The baseline configuration has a thermal performance 10% higher than configuration-1. Extraction improves the performances of the channels. The configuration-2 and configuration-3 have results approximately equal at every extraction ratio. The values are 20% higher than the baseline configuration results for every Reynolds number. Note that the introduction of the guide vane in configuration-3 seems to compensate the deficit of thermal performances in the fully developed region.

As in the fully developed region, Reynolds number has an impact on the thermal performances. As Re increases, the thermal performances decrease in every configuration. The trends of the thermal performances can be approximated with a linear function. The slope of the plotted results is slightly less than in the fully developed region

The conclusion is that as Reynolds increases, the heat transfer increases (Nu), but the efficiency of the passages decreases. This result shows the priority of increasing the thermal capabilities of the internal cooling channels.

Conclusions of chapter 6

Chapter 6 studied the influence of design parameter variations on the flow and heat transfer characteristics. 3D-streamlines were extracted in the full volume from the 2D-3C PIV measurement planes.

Reynolds number variation

- Nu values decrease as Re decreases, whereas Nu/Nu_0 increases.
- The gradients of Nu/Nu_0 are less important as Re increases.
- The heat transfer recovery length from the bend effect in the second leg of the channel is constant for the three Reynolds numbers measured.

Film cooling extraction

- Adding bleeding holes modifies the flow field in the entire test section. The symmetrical velocity profile of the baseline configuration is unbalanced of $0.2D_H$ toward the wall with extraction.
- The effect of extraction on the heat transfer is dependent on the channel region. In the upstream leg, the influence of extraction is hardly noticeable. In the bend region and downstream of the bend, the heat transfer is highly increased on the wall provided with extraction holes.
- On the sidewalls, a slight dissymmetry of the full surface heat transfer distribution is introduced by the extraction. It is due to the dissymmetry of the flow.
- Varying the extraction from 30% to 50% of the inlet massflow does not show any variation in the Nu/Nu_0 results, as long as Nu_0 is based on the channel inlet flow conditions.
- The extraction highly modifies vortex and low streamwise velocity cells, which are present in the bend corners. These cells modify the bend geometry "shown" by the flow. In turn the flow and heat transfer characteristics inside the bend but also upstream of the bend are affected.

e/D_H

- Keeping the same p/e ratio and increasing the e/D_H ratio from 0.1 to 0.15 increases the area-averaged heat transfer levels of about 10%.

Bend back wall angle

- A back wall angled at 30° to the channel web changes the bend corner recirculating cells.
- The heat transfer distribution is modified on the bend back wall; with higher heat transfer gradients than in the baseline configuration.

Turning vane

The configuration-3 bend region is provided with a turning vane and with film cooling extraction holes.

- In the upstream leg, the influence of extraction dominates the influence of the turning vane on the flow and heat transfer distributions.
- The bend region corner cells are highly influenced by the turning vane. It yields a bend heat transfer distribution completely different from the other tested configurations.

Thermal performances

The thermal performances (η) have been compared for all the 22 test cases.

- An increasing Reynolds number leads to a decreasing η. A linear trend is observed.
- Configurations with extraction have better thermal performances if the global bend region ($-6D_H<k<6D_H$) is considered.
- Varying the extraction from 30% to 50% does not influence the thermal performances. Note that the friction factor (f/f_0) is dependant on the extraction variation.
- The introduction of the back wall angle is not favourable to the thermal performances. Indeed, the configuration-1 has the worst thermal performances as the global bend region is considered.

Globally there is no obvious correlation between the Nusselt values on the surface and a specific velocity component above the surface, excepted in certain locations or flow configurations where Nu/Nu_0 gradients are high. In these regions, Nusselt shows a good correlation with the impinging velocity components.

7 NUMERICAL SIMULATIONS (CFD)

Numerical simulations have been performed for the baseline configuration and in the configuration-2. Since the present thesis work focuses on experimental measurements, the aim of the present chapter is to give a brief idea of the CFD capabilities and limitations in predicting both flow and heat transfer measurements in 45° ribbed cooling channels, with or without film cooling extraction. In the present chapter, Computational Fluid Dynamics (CFD) procedures are explained, flow and heat transfer predictions are compared to measurements.

7.1 CFD code and turbulence model

The CFD predictions presented below have been calculated using Fluent 5.4.8. The segregated solver was chosen for the low Mach numbers of the present test cases. The quantities on cell faces have been determined using the second order upwind descretisation scheme.

The two equation k-epsilon turbulence model has been applied to determine turbulent quantities. The near wall treatment has been done by the standard wall function. The average wall y+ of 18 on the configuration walls permit the application of this model.

Note that both the Reynolds Averaged Navier-Stokes and energy equations were resolved. The constant wall temperature case was chosen. The heat transfer coefficient was calculated as follows:

$$\alpha = \dot{q}_{wall} / (T_{wall} - T_{bulk\_local}) \tag{7.1}$$

with the surface heat flux $\dot{q}_{wall}$, the wall temperature T_{wall} and the local bulk temperature, T_{bulk_local}. It should be mentioned that the offset between the local bulk temperature and the gas temperature used in the measurements (see Figure 17) gives a 4% over prediction of the CFD heat transfer value.

7.2 Grid generation

7.2.1 Mesh generator

Meshes were generated from a 3D volume CAD model. The grids were generated with the Centaur 4.5 grid generation package. The grid generator produces meshes composed of unstructured prismatic (wedge) and tetrahedral elements. Centaur is an automatic grid generator, which requires a small amount of user interaction. Grid generation parameter modified by users guide the generation process. Centaur grids are hybrid grids with unstructured prismatic cells at walls and tetrahedral elements within the remaining calculation domain. The walls are provided with 6 layers of prismatic cells. Examples of the grids are shown in 7.2.3.

The hybrid meshing technique consists of placing prismatic elements along the model surface and growing tetrahedral cells far from the walls. Grids are refined in regions of high velocity gradients or geometrical changes (bend region, extraction hole entrance).

7.2.2 Grid dependency

A CFD solution is judged grid independent when there is minimal change in the solution variables. As the number of cells in the solution approaches infinity, an exact solution of the continuum should be achieved. A mesh can be acceptable when its solution is identical to the one of a finer mesh.

A flow and heat transfer grid dependency was performed at Alstom-CH in a single rib module with periodic boundary conditions. An optimum mesh was found with constrains in size limitation and stretching ratio of cells in the middle of the channel. A list of criteria was obtained from this grid independency study. The single rib module criteria were applied to the entire channels, yielding typical meshes of 2.6-3.2 million cells.

A later investigation on the boundary layer resolution showed that limiting the gradient in size of the prism layer can limit the grid-dependence on heat transfer predictions. The growth of the prismatic layer near the wall was modified according to this finding.

7.2.3 Channel meshes

7.2.3.1 Baseline configuration

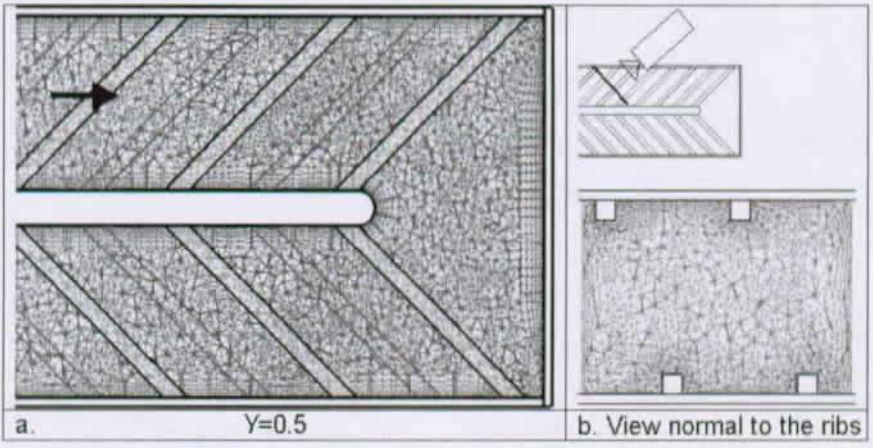

Figure 77: Cuts of the baseline configuration mesh.

Figure 77 gives an overview of the mesh utilised for the CFD calculations. A cut of the mesh at $Y = 0.5$ (Figure 77a) shows the prismatic layer near the walls and the tetrahedral cells in the channel centre. It also shows how the mesh was refined in the bend region, with limitations in both prismatic and tetrahedral cell sizes (<5mm). The view normal to the ribs (Figure 77b) gives the vertical distribution of cells inside the channel. The mesh refinement around the ribs can be noted. Note that the baseline configuration mesh was composed of 2.6 million cells. More than 95% of the wall y+

values were over 12.

7.2.3.2 Configuration-2

Figure 78 gives an overview of the configuration-2 mesh. Convergence problems occurred at the outlet of the 5mm-long extraction holes. Recirculating flow prevented the calculation convergence. The CFD model hole length was set to 50mm instead of 5mm in the Plexiglas model. The modified hole length allowed the flow developing inside the hole, in turn the solution converging.

Numerous cells were necessary for the hole meshing. Thus the number of cells was reduced in the centre part of the cooling channel in order to reach a realistic mesh size. This is clearly noticeable on Figure 78. Despite the coarse mesh in the straight leg channel centre, the refinement criteria remained the same as in the baseline configuration in the bend region and around the holes. The coarse mesh allowed to obtain a mesh for the entire channel of 3.2 million cells. In this case as in the baseline configuration, 95% of the wall y+ values were over 12. Note that a CFD simulation was performed in the configuration-2 mesh, with the hole outlet having a zero massflow outlet (wall conditions). The mean heat transfer and flow differences between the baseline configuration and the configuration-2 were less than 5%. This comparison shows that the coarse mesh does not affect the prediction in the configuration-2.

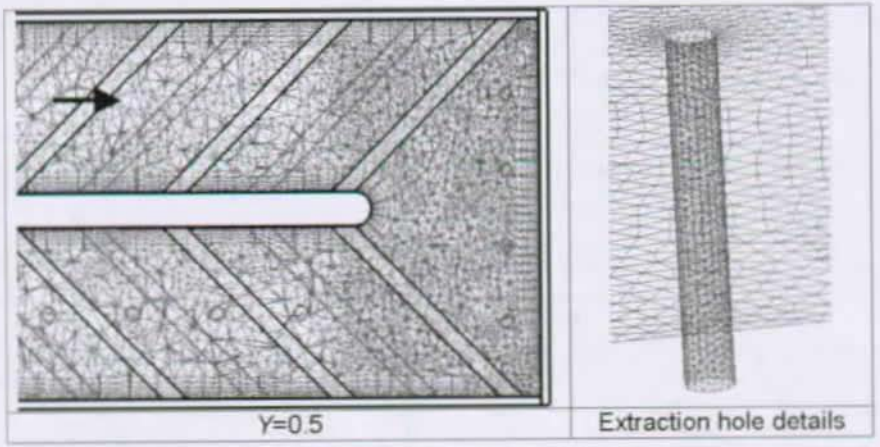

Figure 78: Cuts of the configuration-2 mesh.

7.2.4 Calculation parameters

7.2.4.1 Fluid properties

The density has been calculated using the incompressible-ideal-gas option, which takes temperature changes into account, but ignores the pressure influence on the density. This is a good approximation for the present low Mach number cases. The

thermal conductivity, the specific heat and the dynamic viscosity of the fluid have been considered constant ($k = 0.0242W/mK$, $C_p = 1006J/kgK$ and $\mu = 1.79 \cdot 10^{-5} kg/ms$).

7.2.4.2 Boundary conditions

The calculation was a combined flow and heat transfer calculation. The configurations were calculated with fixed velocity inlet. The outlet boundary conditions at the channel exit and at the hole exit were adjusted by the massflow.

The flow boundary conditions were applied to match the required Reynolds number. This lead in the case of Re=50,000, to an inlet velocity of 7.3m/s and an inlet massflow of 0.089kg/s. The inlet turbulence intensity of 2% was applied according to PIV measurements. The hydraulic diameter of 0.1m was used as the reference length.

The inlet gas temperature was set to 300K. The wall temperature was set to be 400K.

7.2.4.3 Convergence information

The model was run until convergence criteria had been reached. The convergence procedure consisted of two steps. The convergence criteria were initially relaxed to a magnitude of 10^{-3} where first order discretisation schemes were used for the variables. The convergence was reached after approximately 1250 iterations. The model was run again with second order schemes and with convergence criteria of 10^{-4} for all the variables and $5*10^{-7}$ for the energy variable. Around 1000 iterations were necessary to reach the converged solution.

7.3 CFD simulations for the baseline configuration

7.3.1 Area-averaged results

Table 8 gives a comparison between area-averaged Nusselt numbers given by CFD calculations and by measurements. Values are extracted from the fully developed region ($4D_H$ upstream of the bend). They correspond to the rib module A studied in 5.1.3.2. Values on the ribbed walls consider the surface between two consecutive ribs.

CFD calculations tend to over predict the heat transfer on the ribbed walls by about 5-10%. The over prediction becomes less obvious if one take into account the 4% higher values of predictions due to the location of the measured gas temperature (see 7.1). This shows that on the ribbed walls, CFD predictions are in the range of experimental uncertainties.

The difference between measurements and calculations is significant on the outer sidewall. CFD calculations under predict the heat transfer on the smooth outer sidewall by about 25-30%.

Nu/Nu_0	Bottom wall	Top wall	Sidewall
CFD calculations	2.13	2.15	1.63
Measurements	2.08	2.05	2.25

Table 8: area-averaged heat transfer results in the fully developed region: comparison between CFD calculations and measurements.

Figure 79 shows the area-averaged heat transfer distribution along the accumulated distance. The heat transfer trend predicted by CFD is similar to the one of the measurements. The differences between calculation and measurements mentioned in the previous paragraph are valid in the entire upstream leg. The downstream leg calculated values are more different. The bottom wall values are under predicted by about 20%, whereas the top wall values are almost well predicted. The difference between the top and bottom walls is not explainable, but the fact that Nu/Nu_0 maxima are higher on the top wall (i.e. the full surface distribution is not more accurately predicted on the top wall than on the bottom wall). The sidewall heat transfer is poorly predicted all along the channel, with a 25% under prediction in the upstream leg and a 25% over prediction in the downstream leg.

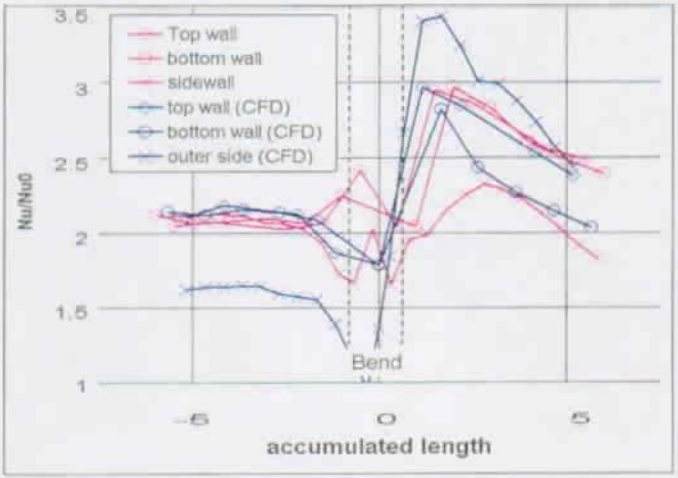

Figure 79: area-averaged heat transfer results in the baseline configuration: comparison between CFD calculations and measurements.

7.3.2 Full surface heat transfer distribution

7.3.2.1 Full channel geometry calculations

Figure 80 gives a comparison of full surface heat transfer distribution between measurements and CFD predictions. The areas are located in the upstream fully developed region of the baseline configuration, at Re=50,000. Both bottom wall and outer sidewall results are plotted.

Global heat transfer pattern is captured by CFD predictions. A high heat transfer region occur downstream of the rib on the bottom wall. It develops along the rib towards the outer sidewall. On the sidewall, the heat transfer is increased between to consecutive ribs, for $0 < Y < 0.3$ and $0.7 < Y < 1$.

The heat transfer results are under-predicted by CFD. Maximum values

downstream of the rib are higher than 5 in the measurements and lower than 3.5 in the predictions. The under-prediction is particularly noticeable on the outer sidewall, where Nu/Nu_0 are not higher than 2.5. This can explain the large difference of area-averaged results on the sidewalls in Table 8.

The heat transfer contours predicted by CFD are smoothed out compared to the measurement results. Details in the surface distribution are not captured by CFD. The U-shaped high heat transfer region downstream of the rib is spread out in the CFD prediction. The region of high heat transfer in the bottom-sidewall corner is not predicted. Nu/Nu_0 gradients on the side walls are not captured.

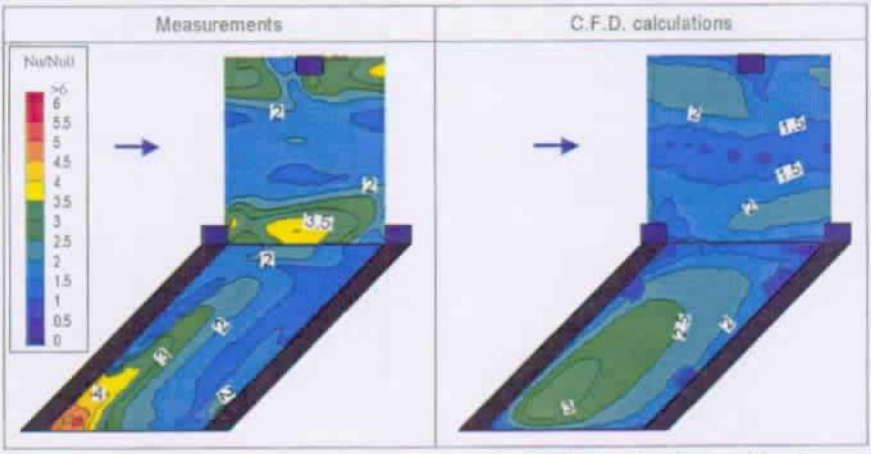

Figure 80: Full surface fully developed heat transfer distribution: baseline configuration (Re=50,000).

Figure 81 gives a comparison of full surface heat transfer distribution between measurements and CFD predictions. The areas are located in the bend region of the baseline configuration, at Re=50,000. Ribbed walls and outer sidewall results are plotted.

Trends described in the fully developed region are valid in the bend region.

On the bottom wall, high heat transfer spots are not located at the same position in the prediction than in the measurements. A region of high heat transfer ($Nu/Nu_0 = 3$) is not captured in the upstream bottom-back corner. The prediction of the heat transfer peak at the end of the web is located further downstream compared to the measurements. This is related to the flow separation point at the web tip being predicted further downstream compared to the measurements. Note that on the bottom wall, the heat transfer levels are well predicted.

On the top wall, discrepancies in the location of the heat transfer maxima is less than on the bottom wall. The high heat transfer region downstream of the last rib at the web tip is well predicted. The Nu/Nu_0 values are higher than on the top wall (higher than 6 in the measurements), and CFD under predicts the maxima (max<5).

On the back wall, the global heat transfer pattern is predicted, the maximum value is located at the same place in both measurements and CFD predictions. However, the levels are still under predicted by about 20-30%.

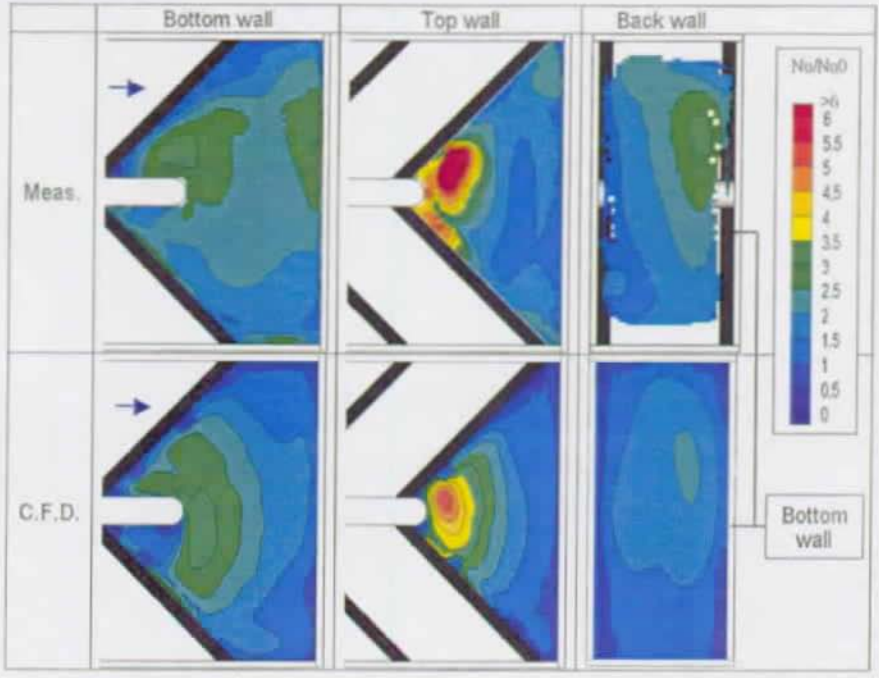

Figure 81: Full surface heat transfer distribution in the bend region of the baseline configuration (Re=50,000).

7.3.3 Flow simulations

Figure 82 shows the velocity magnitude in the centre plane ($Y = 0.5$) of the baseline configuration for a Reynolds number of 50,000. Both measurements and calculations are presented.

The flow prediction in the bend region is reasonably good. All the main flow features are captured by the calculation. The low speed regions in the bend outer corners have the same location and size as in the measurements. At the web tip, the recirculation cells have also approximately the same location. The region of high streamwise velocity near the downstream outer sidewall is also well predicted. Note that the velocity levels are in good agreement.

Some discrepancies are still noticeable. The upstream fully developed region velocity near the web is over predicted by CFD, whereas near the outer sidewall it is under predicted. The flow separation point at the web tip is predicted further downstream compared to the measurements (calculations: $\theta = 120°$; measurements:

$\theta = 60°$). The shape and size of the recirculating cell at the web tip are different in the calculations. The velocity magnitude in the resulting high velocity region near the downstream outer wall is in turn under-predicted.

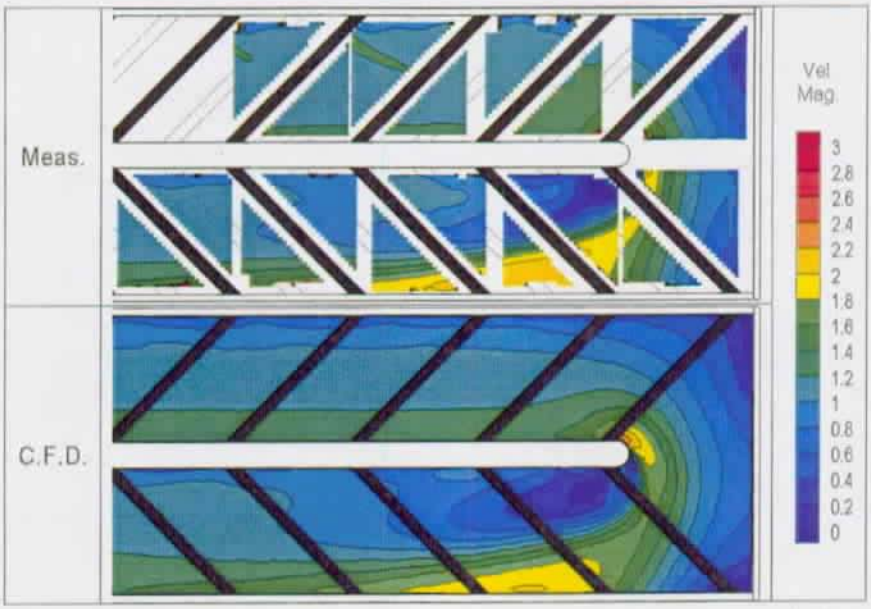

Figure 82: CFD prediction of the baseline configuration centre plane velocity magnitude (baseline configuration, Re=50,000).

Figure 83 gives velocity results in three cross sections of the baseline configuration. Both streamwise velocity and secondary vector fields are plotted. A comparison between the CFD prediction and the measurements is given.

At $X = 2.59$, The streamwise velocity is approximately predicted even though the streamwise velocity maxima are under predicted. The secondary vector field shape and direction of rotation are the same in the prediction as in the measurements. The locations of the two rib-induced counter rotating cells are 0.1-0.2D_H shifted compared to the measurements.

At $\theta = 45°$, the streamwise velocity components are predicted with a good accuracy. Discrepancies appear in the top wall region, where the streamwise velocity is under-predicted by up to 30-50% in the outer bend corner. This could explain the heat transfer under-prediction noticed on the top wall of Figure 81. The secondary vector field prediction presents the four counter rotating vortices. Their rotation direction and size are good. Their location is shifted by about 0.2-0.3D_H compared to the measurements. Note that the results obtained by Schabacker [112] were not able to predict the secondary flow in this region.

At $\theta = 90°$, the streamwise velocity is well predicted, with only small discrepancies near the rib walls around $r = 0.6$. The secondary flow field prediction is worse than in

the other cross sections. No vortex is captured at $Y = 0.6$ $r = 0.7$. However, the radial velocity component is high in the region around $Y = 0.3$ and it is directed towards the back wall. This region of high impinging velocity coincides with the measurements. This is the reason why the region of high heat transfer in Figure 81 is located at the right position on the back wall. Note that the magnitude of the impinging velocity is lower than in the measurements. This can explain why the maximum Nusselt number is lower in the prediction than in the measurements.

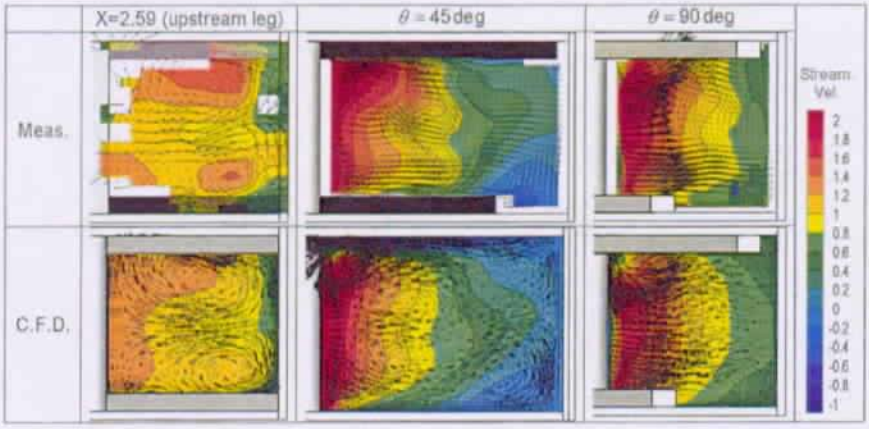

Figure 83: CFD prediction of cross section velocity characteristics (baseline configuration, Re=50,000.

As a conclusion, the CFD tool is able to predict the main complex flow features in the baseline configuration. The CFD capabilities have been improved since the work of Schabacker [112]. This is mainly due to the finer mesh (Schabacker [112]'s-mesh-size=330kcells against 2600kcells for the present work), which is allowable by up to date computers. Hence good results cannot be obtained if the mesh quality is not good enough. The mesh quality is a must, as well as the improvement of turbulence models and the need of unsteady calculations.

Small discrepancies still occur in the flow distributions, especially in the secondary flow. These small differences, associated with the standard wall function lead to the small differences noticed in the heat transfer distributions. The flow must be predicted more accurately if a greater accuracy is wanted in CFD heat transfer prediction. A solution could be to increase the mesh size.

7.3.4 Influence of channel inlet conditions

Figure 84 gives a comparison between two CFD calculations. The two cases differ by the inlet boundary conditions applied. The uniform velocity profile of Figure 84b is the profile utilised in all the calculations presented in chapter 7. The velocity profile shown in Figure 84a is representative of a disturbed velocity profile, due to perturbations at the channel inlet (geometrical problem at the settling chamber – test channel connection). The streamwise velocity is almost 0 near the outer sidewall and

is greater than 1, $0.2D_H$ far from the outer sidewall. Both inlet massflows in the two calculations are different of less than 0.5%. The results of the two walls presented in Figure 84 are representative of all the heat transfer results in the configuration.

Heat transfer results in the two calculations are very similar. The location, shape and levels of the heat transfer patterns are almost the same in both cases. The area-averaged Nusselt numbers differ of less than 0.5% between the two cases.

The inlet velocity profile variation shown in Figure 84 is representative of an in-homogeneity that could exist between measurements and calculations. This figure shows that a variation of the inlet velocity profile does not influence the heat transfer distribution in the bend region ($-6D_H<l<6D_H$). The 13 rib modules upstream of the bend region develop the flow in a same manner for both inlet profiles. Thus differences between CFD predictions do not come from the inlet boundary condition differences. In turn, approximate inlet conditions are sufficient for the setting of such calculation boundary conditions.

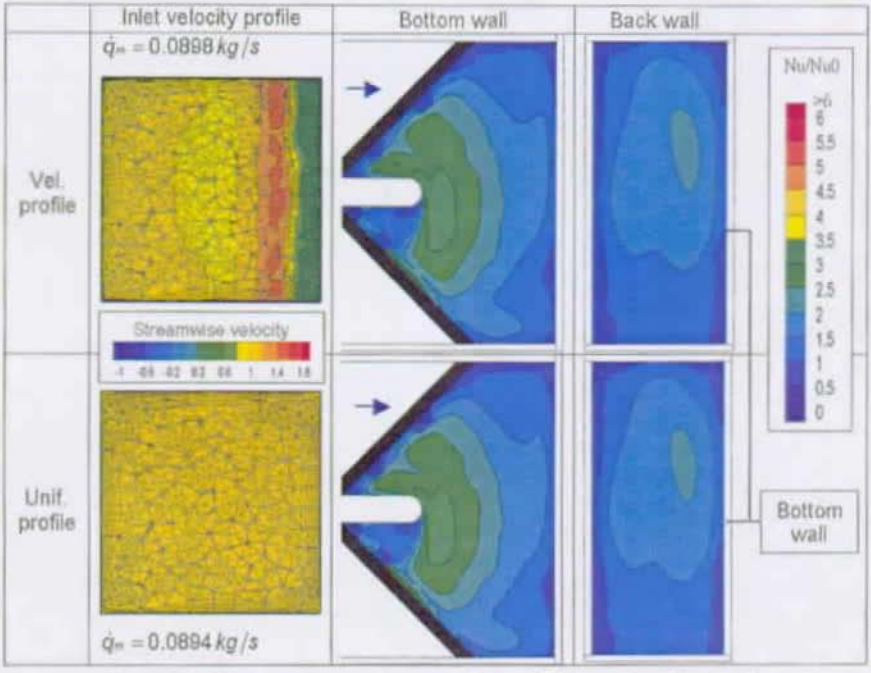

Figure 84: Influence of inlet velocity profile on CFD heat transfer results.

7.4 CFD predictions for various design parameters

The objective of this part is to give a brief overview of the CFD capabilities in predicting the influence of various flow parameters on the heat and flow distributions. Planes representative of the trends in the channel were selected for the figures. They

are the fully developed region, the bottom bend wall and the bend back wall.

7.4.1 Influence of Reynolds number

Figure 85 gives CFD predictions of the heat transfer on the baseline configuration walls at Re=25,000. The fully developed bottom wall and outer sidewall are presented. The bend bottom and back walls are also given. The figure can be compared to Re=50,000 in Figure 80 and Figure 81.

In the fully developed region, the Nu/Nu_0 distribution shape is similar to the one at Re=50,000. On both ribbed and outer walls, the Nu/Nu_0 levels are higher than at Re=50,000. This confirms the trend found with the measurements. However, the area-averaged value increase is lower than observed in the measurements. Nu/Nu_0 at Re=25,000 are only 5% higher than values at Re=50,000 (against 15% in the measurements).

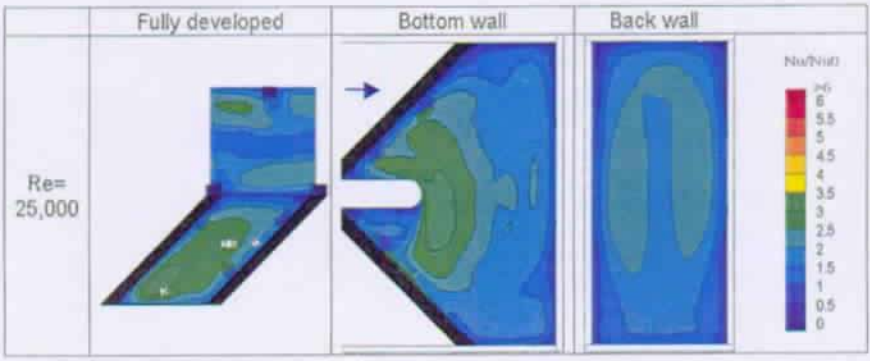

Figure 85: Influence of Reynolds number on CFD heat transfer results (baseline configuration).

In the bend region, Reynolds number does not influence the heat transfer distribution in the same manner than in the measurements. The heat transfer distribution on the bottom bend wall is similar at both Re=25,000 and Re=50,000. This is in contradiction with Figure 48, which shows a clear modification of the heat transfer distribution at Re=25,000. On the back wall, the heat transfer distribution is different from Re=50,000. The distribution is symmetrical around the Y=0.5 axis. The distribution does not show the high heat transfer region near the upstream bottom wall. This is in contradiction with the measurements, where the distribution on the back wall is not modified in shape, but in levels (see Figure 107).

Figure 86 gives the flow distribution in two cross sections of the baseline configuration at Re=25,000. The velocity components have been normalised by the bulk inlet velocity. The distribution is very similar to the one at Re=50,000 (Figure 83). This can explain that the heat transfer distribution is very similar between Re=25,000 and 50,000. Although no flow measurements have been performed at Re=25,000, one can think that the flow is modified by the Reynolds number, thus inducing differences in the heat transfer distribution. This can be one explanation of the bad prediction of

heat transfer at Re=25,000. It must also be mentioned that the same mesh was used at both Re=25,000 and Re=50,000. This lead to Y+ values lower than 8 in the case of Re=25,000. This is beyond the range of validity of the standard wall function. This could also be one reason for the explanation of the bad prediction of heat transfer at Re=25,000.

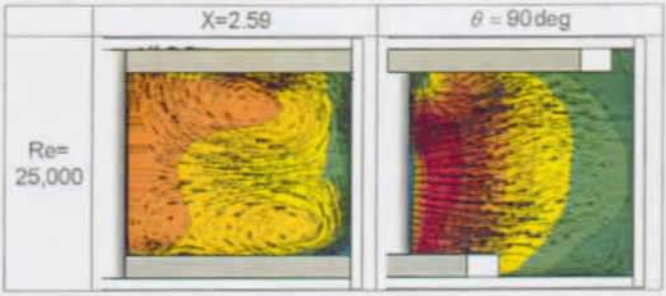

Figure 86: Influence of Reynolds number on CFD flow results (baseline configuration).

7.4.2 Influence of extraction

Figure 87 gives CFD predictions of the heat transfer on the configuration-2 walls at Re=50,000. The fully developed bottom wall and outer sidewall are presented. The bend bottom and back walls are also given. The figure can be compared to Re=50,000 in Figure 80 and Figure 81.

In the fully developed region, no influence of the extraction can be noticed in heat transfer CFD results. The heat transfer distributions are identical at 10% and 50% extractions. The heat transfer distributions are also equal to the distribution in the baseline configuration (Figure 80). This leads to the conclusion that the extraction influence noted in Figure 53b is not captured by the CFD predictions.

On the bottom bend wall, the influence of extraction is noticeable around the extraction holes. Nu/Nu_0 levels are higher than 6 around the hole inlets. The CFD prediction does not capture the channel cross flow influence on the heat transfer around the holes (see measurements Figure 61). The distribution around the holes is constant in the radial direction from the hole centres. Apart from the hole vicinity, the heat transfer distribution remains unchanged from the baseline configuration distribution. Note that an increasing extraction (from 10% to 50%) increases the Nu/Nu_0 values around the hole entrance, decreases the Nu/Nu_0 values everywhere else, but do not modify the heat transfer distribution shape.

The back wall heat transfer is not influenced compared to the baseline configuration when the extraction is set at 10%. The influence occurs at 50% extraction. The heat transfer maximum is not located near the bottom wall in the upstream part of the bend. It is located near the top wall at $Z = 0$. The distribution on the back wall is very different from the distribution given by the measurements. The explanation can be given by the flow observation (see next paragraphs). Note that even though the distributions are different from 10% extraction to 50% extraction, the

area-averaged values are only 2% different.

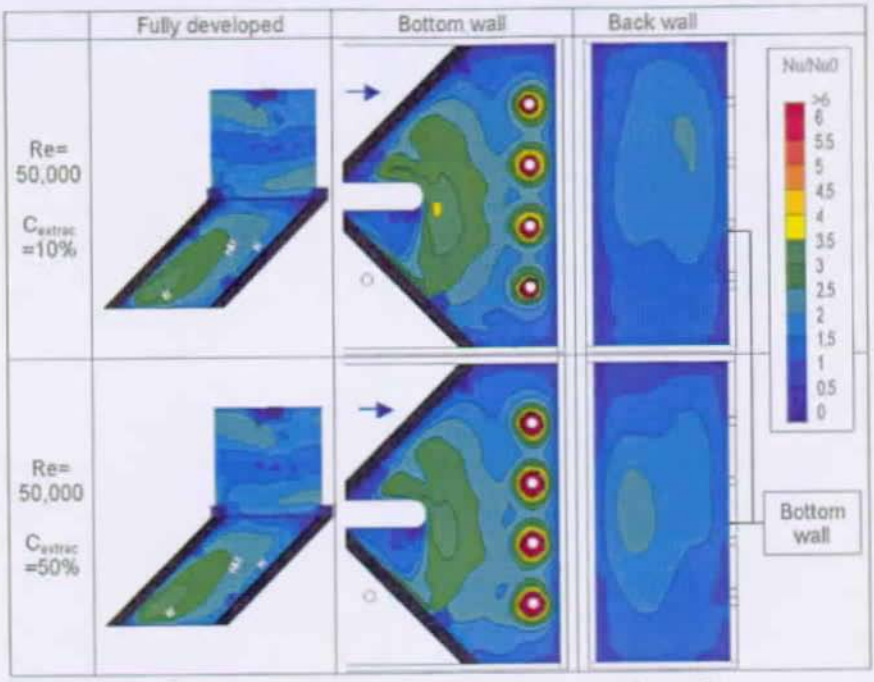

Figure 87: Influence of extraction on CFD heat transfer results.

Figure 88 shows the flow distribution in two cross sections in the configuration-2 (at X=2.59 in the upstream leg and at $\theta = 90$deg in the bend region). The flow distribution are extracted from CFD calculations at C_{extrac}=10% and 50% and from the measurements in the configuration-2 at C_{extrac}=50%.

In the upstream fully developed region, the CFD predictions do not capture the flow asymmetry measured by PIV. The CFD secondary and streamwise flow distributions are similar to the one in the baseline configuration channel. This similarity between the three calculated cases (baseline, configuration-2 10% and configuration-2 50%) explains why the heat transfer distributions in the fully developed region arte identical in Figure 80 and Figure 87.

At $\theta = 90°$ in the bend region, the flow distribution predicted by CFD is hardly influenced by the extraction, . The CFD flow at C_{extrac}=10% is very similar to the one of Figure 83. At C_{extrac}=50%, it is influenced by the hole presence. From the back wall vicinity (r=1.1) up to r=0.8, the secondary flow is directed towards the bottom wall from Y=0 up to Y=0.7. Near the top wall (Y=0.7 to Y=1), the flow impinges on the back wall with higher velocity than at C_{extrac}=10%. This can explain why at C_{extrac}=50%, the heat transfer maximum is located in this region on the back wall. The streamwise distribution is also influenced. The streamwise velocity profile is not symmetrical

around Y=0.5. The part near the bottom wall is slower than the part near the top wall.

At $\theta = 90°$ in the bend region, the predictions are very different from the measurements. The high impinging flow, which occurs from Y=0.1 to Y=0.6 in the measurements is not captured by CFD. The region of high impingement predicted by CFD is located at Y=0.7, whereas it is located at Y=0.3 in the measurement results. This lead to the differences in heat transfer distribution noticed in Figure 87.

Note that the secondary flow field in the downstream leg of the configuration-2 shows a dissymmetry comparable to the measurement one. The upper vortex occupies 70% of the cross section. However CFD doe not capture the extraction influence in the upstream leg.

These flow discrepancies are thought to be due to the recirculating cell prediction in the bend corners. The three vortices described in Figure 58 seemed to influence the flow in the entire channel. These vortices are mise-predicted by CFD. The predicted cells in the upstream and downstream corners are bigger than in the measurements. This leads to a higher acceleration near the web and lower flow near the back wall. Furthermore, the predicted top-back wall vortex is smaller than the measured one. This leads to a smaller acceleration of the incoming flow as it approaches the back wall. Hence, the predicted heat transfer peaks on the back wall are lower than in the measurements. Note that this problem in the recirculating cell prediction could come from the turbulence model.

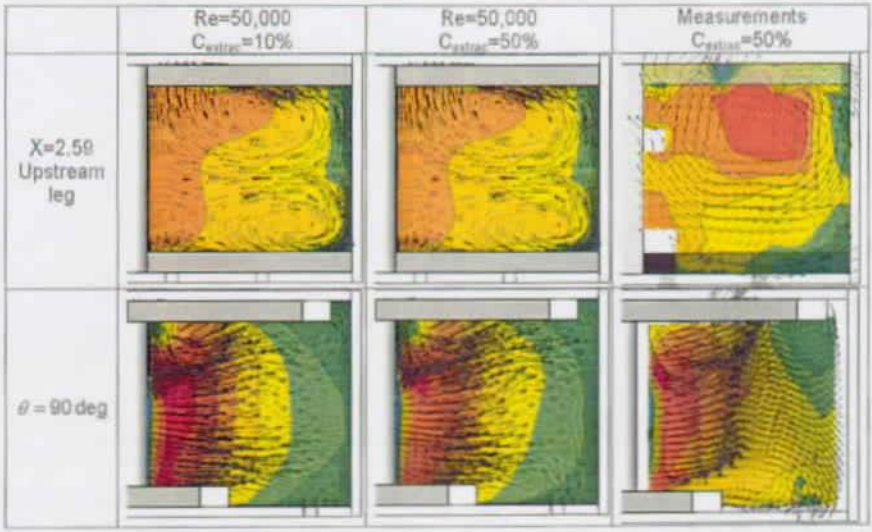

Figure 88: Influence of extraction on CFD flow results.

Conclusions of chapter 7

CFD calculations have been performed in order to show CFD capabilities and limitations in the prediction of both flow and heat transfer in internal coolant channel geometries.

Baseline configuration

The calculations show a "smoothed out" heat transfer distribution compared to the measurements.

- On the ribbed walls, the area-averaged values in the upstream leg are over predicted by about 5%. In the downstream leg the bottom wall values are under predicted by 20% and the top wall values are well predicted. On the sidewalls predictions are 25% off the measurements all along the channel.
- The comparison of the velocity magnitude distribution shows an acceptable agreement. Note that in Schabacker [112], CFD could not predict the secondary flow field in the bend region. This improvement I mainly due to the improvement of the mesh quality.
- The predicted bend corner recirculating cells are over predicted in size. The predicted flow separation at the end of the dividing wall occurs slightly downstream of the measured separation.
- CFD predicts well the "important" effects of the channel geometry on both the flow and heat transfer. "Detailed" effects are not captured by CFD.

Reynolds number variation

The CFD predictions do not show any difference between both Re=25,000 and Re=50,000. The differences showed in the measurements are too small for CFD.

Film cooling extraction

- The influence of extraction is not fully predicted by CFD. Around the extraction holes, a heat transfer increase is noticed, but it does not correspond to the measurement results.
- Recirculation cells in the bend region are not predicted accurately. Hence, the influence of the extraction far upstream of the bend in both flow and heat transfer distributions are not captured.

8 SUMMARY AND CONCLUSIONS

8.1 Summary of the present work

An experimental investigation of the flow and heat transfer characteristics in internal coolant passages of gas turbine airfoils have been conducted. The PIV method was employed for the flow measurements. This measurement method obtains the instantaneous velocity field of the flow in planes. From these measurements, the mean velocity field and the turbulence quantities of the flow can be calculated. The transient liquid crystal technique was adopted for the heat transfer measurements. Full surface Nusselt number distributions were obtained on all the five outer walls of the test models.

A stereoscopic PIV system was used and automated. The stereoscopic method allowed disposing on the systematic error due to out-of-plane velocity motion. It also allowed measuring the three velocity components in measurement planes. The system was capable of measuring 100 planes in each configuration. Each measurement plane was composed of 30*30 measurement points. The statistical analysis of the flow was performed from 1250 samples per measurement point.

The transient TLC technique was adapted in large-scale models of internal cooling channels. Heater grids were placed in the channel inlet to create a gas temperature change. The gas temperature evolution in location was taken into account in the data processing. The Duhamel theorem was used to resolve the gas temperature evolution in time.

The heat transfer measurement technique was validated in known heat transfer conditions. A good agreement with correlations was obtained in the region of interest. Comparison with other measurement technique results (steady state heat transfer; mass transfer) demonstrated the confidence in the present measurement results.

A test rig was designed and constructed for the experiments to meet the requirements of the intended investigation. A modular concept was chosen for the test rig design that allows for an easy exchange of the components. For the present investigation, the test section was a large scale model of a two-pass coolant passage with a sharp 180° bend. Stereoscopic PIV and TLC measurements were obtained in four different coolant passage configurations:

- A passage with 45° ribs (baseline configuration).
- A passage similar to the baseline configuration with extraction holes simulating film-cooling extraction.
- A passage with film-cooling extraction and a turning vane in the bend region.
- A passage with ribs 50% bigger than in the baseline configuration. This passage also had a turn region back wall angled at 30° to the incoming flow.

The four configurations were tested at three Reynolds numbers (25,000, 50,000, 70,000 based on the hydraulic diameter). The configurations with extraction were tested at three extractions (30%, 40%, 50% of the inlet massflow).

CFD simulations have been performed for two of the four measured passage configurations. For the calculations, the unstructured flow solver FLUENT/UNS was employed. The baseline geometry was calculated at two Reynolds numbers (25,000 and 50,000). The configuration with film cooling extraction was tested at Re=50,000 for two extractions (10%, 50%).

8.1.1 Summary of chapter 5: 2-pass coolant channel with 45° rib arrangement.

Chapter 5 presented flow and heat transfer results in a 2-pass coolant channel with 45° rib arrangement. The channel geometry and flow conditions are representative for internal coolant channels of gas turbine airfoils. Comparison with previous published results in similar channels has been given in Annex A.

The flow and heat transfer have been described in details in the fully developed flow region. This region is representative of most the internal coolant passages with inclined ribs. The flow and heat transfer have also been related in the 180° turn region, and downstream of the turn where the flow recovers from the bend effect.

Fully developed flow region

The flow was measured in details in the fully developed flow region ($16D_H$ downstream of the channel inlet = $3D_H$ upstream of the bend region). The flow in this region has been described in several literature references. The full field detailed measurements of the present work confirmed and gave details on observations made in previous works. The two counter-rotating secondary flow structure has been particularly described. The two secondary vortices in channel cross-sections were shown to be due to the interaction of the rib induced and the mainstream flows. Note that the secondary motion divides the flow along the channel into two separate regions. The flow in the two halves ($Y<0.5$ and $Y>0.5$) is constrained to remain in the same region along both straight legs.

The 45° ribs increase the heat transfer of more than a factor 2 compared to a smooth channel. Nu/Nu_0 area-averaged values are 2.1 on the ribbed walls (2.8 if the rib is taken into account), and 2.25 on the outer sidewall. However, despite the benefit from a high area-averaged heat transfer value, the heat transfer gradients are important. Nu/Nu_0 can vary of a factor 6 in less than $0.3D_H$. This can lead to thermal stresses into the blade. Note that the heat transfer on the sidewall is approximately equal to the one on the ribbed walls. This can also lead to high thermal stresses in the blade.

24 measurement planes in the fully developed flow region have been interpolated in a 3D volume from $3D_H$ to $1D_H$ upstream of the bend region. 3D-streamlines were extracted from this volume. A study of the 3D-streamlines revealed the behaviour of the recirculating cell, which develops downstream of each 45° rib. A rib-induced vortex develops downstream of each rib, flows along the rib, impinges on the outer wall near the bottom wall, flows towards the top wall along the outer wall for $Y<0.5$, and goes back towards the web along the $Y=0.5$ plane.

The complex phenomenon of the vortex and mainstream flow combination, which governs the heat transfer distribution in the straight legs of the coolant passage with inclined ribs have been connected from the combined flow and heat transfer measurements. The rib-induced vortex dominates the fully developed heat transfer distribution. The impinging velocities induced by the vortex, and more generally by the

secondary flow, are strongly linked with the regions of high heat transfer. The Chapter 5 provided results to understand how to use the secondary flow and especially the inclined rib-induced vortex.

Bend region

The flow in the bend region is more complex than in the upstream fully developed flow region. Two curvature-induced vortices are added to the secondary flow rib induced vortices. The streamwise velocity profile is also modified. The flow is accelerated towards the web tip and is directed against the outer sidewall at the bend outlet.

The flow modifications influence the heat transfer distribution. The full surface heat transfer distribution shows different characteristics than in the fully developed region. On the ribbed walls, regions of high heat transfer occur at the web tip, where the flow is accelerated. The location of the last rib in the bend has an impact on this high heat transfer region. Therefore the top and bottom wall bend regions present different heat transfer distributions.

The area-averaged Nu/Nu_0 values are higher than in the fully developed region. In the upstream part of the bend, Nu/Nu_0 is 8% and 18% higher than in the fully developed region, on the bottom and top walls, respectively. The Nu/Nu_0 values in the downstream part of the bend are approximately equal to the fully developed region values.

Downstream leg region

The flow recovers from the bend effect in the downstream leg. The high streamwise velocity region in the vicinity of the downstream outer sidewall decreases as the flow is directed in the downstream leg. $4.5D_H$ downstream of the bend region, the streamwise velocity has not reached the upstream fully developed profile. $3D_H$ downstream of the bend region, the secondary flow has almost reached the upstream leg fully developed secondary flow pattern. Note that due to the symmetrical placement of the ribs compared to the web, the secondary flow impinges on the downstream outer wall, as it impinges on the upstream web wall.

On the ribbed walls, the heat transfer also recovers from the bend effect. It takes longer to reach the fully developed Nu/Nu_0 values than to redevelop the secondary flow. It is attributed to the fact that the streamwise velocity profile governs the heat transfer level in the rib induced U-shape heat transfer region on the ribbed walls. $10D_H$ downstream of the bend region, the area heat transfer levels are still 5-10% higher than in the upstream fully developed region.

The sidewall heat transfer distribution differs from the upstream sidewall. This is due to the symmetrical rib placement in the two channel legs. The heat transfer distribution is homogeneous, with lower values than in the upstream leg. The heat transfer value is dominated by the local streamwise velocity component parallel to the walls. $10D_H$ downstream of the bend region, the heat transfer distribution on the outer sidewall is representative of the upstream web heat transfer distribution in the fully developed flow region.

Note that in every region of the channel the Nu/Nu_0 values are always higher

than 1, indicating that at every location the 45° rib arrangement better cools the channel than smooth walls. It should also be mentioned that the heat transfer distribution is mainly explainable by the strength of the impinging velocity component on the walls.

8.1.2 Summary of chapter 6: Influence of design Parameter modification.

Chapter 6 studied the influence of design parameter variations (Reynolds number, film cooling extraction, bend feature geometries) on the flow and heat transfer characteristics. Results in the four tested geometries were shown in the entire bend vicinity ($-6D_H<k<6D_H$). 3D-streamlines were extracted in the full volume from the 2D-3C PIV measurement planes. They allowed understanding the flow and the influence of design parameters in the bend region.

6.2.4.3 showed that globally there is no obvious correlation between the Nusselt values on the surface and a specific velocity component above the surface. In certain locations or flow configurations, where Nu/Nu_0 gradients are high, correlations can be found between Nusselt and velocity components. This is the case at locations where the flow impinges on the surface. In these regions, Nusselt shows a good correlation with the impinging velocity components, especially with the normal stress normal to the surface. In other regions where Nu/Nu_0 values and gradients are low, no velocity component is clearly correlated with Nusselt number.

Reynolds number variation

Varying the Reynolds number influences the heat transfer results. Nu values decrease as Re decreases, whereas Nu/Nu_0 increases. The gradients of Nu/Nu_0 in various regions of the channel are also more important as Re decreases. The full surface heat transfer results show an increase of Nu/Nu_0 values over the entire surfaces as Re decreases whereas contour shapes remain the same in all the measured zones. An exception must be made in the bend region, where some details of distribution are modified at Re=25,000. Note that the heat transfer recovery length from the bend effect in the second leg of the channel is constant for the three Reynolds numbers measured.

Film cooling extraction

- Adding bleeding holes, and having a high ratio between the channel inlet mass flow and the extracted mass flow, strongly influences the flow in the two-legged cooling channel. It modifies the flow field in the entire test section, in the region where the extraction occurs, but also far upstream in the first leg of the channel. The influence on the streamwise velocity profiles is sensitive, but the greatest influence occurs on the secondary flow motions. The secondary flow moves from its symmetrical shape, in the baseline configuration, to a strongly asymmetrical shape in the configuration-2. The streamwise symmetrical profile of the baseline configuration is unbalanced toward the wall with extraction, and the symmetry plane (Y=0.5) is displaced downward by about 20% of D_H. The secondary flow has to adapt to the streamwise conditions, and as a consequence is highly modified. All along the channel, the lower parts of the baseline secondary flow motion have almost disappeared, and the upper parts have been scaled by a factor 1.5 in the Y direction.

• The effect of extraction on the heat transfer, compared to the baseline configuration, is dependent on the channel region. In the upstream leg, the influence of extraction is hardly noticeable. In the bend region and downstream of the bend, the heat transfer is highly increased on the wall provided with extraction holes. The improvement of area-averaged values is mainly due to a heat transfer enhancement in the vicinity of the hole entrance. A slight effect occurs on the walls without extraction holes. On the sidewalls, only a slight dissymmetry of the full surface heat transfer distribution is introduced by the extraction. It is due to the dissymmetry of the flow.

Varying the extraction from 30% to 50% of the inlet massflow does not show any variation in the Nu/Nu_0 results, as long as Nu_0 is based on the channel inlet flow conditions.

• Both modifications of flow and heat transfer characteristics of the channel can be explained by the flow structure in the bend region. Vortex and low streamwise velocity cells are present in the bend corners (upstream and downstream bend corners, top-back wall corner). They modify the bend geometry "shown" by the flow. In turn the flow characteristics inside the bend but also upstream of the bend are affected.

The extraction highly modifies the bend corner cells. Thus the flow has a different structure in the bend and upstream of the bend. The bend corner cells in the configuration-2 guide the flow, which highly impacts on the bend walls. The resulting heat transfer levels on the bend bottom and back walls are increased. The global distribution shape remains approximately the same from the baseline configuration to the configuration-2. CFD calculations have to predict accurately these bend corner cells to capture details in the heat transfer distribution. Note that the Reynolds number must have also an effect on the bend corner cells, which could explain differences in the heat transfer distribution.

e/D_H

The parameter e/D_H was varied in configuration-1 (e/D_H =0.15). Keeping the same p/e ratio and increasing the e/D_H ratio increases the area-averaged heat transfer levels. This is due to the fact that the high heat transfer region behind the ribs spreads more towards the sidewalls than at e/D_H =0.1.

A difference was noted between the top and bottom walls heat transfer distributions. Top wall results are 4% higher than bottom wall results. This is due to the flow asymmetry around the Y=0.5 plane. This asymmetry was attributed to the back wall angle in the bend region, and not to the e/D_H variation.

Bend back wall angle

The configuration-1 back wall is angled at 30° to the channel web. This back wall configuration changes the bend corner recirculating and low streamwise velocity component cells. The flow is directed towards the bottom part of the back wall in the upstream part of the bend, where a high heat transfer region occurs. This region could lead to thermal stresses on the back wall. The downstream corner cell occupies a volume of approximately $0.5D_H^3$. In this region the flow is stagnant and unsteady. An addition of dust holes at that location could prevent flow stagnation and low heat transfer. Note that due to the size of the ribs ($0.15D_H$) and to the back wall angle, the ribs do not extend in the bend region. This makes the heat transfer homogeneous with less potential hot spots on the ribbed wall bend region.

Turning vane

The configuration-3 bend region is provided with a turning vane. The bottom wall is also equipped with film cooling holes as the configuration-2.

In the upstream leg the flow and heat transfer show similar characteristics to the configuration-2 flow characteristics. The influence of extraction dominates the influence of the turning vane on the upstream leg flow and heat transfer distributions.

The bend region corner cells are highly influenced by the turning vane. A recirculation cell is attached to the downstream suction side of the turning vane. This recirculating cell governs the flow distribution in the bend region. It yields a back wall *heat transfer distribution completely different from the other configurations: the* distribution is symmetrical around the Y=0.5 plane, and heat transfer gradients occur mainly in the spanwise direction.

Thermal performances

The 22 various geometry and flow configurations tested can be compared with their ability to cool a blade for low pressure-drop. The so-called thermal performances (η) have been compared for all the test cases. The results can be summarised as follows:

- An increasing Reynolds number leads to a decreasing η. A linear trend is observed.
- Configurations with extraction have better thermal performances if the global bend region ($-6D_H<k<6D_H$) is considered.
- Varying the extraction from 30% to 50% does not influence the thermal performances. Note that the friction factor (f/f_0) is dependant on the extraction variation.
- The configuration-1 (e/D_H =0.15 and back wall angled at 30°) presents thermal performances in the upstream fully developed region equal to the baseline configuration. However the configuration-1 has the worst thermal performances as the global bend region is considered. The introduction of the back wall angle is not favourable. The introduction of dust holes in the downstream bend corner could improve the configuration-1 geometry.

8.1.3 Summary of chapter 7: Numerical simulations (CFD).

CFD calculations have been performed in the internal coolant passage models. The flow simulation programme Fluent 5 was used to calculate predictions of both flow and heat transfer. The k-epsilon turbulence model was utilised, with standard wall function. The baseline configuration and the configuration-2 were run. The automated hybrid mesh generator Centaur 4.5 was used to create the channel meshes. 2.6 million and 3.2 million cell meshes were created for the baseline and the configuration-2, respectively.

The objective of chapter 7 was to show CFD capabilities and limitations in the prediction of both flow and heat transfer in internal coolant channel geometries. The CFD calculations allowed demonstrating CFD progress in internal cooling from the work of Schabacker [112].

Baseline configuration

Generally the heat transfer of the channel was reasonably predicted by CFD in the baseline configuration. The calculations show a "smoothed out" heat transfer distribution compared to the measurements. On the ribbed walls, the area-averaged values in the upstream leg are over predicted by about 5%. In the downstream leg the bottom wall values are under predicted by 20% and the top wall values are well predicted. On the sidewalls predictions are 25% off the measurements all along the channel.

The flow investigations can serve to understand how the flow predictions can influence the heat transfer predictions. Comparing the flow distribution with the measurement results, the main flow and secondary vortex structures were reasonably predicted by CFD.

- The comparison of the velocity magnitude distribution shows an acceptable agreement. Note that in Schabacker [112], CFD could not predict the secondary flow field in the bend region.
- The predicted fully developed flow shows a massflow shift to the inner web compared to the measurements, which lowers the peak velocity levels within the rest of the cross-sections. This trend follows up in the bend region.
- The predicted bend corner recirculating cells are over predicted in size. The predicted flow separation at the end of the dividing wall occurs slightly downstream of the measured separation.

As a summary, CFD predicts well the "important" effects of the channel geometry on both the flow and heat transfer. Maxima are predicted approximately at the right location. Vortices are all predicted with the right rotating direction. However "detailed" effects are not captured by CFD. There are some heat transfer effects that cannot be explained simply by the main flow distribution. Increasing the mesh size can improve the prediction of distinctive heat transfer peaks, and can reduce the "smoothed out" effect on heat transfer distributions due to CFD.

A solution could be to use other turbulence models, or to take into account the unsteadiness of the flow by time dependant simulations. A finer mesh could also be used, which would require bigger computer resources than available for the present work.

Reynolds number variation

The CFD predictions do not show any difference between both Re=25,000 and Re=50,000. The differences showed in the measurements are too small for CFD. The area-averaged results are farther from the measurements at Re=25,000 than at Re=50,000. On the bend back wall, the heat transfer differs from the measurements not only in levels, but also in shape.

These discrepancies can be partly attributed to the mesh used. The mesh is the same as at Re=50,000. Y^+ values are lower at Re=25,000 than at Re=50,000. Some regions have Y^+ values lower than the Y^+ limit of the standard wall function.

Film cooling extraction

The influence of extraction is not fully predicted by CFD. Around the extraction holes, a heat transfer increase is noticed, but it does not correspond to the

measurement results. No influence of extraction is noticed on heat transfer at distances larger than $0.5D_H$ from the extraction holes. Recirculation cells in the bend region are not predicted accurately. Hence, the influence of the extraction far upstream of the bend in both flow and heat transfer distributions are not captured.

Chapter 7 highlighted progress of CFD tools during the last four years. Results show good capabilities of prediction in the baseline configuration (Re=50,000). However once parameters are varied as Reynolds number or extraction, discrepancies become higher. Systematic calculations are still to be done in order to use CFD as a confident tool in the cooling channel design.

8.2 Conclusions

1. *Measurements*:

For the first time, the PIV and TLC techniques were employed simultaneously for a detailed investigation of the turbulent flow and heat transfer characteristics within internal coolant passages connected with 180° turns. Both measurement techniques were shown capable of obtaining measurements with high spatial resolution. Flow results were given in the full bend region volume. Heat transfer measurements were reported on all the five channel walls of the models. The measurements results indicate how to use such cooling channels in blades to overcome the external heat load.

2. *Knowledge of heat transfer and flow phenomena*:

- The comparison of measurements with well-used 1D heat transfer correlations showed a 10-15% difference. Comparison with full surface published results showed a good agreement in the heat transfer distribution. The present work results have a higher spatial resolution than previous published results.
- The area-averaged heat transfer results gave relative values of the bend heat transfer compared to the fully developed region. This gives an indication how the straight channel correlations can be used to predict the heat transfer in the bend region and downstream of the bend. Note that systematic measurements were not numerous enough so that correlations in the bend region could have been built.
- The measurements described the flow structure in the fully developed region. The two secondary counter-rotating vortex cells in 45° ribbed straight channels are due to the interaction of the rib induced vortex and mainstream flow. The flows in the two halves ($Y<0.5$ and $Y>0.5$) are constrained to remain in the same region all along both straight legs.
- The area-averaged heat transfer results undergo the effect of the 180° turn. The evolution of the results along the cooling channel is explainable by the full surface heat transfer distribution. The heat transfer is fully developed in the upstream bend region. It increases in the bend region and downstream of the bend region. This is due to the incoming flow impact at certain locations in the bend. The heat transfer distribution reaches the upstream fully

developed distribution downstream of the bend.

- The regions of high heat transfer in the channels have been linked with high impinging flow regions. High gradients of mean impinging velocity components near the walls induce high heat transfer on the wall. In these regions, the Nusselt number showed a good correlation with the Reynolds normal stress corresponding to the impinging velocity.
- The secondary flow motion dominates the heat transfer in the entire cooling channel. In the fully developed region, the rib-induced vortex governs the heat transfer distribution on the ribbed walls behind the ribs, and also on the sidewalls. In the bend region, the bend corner flow cells (with low streamwise velocity motion) deviate the bend incoming flow. They act as if the sharp bend geometry was modified. This geometry modification is very dependant on the studied configuration. The resulting heat transfer distribution is thus strongly configuration dependant.
- Thermal performances were measured in 22 various geometry and flow test cases. As the full bend region is considered ($-6D_H<k<6D_H$), the configurations with extractions have the best thermal performances at all the tested Reynolds numbers. The variation of the extraction ratio does not modify substantially the thermal performances.

3. *Contribution to validation and improvement of current CFD tools*:
   - CFD tools has benefited from the tremendous progress of computing power. 3D simulations of internal cooling configurations are now possible. CFD predictions have gained accuracy in such highly 3D flow problems. The predictions compared well with the measurements, with worst discrepancies of 25%.
   - The CFD capability improvement is mainly due to the better mesh quality that can be handled by present computers.
   - The database, which was build during this PhD work, constitutes a good benchmark for CFD predictions in non-rotating coolant channels.

8.3 Future work

- In the present study, four geometries were tested. More than a single geometrical parameter were modified from one geometry to the other (e.g. configuration-1: e/D_H + bend back wall angle). New geometries should be investigated, in which only one single geometrical parameter would be modified. The influence of this single parameter could be determined.

- Systematic measurements with numerous Reynolds numbers and extractions should be performed in the bend region. This would allow building heat transfer correlations in two-pass channels connected with 180° sharp turns.

- The exploitation of the four databases could be done by CFD. This is especially true for both configuration-1 and configuration-3, which were not calculated during the present thesis work.

- Finer CFD meshes as well as various turbulence models should be tested in order to improve the measurement – prediction comparison (According to literature, V2F turbulence model seems to be promising in such internal coolant channels).

- Engine-like geometries should be tested with the same measurement techniques used in the present work. The databases, which would be build, could help the validation of CFD codes. Indeed, CFD is more and more capable of predicting heat transfer and flow in real engine geometries. Benchmarks are thus needed.

- The flow in the internal coolant passages of turbine blades is subjected to the effects of rotation. The additional effect of the rotation-induced Coriolis forces on the flow is not well understood and should be investigated with the PIV technique. The effect of both Coriolis and buoyancy forces on the heat transfer should also be investigated.

REFERENCES

1. Acharya, S., Dutta, S., Myrum, T.A. and Baker, R.S. (1993). *Periodically developed flow and heat transfer in a ribbed duct.* Int. J. Heat Mass Transfer, 36, 8, 2069-2082.
2. Adrian, R.J. (1991). *Particle-Imaging techniques for experimental fluid mechanics.* Annual Review of Fluid Mechanics, 23, 261-304.
3. Armstrong, J. and Winstanley, D. (1988). *A review of staggered array pin fin heat transfer for turbine cooling applications.* Journal of Turbomachinery, 110, 94-103.
4. Astarita, T. and Cardone, G. (2000). *Thermofluidynamic analysis of the flow in a sharp 180° turn channel.* Experimental Thermal and Fluid Science, 20, 188-200.
5. Beitz, W. and Küttner, K.H. (1990). *Taschenbuch für Maschinenbau* (Springer-Verlag), Thesis.
6. Bendat, J.S. and Piersol, A.G. (1986). *Random data.* In: *Random data* (John Wiley & Sons, Inc.).
7. Bonhoff, B., Leusch, J. and Johnson, B.V. (1999). *Predictions of flow and heat transfer in sharp 180-deg turns of gas turbine coolant channels with and without turning vanes.* Proceedings of the 33rd National Heat Transfer Conference. Albuquerque, New Mexico, USA. August 15-17, 1999. NHTC99-299.
8. Bonhoff, B., Schabacker, J., Parneix, S., Leusch, J., Johnson, B.V. and Bölcs, A. (1998). *Experimental and numerical study of developed flow and heat transfer in coolant channels with 45 and 90 degree ribs.* Proceedings of the Turbulent heat transfer II. Manchester, UK. May 31-June 5 1998. 99-GT-123.
9. Bons, J.P. and Kerrebrock, J.L. (1999). *Complementary velocity and heat transfer measurements in a rotating cooling passage with smooth walls.* Journal of Turbomachinery, 121 October 1999, 651-662.
10. Bunker, R.S. and Metzger, D.E. (1990). *Local heat transfer in internally cooled turbine airfoil leading edge regions. Part I: Impingement cooling without film coolant extraction.* Journal of Turbomachinery, 112, 451-458.
11. Butler, R.J. and Baughn, J.W. (1996). *The effect of the thermal boundary condition on transient method heat transfer measurements on a flat plate with laminar boundary layer.* Journal of Heat Transfer, 118 November 1996, 831-837.
12. Byerley, A.R., Jones, T.V. and Ireland, P.T. (1992). *Internal cooling passage heat transfer near the entrance to a film cooling hole: Experimental and computational results.* Proceedings of the International Gas Turbine & Aeroengine Congress & Exhibition. Cologne, Germany. 1992. 92-GT-241.
13. Byerley, A.R., Jones, T.V., Ireland, P.T. and Ashton, S.A. (1988). *Detailed heat transfer measurements near and within the entrance of a film cooling hole.* Proceedings of the International Gas Turbine & Aeroengine Congress. Amsterdam, The Netherlands. June 6-8, 1988. 88-GT-155.
14. Cardone, G., Astarita, T. and Carlomagno, G.M. (1998). *Wall heat transfer in static and rotating 180° turn channels by quantitative infrared thermography.* An international Journal of Thermal Sciences, 37 N° 8, September 1998, 644-652.
15. Cardone, G., Astarita, T. and Carlomagno, G.M. (2000). *Heat transfer in a 180° turn ribbed square channel.* Proceedings of. 2000. 553.1-553.8.
16. Casarsa, L., Cakan, M. and Arts, T. (2002). *Characterization of the velocity and heat transfer fields in an internal cooling channel with high blockage ratio.* Proceedings of the Turbo Expo 2002. Amsterdam, The Netherlands. June 3-6 2002. GT-2002-30207.
17. Chandra, P.R. and Han, J.C. (1989). *Pressure drop and mass transfer in two-pass ribbed channels.* Journal of Thermophysics and Heat Transfer, 3 3, 315-320.
18. Chanteloup, D., *Brite-Euram ICTB - EPFL static rig: Flow measurement final report*, . 2001, EPFL: Lausanne.
19. Chanteloup, D., *EPFL static rig: Flow measurement final report*, . 2001, EPFL: Lausanne.
20. Chanteloup, D. and Bölcs, A. (2001). *Particle image velocimetry investigation of the flow characteristics in two-leg internal coolant passages of gas turbine airfoils.* Journal of Power and Energy, IMechE, 215 No A6, 743-752.

21. Chanteloup, D. and Bölcs, A. (2001). *PIV investigation of the flow characteristics in 2-leg internal coolant passages of gas turbine airfoils.* Proceedings of the Euroturbo, 4th European conference on turbomachinery fluid dynamics and thermodynamics. Firenze, Italy. 2001.

22. Chanteloup, D. and Bölcs, A. (2001). *PIV investigation of the flow characteristics in 2-leg internal coolant passages of gas turbine airfoils with film cooling hole ejection.* Proceedings of the International Symposium on Experimental and Computational Aerothermodynamics of Internal Flows. Gdansk, Poland. 2001.

23. Chanteloup, D. and Bölcs, A. (2002). *Experimental investigation of heat transfer in two-pass coolant passages with ribs and film cooling hole ejection.* Proceedings of the ASME-CIE-ES02. Montreal, Canada. Sept 29 - Oct 03 2002. DETC2002/CIE-34417.

24. Chanteloup, D. and Bölcs, A. (2002). *Flow characteristics in 2-leg internal coolant passages of gas turbine airfoils with film cooling hole ejection.* Journal of Turbomachinery, 124 3, 499-507.

25. Chanteloup, D. and Bölcs, A. (2002). *Flow characteristics in 2-leg ribbed internal coolant passages of gas turbine airfoils with turning vane and film cooling hole ejection.* Proceedings of the The 9th of International Symposium on Transport Phenomena and Dynamics of Rotating Machinery. Honolulu, Hawaii, USA. February 10-14 2002. HT-004.

26. Chanteloup, D., Juaneda, Y. and Bölcs, A. (2002). *Combined 3D flow and heat transfer measurements in a 2-pass internal coolant passage of gas turbine airfoils.* Proceedings of the ASME Turbo Expo 2002. Amsterdam, The Netherlands. June 03-06 2002. GT-2002-30214.

27. Cheah, S.C., Iacovides, H., Jackson, D.C., Li, H. and Launder, B.E. (1994). *LDA investigation of the flow development through rotating U-Ducts.* Proceedings of the International Gas Turbine & Aeroengine Congress & Exhibition. 1994. 94-GT-226.

28. Cho, H.H., Wu, S.J. and Kwon, H.J. (1999). *Local Heat/Mass Transfer Measurements in a Rectangular Duct with Discrete Ribs.* Proceedings of the International Gas Turbine & Aeroengine Congress & Exhibition. Indianapolis, Indiana, USA. 1999. 99-GT-121.

29. Chyu, M.K. and Natarajan. (1989). *Local heat transfer on a flat surface roughened with broken ribs.* Heat Transfer in Gas Turbine Engines, 1989, 25-31.

30. Chyu, M.K. and Wu. (1989). *Combined effects of rib angle-of-attack and pitch-to-height ratio on mass transfer from a surface with transverse ribs.* Experimental Heat Transfer, 2 1989, 291-308.

31. D'Orgeville, M., *Etude de la technique de mesure instationnaire du transfert de chaleur par cristaux liquides*, 2000, EPFL: Lausanne.

32. D'Urbano, M., *Mise au point d'un systéme de mesure de transfert de chaleur par la méthode TLC.* 2000, EPFL: Lausanne.

33. Durret, R.P., Stevenson, W.H. and Thompson, H.D. (1988). Radial and axial turbulent flow measurements with an LDV in an axisymmetric sudden expansion airflow. J. Fluids Engineering, 110 December, 367-372.

34. Ekkad, S.V. and Han, J. (1995). *Local heat transfer distributions near a sharp 180° turn of a two-pass smooth square channel using a transient liquid crystal image technique.* Journal of Flow Visualisation and Image Processing, 2 1995, 285-297.

35. Ekkad, S.V. and Han, J.C. (1995). *Local heat transfer distributions near a sharp 180° turn of a two-pass smooth square channel using a transient liquid crystal image technique.* Journal of Flow Visualisation and Image Processing, 2, 285-297.

36. Ekkad, S.V. and Han, J.C. (1997). *Detailed heat transfer distributions in two-pass square channels with rib turbulators.* International journal of heat and mass transfer, 40 11, 2525-2537.

37. Ekkad, S.V., Yizhe Huang and Han, J.C. (1998). *Detailed heat transfer distributions in two-pass square channels with rib turbulators and bleed holes.* International journal of heat and mass transfer, 41 23, 3781-3791.

38. Elfert, M. and Jarius, M.P. (2002). *Steady fluid flow investigation using L2F and PIV in a multi-pass coolant channel.* Proceedings of the 9thsymposium on transport phenomena and dynamics of rotating machinery. Honolulu, Hawaii, USA. February 10-14, 2002 2002. HT-ABS-033.

39. Faramarzi, J. and Logan, E. (1991). *Reattachment length behind a single roughness element in turbulent pipe flow.* Journal of Fluids Engineering, 113 December 1991, 712-714.

40. Florschuetz, L.W., Berry, R.A. and Metzger, D.E. (1981). *Streamwise flow and heat transfer distributions for jet array impingement with crossflow.* Journal of Heat Transfer, 103, 337-342.

41. Frost, W. and Moulden, T.H. (1977). *Handbook of turbulence* (Plenum Press).

42. Gao, X. and Sundén, B. (2001). *Heat transfer and pressure drop measurements in rib-roughened rectangular ducts.* Experimental Thermal and Fluid Science, 24 2001, 25-34.

43. Gauthier and Riethmuller (1988). *Application of PIDV to complex flows: Measurement of the third velocity component.* In: *Particle image displacement velocimetry* (VKI), Vol. LS 1988-06.

44. Gee, L.D. and Webb, R.L. (1979). *Forced Convection Heat Transfer in Helically Rib-roughened Tubes.* Journal of Heat and Mass Transfer, 23, 1980, 1127-1136.

45. Gillepsie, D.R.H., Byerley, A.R., Ireland, P.T., Wang, Z., Jones, T.V. and Kohler, S.T. (1996). *Detailed measurements of local heat transfer coefficient in the entrance to normal and inclined film cooling holes.* Journal of Turbomachinery, 118 April 1996, 285-290.

46. Goldstein, R.J. and Cho, H.H. (1995). *A review of mass transfer measurements using naphtalene sublimation.* In: *Experimental thermal and fluid science* (Elsevier Science Inc), Vol. 10, 416-434.

47. Haasenritter, A., Amro, M. and Weigand, B. (2002). *An experimental and numerical study of the heat transfer performance of sharp-edged and rounded ribs in square ducts.* Proceedings of the The 9th International Symposium on Transport Phenomena and Dynamics of Rotating Machinery. Honolulu, Hawaii, USA. February 10-14, 2002 . HT-003.

48. Haasenritter, A. and Weigand, B. (2001). *Heat Transfer in Triangular Rib-Roughened Channels.* Proceedings of the National Heat Transfer Conference. Anaheim, California, USA. June 10-12, 2001 2001. NHTC2001-20245.

49. Han, J.C. (1983). *Heat transfer and friction in channels with two opposite rib-roughened walls.* Journal of Heat Transfer, 106 1984, 774-781.

50. Han, J.C. (1988). *Heat transfer and friction characteristics in rectangular channels with rib turbulators.* Journal of Heat Transfer, 110 1988, 321-328.

51. Han, J.C. and Chandra, P.R., *Local Heat/Mass Transfer and Pressure Drop in a Two-Pass Rib-Roughened Channel for Turbine Airfoil Cooling.* 1987, Lewis Research Center NASA.

52. Han, J.C. and Dutta, S. (2000). *Recent Developments in Turbine Blade Internal Cooling.* Proceedings of the Turbine-2000: International Symposium on Heat Transfert in Gas Turbine Systems. Cesme, Izmir, Turkey. August, 13-18, 2000 2000. Annals of the New York Academy of sciences, 934, 162-178.

53. Han, J.C., Dutta, S. and Ekkad, S. (2000). *Gas turbine heat transfer and cooling technology* (Taylor & Francis).

54. Han, J.C., Glicksman and Rohsenow. (1978). *An investigation of heat transfer and friction for rib roughened surfaces.* Journal of Heat and Mass Transfer, 1 1978, 1143-1156.

55. Han, J.C., Ou, Park, J.S. and Lei. (1989). *Augmented heat transfer in rectangular channels of narrow aspect ratios with rib turbulators.* Journal of Heat and Mass Transfer, 32 N09, 1989, 1619-1630.

56. Han, J.C. and Park, J.S. (1988). *Developing heat transfer in rectangular channels with rib turbulators.* Journal of Heat and Mass Transfer, 31 1988, 183-195.

57. Han, J.C., Park, J.S. and Lei. (1985). *Heat transfer enhancement in channels with turbulence promoters.* Journal of Engineering for Gas and Turbine power, 107 1985, 628-635.

58. Han, J.C., Park, J.S. and Lei, C.K. (1985). *Heat transfer enhancement in channels with turbulence promoters.* Journal of Engineering for Gas and Turbine power, 107 1985, 628-635.

59. Han, J.C. and Zhang, P. (1991). *Effects of Rib-Angle Orientation on Local Mass Transfer Distribution in a Three-Pass Rib-Roughened Channel.* Journal of Turbomachinery, 113 January 1991, 123-130.

60. Han, J.C. and Zhang, P. (1992). *High performance heat transfer ducts with parallel broken and V-shaped broken ribs.* Journal of Heat and Mass Transfer, 35 1992, 513-523.

61. Han, J.C., Zhang, P. and Lee. (1991). *Augmented heat transfer in square channels with parallel, crossed, and V-shaped angled ribs.* Journal of Heat, 113 January 1991, 590-596.

62. Hennecke, K. *Heat transfer problems in aero-engines.* In: *Heat and mass transfer in rotating machinery* (Springer-Verlag), 353-379. Heidelberg.

63. Hermanson, K., Parneix, S., Von Wolfersdorf, J. and Semmler, K. (2000). *Prediction of Pressure Loss and Heat Transfer in Internal Cooling Passages.* Proceedings of the Turbine-2000: International Symposium on Heat Transfer in Gas Turbine Systems. Cesme, Izmir, Turkey. August 13-18, 2000 . 934, 448-455.

64. Hinze, J.O. (1975). *Turbulence* (New-York, McGraw-Hill),

65. Hirota, M., Fujita, H., Syuhada, A., Araki, S., Yoshida, T. and Tanaka, T. (1999). *Heat/mass transfer characteristics in two-pass smooth channels with a sharp 180-deg turn.* International Journal of Heat and Mass Transfer, 42 20, 3757-3770.

66. Höcker, R. (1996). *Optimization of transient heat transfer measurements using thermochromic liquid crystals based on an error estimation.* Proceedings of the International Gas Turbine & Aeroengine Congress & Exhibition. Birmingham, UK. 1996. 96-GT-235.

67. Hong, Y. and Hsieh, S. (1991). *An Experimental Investigation of Heat Transfer Characteristics for Turbulent Flow over Staggered Ribs in a Square Duct.* Experimental Thermal and Fluid Science, 4 1991, 714-722.

68. Hsieh and Hong. (1987). *Separation flow over repeated surface-mounted ribs in a square duct.* AIAA Journal, 27, No6 1987, 770-776.

69. Hsieh, S.S. and Hong, Y.J. (1987). *Separation flow over repeated surface-mounted ribs in a square duct.* AIAA Journal, 27, No6 1987, 770-776.

70. Huang, Y., Ekkad, S.V. and Han, J.C. (1998). *Detailed heat transfer distributions under an array of orthogonal impinging jets.* Journal of Thermophysics and heat transfer, 12 1, 73-79.

71. Humphrey, J.A.C., Whitelaw, J.H. and Yee, G. (1981). *Turbulent flow in a square duct with strong curvature.* Journal of Fluid Mechanics, 103, 443-463.

72. Iacovides, H., Jackson, D.C., Kelemenis, G. and Launder, B.E. (1999). *The Measurement of Local Wall Heat Transfer in Stationary U-Ducts of Strong Curvature, with Smooth and Rib Roughened Walls.* Proceedings of the International Gas Turbine & Aeroengine Congress & Exhibition. Indianapolis, Indiana, USA. 1999. 99-GT-254.

73. Iacovides, H. and Launder, B.E. (1995). *Computational fluid dynamics applied to internal gas-turbine cooling: A review.* Inter. J. Heat and Fluid Flow, 16, 454-470.

74. Johnson, R.W. and Launder, B.E. (1985). *Local heat transfer behaviour in turbulent flow around a 180 deg bend of square cross section.* Proceedings of the International Gas Turbine & Aeroengine Congress & Exhibition. 1985. 85-GT-68.

75. Juaneda, Y., *Etude du transfert de chaleur dans un canal d'aube de turbine à gaz.* 2001, EPFL: Lausanne.

76. Kays, W.M. and Crawford, M.E. (1993). *Convective Heat and Mass Transfer* (McGraw Hill),

77. Kukreja, R.T. and Lau, S.C. (1998). *Distributions of local heat transfer coefficient on surfaces with solid and perforated ribs.* Enhanced heat transfer, 5, 9-21.

78. Kukreja, R.T., Lau, S.C. and Mc Millin, R.D. (1993). *Local heat/mass transfer distribution in a square channel with full and V-shaped ribs.* Journal of Heat and Mass Transfer, 36, 2013-2020.

79. Kumaran, T.K., Han, J.C. and Lau, S.C. (1991). *Augmented heat transfer in a pin fin channel with short or long ejection holes.* International Journal of Heat and Mass Transfer, 35 10, oct 1991, 2617-2628.

80. Lakshminarayana, B. (1996). *Fluid Dynamics and Heat Transfer of Turbomachinery* (John Wiley & Sons, Inc), Thesis.

81. Lau, S.C., Kukreja, R.T. and McMillin, R.D. (1992). *Turbulent heat transfer in a square channel with staggered discrete ribs.* Journal of Thermophysics and Heat Transfer, 6, 1, 171-173.

82. Lau, S.C., McMillin, R.D. and Han, J.C. (1989). *Turbulent heat transfer and friction in a square channel with discrete rib turbulators.* Heat Transfer in Gas Turbine Engines, 1989, 33-41.

83. Lau, S.C., McMillin, R.D. and Han, J.C. (1991). *Heat transfer characteristics of turbulent flow in a square channel with angeled discrete ribs.* Journal of Turbomachinery, 113 3, 367-374.

84. Lau, S.C., McMillin, R.D. and Kukreja, R.T. (1991). *Effects of V-shaped rib arrays on turbulent heat transfer and friction of fully developed flow in a square channel.* Journal of Heat and Mass Transfer, 34 1991, 1605-1615.

85. Lau, S.C., McMillin, R.D. and Kukreja, R.T. (1992). *Segmental heat transfer in a pin fin channel with ejection holes.* International Journal of Heat and Mass Transfer, 35 6, Jun 1992, 1407-1417.

86. Launder, B.E. (1988). *On the computation of convective heat transfer in complex flows.* Journal of Heat Transfer, 10, 1112-1128.

87. Liou, T.M., Chang, Y. and Hwang, D.W. (1990). *Experimental and computational study of turbulent flows in a channel with two pairs of turbulence promoters in tandem.* Journal of Fluids Engineering, 112 1990, 302-310.

88. Liou, T.M. and Chen, C.C. (1997). *LDV study of developing flows through a smooth duct with a 180deg straight-corner turn.* Proceedings of the International Gas Turbine & Aeroengine Congress & Exhibition. 1997. 97-GT-283.

89. Liou, T.M., Chen, C.C. and Tsai, T.W. (1999). *Heat transfer and fluid flow in a square duct with 12 different shaped vortex generators.* Proceedings of the International Gas Turbine & Aeroengine Congress & Exhibition. Indianapolis, Indiana, USA. 1999. 99-GT-255.

90. Liou, T.M. and Hwang, D.W. (1993). *Effect of ridge shapes on turbulent heat transfer and friction in a rectangular channel.* Int. J. Heat Mass Transfer, 36 4, 931-940.

91. Liou, T.M. and Kao, C.F. (1988). *Symmetric and asymmetric turbulent flows in a rectangular duct with a pair of ribs.* Journal of Fluids Engineering, 110 1988, 373-379.

92. Liou, T.M., Tzeng, Y.Y. and Chen, C.C. (1998). *Fluid flow in a 180deg sharp turning duct with different divider thicknesses.* Proceedings of the International Gas Turbine & Aeroengine Congress & Exhibition. 1998. 98-GT-189.

93. Liou, T.M., Tzeng, Y.Y. and Chen, C.C. (1999). *Fluid flow in a 180 deg sharp turning duct with different divider thicknesses.* Journal of Turbomachinery, 121 July 1999, 569-576.

94. Liou, T.-M., Chang and Hwang. (1990). *Experimental and computational study of turbulent flows in a channel with two pairs of turbulence promoters in tandem.* Journal of Fluids Engineering, 112 1990, 302-310.

95. Liou, T.-M. and Kao. (1988). *Symmetric and asymmetric turbulent flows in a rectangular duct with a pair of ribs.* Journal of Fluids Engineering, 110, 1988, 373-379.

96. Lourenco, L.M. (1988). *Some Comments on Particle Image Displacement Velocimetry.* In: *Lecture Series* (Von Karman Institute for Fluid Dynamics), Vol. 06.

97. Martin, H. (1977). *Heat and mass transfer between impinging gas jets and solid surfaces.* In: *Advances in heat transfer* (Academic Press, New York), Vol. 13.

98. Metzger, D.E., Florschuetz, L.W., Takeushi, D.I., Behee, R.D. and Berry, R.A. (1979). *Heat transfer characteristics for inline and staggered arrays of circular jets with crossflow of spent air.* Journal of Heat Transfer, 101, 526-531.

99. Metzger, D.E. and Sahm, M.K. (1986). *Heat transfer around sharp 180° turns in smooth rectangular channels.* Journal of Heat Transfer, 108, 500-506.

100. Mochizuki, S., Murata, A. and Fukunaga, M. (1997). *Effects of rib arrangements on pressure drop and heat transfer in a rib-roughened channel with a sharp 180 deg turn.* Journal of Turbomachinery, 119 3, 610-616.

101. Moon, H.K., O'Connel, T. and Glezer, B. (1999). *Channel height affect on heat transfer and fristion in a dimpled passage.* Proceedings of the International Gas Turbine & Aeroengine Congress & Exhibition. Indianapolis, Indiana, USA. 1999. 99-GT-163.

102. Park, J.S., Han, J.C., Huang, Y. and Ou, S. (1992). *Heat transfer performance comparisons of five different rectangular channels with parallel angled ribs.* International Journal of Heat and Mass Transfer, 35 11, 2891-2903.

103. Parneix, S., Behnia, M. and Durbin, P.A. (1999). *Predictions of turbulent heat transfer in an axisymmetric jet impinging on a heated pedestal.* Journal of Heat Transfer, 121, 43-49.

104. Plevich (1984). *Pressure losses and flow visualisation in rectangular duct 180deg turns* (Arizona State University), MS Thesis.

105. Prakash, C. and Zerkle, R. (1992). *Prediction of turbulent flow and heat transfer in a radial rotating square duct.* Journal of Turbomachinery, 114, 835-846.

106. Prasad, A.K. and Adrian, R.J. (1993). *Stereoscopic Particle Image Velocimetry Applied to Liquid Flows.* Experiments in Fluids, 15, 49-60.

107. Raffel, M., Willert, C.E. and Kompenhans, J. (1997). *Particle Image Velocimetry. A practical guide* (Springer), ISBN 3-540-63683-8.

108. Rathjen, L. (2003). *Experimentelle wärme-/stoffübergangsuntersuchungen an einem rotierenden kühlkanalmodell mit rippen.* In: *PhD Thesis* (TU Darmstadt).

109. Rathjen, L., Sivade, C., Henneke, D.K. and Semmler, K. (2002). *Detailed experimental and numerical heat/mass transfer investigations in a rotating two-pass coolant channel with staggered 45deg ribs.* Proceedings of the The 9th of International Symposium on Transport Phenomena and Dynamics of Rotating Machinery. Honolulu, Hawaii, USA. February 10-14 2002. HT-034.

110. Rau, G. (1998). *Einfluss der Rippenanordnung auf das Strömungsfeld und den Wärmeübergang in einem Kühlkanal mit quadratischem Querschnitt.* In: *PHD Thesis* (Technischen Universität Darmstadt), Vol. D17.

111. Rau, G., Cakan, M., Moeller, D. and Arts, T. (1998). *The effect of periodic ribs on the local aerodynamic and heat transfer performance of a straight cooling channel.* Journal of Turbomachinery, 120 2, 368-375.

112. Schabacker, J. (1998). *PIV investigation of the flow characteristics in an internal coolant passages of gas turbine airfoils with two ducts connected by a sharp 180° bend.* In: *PHD Thesis* (Ecole Polytechnique fédérale de Lausanne), Vol. n°1816.

113. Schabacker, J. and Bölcs, A. (1996). *Investigation of Turbulent Flow by means of the PIV Method.* Proceedings of the 13th Symposium on Measuring Techniques for Transonic and Supersonic Flows in Cascades and Turbomachines. Zurich, Switzerland. September, 5-6 1996.

114. Schabacker, J., Bölcs, A. and Johnson, B.V. (1998). *PIV investigation of the flow characteristics in an internal coolant passage with two ducts connected by a sharp 180° bend.* Proceedings of the International Gas Turbine & Aeroengine Congress & Exhibition. Stockholm, Sweden. June, 2-5 1998. 98-GT-544.

115. Schabacker, J., Bölcs, A. and Johnson, B.V. (1999). *PIV investigation of the flow characteristics in an internal coolant passage with 45° rib arrangement.* Proceedings of the International Gas Turbine & Aeroengine Congress & Exhibition. Indianapolis, Indiana, USA. June, 7-10 1999. 99-GT-120.

116. Schnieder, M., Höcker, R. and von Wolfersdorf, J. (2001). *Heat transfert and pressure loss in a 180°-turn of a rectangular, rib roughened two passage channel.* Proceedings of the ExHFT-5: 5th world conference on experimental heat transfert, fluid mechanics and thermodynamics. Thessaloniki, Greece. September 24-28, 2001.

117. Shen, J.R., Wang, Z., Ireland, P.T. and Jones, T.V. (1996). *Heat transfer enhancement within a turbine blade cooling passage using ribs and combinations of ribs with film cooling holes.* Journal of Turbomachinery, 118 July 1996, 428-434.

118. Takeishi, K.-I. and Aoki, S. (2000). *Contribution of Heat Transfer to Turbine Blades and Vanes for High Temperature Industrial Gas Turbines. Part2: heat Transfer on Serpentine Flow Passage.* Proceedings of the Turbine-2000: International Symposium on Heat Transfer in Gas Turbine Systems. Cesme, Izmir, Turkey. August 13-18, 2000. 934, 473-480.

119. Taslim, M.E., Li, T. and Spring, S.D. (1995). *Experimental study of the effects of bleed holes on heat transfer and pressure drop in trapezoidal passages with tapered turbulators.* Journal of Turbomachinery, 117 2, April 1995, 281-289.

120. Taslim, M.E. and Wadsworth, C.M. (1994). *An experimental investigation of the rib surface-averaged heat transfert coefficient in a rib-roughened square passage.* Proceedings of the International Gas Turbine & Aeroengine Congress & Exposition. The Hague, Netherlands. 13-16, June 1994 1994. 94-GT-162.

121. Taslim, M.E. and Wadworth, C.M. (1994). *An experimental investigation of the rib surface-averaged heat transfer coefficient in a rib-roughened square passage.* Proceedings of the International Gas Turbine & Aeroengine Congress & Exhibition. The Hague, The Netherlands. June 13-16, 1994 1994. 94-GT-162.

122. Terekhov, V.I., Kalinina, S.V. and Mskvidobadze, Y.M. (1997). *Heat transfer coefficient and aerodynamics resistance on a surface with a single dimple.* J. of Enhanced Heat Transfer, 4 , 131-145.

123. Thurman, D. and Poinsatte, P. (2001). *Experimental heat transfer and bulk air temperature measurements for a multipass internal cooling model with ribs and bleed.* Journal of Turbomachinery, 123 January 2001, 90-96.

124. Tse, D.G.N. and Steuber, G.D. (1997). *Flow in rotating square serpentine coolant passage with skewed trips.* Proceedings of the International Gas Turbine & Aeroengine Congress & Exhibition. 1997. 97-GT-529.

125. Vogel, G. and Weigand, B. (2001). *A new evaluation method for transient liquid crystal experiments.* Proceedings of the National Heat Transfer Conference. Anaheim, California, USA. June, 10-12 2001. NHTC01-1511.

126. Vogel, J.C. and Eaton, J.K. (1985). *Combined heat transfer and fluid dynamic measurements downstream of a backward-facing step.* J. Heat Transfer, 107, 922-929.

127. Wang, Z. (1991). *The application of thermochromic liquid crystals to detailed turbine blade cooling measurements.* In: *Thesis* (Department of Engineering Science, Oxford).

128. Wang, Z., Gillepsie, D.R.H. and Ireland, P.T. (1996). *Advances in heat transfer measurements using liquid crystals.* In: *Turbulent Heat Transfer* (Engineering Foundation), 1-25. San Diego.

129. Wang, Z., Ireland, P.T., Kohler, S.T. and Chew, J.W. (1996). *Heat transfer measurements to a gas turbine cooling passage with inclined ribs.* Proceedings of the International Gas Turbine & Aeroengine Congress & Exhibition. Birmingham, UK. June, 10-13, 1996 1996. 96-GT-542.

130. Webb. (1970). *heat transfer and friction losses in tubes with repeated-rib roughness.* Journal of Heat and Mass Transfer, 14 1970, 601-617.

131. Webb, R.L., Eckert, E.R.G. and Goldstein, R.J. (1970). *Heat transfer and friction losses in tubes with repeated-rib roughness.* Journal of Heat and Mass Transfer, 14 1970, 601-617.

132. Weigand, B., Semmler, K. and Von Wolfersdorf, J. (2000). *Heat Transfert Technology for Internal Passages of Air-Cooled Blades for Heavy-Duty Gas turbines.* Proceedings of the Turbine-2000: International Symposium on Heat Transfert in Gas Turbine Systems. Cesme, Izmir, Turkey. August, 13-18, 2000 2000. Annals of the New York Academy of sciences, 934, 179-193.

133. Weigand, B., Von Wolfersdorf, J. and Neumann, S.O. (2001). *Internal cooling for industrial gas turbines: Present state and novel approaches.* Proceedings of the 5th ISAIF. Gdansk, Poland. September, 4-7, 2001 2001. IFFM publishers, 1, 67-75.

134. Westerweel, J. and Nieuwstadt, F.T. (1991). *Performance Tests on 3-Dimensional Velocity Measurements with a Two-Camera Digital Particle-Image-Velocimeter.* In: *Laser Anemometry* (ASME 1991), Vol. 1, 349-355.

135. Zhang, Y.M., Gu, W.Z. and Han, J.C. (1994). *Heat transfer and friction in rectangular channels with ribbed or ribbed-grooved walls.* Journal of Heat Transfer, 116 1, 58-65.

APPENDIX

A Comparison with published results

A study has been performed to compare the present results with published investigations. Such comparison study yields three main results. First it assesses the quality of the present results, as well as their measurement uncertainties. Second it stresses the great influence that internal cooling system parameters can have on heat transfer and pressure drop measurements. Finally it gives an idea of the various results on cooling channel fully developed flow region, which can be found in literature. Following are the summary and conclusions of the comparison study.

A.1 Pressure distribution

A.1.1 Correlations

Table 9 shows a comparison between the present channel friction factor and a correlation for 45° rib-arrangements presented in Han and Park [56] (Han). The correlation was extrapolated beyond Han's test range ($0.047 < e/D_H < 0.078$). The result from the present study is an average of measurements in the fully developed section of the first leg. The Han correlation is 30% lower than the present results. Measurements and numerical simulations of Haasenritter et al. [47] showed a friction factor approximately equal to that measured in the present study. The differences with the Han and Park [56] correlation are thought to be due to geometrical differences between the test channels, especially the rib height and blockage ratio.

Re=50,000	Present results	Han and Park [56]	Haasenritter et al. [47]
f	0.066	0.047	0.064

Table 9: Fully developed friction factor compared to Han and Park [56] correlation.

A.1.2 Mass transfer analogy

Rathjen [108] performed pressure measurements in a similar channel to the baseline configuration. The hydraulic diameter was fixed to 30mm. The Reynolds number was set to 50,000. The pressure drop was measured between locations $3.3D_H$ upstream of the ribbed region and $4.2D_H$ downstream of the ribbed region. $14D_H$ were ribbed in both the upstream and downstream legs. Note that even though the number of rib modules is not equal to the present baseline configuration, the pressure drop of the entire channels should be similar, since the major part of the pressure drop is due to the bend region (see 5.2.2).

The ratio $\Delta P / \frac{1}{2}\rho V^2$ is compared between Rathjen [108] measurements and the

present baseline configuration. The ratios are 11.8 and 12.1 in the baseline configuration and Rathjen [108]'s configuration, respectively. The 2.5% difference states that measurements are comparable, giving an increased confidence in the present pressure measurements.

A.2 Heat transfer

A.2.1 Correlations

Re=50,000	Present Results	Han and Park [56]
Str	0.0091	0.0085
Sts outer	0.0073	0.0067
Sts web	0.0054	0.0067

Table 10: Fully developed area-averaged Stanton numbers compared to Han and Park [56] correlation.

Comparisons with heat transfer published correlations were carried out. A representative example of these comparisons is given in Table 10. Table 10 gives values of area-average Stanton number in the fully developed region of the baseline configuration, at $Re = 50000$. Measurements were normalised by the projected area to compare with the correlations. *Str, Sts outer* and *Sts web* represent the area-averaged Stanton numbers for the ribbed wall, outer and web walls respectively. Heat transfer results and correlations are in good agreement, taking into account the measurement and correlation uncertainties (±8% and ±10% respectively), and the blockage ratio differences between Han and Park [56] and the test geometries. Note that Han and Park [56] smooth wall values were obtained from the mean value of both smooth walls.

Figure 89 provides a comparison between the baseline fully developed heat transfer measurements and a few correlations in literature. Stanton numbers are plotted, since it is the most common variable correlated in literature. Table 11 gives the relationship between the figure legends and the correlation references.

Han [49] and Han and Park [56] correlated their measurements using a momentum transfer analogy. They both used, two parallel, infinite plates, and channels with two ribbed walls and two smooth walls. Han and Chandra [51] gave two correlations directly constructed from measurements. Geometrical and flow ranges, which were used to build these four correlations, were extended to allow a comparison with the present study.

Measurements are well consistent with the correlations, especially if one takes into account the accuracy of the correlations (±10%). Correlations from Webb et al. [131] and Gee and Webb [44] deviate further from the majority of the results. This is thought to be due to the large geometrical differences between the channels used for the experiments: Webb et al. [131] measured the heat transfer in a cylindrical tube with roughness ($0.01 < e/D_H < 0.04$) inclined at 90° and Gee and Webb [44] measured the heat transfer in cylindrical tubes with helical roughness ($0.01 < e/D_H < 0.102$).

Reference	Figure legend
Han and Park [56]	Han 1
Han and Chandra [51]	Han 2
Han and Chandra [51]	Han 3
Han [49]	Han 4
Gee and Webb [44]	Webb
Webb et al. [131]	

Table 11: Legend explanation of Figure 89.

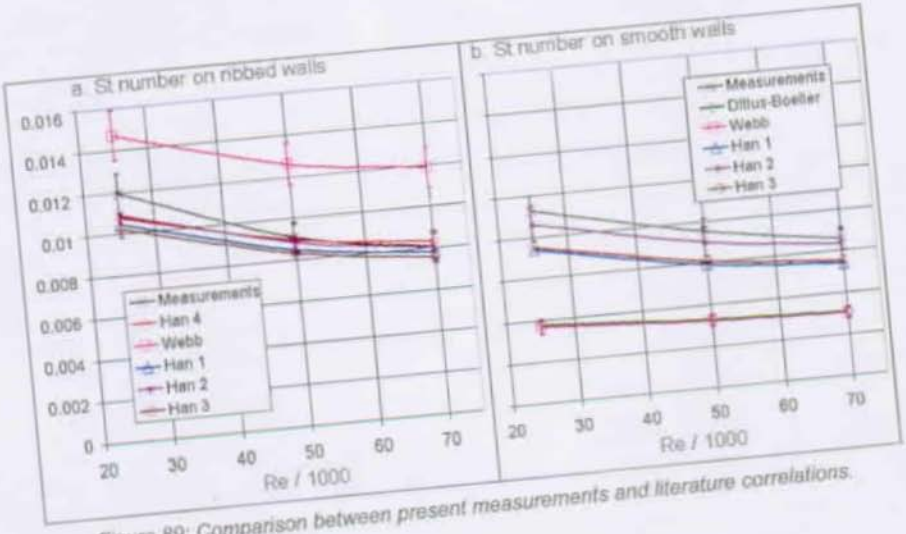

Figure 89: Comparison between present measurements and literature correlations.

A.2.2 *Mass transfer analogy*

Rathjen [108] performed mass transfer measurements in a geometry similar to the baseline configuration. All the dimensionless geometrical parameters were the same as in the baseline configuration. The hydraulic diameter was fixed to 30mm. The Reynolds number was set to 50,000. The only difference was the channel length shortened to $14D_H$ due to space limitation in the test rig.

The measurement technique was the naphthalene sublimation technique. This method allows determining the mass transfer coefficient. The technique has been described in Goldstein and Cho [46].

The heat and mass transfer analogy analogy can be applied and leads to heat transfer results. This technique is based on the assumption of constant property flow, which allows decoupling the continuity and momentum equations. In turbulent flows, it is necessary to compare the Sherwood numbers with Nusselt numbers as ratios to references, in order to reach sufficient accuracy. Therefore Sh/Sh_0 and Nu/Nu_0 are

compared where Sh, Sh_0 are defined as follow:

$$Sh = \frac{h_m D_H}{D} \qquad \text{with } h_m \text{ the mass transfer coefficient} \qquad (10.1)$$

$$Sh_0 = 0.023 \mathrm{Re}^{0.8} Sc^{0.4} \qquad \text{Dittus-Boelter value for smooth channels} \qquad (10.2)$$

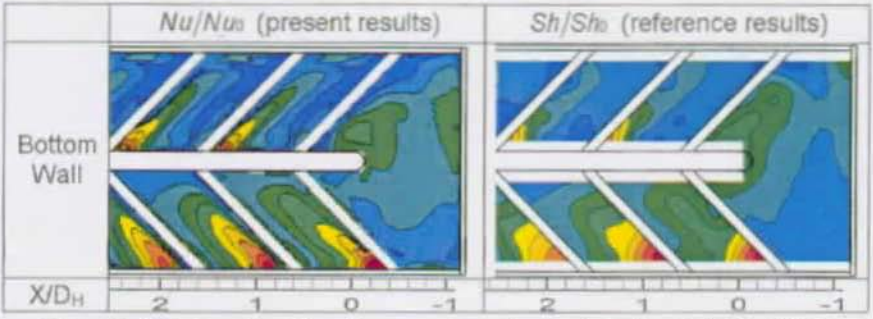

Figure 90: Bottom wall heat transfer comparison of present results with Rathjen [108].

Figure 90 shows the heat and mass transfer distributions on the bottom walls of the baseline configuration (Figure 90a) and of Rathjen [108] (Figure 90b). Reynolds number was set to 50,000.

Heat and mass transfer distribution global trends are similar in the two graphs. The high coefficient regions are located approximately at the same place. The impact of the bend modifies the heat transfer in the bend region and downstream of the bend in the same manner. Note that a lattice is necessary to maintain the copper ribs in the test model during the mass transfer tests. Thus no measurements are available on the ribbed walls in the vicinity of the web ($0.1D_H$) and of the outer sidewalls ($0.1D_H$).

The differences between the two measurement results are mainly discrepancies in distribution details. The differences can be explained as follows: The mass transfer measurement spatial resolution is lower than the heat transfer spatial resolution ($69.5 meas.\ points/D_H^2$ against $2500 meas.\ points/D_H^2$). Thus details are not captured by the mass transfer measurement technique. Another explanation can be the flow field, which can be different between the test models. Indeed, on the one hand the present baseline configuration channel length is longer than the mass transfer model. On the other hand, the channel geometry is modifying during the mass transfer test. The naphthalene layer decreases of a maximum of 6% of the rib height between the beginning and the end of a test.

In the bend region, the discrepancies between the two measurement techniques cannot be explained only by the spatial resolution differences. The slight differences that might occur between both bend geometries can have some effect on the flow, in turn on the heat transfer distribution. Another parameter, which is different from one measurement technique to the other, is the thermal boundary conditions. The mass transfer measurements are conducted at constant temperature, whereas T_{gas} and T_{wall}

evolve in the transient TLC technique.

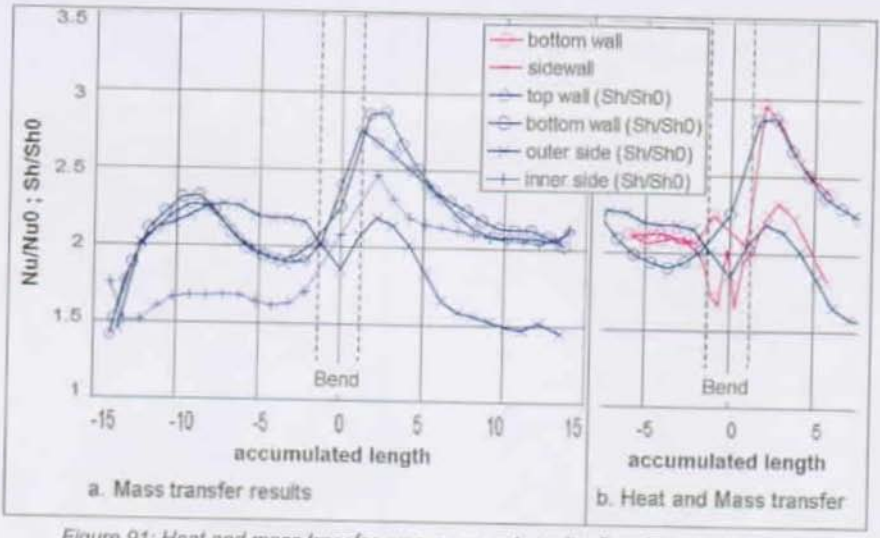

Figure 91: Heat and mass transfer area-averaged results: Baseline configuration.

Figure 91 shows a comparison between area-averaged heat and mass transfer measurements performed in the baseline configuration at Re=50,000.

Figure 91a gives Sh/Sh_0 evolution along the channel on all walls, including the web walls. On the ribbed walls, the mass transfer undergoes the flow development effect up to $8-10D_H$, and then reaches a plateau value. This is in agreement with the flow results of Schabacker [112], which showed that the mean velocities take $8D_H$ to reach fully developed characteristics. The bend affects the mass transfer distribution, with an increase in the bend itself, and a decrease downstream of the bend. The smooth sidewalls show the same effects, with a noticeable symmetrical shape upstream and downstream of the bend, between the outer sidewall and the web. Note that the outer sidewall downstream value and the web upstream values are equal, which confirms the statement made in 5.1.3.2.

Figure 91b shows a comparison between mass transfer and present heat transfer results. The differences that were noticed in Figure 90 are also present in the area-averaged results.

In the upstream leg, heat and mass transfer results are different. On the ribbed walls, the heat transfer coefficient is higher of 10% than the mass transfer coefficient. The mass transfer plot does not reach a plateau value upstream of the bend region. This could be explained by the shorter channel, which does not allow the flow to reach fully developed conditions. On the sidewalls, both measurement techniques give results closer to each other.

In the bend region, results are different from one measurement technique to the other. This both due to the zone definition for the area averaging, and to the full surface heat transfer distribution noticed in Figure 90.

In the downstream leg, bottom wall values are equal, and the sidewall values are 10% different. Note that the bend region in the mass transfer measurements is not separated into two parts in the bend region as it is in the heat transfer measurements.

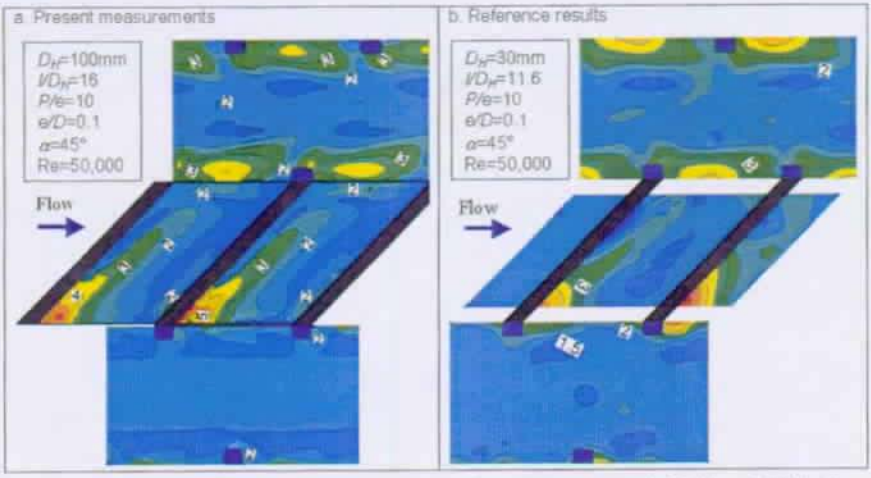

Figure 92: Full surface heat transfer comparison of present results with Rathjen [108] (bottom wall and sidewalls).

Figure 92 shows a comparison of full surface heat transfer results, between the present baseline configuration results (Figure 92a) and results from Rathjen [108] (Figure 92b). The present results were already described in Figure 34. The downstream sidewall is also plotted in Figure 92a, representing the web heat transfer results for reasons explained in 5.1.3.2. Rathjen [108] results are extracted from the upstream leg at l/D_H=11.6. Note that the mass transfer results presented in Figure 92b have a resolution twice higher than in Figure 90 and Figure 91 (139*meas. points*/D_H^2).

The heat and mass transfer distributions are similar in the rib module. The heat transfer shape is the same downstream of the upstream rib. Some differences occur in the detailed distribution. No coefficient increase is visible near the outer sidewall. This is due to the fact that no mass transfer measurements are available in that area. The difference in heat transfer maxima just downstream of the ribs (3 for mass transfer, 4 for TLC) can be explained by the different thermal boundary conditions in both experiments (constant T for mass transfer, increasing T_{gas} and T_{wall} for transient heat transfer). Other differences can come from the lower resolution of the mass transfer results especially in the vicinity of the rib walls. The measurement uncertainties of both measurement techniques can also yield differences.

On the sidewalls, the distributions are more similar than on the ribbed wall. On the outer sidewall the gradients and the levels are quite identical. On the inner sidewall, measurement problems seemed to influence the results, but the global value is of the same order as the heat transfer value.

The conclusions from part A.2.2 can be drawn as follows. The mass transfer

measurement technique applied in a similar geometry as the baseline configuration, gives similar results to the present heat transfer results. Differences in the detailed coefficient distributions seem to be due to the spatial lack of resolution of the mass transfer measurement technique. However, the area-averaged results compare with reasonable agreement. The discrepancies are in the order of magnitude of the measurement uncertainties.

This comparison allows gaining confidence in both measurement results. Furthermore, both heat and mass transfer data sets are complementary. Indeed, heat transfer results give a better resolution in particular regions of the baseline configuration. Mass transfer measurements were also performed in models in rotation, giving information on the impact of rotation-induced Coriolis forces on the mass transfer distribution (readers are referred to Rathjen [108] for details).

A.2.3 Straight channel results

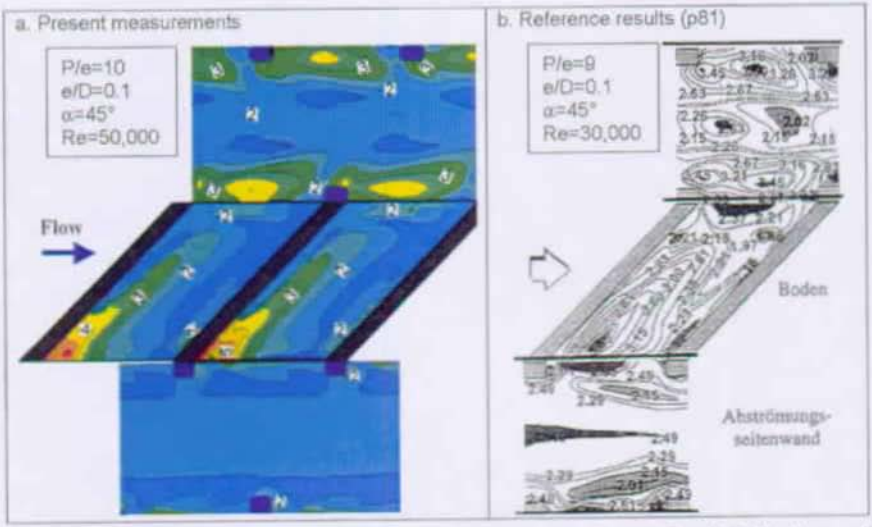

Figure 93: Full surface heat transfer comparison of present results with Rau [110] (bottom wall and sidewalls).

Nu/Nu_0	Bottom wall	Side wall	Web
Present results	2.38	2.56	1.75
Reference	2.4	2.6	2.3

Table 12: Area-averaged heat transfer results: present baseline configuration (Re=25,000) and p81 of Rau [110] (Re=30,000).

Figure 93 shows a comparison of full surface heat transfer results, between the present baseline configuration results (Figure 93a) and results from Rau [110] (Figure

93b). Figure 93a is identical to Figure 92a. Rau [110] made steady state liquid crystal heat transfer measurements in a straight channel with 45° ribs on two walls. The ribs were symmetrically distributed. The Reynolds number was set to 30,000, the pitch over height ratio was 9.

Even though the internal channel geometries are not exactly similar, results on both figures are comparing well. The Nu/Nu_0 levels are of the same order of magnitude over the surface. The high and low heat transfer regions are located at the same place and have the same shape. Small differences occur on the sidewall in the location of the high heat transfer regions. Bigger differences are present on the web, where a region of high heat transfer at mid channel height in Rau [110] does not take place in the baseline configuration.

Table 12 gives an indication of area-averaged results in Rau [110] (Re=30,000), compared to results taken in the rib module of Figure 93a, at Re=25,000. Nu/Nu_0 values are very close between both experiments, except on the web. This can be attributed to several reasons. First the baseline web is located downstream of the bend, thus is not as representative of the straight channel as the other walls. However, mass transfer measurements in A.2.2 showed that Sh/Sh_0 is 27% lower on the web than on the outer wall. This is in agreement with present heat transfer results. Second Rau [110] results on this wall present unexplained differences between the one-wall-ribbed channel and the two-wall-ribbed channel, which could be due to measurement errors. Finally, the channel geometries are different and could yield different results. This last reason does not seem to be realistic since both bottom and sidewall results are comparable.

The conclusions from this comparison can be drawn as follow. The heat transfer contour shape (especially on the ribbed walls) in the fully developed region seems to be influenced first by the rib angle. In a second order, it seems to be influenced by Reynolds number, staggered or symmetrical arrangement, P/e and e/D_H. It is also noted that the staggered arrangement modifies the heat transfer on the sidewalls, but not on the ribbed walls. Finally, this comparison increases the confidence in the present measurement technique.

A.3 Conclusions

A comparison of the present results has been performed with several previous works, concerning the area-averaged results on the one hand, and the full surface detailed heat transfer distribution on the other hand.

- Values from the well-known Han's correlations were compared to the present area-averaged values in the fully developed region. The correlations are derived directly from measurements or from heat-momentum transfer analogy. Although the ranges of the correlations have been extended beyond the range of Han's correlations, present measurement values only present a 5-8% difference compared to the correlations.
- Rathjen [108] performed mass transfer measurements in a similar channel to the present study (scaled by a factor 1/3). Reynolds number and geometrical characteristics were identical to the present work. The area-averaged mass transfer results are 10% different from the present heat transfer results, all along the zone of common measurement.

- Rathjen [108] full surface mass transfer distribution was compared in the fully developed region and in the bend region. The normalised heat and mass transfer results are of the same level in the major part of the channel. Mass transfer measurements showed a lower accuracy in predicting distribution details. This was mainly due to the lower spatial resolution of this technique.
- Rau [110] performed steady state TLC measurements in a straight channel with parallel 45° ribs. A difference of less than 5% was noted with the present results, although the configurations tested were not exactly similar.

The conclusions of the various comparisons can be summarised as follows. The heat transfer distribution is given in details by the TLC methods. Note that these details needs to be accurately predicted by CFD codes, in order to be able to use 3D codes in the cooling channel design. Despite discrepancies in the heat transfer details given by the mass transfer technique, area-averaged results are identical for all the measurement techniques, if one takes into account the measurement accuracies.

B Flow characteristics bend region cross sections

Kinetic turbulent energy, mean streamwise velocity contours and secondary flow vectors were obtained in the four configurations at $\theta = 0°$, 45°, 90°, 135° and 180° in the bend. They can be compared to Figure 40, which refers to the baseline configuration.

Configuration-1

Figure 94 shows the secondary flow characteristics in configuration-1. One characteristic of the configuration-1 geometry is the inclination of the bend outer wall, (also called back wall), at 30° to the straight legs. The flow field is significantly modified by this geometrical characteristic.

At θ=0°, the flow is similar to the fully developed flow except near the bend where it has begun to accelerate, indicating that it has entered the bend region.

At θ=45°, the cross section is at its smallest in the configuration, due to the angled the back wall end the distance from the divider tip to the back wall along x-axis kept to $1D_H$. The flow field has to adapt to this surface reduction. The streamwise velocity increases near the bend up to values of 2 times the bulk velocity. The secondary flow undergoes the effects of the curvature, but the four Dean vortices noticed in the baseline geometry are not detectable. The secondary flow impinges on the back wall at $Y < 0.15$ and is strongly directed towards the top wall along the back wall for $Y > 0.15$.

At θ=90°, the surface has increased to $1D_H^2$. The streamwise flow pattern is similar to the one at 45°; the maxima are lower because of the deceleration. The slow ($<0.8U_b$) streamwise velocity region already present near the back wall has increased. The secondary flow shows to be dominated by the curvature, and a vortex evolves in the upper corner near the web tip, accompanied by a high turbulent kinetic energy (>10%). The secondary flow impinges on the back wall all along the back wall; it is responsible for the high heat transfer noticed in this region in Figure 71.

At θ=135°, the flow undergoes the curvature and the back wall angle. Due to the strong curvature, a detachment occurs all along the web tip ($r < 0.1$). The zone of high shear leads to high values of k ($k > 10\%$). Another adverse pressure gradient occurs in the bend outer corner, yielding a large recirculating cell of approximately $0.5D_H$. Note that the turbulent kinetic energy here, is low ($k < 2.5\%$); regions of hot spot are expected in the outer corner.

At θ=180°, the secondary flow is still dominated by the bend influence. The recirculating area near the web is still active and covers the entire divider height. The high kinetic energy is directed towards the outer wall, with peak values around 2 times U_b, at $Z = 0.6$. The shear region between the recirculating and the zones of high velocity is a region of high stress, and as a consequence a region of high turbulent kinetic energy. Note that immediately downstream of the first rib on the top wall, the secondary flow field begins to recover from the bend effect, with the presence of the upper vortex directing the fluid towards the outer wall.

Configuration-2

Figure 95 shows the flow characteristics in cross-sections of the configuration-2

bend. The flow in the bend starts with the secondary structure from the ribs at θ=0°. At θ=0°, the streamwise velocity distribution and the secondary flow patterns in the centre region show the effects of the bend. The streamwise flow near the inner web has begun to accelerate, indicating that this flow has entered the bend region. In configuration-2, the secondary flow near the outer wall is mainly directed towards the bottom wall and is not symmetrically distributed about $Y = 0.5$ as in the baseline case. The main impact is the inclusion of a high streamwise velocity core in the channel centre region. Note that near the web the secondary flow vectors are towards the web.

At θ=45°, the streamwise velocity increases to more than 2 near the inner web, and has a small region of negative velocities in the lower outside corner region. The high streamwise velocity near the inner web is compatible with the conservation of angular momentum in the bend region. The secondary flows are very different from the baseline case, to the configuration-2 case. In the latter, instead of the four Dean vortices present in the baseline case, only two counter-rotating vortices occur. They have the same rotating direction as the two baseline case upper vortices, and their size are approximately twice bigger. Note that near the web, the secondary flow vectors are directed away from the web in both configurations.

At θ=90°, the streamwise velocities of the flow have decreased near the web. The two secondary cells are still present, but their locations have been strongly modified by the bend-induced flow.

At θ=135°, the flow has separated from the web and the streamwise velocities are negative. The streamline velocity contours are similar to the baseline configuration. The streamwise velocity has a negative value near the outer wall, indicating a small recirculation cell.

At θ=180°, a small region of recirculation occurs near the web and the lower wall. The rib induced secondary flow motion is redeveloping. The streamwise profiles are very similar to the baseline configuration; the effect of the flow extraction is, however increasing, yielding smaller streamwise velocity magnitudes. Note that the highest streamwise velocities have moved from near the web to the outer half of the passage, and are 1.5 to 2.0 times the bulk velocity. The secondary flow is very different from the baseline configuration; the flow goes from the top to the bottom wall along the web, crosses the channel up to the top outer wall, and goes down to the bottom wall along the outer wall. This phenomenon is similar to that encountered in the upper half of the baseline secondary flow motion.

Note that high turbulent kinetic energy values are still located in region of high shear, i.e. in region of high streamwise velocity gradients. It is as high as 10% in the corner near the web in the bend inlet ($\theta \leq 90\text{deg}$), and in the shear region of the separation bubble near the web tip in the second half of the bend ($\theta \geq 90\text{deg}$).

Configuration-3

Figure 96 shows the effect of the configuration-3 bend geometry on the flow field. The guide vane in the bend has highly modified the flow field in this region. Due to a poor optical access through the guide vane, the measurements are only given in the $r > 0.7$ region.

At θ=0°, the streamwise component reaches peak values of 2 times U_b, in the area $Y \geq 0.4$, indicating that the presence of the guide vane accelerates the flow field. The vortex part located between the guide vane and the outer wall, is identifiable in

the secondary vector field. The flow is directed from the top wall towards the bottom wall near the outer wall and in the opposite direction near the guide vane, verifying the continuity.

At θ=45°, the cross section surface has increased, modifying the flow structure. The diffuser shape down slows the flow (max $U_\theta \approx 1.6U_b$), and creates small detachment areas near the outer wall and the guide vane. A curvature induced secondary vortex is identifiable in the corner between the guide vane and the top wall. It is in contra rotation from the main one. These flow modifications create parallel zones of high turbulent kinetic energy.

At θ=90°, the flow has been modified because of the strong curvature and because of the cross section reduction. The curvature-induced vortices present at θ=45°, are equally distributed each side of the $Y = 0.5$ plane. The change in size of the lower vortex is attributed to the flow being sucked down by the extraction. The flow is also accelerated by the cross section reduction; zones of high streamwise velocities are located in the outer corners, with peak values of $1.5U_b$. The favourable pressure gradient created by the extraction leads to a larger area of streamwise component peak values near the bottom wall. Note that the streamwise velocity maxima are lower than at θ=45°, indeed the extracted flow through the first two holes, has decreased the duct massflow by 5%.

At θ=135°, both the extraction and the diffuser shape between the guide vane and the outer wall, have created important flow modifications from θ=90°. A low streamwise velocity region ($<0.2U_b$) near the guide vane is located near the guide vane, accompanied with a small recirculation bubble. The secondary vector field shows that the 90° contra rotating vortex structure has disappeared and is replaced by two other contra rotating vortices rotating in opposite directions.

At θ=180°, the flow is accelerated again. The recirculating bubble isn't present and the secondary flow pattern is similar to 135°, with smaller sizes.

The turbulent kinetic energy remains homogeneous along the bend, with values comparable to the values inside the upstream leg, indicating that the flow is stabilised by the curvature- and extraction-induced accelerations.

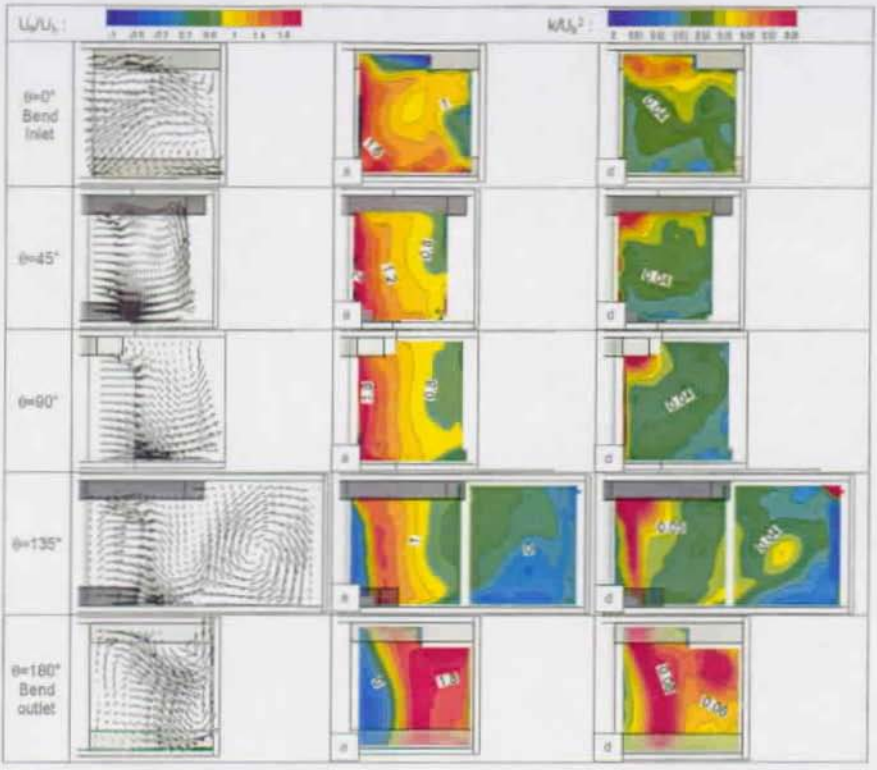

Figure 94: Configuration-1 turbulent kinetic energy, mean streamwise velocity contours and secondary flow vectors obtained at θ=0°, 45°, 90°, 135° and 180° in the bend, normalized by U_b (Re=50,000). (a: Streamwise velocity, U; d: Turbulent kinetic energy).

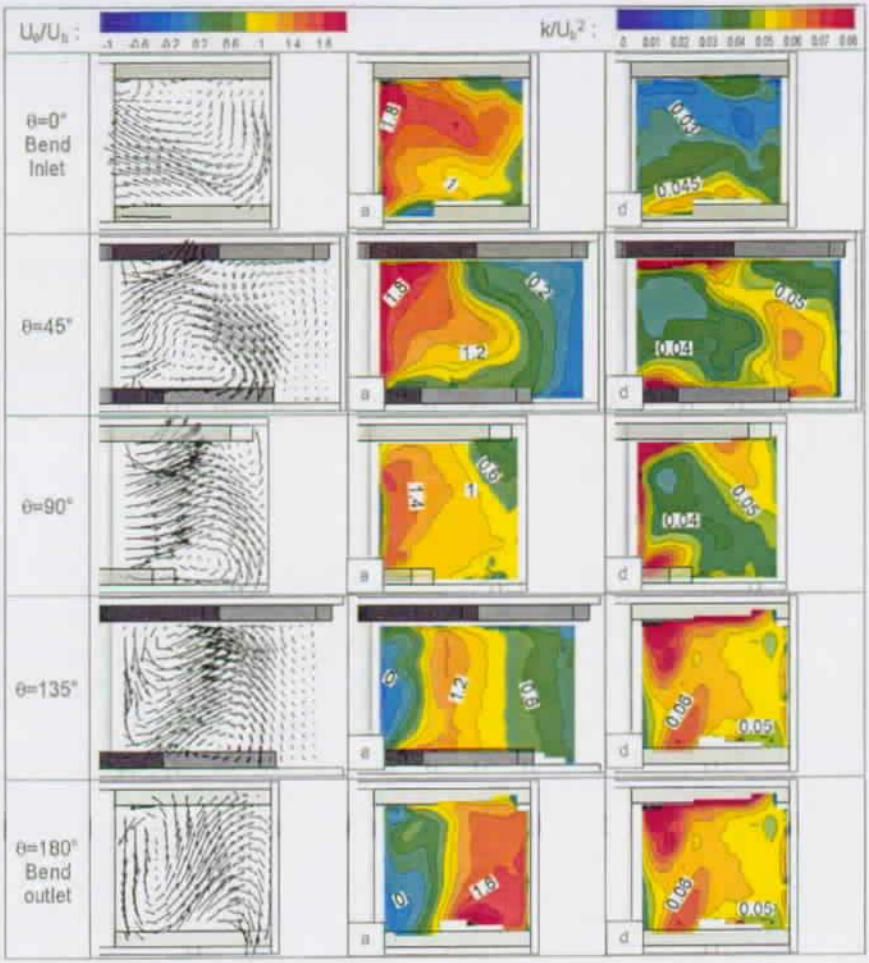

Figure 95: Configuration-2 turbulent kinetic energy, mean streamwise velocity contours and secondary flow vectors obtained at θ=0°, 45°, 90°, 135° and 180° in the bend, normalized by U_b (Re=50,000). (a: Streamwise velocity, U; d: Turbulent kinetic energy).

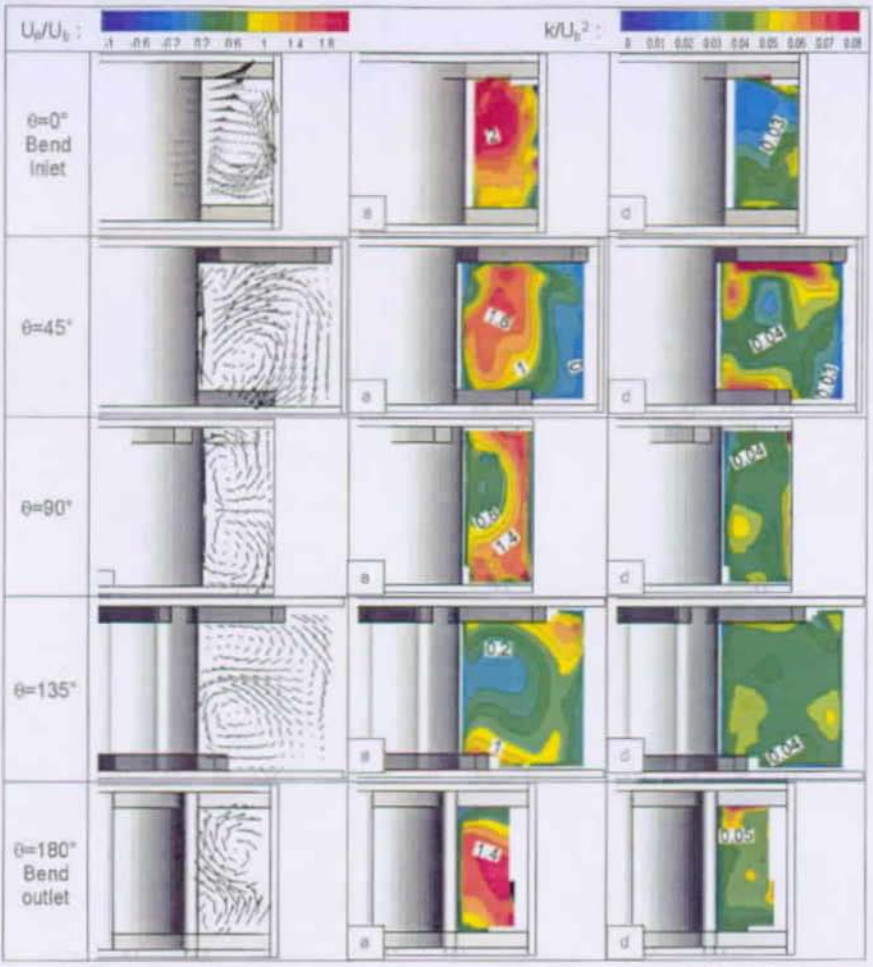

Figure 96: Configuration-3 turbulent kinetic energy, mean streamwise velocity contours and secondary flow vectors obtained at θ=0°, 45°, 90°, 135° and 180° in the bend, normalized by U_b (Re=50,000). (a: Streamwise velocity, U; d: Turbulent kinetic energy).

C Streamwise velocity profiles for the four studied bend geometries

The next four figures sum up the evolution of the streamwise velocity, from $3D_h$ upstream, inside and up to $4D_h$ downstream of the bend. Five slices are presented at various distances from the ribbed walls; the centre plane is located at $Y = 0.5$.

The periodic fully developed characteristics can be noticed in all the geometries, although differences are present between the configurations. These differences are mainly due to the geometrical parameters, which evolve from one configuration to another. The flow characteristics shown in the present appendix is to be related to the corner cell structures shown in 6.2.4 and 6.3.

The figures present the global shape of the flow field for a characterisation of CFD capabilities in predicting global flow field distribution in internal coolant passages. Predicting behaviour in the recirculating cell is an important issue. Indeed, they strongly influence the flow field in the whole channel and the cooling efficiency is highly dependent on the flow characteristics. The location and size of the recirculating cells, in the bend corners, must be accurately predicted. Indeed, the upstream corners lead to recirculating zones really different from the bottom wall to the top wall on one hand, and from one geometry to the other on the other hand.

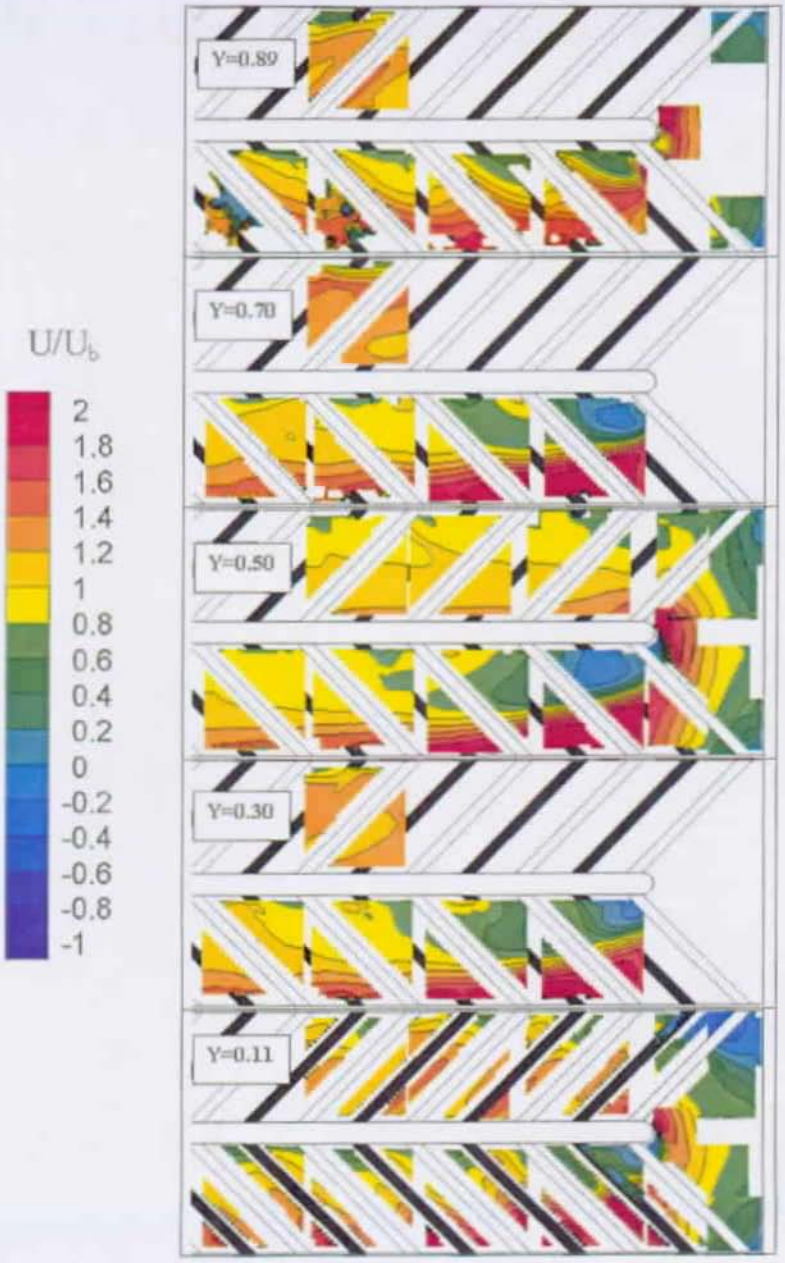

Figure 97: Baseline configuration streamwise velocity contours upstream, inside and downstream of the bend, -1.1 < X < 4.0 at five distances from the bottom wall (U / Ub, Re=50,000).

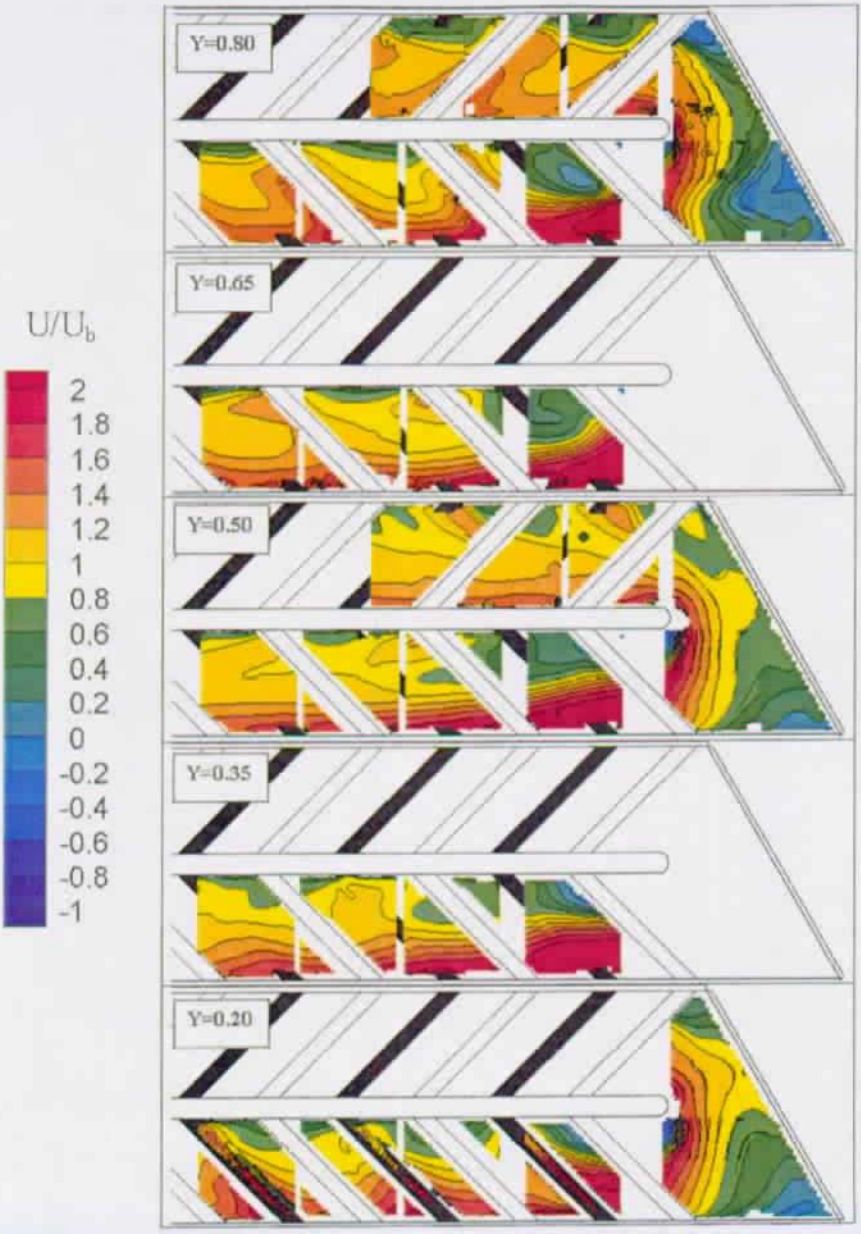

Figure 98: Configuration-1 streamwise velocity contours upstream, inside and downstream of the bend, -1.1 < X < 4.0 at five distances from the bottom wall (U / Ub, Re=50,000).

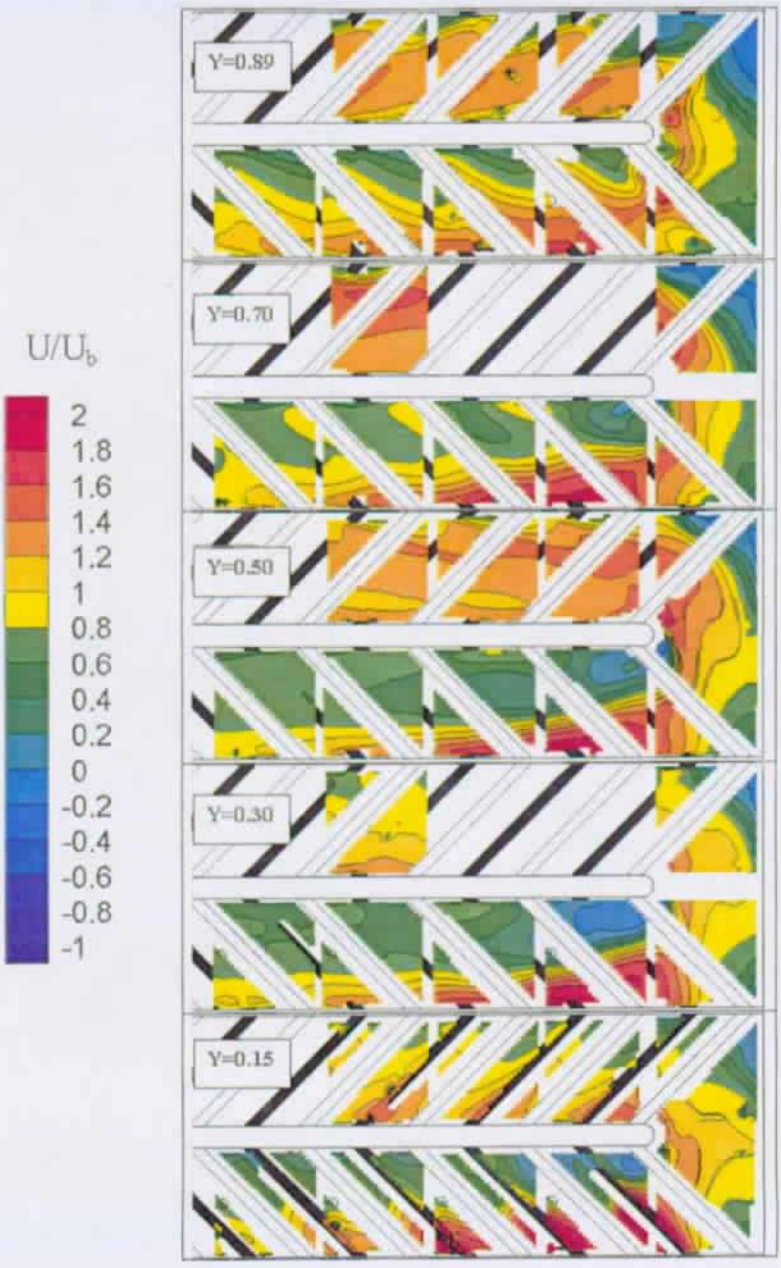

Figure 99: Configuration-2 streamwise velocity contours upstream, inside and downstream of the bend, -1.1 < X < 4.0 at five distances from the bottom wall (U / Ub, Re=50,000).

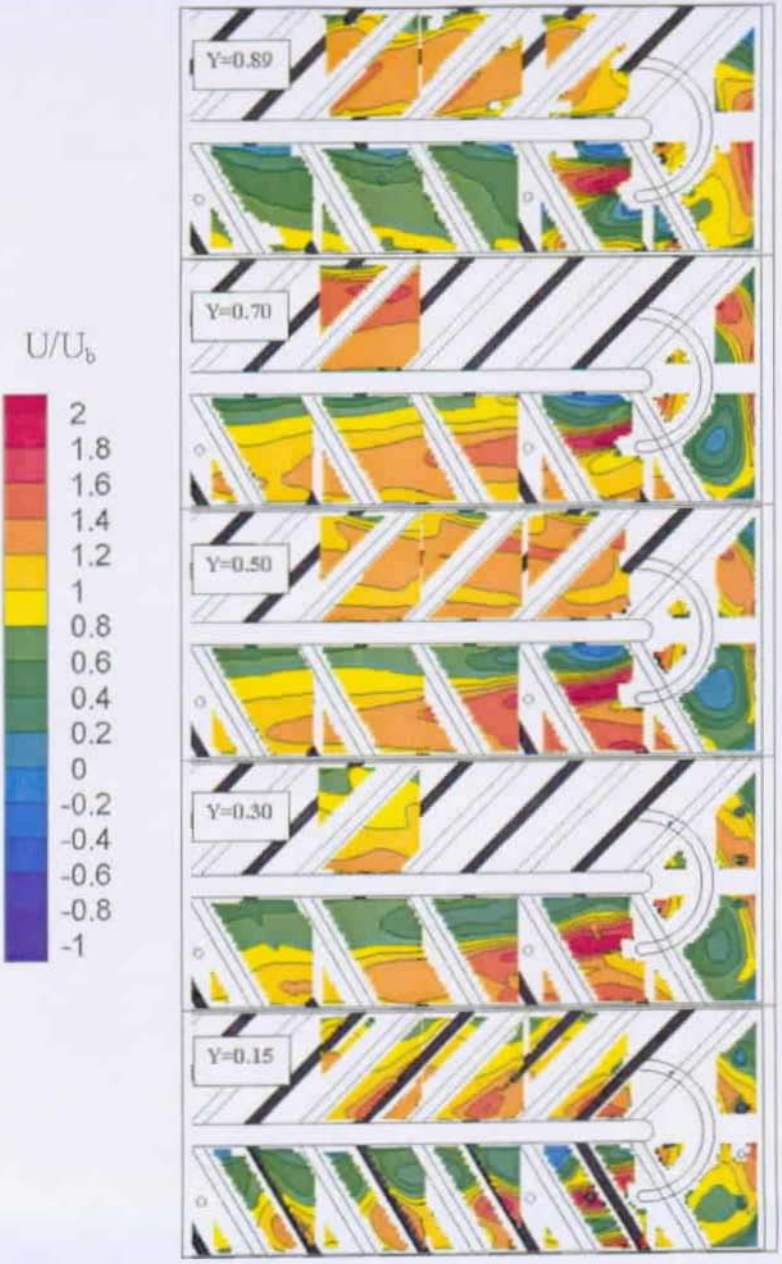

Figure 100: Configuration-3 streamwise velocity contours upstream, inside and downstream of the bend, -1.1 < X < 4.0 at five distances from the bottom wall (U / Ub, Re=50,000).

D Baseline configuration complementary results

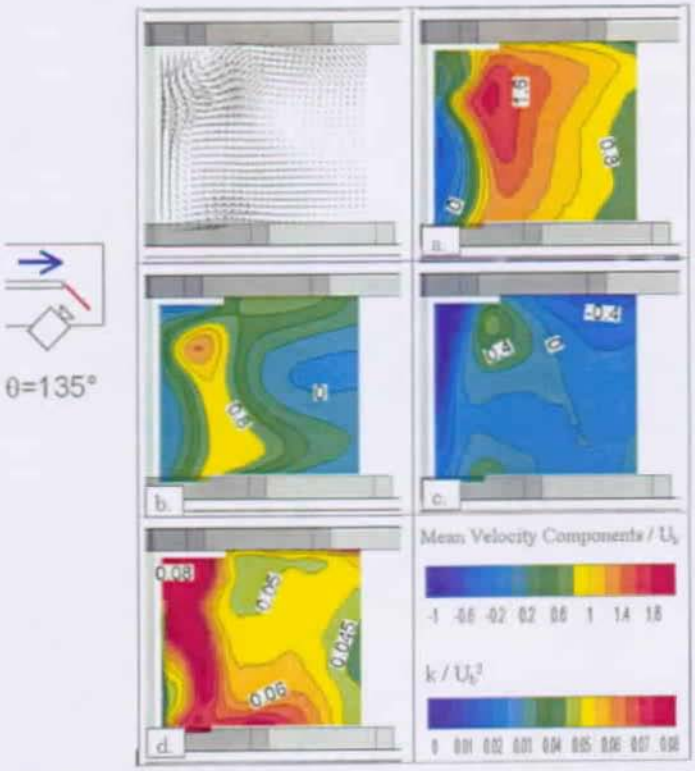

Figure 101: Baseline configuration velocity contours in plane θ=135°, normalized by Ub (Re=50,000). (a: Streamwise velocity, U; b: Velocity along Z-axis, W; c: Vertical velocity along Y-axis, V; d: Turbulent kinetic energy).

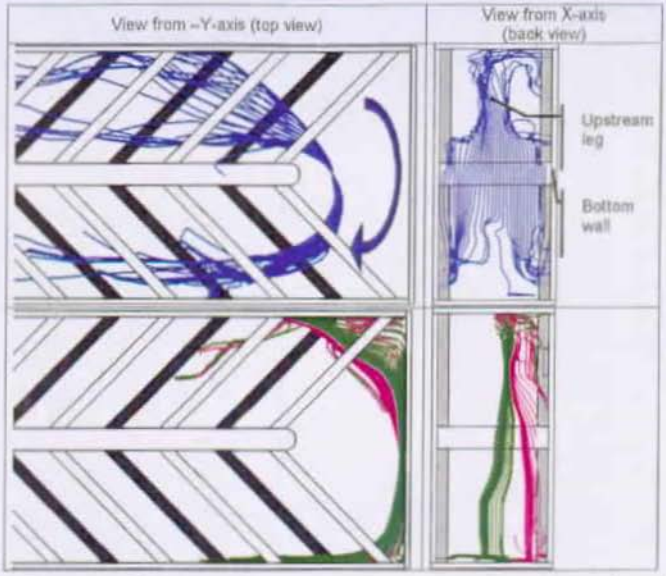

Figure 102: Examples of 3D-streamline evolution from the upstream to the downstream leg (baseline configuration).

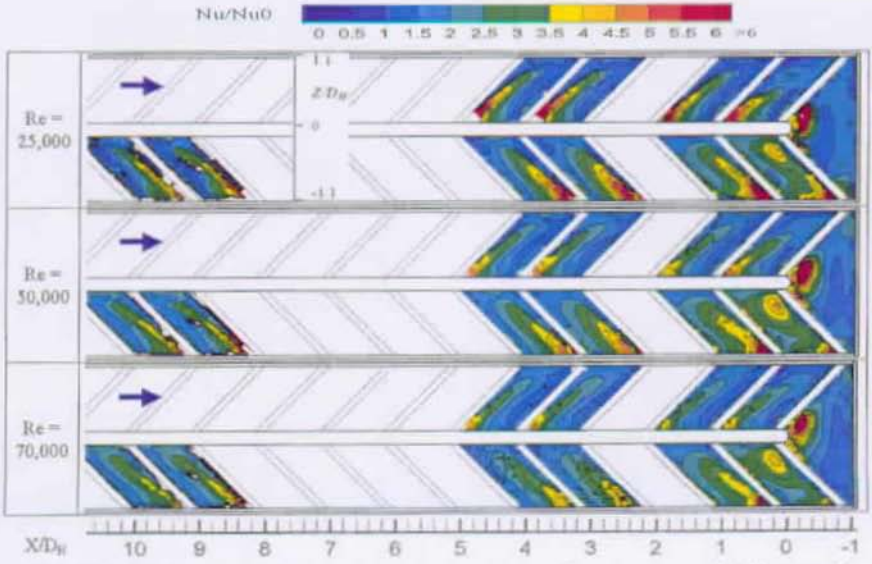

Figure 103: Full surface heat transfer on the baseline configuration top wall: Influence of Reynolds number.

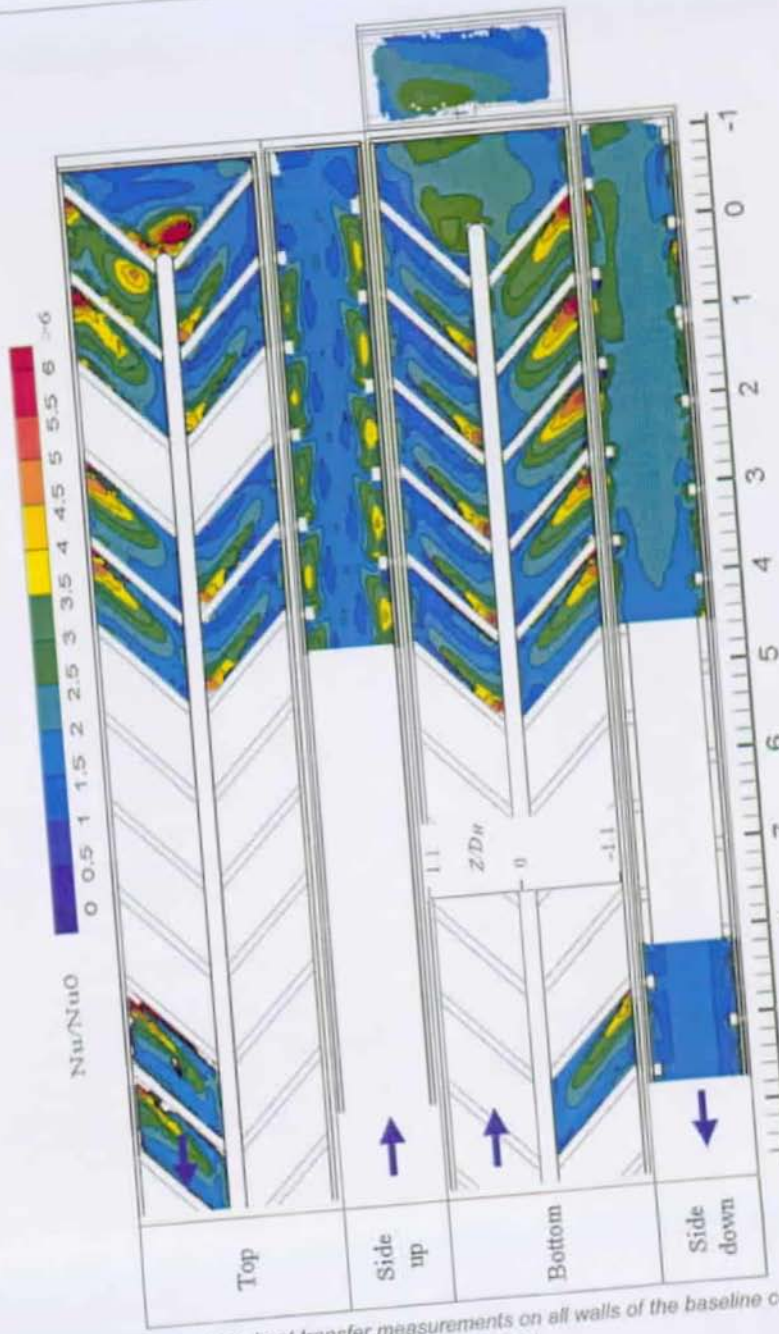

Figure 104: Full surface heat transfer measurements on all walls of the baseline configuration (Re=50,000).

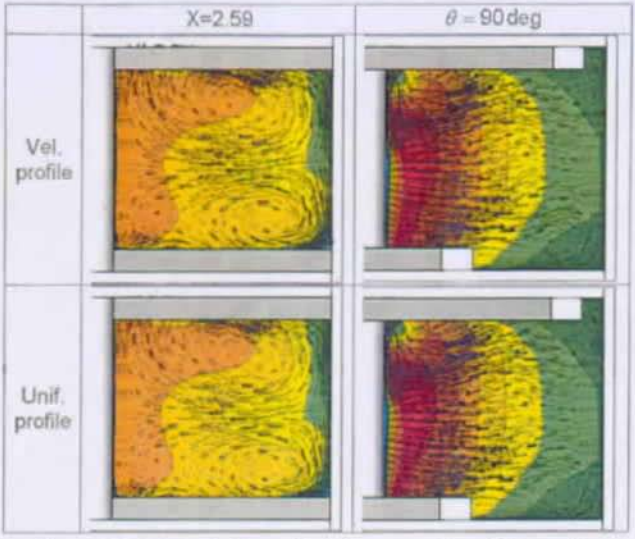

Figure 105: Inlet velocity profile influence on flow CFD results.

E Configuration-1 complementary results

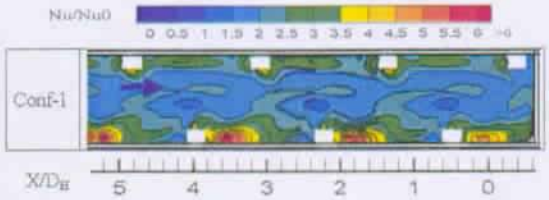

Figure 106: Full surface heat transfer distribution on the configuration-1 upstream outer sidewall (Re=50,000).

F Configuration-2 complementary results

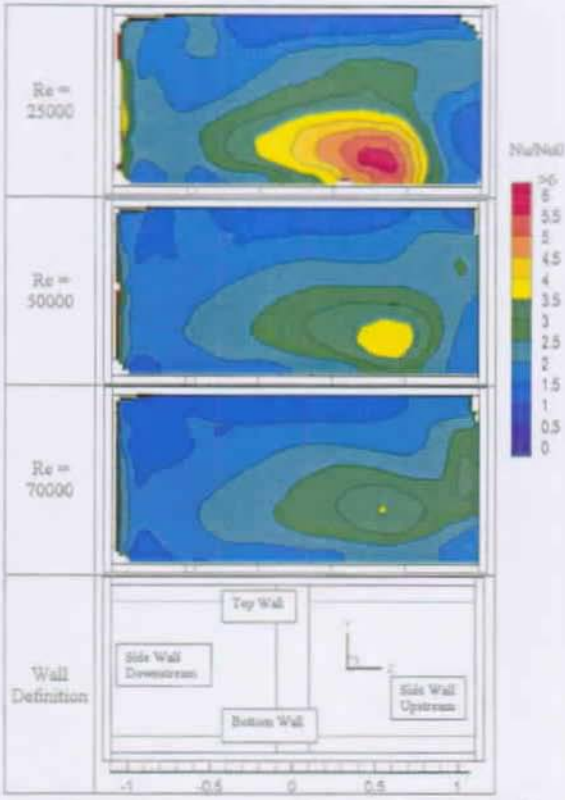

Figure 107: heat transfer distribution on the configuration-2 back wall: influence of Reynolds number.

G Configuration-3 complementary results

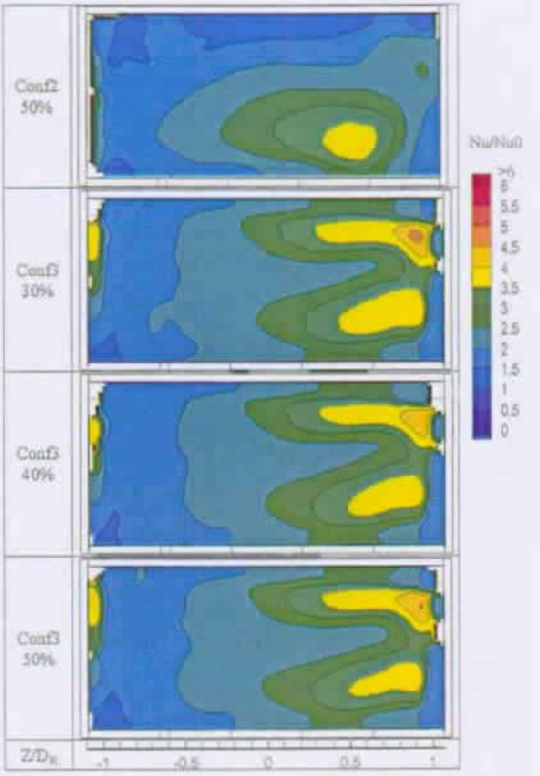

Figure 108: Extraction influence on the back wall. Full surface heat transfer in the configuration-3 (Re=50,000).

H List of references related to the present thesis work

Several publications have been performed during this PhD work. These references give further details on the results shown in the present report.

Chanteloup and Bölcs [22]
Chanteloup and Bölcs [20]
Chanteloup and Bölcs [25]
Chanteloup et al. [26]
Chanteloup and Bölcs [24]
Chanteloup and Bölcs [23]

Denis CHANTELOUP
October 27, 1974
French
Single

TRAININGS AND WORK EXPERIENCE:

From 1998	**EPF Lausanne, Laboratoire de Thermique Appliquée et de Turbomachines** PhD thesis: "Experimental Investigation of Heat Transfer and Flow Characteristics in Various Geometries of 2-pass Internal Cooling Passages of Gas Turbine Airfoils"
1998	**Alstom** (former ABB, corporate research centre in Baden-Dättwil, Switzerland) Diploma work: "Mise en Place et Validation d'un Système de Mesure par PIV en Vue de l'Etude du Refroidissement par Jet Impactant des Aubes de Turbines à Gaz"
1997	**DLR** (German space institut, Göttingen, Germany)
1996	**CNPE**, Creys Malville, Isère, France (Super Phœnix nuclear power plant) **SCHNEIDER ELECTRIQUE**, Grenoble, France

EDUCATION:

From 1998	**EPF Lausanne**, PhD student in the "Laboratoire de Thermique appliquée et Turbomachines ». Supervisor : professor Albin BOELCS
1995-1998	**Ecole Centrale de Lille**, France, engineering studies, fluid mechanics speciality (graduated in 1998)
1992-1995	**Lycée Champollion**, Grenoble, Isère, France. Preparation for the "concours des grandes écoles" (Engineering school contest)

RELATED SKILLS:

Languages	French	mother tongue
	English	fluent English
	German	working knowledge of German